GEOCHEMICAL CONTROLS OF THE MICROBIALLY MEDIATED REDOX CYCLING OF URANIUM AND IRON

A Dissertation
Presented to
The Academic Faculty

by

Keaton Michael Belli

In Partial Fulfillment
of the Requirements for the Degree
Doctor of Philosophy in the
School of Earth and Atmospheric Sciences

Georgia Institute of Technology
May 2018

GEOCHEMICAL CONTROLS OF THE MICROBIALLY MEDIATED REDOX CYCLING OF URANIUM AND IRON

Approved by:

Dr. Martial Taillefert, Advisor
School of Earth and Atmospheric Sciences
Georgia Institute of Technology

Dr. Thomas J. DiChristina
School of Biology
Georgia Institute of Technology

Dr. Joel Kostka
School of Earth and Atmospheric Sciences
Georgia Institute of Technology

Dr. Yuanzhi Tang
School of Earth and Atmospheric Sciences
Georgia Institute of Technology

Dr. Philippe Van Cappellen
Department of Earth and Environmental Sciences, Water Institute
University of Waterloo

Date Approved: April 3, 2018

ACKNOWLEDGEMENTS

I would like to thank my advisor, Dr. Martial Taillefert, for his support and guidance over the past 7 years. I would not be writing this today were it not for your zeal for science, especially field work, which initially sparked my interest in research. Thank you for fostering within me a sense of scientific independence and encouraging me to pursue my own ideas, even when they led me to many dead ends and eventually to Ethiopia.

Thank you to the rest of my thesis committee for your mentorship and expertise which have improved this body of work. Dr. Thomas DiChristina, your enthusiasm for science is contagious and has been a great source of inspiration. Dr. Philippe Van Cappellen, thank you for challenging me to approach problems from different perspectives and to never lose sight of the fundamentals. Dr. Yuanzhi Tang and Dr. Joel Kostka, thank you for your insights and for setting examples of scientific excellence.

To members of the Taillefert research group – Deidre, Colin, Morris, Lin, Kate, Jordon, Anna, Nicole, Eryn, Shannon, and Nan – thank you for your friendship and comradery during long hours both in the lab and aboard the R/V *Savannah*.

I am especially grateful for the rich friendships I have developed during my time at Georgia Tech. To Emily, Nadia, Mary, Jake, Jessica, Meg, and Dana, thank you for your support and encouragement over the years.

Finally, thank you to my family for your unwavering support, especially my parents, who made learning fun and nurtured my creativity at every opportunity. At this point, I think it is safe to conclude that it all paid off.

TABLE OF CONTENTS

ACKNOWLEDGEMENTS iii

LIST OF TABLES vii

LIST OF FIGURES ix

LIST OF SYMBOLS AND ABBREVIATIONS xxi

SUMMARY xxiii

CHAPTER 1. INTRODUCTION 1
1.1 Overview and motivations 1
1.2 Uranium chemistry and geochemical controls of uranium mobility 2
1.3 Interactions of uranyl with the mineral-water interface 7
1.4 Uranium redox transformations 9
1.4.1 Chemical redox processes 9
1.1.1 Biological redox processes 17
1.2 Effects of aqueous speciation on uranium reactivity 19
1.5 Remediation of uranium-contaminated subsurfaces 26
1.5.1 Physical remediation strategies 26
1.5.2 Chemical remediation strategies 27
1.5.3 Bioremediation strategies 30
1.6 Research scope and objectives 33

CHAPTER 2. MATERIALS AND METHODS 37
2.1 Cell cultures 37
2.2 Synthesis of iron oxides 38
2.2.1 2-line ferrihydrite 38
2.2.2 Al-substituted 2-line ferrihydrite 40
2.3 Analytical techniques 41
2.3.1 pH 41
2.3.2 Dissolved inorganic carbon (DIC) 41
2.3.3 Inductively-coupled plasma mass spectrometry (ICP-MS) 43
2.3.4 Colorimetry 44
2.3.5 Adenosine triphosphate (ATP) assay 46
2.3.6 Solid phase analyses 49
2.3.7 Voltammetry 50
2.4 Computational techniques 56
2.4.1 Geochemical equilibrium modeling using PHREEQC 56
2.4.2 Model parameter estimation using PEST 58

CHAPTER 3. EFFECTS OF AQUEOUS URANYL SPECIATION ON THE KINETICS OF MICROBIAL URANIUM REDUCTION 60
3.1 Abstract 60

3.2 Introduction 61
3.3 Materials and Methods 64
3.3.1 Cell cultures 64
3.3.2 Bioreduction incubations 65
3.3.3 Cell viability assays 67
3.3.4 Speciation-dependent biogeochemical kinetic model 68
3.4 Results 73
3.4.1 Effect of uranyl speciation on U(VI) bioreduction rates 73
3.4.2 Effect of uranyl speciation on cell viability 77
3.4.3 Biogeochemical kinetic model 81
3.5 Discussion 82
3.5.1 Lag phases 82
3.5.2 Effect of DIC, Ca^{2+}, and Mg^{2+} on U(VI) bioreduction rates 83
3.5.3 Effect of non-carbonate uranyl species on U(VI) bioreduction rates 86
3.5.4 Uranium toxicity 87
3.5.5 Mechanism of speciation-dependent U(VI) bioreduction 90
3.5.6 Implications for bioremediation 92
3.6 Conclusions 98
3.7 Acknowledgments 99

CHAPTER 4. GEOCHEMICAL CONTROLS OF THE MICROBIALLY MEDIATED REDOX CYCLING OF URANIUM AND IRON 100
4.1 Abstract 100
4.2 Introduction 101
4.3 Materials and methods 106
4.3.1 Cell cultures 107
4.3.2 Synthesis of 2-line ferrihydrite 107
4.3.3 Bioreduction Experiments 107
4.3.4 Analytical techniques 108
4.3.5 Pseudo-first order rate constant calculations 111
4.3.6 Thermodynamic calculations 111
4.3.7 Biogeochemical kinetic model 113
4.4 Results 117
4.4.1 Batch incubations with either U(VI) or ferrihydrite as the sole terminal electron acceptor 117
4.4.2 Batch incubations with U(VI) and ferrihydrite provided simultaneously as terminal electron acceptors 123
4.4.3 Characterization of the final iron solid phases 126
4.4.4 Biogeochemical kinetic model 128
4.5 Discussion 132
4.5.1 Effect of solution composition on uranium removal in the absence of ferrihydrite 132
4.5.2 Effect of ferrihydrite on uranium removal 134
4.5.3 Geochemical controls of iron as a reductant or oxidant of uranium 139
4.5.4 Implications for uranium bioremediation 143
4.6 Conclusions 144
4.7 Acknowledgements 146

CHAPTER 5. EFFECTS OF ALUMINUM-SUBSTITUTED FERRIHYRDITE ON THE MICROBIALLY MEDIATED REDOX CYCLING OF URANIUM 148
5.1 Abstract 148
5.2 Introduction 149
5.3 Materials and Methods 151
5.3.1 Synthesis of 2-line (Al-)ferrihydrite 151
5.3.2 Bioreduction incubations 151
5.3.3 Abiotic U(IV) oxidation incubations 152
5.3.4 Analytical techniques 153
5.3.5 Kinetic calculations 155
5.3.6 Thermodynamic calculations 156
5.4 Results 157
5.4.1 Bioreduction incubations amended with U(VI) and ferrihydrite as sole TEAs 157
5.4.2 Bioreduction incubations amended with both U(VI) and ferrihydrite 160
5.4.3 Characterization of the solid phase produced in the bioreduction incubations 163
5.4.4 Kinetics of abiotic U(IV) oxidation by (Al-)ferrihydrite 166
5.5 Discussion 166
5.5.1 Effect of Al-substitution on microbial reduction of ferrihydrite 166
5.5.2 Effect of Al-substitution on uranium and iron redox cycling 167
5.5.3 Mechanism of enhanced U(IV) oxidation by Al-ferrihydrite 170
5.5.4 Role of secondary mineralization in uranium removal 173
5.5.5 Environmental implications 174
5.5.6 Acknowledgements 174

CHAPTER 6. CONCLUSIONS 176
6.1 Recommendations for future work 181

APPENDIX A. SUPPLEMENTARY DATA FOR CHAPTER 2 184

APPENDIX B. SUPPLEMENTARY DATA FOR CHAPTER 3 189

APPENDIX C. SUPPLEMENTARY DATA FOR CHAPTER 4 215

APPENDIX D. SUPPLEMENTARY DATA FOR CHAPTER 5 256

REFERENCES 268

LIST OF TABLES

Table 2.1	Lysogeny broth (LB) medium composition	37
Table 2.2	Composition of stock solutions used to prepare M1 growth medium	39
Table 2.3	Method parameters for HMDE measurements	51
Table 2.4	Method parameters for Au/Hg microelectrode measurements	54
Table 3.1	Uranium bioreduction incubations: Solution composition, initial aqueous U(VI) speciation assuming thermodynamic equilibrium, and measured overall U(VI) bioreduction rates.	75
Table 3.2	Viability assays: Solution composition, aqueous U(VI) speciation assuming thermodynamic equilibrium, and survival rate.	79
Table 3.3	Optimized rate constants, toxic inhibition factor (F_{toxic}) parameters, and their 95% confidence limits for the speciation-dependent U(VI) bioreduction rate law.	83
Table 3.4	Solution composition, overall pseudo-first order rate constant (k_{obs}), toxic inhibition factor (F_{toxic}), and calculated thermodynamic parameters for bioreduction incubations over a range of U(VI) bioavailability.	85
Table 4.1	Reactions and equations included in the PHREEQC kinetic model	114
Table 4.2	Rate laws included in the kinetic model for the reactions listed in Table 4.1	114
Table 4.3	Optimized parameters for the PHREEQC kinetic model	130
Table 5.1	Measured concentration of initial adsorbed U(VI) (U_{ads}), measured final U:Fe molar ratio, and calculated final concentration of solid-associated uranium (U_{SA}) in incubations with *S. putrefaciens* containing both U(VI) and ferrihydrite as TEAs	161
Table A.1	Ferrihydrite surface complexation constants added to the PHREEQC database	184
Table A.2	Magnetite surface complexation constants added to the PHREEQC database	185

Table A.3	Mineral surface properties of iron oxides included in the PHREEQC surface complexation model	185
Table A.4	Solubility products (K_{sp}) of solid phases added to the PHREEQC database	186
Table A.5	Formation constants of aqueous complexes added to the PHREEQC database	186
Table B.1	Groundwater composition at DOE IFRC sites used in aqueous uranyl speciation calculations for Figure 3.5	191
Table C.1	Standard state redox potentials (E_h^0) for half-reactions of U(VI)/UO_2(am), $Fe(OH)_3$/Fe(II), and U(VI)/$U(IV)_{mono}$ redox couples used to calculate the overall E_h at each sampled time point	217
Table C.2	Surface complexation constants included in PHREEQC	218
Table C.3	Mineral surface properties of iron oxides included in the PHREEQC surface complexation model	219
Table C.4	Measured initial solution composition and calculated aqueous uranyl speciation assuming thermodynamic equilibrium in batch incubations with *S. putrefaciens*	219
Table C.5	Measured concentration of initial adsorbed U(VI), measured final U:Fe molar ratio, calculated final concentration of solid-associated uranium, and modeled final concentration of solid-associated uranium in *S. putrefaciens* incubations containing both U(VI) and ferrihydrite as TEAs	225
Table D.1	Composition of modified M1 medium	257
Table D.2	Measured initial solution composition and calculated aqueous uranyl speciation assuming thermodynamic equilibrium in batch incubations with *S. putrefaciens*	259

LIST OF FIGURES

Figure 1.1 Uranyl speciation as a function of pH at the US Department of Energy (DOE) Integrated Field Research Challenge (IFRC) site in Rifle, Colorado. For simplification, uranyl complexes with the same ligand but with different stoichiometries are presented as the summation of those species (ΣU(VI)-OH: UO_2OH^+, $UO_2(OH)_2^0$, $UO_2(OH)_3^-$, $UO_2(OH)_4^{2-}$, $(UO_2)_2OH^{3+}$, $(UO_2)_2(OH)_2^{2+}$, $(UO_2)_3(OH)_4^{2+}$, $(UO_2)_3(OH)_5^+$, $(UO_2)_3(OH)_7^-$, $(UO_2)_4(OH)_7^+$; ΣU(VI)-SO_4: $UO_2SO_4^0$, $UO_2(SO_4)_2^{2-}$, $UO_2(SO_4)_3^{4-}$; ΣU(VI)-Cl: UO_2Cl^+, $UO_2Cl_2^0$; ΣU(VI)-CO_3: $UO_2CO_3^0$, $UO_2(CO_3)_2^{2-}$, $UO_2(CO_3)_3^{4-}$, $(UO_2)_3(CO_3)_6^{6-}$, $(UO_2)_2CO_3(OH)_3^-$, $(UO_2)_3O(OH)_2(HCO_3)^+$, $(UO_2)_{11}(CO_3)_6(OH)_{12}^{2-}$; ΣCa-U(VI)-$CO_3$: $CaUO_2(CO_3)_3^{2-}$, $Ca_2UO_2(CO_3)_3^0$). Uranyl speciation was calculated in PHREEQC, updated with the most recent thermodynamic data for solid and aqueous uranyl species (Dong and Brooks 2006; Guillaumont et al. 2003), for 10 μM U(VI) using measured groundwater composition (3.3 mM DIC, 6.8 mM Na^+, 4.8 mM Ca^{2+}, 4.6 mM Mg^{2+}, 44 mM NH_4^+, 8.4 mM SO_4^{2-}, 2.8 mM Cl^-, 60 μM NO_3^- (Campbell et al. 2011; Zachara et al. 2013)). 5

Figure 1.2 Uranyl speciation with dissolved phosphate as a function of pH at the US DOE IFRC site in Oak Ridge, Tennessee. For simplification, uranyl complexes with the same ligand but with different stoichiometries are presented as the summation of those species (ΣU(VI)-OH: UO_2OH^+, $UO_2(OH)_2^0$, $UO_2(OH)_3^-$, $UO_2(OH)_4^{2-}$, $(UO_2)_2OH^{3+}$, $(UO_2)_2(OH)_2^{2+}$, $(UO_2)_3(OH)_4^{2+}$, $(UO_2)_3(OH)_5^+$, $(UO_2)_3(OH)_7^-$, $(UO_2)_4(OH)_7^+$; ΣU(VI)-SO_4: $UO_2SO_4^0$, $UO_2(SO_4)_2^{2-}$, $UO_2(SO_4)_3^{4-}$; ΣU(VI)-Cl: UO_2Cl^+, $UO_2Cl_2^0$; ΣU(VI)-CO_3: $UO_2CO_3^0$, $UO_2(CO_3)_2^{2-}$, $UO_2(CO_3)_3^{4-}$, $(UO_2)_3(CO_3)_6^{6-}$, $(UO_2)_2CO_3(OH)_3^-$, $(UO_2)_3O(OH)_2(HCO_3)^+$, $(UO_2)_{11}(CO_3)_6(OH)_{12}^{2-}$; ΣCa-U(VI)-$CO_3$: $CaUO_2(CO_3)_3^{2-}$, $Ca_2UO_2(CO_3)_3^0$; ΣU(VI)-PO_4: $UO_2PO_4^-$, $UO_2HPO_4^0$, $UO_2H_2PO_4^+$, $UO_2H_3PO_4^{2+}$, $UO_2(H_2PO_4)_2^0$, $UO_2(H_2PO_4)(H_3PO_4)^+$). Uranyl speciation was calculated in PHREEQC, updated with the most recent thermodynamic data for solid and aqueous uranyl species (Dong and Brooks 2006; Guillaumont et al. 2003), for 10 μM U(VI) using 1 mM DIC, 35 μM PO_4^{3-}, and measured groundwater composition (32.9 mM Na^+, 2.4 mM K^+, 25.1 mM Ca^{2+}, 6.8 mM Mg^{2+}, 10 μM Sr^{2+}, 7.3 mM Cl^-, 133 μM NO_3^-, 9.9 mM SO_4^{2-} (Wu et al. 2006a)). 6

Figure 1.3 Gibbs free energy of reaction (ΔG_r) as a function of pH for the reduction of UO_2^{2+} to UO_2(am) coupled to the oxidation of reduced (A) sulfur, (B) iron, (C) manganese, and (D) nitrogen in a typical uranium-contaminated groundwater (only 1 and 2 e^- transfer reactions were considered). A negative ΔG_r indicates that reduction 11

of UO_2^{2+} is thermodynamically favorable, while a positive ΔG_r indicates that the oxidation of UO_2(am) is thermodynamically favorable. ΔG_r ($\Delta G_r = \Delta G_r^0 + RT\ln(Q)$, where Q is the reaction quotient) was calculated using measured groundwater composition at the US DOE IFRC site in Rifle, Colorado (Campbell et al. 2011; Zachara et al. 2013). 'Free' hydrated UO_2^{2+} concentrations were calculated as a function of pH using PHREEQC, updated with the most recent thermodynamic data for solid and aqueous uranyl species (Dong and Brooks 2006; Guillaumont et al. 2003)). A concentration of 10 μM was used for HS^-, Fe^{3+}, Mn^{3+}, N_2, N_2O, NO, NO_2^-, and NH_2OH.

Figure 1.4 Redox potentials (E_h) of terminal electron acceptors for microbial respiration at the US DOE IFRC site in Rifle, Colorado. The right side is an expanded view of E_h for individual uranyl species, demonstrating the influence of uranyl speciation on the U(VI)/UO_2(am) redox potential. E_h was calculated with the Nernst equation ($E_h = E_h^0 - (RT/nF)\ln(Q)$, where Q is the reaction quotient) using groundwater composition at the Rifle site (Campbell et al. 2011; Zachara et al. 2013). Uranyl speciation was calculated as a function of pH using PHREEQC, updated with the most recent thermodynamic data for solid and aqueous uranyl species (Dong and Brooks 2006; Guillaumont et al. 2003). A concentration of 10 μM was used for N_2 and HS^-. 21

Figure 1.5 Schematic of biogeochemical processes controlling the mobility of uranium in the subsurface. Abbreviations: P_{org}HB, organophosphate hydrolyzing bacteria; FeOB, iron-oxidizing bacteria; MRB, metal-reducing bacteria; SRB, sulfate-reducing bacteria. 25

Figure 2.1 Typical (A) signal output (11-point moving average) and (B) calibration curve for dissolved inorganic carbon (DIC) measurements using flow injection analysis with conductivity detection. Note that the blank peak area value has been subtracted from all standards and the slope of the linear regression has been forced through the origin. 42

Figure 2.2 Typical (A) signal output and (B) calibration curve for ICP-MS measurements of total dissolved uranium. A 500 ppt U standard (blue) was run periodically as a quality control, and Ho (black) and Bi (red) were used as internal standards to correct the signal for instrument drift. Recovery of the quality control (open circles) was 96 – 103% for the data shown. Note that the blank signal value has been subtracted from all standards and the slope of the linear regression has been forced through the origin. Symbols and error bars represent the mean and instrument precision (n=3), respectively. 43

Figure 2.3 Typical calibration curve for ATP using the Promega BacTiter-Glo™ Microbial Cell Viability Assay. The same calibration curve is represented on a (A) linear and (B) logarithmic scale to demonstrate the linearity of the signal over a large range of ATP concentration. Note that the blank signal value has been subtracted from all standards and the slope of the linear regression has been forced through the origin. 48

Figure 2.4 A) Voltammograms showing the appearance of three distinct peaks at pH 2 (-0.2 V), 6 (-0.6 V), and 9 (-1.2 V) in a solution of 100 μM uranyl acetate and 10 mM $NaHCO_3$. B) Percent normalized peak surface area was compared to percent uranyl speciation to identify the peaks at -0.2, -0.6, and -1.2 V as UO_2^{2+}, $UO_2(CO_3)_2^{3-}$, and $UO_2(CO_3)_3^{4-}$, respectively. 52

Figure 2.5 A) Calibration curve for UO_2^{2+} in 30 mM $NaHCO_3$ (pH 2.6). B) Calibration curve for $UO_2(CO_3)_3^{4-}$ in 30 mM NaHCO3 (pH 8.92). Inset figures show voltammograms for each calibration standard. 53

Figure 2.6 Times series of total dissolved uranium (U_d, by ICP-MS) and $UO_2(CO_3)_3^{4-}$ (by voltammetry) and concentrations in U(VI) bioreduction incubations with *S. putrefaciens* correlate strongly (R^2 = 0.99), thus validating the newly developed technique. Closed symbols represent biotic incubations whereas open symbols represent abiotic controls. Error bars represent the standard deviation from duplicate incubations. 55

Figure 3.1 Averaged, time-corrected total dissolved uranium concentration time series in duplicate bioreduction incubations conducted without added Ca^{2+} and Mg^{2+} at pH (A) 6.5, (B) 7.5, and (C) 8.1 in the presence of various concentrations of DIC, and amended with various concentrations of (D) Ca^{2+} and (E) Mg^{2+} at pH 8.1 in the presence of a constant DIC concentration. Symbols represent measured values and solid lines represent optimized model outputs. Error bars represent duplicate incubations. 74

Figure 3.2 Viability assays of *S. putrefaciens* following 6 hours of exposure to 1 mM U(VI) at pH 7.2±0.2 with various concentrations of DIC, Ca^{2+}, and Mg^{2+}. Shown is cell density as a function of time (growth curves) in the presence of (A) 10 mM (■), 30 mM (○), and 50 mM (▲) DIC; (B) 10 mM DIC and 0 mM (■), 1 mM (○), and 5 mM (▲) Ca^{2+}; and (C) 10 mM DIC and 0 mM (■), 1 mM (○), and 5 mM (▲) Mg^{2+}. Dashed lines represent cell density as a function of time for control cells not exposed to U(VI). Error bars represent duplicate assays. Cells were grown anaerobically on fumarate as TEA and lactate as electron donor in M1 medium. 78

Figure 3.3 Correlation between survival rate of *S. putrefaciens* and the concentration of the sum of all uranyl non-carbonate species in viability assays of cells exposed to 1 mM U(VI) at pH 7.2±0.2 in the presence of various concentrations of DIC, Ca^{2+}, and Mg^{2+}. A two-parameter logistic function (Equation 3.9) was fitted to the data (R^2 = 0.97). Nearly identical correlations are observed between survival rate and concentrations of select individual uranyl non-carbonate complexes (e.g. UO_2^{2+}, UO_2OH^+, $(UO_2)_2OH_3^+$). Standard deviations represent propagated error from fitting the exponential region of growth curves. 81

Figure 3.4 Measured (○) and modeled (●) overall pseudo-first order rate constants (k_{obs}) versus the sum of the concentrations of (A) non-carbonate, (B) carbonate, and (C) ternary carbonate U(VI) species for all incubation conditions. Error bars represent the standard deviation of the slope of the linear regression used to obtain k_{obs} from averaged duplicate incubations or model output. 93

Figure 3.5 Calculated aqueous uranyl speciation (lines) and bioreduction rate (●) as a function of pH using background groundwater composition at the (A) Hanford, (B) Rifle, and (C) Oak Ridge US Department of Energy (DOE) Integrated Field Research Challenge (IFRC) sites (Table B.1), assuming a 3 mM acetate injection to stimulate metal-reducing bacteria. Solid vertical lines represent the minimum and maximum measured pH at each site. Bioreduction rates were calculated using the proposed biogeochemical kinetic model and the optimized model parameters (Table 3.3). 95

Figure 4.1 Time series of (A-C) dissolved uranium (U_d), (D-F) total Fe(II) ($Fe(II)_T$), (G-I) dissolved Fe(II) ($Fe(II)_d$), and (J-L) ascorbate-extractable solid phase iron (Fe_{asc}) in incubations amended with either 180 µM U(VI) (blue), 5 mM ferrihydrite (orange), or both (green) as terminal electron acceptors, and either 20 mM (circles) or 40 mM (triangles) DIC only (left), DIC and 800 µM calcium (center), or DIC and 300 µM silica (right). Filled symbols and lines represent biotic incubations with *S. putrefaciens* (inoculated at t=0) whereas open symbols represent abiotic controls. Symbols and error bars represent the average and standard deviation from triplicate incubations. 118

Figure 4.2 Pseudo-first order rate constants (k_{obs}) of the initial (A) removal of dissolved uranium (U_d) and (B) production of total Fe(II) ($Fe(II)_T$) in incubations of *S. putrefaciens* amended with either 180 µM U(VI) (blue), 5 mM ferrihydrite (orange), or both (green) as terminal electron acceptors, and either 20 mM (solid bars) or 40 mM (hashed bars) DIC only, DIC and 800 µM calcium (+Ca), or DIC and 300 µM silica (+Si). Values of k_{obs} were calculated for individual incubations 121

and presented as the average and standard deviation for each condition (n=3).

Figure 4.3 Powder X-ray diffraction (XRD) patterns of solid phase products in incubations amended with 5 mM ferrihydrite (+Fe) or both 180 μM U(VI) and 5 mM ferrihydrite (+U+Fe) as terminal electron acceptors, and either 20 or 40 mM (A-D) DIC-only, (E-H) DIC and 800 μM calcium (+Ca), and (I-L) DIC and 300 μM silica (+Si). Black lines represent biotic incubations and grey lines represent abiotic controls. Signals are normalized to the maximum intensity in each condition and smoothed using a 10-point moving average. Peaks are indexed with M for magnetite, L for lepidocrocite, and S for siderite. 127

Figure 4.4 Measured and modeled time series of DIC-only incubations conducted with *S. putrefaciens* in the presence of 5 mM ferrihydrite and 180 μM U(VI) as terminal electron acceptors and (A, C, and E) 20 mM or (B, D, and F) 40 mM DIC. The same experimental data are presented in Figure 4.1. Symbols represent measured concentrations of dissolved uranium (U_d) (circles), dissolved Fe(II) ($Fe(II)_d$) (triangles), and total Fe(II) ($Fe(II)_T$) (squares). Lines represent output of the kinetic model using the optimized rate parameters from Table 4.3. (C and D) Dashed lines representing solid phase iron species are indexed with Fh for ferrihydrite, Mag for magnetite, and Sid for siderite. The solid line represents the sum of the amorphous iron species (i.e., ferrihydrite and magnetite). (E and F) The solid line represents the Gibbs free energy of reaction (ΔG_r) for the oxidation of monomeric U(IV) by ferrihydrite calculated by the model at each time step. The dashed line represents the threshold ΔG_r, above which adsorbed U(VI) is reduced by adsorbed Fe(II) and below which monomeric U(IV) is oxidized by ferrihydrite. 131

Figure 4.5 Pseudo-first order rate constants (k_{obs}) of uranium removal versus the initial concentration of uranyl non-carbonate species in incubations of *S. putrefaciens* amended with either 180 μM U(VI) (+U, open symbols) or both 180 μM U(VI) and 5 mM ferrihydrite (+U+Fe, closed symbols) as terminal electron acceptors and either 20 mM (circles) or 40 mM (triangles) DIC only (red), DIC and 800 μM calcium (blue), or DIC and 300 μM silica (purple). Arrows indicate the effect of ferrihydrite on k_{obs} and aqueous uranyl speciation. Values of k_{obs} were calculated for individual incubations and presented as the average and standard deviation for each condition (n=3). 133

Figure 4.6 Time series of calculated (A-C) $U(VI)/U(IV)_{mono}$ and (D-F) $Fe(OH)_3/Fe(II)$ redox potentials (E_h) at each sampled time point in incubations of *S. putrefaciens* amended with 5 mM ferrihydrite and 180 μM U(VI), and either 20 mM (open) or 40 mM (closed) (A and 141

D) DIC only, (B and E) DIC and 800 μM calcium, or (C and F) DIC and 300 μM silica. Symbols and error bars represent the average and standard deviation of 10,000 Monte Carlo sampled E_h values of individual aquous U(VI) and Fe(II) complexes.

Figure 4.7 Calculated (A) potentials (E_h) of the $Fe(OH)_3$/Fe(II) and U(VI)/UO_2(am) redox couples and (B) the Gibbs energy of reaction (ΔG_r) of the oxidation of amorphous uraninite by ferrihydrite as a function of DIC concentration at the US Department of Energy (DOE) Integraded Field Research Challenge (IFRC) site in Rifle, Colorado. Calculations were conducted at pH 7 using a total U(VI) concentration of 1 μM, total Fe(II) concentrations of 10, 100, and 500 μM, and background Rifle groundwater composition (Zachara et al., 2013). Solid lines and shaded envelopes represent the average and standard deviation of 10,000 Monte Carlo sampled E_h and ΔG_r values. 145

Figure 5.1 Time series of (A-C) total dissolved uranium (U_d), (D-F) total Fe(II) ($Fe(II)_T$), and (G-I) dissolved Fe(II) ($Fe(II)_d$) in incubations amended with either 20 mM (circles) or 40 mM (triangles) DIC and either 180 μM U(VI) (blue), 5 mM of 0 (left), 5 (center), or 10 (right) mol% Al-ferrihydrite (orange), or both (green) as terminal electron acceptors. Filled symbols and lines represent biotic incubations with *S. putrefaciens* whereas open symbols represent abiotic controls. Symbols and error bars represent the average and standard deviation from triplicate incubations. 158

Figure 5.2 Pseudo-first order rate constants (k_{obs}) of the initial (A) removal of total dissolved uranium (U_d) and (B) production of total Fe(II) ($Fe(II)_T$) in incubations of *S. putrefaciens* amended with either 180 μM U(VI) (blue), 5 mM 0, 5, or 10 mol% Al-ferrihydrite (orange), or both (green) as terminal electron acceptors, and either 20 mM (solid bars) or 40 mM (hashed bars) DIC. Values of k_{obs} were calculated for individual incubations and presented as the average and standard deviation for each condition (n=3). 159

Figure 5.3 Powder X-ray diffraction (XRD) patterns of final solid phase products in incubations amended with 5 mM of (A-D) 0, (E-H) 5, or (I-L) 10 mol% Al-ferrihydrite (+Fh) or both 180 μM U(VI) and 5 mM (Al-)ferrihydrite (+U+Fh) as terminal electron acceptors, and either 20 or 40 mM DIC. Black lines represent biotic incubations and grey lines represent abiotic controls. Signals are normalized to the maximum intensity in each condition and smoothed using a 10-point moving average. Peaks are indexed with M for magnetite, L for lepidocrocite, and S for siderite. 164

Figure 5.4 Time series of calculated Gibbs energies of reaction (ΔG_r) of $U(IV)_{mono}$ oxidation by pure ferrihydrite at each sampled time point in incubations with *S. putrefaciens* amended with either (A) 20 mM or (B) 40 mM DIC and both 180 µM U(VI) and 5 mM of 0 (circles), 5 (triangles), or 10 (squares) mol% Al-ferrihydrite as terminal electron acceptors. Symbols and error bars represent the average and standard deviation of the ΔG_r calculated from 10,000 Monte Carlo sampled pairs of E_h values for the $U(VI)/U(IV)_{mono}$ and $Fe(OH)_3/Fe(II)$ redox couples. 170

Figure B.1 Correlation between survival rate of *S. putrefaciens* strain 200 and the concentration of a) UO_2^{2+} ($R^2 = 0.98$), b) UO_2OH^+ ($R^2 = 0.98$), c) $(UO_2)_2OH^{3+}$ ($R^2 = 0.98$), d) the sum of all the ternary uranyl carbonate species ($R^2 = 0.97$), and e) the sum of all the uranyl carbonate species ($R^2 = 0.04$) in viability assays of cells exposed to 1 mM U(VI) at pH 7.2±0.2 in the presence of various concentrations of DIC, Ca^{2+}, and Mg^{2+} (Table 3.2). A two-parameter logistic function (Equation 3.9) was fitted to the data. Standard deviations represent propagated error from fitting the exponential region of growth curves to obtain survival rates. 189

Figure B.2 Correlation between measured and modeled overall pseudo-first order rate constants k_{obs} for all bioreduction incubation conditions. A linear regression (bold solid line) was fitted to the data ($R^2 = 0.69$). The slope of the linear regression (0.53±0.10) is less than 1.0 and the y-intercept ($3.6\pm2.6\times10^{-12}$ L/cell/day) is near the origin, indicating that the model generally underpredicts k_{obs} for incubations with the largest measured values. Neglecting the three incubations with the largest measured k_{obs} values improves the correlation between modeled and measured k_{obs} ($R^2 = 0.80$) and the slope of the linear regression (0.83±0.13), reflecting the difficulty in modeling rates accurately when uranium bioreduction kinetics transitions from being controlled by bioavailability to being controlled by toxicity. Error bars represent the standard deviation of the slope of the linear regression used to obtain k_{obs} from averaged duplicate incubations or model output. Solid lines represent the 95% confidence band for the linear regression. 190

Figure C.1 Time series of (A) dissolved calcium and (B) dissolved magnesium in incubations with *S. putrefaciens* amended with 800 µM calcium, 20 mM (circles) or 40 mM DIC (triangles), and either 180 µM U(VI) (blue), 5 mM ferrihydrite (orange), or both (green) as terminal electron acceptors. Filled symbols and lines represent biotic incubations and open symbols represent abiotic controls. Symbols and error bars represent the average and standard deviation of measurements from triplicate incubations. 220

Figure C.2 Time series of dissolved silica in incubations with *S. putrefaciens* amended with 300 μM silica, 20 mM (circles) or 40 mM DIC (triangles), and either 180 μM U(VI) (blue), 5 mM ferrihydrite (orange), or both (green) as terminal electron acceptors. Filled symbols and lines represent biotic incubations and open symbols represent abiotic controls. Symbols and error bars represent the average and standard deviation of measurements from triplicate incubations. 221

Figure C.3 Time series of percent dissolved Fe(II) in incubations with *S. putrefaciens* amended with 20 mM (circles) or 40 mM (triangles) (A) DIC-only, (B) DIC and 800 μM calcium, and (C) DIC and 300 μM silica, and either 5 mM ferrihydrite (orange) or both 180 μM U(VI) and 5 mM ferrihydrite (green) as terminal electron acceptors. Symbols and error bars represent the average and standard deviation of measurements from triplicate incubations. 222

Figure C.4 Time series of dissolved Fe(III) ($Fe(III)_d$) in incubations with *S. putrefaciens* amended with 20 mM (right) or 40 mM (left) (A-B) DIC-only, (C-D) DIC and 800 μM calcium, or (E-F) DIC and 300 μM silica, and either 5 mM ferrihydrite (orange) or both 180 μM U(VI) and 5 mM ferrihydrite (green) as terminal electron acceptors. Symbols and error bars represent the average and standard deviation of triplicate incubations. 223

Figure C.5 Time series of iron mass balance ($[Fe(III)_{solid}] - [Fe_{asc}]$) in incubations with *S. putrefaciens* amended with 20 mM (circles) or 40 mM (triangles) (A) DIC-only, (B) DIC and 800 μM calcium, and (C) DIC and 300 μM silica, and either 5 mM ferrihydrite (orange) or both 180 μM U(VI) and 5 mM ferrihydrite (green) as terminal electron acceptors. Symbols and error bars represent the average and standard deviation of measurements from triplicate incubations. The concentration of $Fe(III)_{solid}$ was calculated from measured concentrations of total iron, total Fe(II), and dissolved Fe(III) ($[Fe(III)_{solid}] = [Fe_{T,0}] - [Fe(II)_T] – [Fe(III)_d]$). Positive values indicate an excess of crystalline Fe(III)-bearing solids which were excluded from Fe_{asc}, whereas negative values indicate an excess of Fe(II)-bearing solids which were included in Fe_{asc}. 224

Figure C.6 Time series to total dissolved uranium (U_d) in incubations with *S. putrefaciens* amended with 180 μM U(VI) as the sole TEA and either 20 mM (left) or 40 mM (right) (A-B) DIC-only, (C-D) DIC and 800 μM calcium, and (E-F) DIC and 300 μM silica. Symbols and error bars represent the average and standard deviation of measurements from triplicate incubations. The solid black line represents the output from the kinetic model using the optimized parameters listed in Table 4.3. In order to reproduce the abrupt decrease in uranium removal rate 226

observed halfway through the (A) DIC-only and (E) silica-amended 20 mM DIC incubations, rate constants of U(VI) bioreduction were decreased to 5 percent of the optimized values after 2 days of simulation.

Figure C.7 Measured and modeled time series of calcium-amended incubations with *S. putrefaciens* conducted in the presence of 5 mM ferrihydrite and 180 μM U(VI) as terminal electron acceptors and (A, C, and E) 20 mM or (B, D, and F) 40 mM DIC. The same experimental data are presented in Figure 4.1. Symbols represent measured concentrations of dissolved uranium (U_d) (circles), dissolved Fe(II) ($Fe(II)_d$) (triangles), and total Fe(II) ($Fe(II)_T$) (squares). Lines represent output of the kinetic model using the optimized rate parameters from Table 4.3. (C and D) Lines representing solid phase iron species are indexed with Fh for ferrihydrite, Mag for magnetite, and Sid for siderite. The solid black line represents the sum of the amorphous iron species (i.e., ferrihydrite and magnetite). (E and F) The solid black line represents the Gibbs energy of reaction (ΔG_r) for the oxidation of monomeric U(IV) by ferrihydrite calculated by the model at each time step. The dashed black line represents the threshold ΔG_r, above which adsorbed U(VI) is reduced by adsorbed Fe(II) and below which U(IV) is oxidized by ferrihydrite. 227

Figure C.8 Measured and modeled time series of silica-amended incubations with *S. putrefaciens* conducted in the presence of 5 mM ferrihydrite and 180 μM U(VI) as terminal electron acceptors and (A, C, and E) 20 mM or (B, D, and F) 40 mM DIC. The same experimental data are presented in Figure 4.1. Symbols represent measured concentrations of dissolved uranium (U_d) (circles), dissolved Fe(II) ($Fe(II)_d$) (triangles), and total Fe(II) ($Fe(II)_T$) (squares). Lines represent output of the kinetic model using the optimized rate parameters from Table 4.3. (C and D) Lines representing solid phase iron species are indexed with Fh for ferrihydrite, Mag for magnetite, and Sid for siderite. The solid black line represents the sum of the amorphous iron species (i.e., ferrihydrite and magnetite). (E and F) The solid black line represents the Gibbs energy of reaction (ΔG_r) for the oxidation of monomeric U(IV) by ferrihydrite calculated by the model at each time step. The dashed black line represents the threshold ΔG_r, above which adsorbed U(VI) is reduced by adsorbed Fe(II) and below which U(IV) is oxidized by ferrihydrite. 228

Figure C.9 Images of incubations amended with 20 mM (A) DIC-only, (B) DIC and 800 μM calcium, and (C) DIC and 300 μM silica after 12 days of reaction. 229

Figure C.10 Images of incubations amended with 40 mM (A) DIC-only, (B) DIC and 800 μM calcium, and (C) DIC and 300 μM silica after 12 days of reaction. 230

Figure D.1 Powder X-ray diffraction (XRD) patterns of the synthesized (A) 0, (B) 5, and (C) 10 mol% Al-ferrihydrite stock suspensions used in this study. Only two broad peaks attributed to 2-line ferrihydrite were identified, demonstrating the absence of secondary Al phases formed during synthesis. Signals are normalized to the maximum intensity of each pattern and smoothed using a 10-point moving average. 256

Figure D.2 Determination of ferrozine extraction efficiency for measuring dissolved and adsorbed Fe(II) in the presence of (Al-)ferrihydrite. 10 μM Fe(II) ($Fe(NH_4)_2(SO_4)2{\cdot}6H_2O$ in 0.1 M HCl) was amended to uranium-free incubations containing modified M1 medium, 15 mM PIPES (pH 8), 40 mM DIC, and autoclaved, fumarate-grown cells of *S. putrefaciens* (approximately 2×10^7 cell/mL) with (solid bar) or without (open bar) 1 mM (Al-)ferrihydrite. After 30 minutes of equilibration, ferrozine-extractable Fe(II) ($Fe(II)_{ext}$) was measured in unfiltered aliquots as described previously (Ginder-Vogel et al., 2010). The dashed line represents the input concentration of Fe(II). Error bars represent triplicate measurements of each incubation. 97±2% of added Fe(II) was recovered in the ferrihydrite-free control, demonstrating that Fe(II) was not oxidized during the equilibration period. The ferrozine extraction recovered between 87±11% and 105±22% of dissolved and adsorbed Fe(II) in incubations amended with (Al-)ferrihydrite, validating the extraction procedure. 258

Figure D.3 Time series of percent dissolved Fe(II) normalized to total Fe(II) in incubations with *S. putrefaciens* amended with either 5 mM of: (A) 0, (B) 5, or (C) 10 mol% Al-ferrihydrite (orange) or both 180 μM U(VI) and 5 mM (Al-)ferrihydrite (green) as terminal electron acceptors, and either 20 mM (circles) or 40 mM (triangles). Symbols and error bars represent the average and standard deviation of measurements from triplicate incubations. 260

Figure D.4 Time series of dissolved Fe(III) ($Fe(III)_d$) in incubations with *S. putrefaciens* amended with either 5 mM of: (A and D) 0, (B and E) 5, or (C and F) 10 mol% Al-ferrihydrite (orange) or both 180 μM U(VI) and 5 mM (Al-)ferrihydrite (green) as terminal electron acceptors and either 20 mM (right) or 40 mM (left) DIC. Symbols and error bars represent the average and standard deviation of triplicate incubations. 261

Figure D.5 Time series of total dissolved aluminum (Al_d) in incubations with *S. putrefaciens* amended with either 5 mM of: (A and C) 5 or (B and D) 10 mol% Al-ferrihydrite (orange) or both 180 μM U(VI) and 5 mM 262

(Al-)ferrihydrite (green) as terminal electron acceptors and either 20 mM (right) or 40 mM (left) DIC. Symbols and error bars represent the average and standard deviation of measurements from triplicate incubations.

Figure D.6 Images of incubations amended with 20 mM DIC and (A) 0, (B) 5, and (C) 10 mol% Al-ferrihydrite after 12 days of reaction. 263

Figure D.7 Time series of iron mass balance ($[Fe(III)_{solid}] - [Fe_{asc}]$) in incubations with *S. putrefaciens* amended with either 5 mM of: (A) 0, (B) 5, or (C) 10 mol% Al-ferrihydrite (orange) or both 180 μM U(VI) and 5 mM (Al-)ferrihydrite (green) as terminal electron acceptors, and either 20 mM (circles) or 40 mM (triangles) DIC. Symbols and error bars represent the average and standard deviation of measurements from triplicate incubations. The concentration of solid Fe(III) ($Fe(III)_{solid}$) was calculated from measured concentrations of initial total iron ($Fe_{T,0}$), total Fe(II) ($Fe(II)_T$), and dissolved Fe(III) ($Fe(III)_d$) (i.e., $[Fe(III)_{solid}] = [Fe_{T,0}] - [Fe(II)_T] - [Fe(III)_d]$). The difference between the calculated concentration of $Fe(III)_{solid}$ and the measured concentration of ascorbate-extractable solid phase iron (Fe_{asc}) indicates the redox state and crystallinity of the total solid phase at each time point. Positive values ($[Fe(III)_{solid}] > [Fe_{asc}]$) indicate an excess of crystalline Fe(III)-bearing solids which were excluded from the ascorbate-extractable fraction of solid phase iron, whereas negative values ($[Fe(III)_{solid}] < [Fe_{asc}]$) indicate an excess of Fe(II)-bearing solids which were included in the ascorbate-extractable fraction of solid phase iron. 264

Figure D.8 Images of incubations amended with 40 mM DIC and (A) 0, (B) 5, and (C) 10 mol% Al-ferrihydrite after 12 days of reaction. 265

Figure D.9 Time series of (A) ferrozine-extractable Fe(II) ($Fe(II)_{ext}$) and (B) total dissolved uranium (U_d) produced in abiotic U(IV) oxidation incubations with 0, 5, or 10 mol% Al-ferrihydrite. Filled symbols represent incubations containing both U(IV) solids and (Al-)ferrihydrite, whereas open symbols represent control incubations without either (A) uranium or (B) iron. (B) The dashed line represents the expected concentration of U_d based on the production of Fe(II) assuming stoichiometric oxidation of U(IV) by Fe(III). Symbols and error bars represent the average and standard deviation of duplicate incubations. 266

Figure D.10 U(IV) oxidation rate versus the Al content of ferrihydrite in abiotic U(IV) oxidation incubations. A linear regression (black line) was fitted to the data ($R^2 = 0.05$). U(IV) oxidation rates were calculated 267

for individual incubations and presented as the average and standard deviation for each condition (n=2).

Figure D.11 Pseudo-first order rate constants (k_{obs}) of Fe(III) reduction versus dissolved Fe(III) ($Fe(III)_d$) net production rates for incubations with *S. putrefaciens* amended with 5 mM (Al-)ferrihydrite as the sole terminal electron acceptor. Linear regressions (black lines) were fitted to data from incubations amended with (A) 40 mM DIC, (B) 20 mM DIC, or (C) all (Al-)ferrihydrite-only incubations. Symbols represent data for individual incubations, and error bars represent the standard error of the slope of the linear regression used to calculate the k_{obs} or rate for each incubation. Dashed lines represent the 95% confidence band for the linear regression. 267

LIST OF SYMBOLS AND ABBREVIATIONS

ΣPO_4^{3-}	sum of all dissolved orthophosphate species
DOE	Department of Energy
IFRC	Integrated Field Research Challenge
pH_{zpc}	pH of zero point charge
ΔG_r	Gibbs free energy of reaction
SRB	sulfate-reducing bacteria
ΣH_2S	sum of all dissolved sulfide species
Q	reaction quotient
R	ideal gas constant
T	temperature
MRB	metal-reducing bacteria
TEA	terminal electron acceptor
E_h	redox potential
$P_{org}HB$	organic phosphate hydrolyzing bacteria
FeOB	iron oxidizing bacteria
MCL	maximum contaminant level
EPA	Environmental Protection Agency
PRB	permeable reaction barrier
DNRA	dissimilatory nitrate reduction to ammonium
LB	lysogeny broth
OD_{600}	optical density at 600 nm
ICP-MS	inductively coupled plasma mass spectrometry

DIC	dissolved inorganic carbon
$Fe(II)_d$	dissolved Fe(II)
$Fe(III)_d$	dissolved Fe(III)
$Fe(II)_T$	total Fe(II)
Fe_{Td}	total dissolved iron
Fe_{asc}	ascorbate-extractable solid phase iron
Fe_T	total iron
ATP	adenosine triphosphate
XRD	X-ray diffraction
LOD	limit of detection
U_d	total dissolved uranium
U_{ads}	adsorbed uranium
U_{SA}	solid-associated uranium
DOC	dissolved organic carbon
X	biomass
t	time
K_s	half-saturation constant of substrate *S*
IC_{50}	concentration at 50% inhibition
LC_{50}	50% lethal concentration
β	equilibrium formation constant
F_{toxic}	toxic inhibition factor
F_T	thermodynamic driving force
χ	average stoichiometric number of the reaction
ΔG_C	Gibbs free energy conserved through formation of ATP

SUMMARY

Mining and processing of uranium ore, followed by improper disposal and aging nuclear waste infrastructure, have left behind a legacy of uranium contamination across the United States. Uranium bioreduction, an *in situ* bioremediation strategy which promotes microbial reduction of the aqueous uranyl ion (U(VI)) to insoluble uranous (U(IV)) solids, has proven successful at decreasing groundwater uranium concentrations below regulatory limits. The ability to predict the fate of uranium following biostimulation of the subsurface microbial community remains limited, however, due to knowledge gaps in the biogeochemical cycling of uranium and its coupling with the biogeochemical transformations of iron. The objective of this dissertation was to determine what microbiological and geochemical processes control the dynamic cycling of uranium between soluble and insoluble phases using a combination of well-defined pure culture incubations and a biogeochemical kinetic model that includes equilibrium speciation calculations and the resultant effects on reaction thermodynamics.

Batch incubations with *Shewanella putrefaciens*, a model metal-reducing bacterium, demonstrated that uranyl non-carbonate species represent the most bioavailable and readily reducible fraction of U(VI), despite being the least abundant species in solution. The rate of U(VI) bioreduction was found to reflect the balance between the bioavailability and toxicity of U(VI) to *S. putrefaciens*, both of which are a function of the concentration of uranyl non-carbonate species. A biogeochemical kinetic model which accounted for the effects of aqueous uranyl speciation on the kinetics of U(VI) bioreduction was able to reproduce time series of uranium removal across a wide range of geochemical conditions,

highlighting the importance of including aqueous uranyl speciation, including minor complexes, in future models.

In the presence of pure ferrihydrite, a poorly crystalline Fe(III) oxy(hydr)oxide, abiotic uranium-iron redox cycling, together with U(VI) bioreduction, controlled rates of uranium removal from solution. The concentration of dissolved Fe(II), through changes in the $Fe(OH)_3$/Fe(II) redox potential, determined whether iron acted as a reductant or an oxidant of uranium. Accounting for the thermodynamic favorability of uranium-iron redox cycling was necessary to reproduce uranium removal using a biogeochemical kinetic model developed as part of this study. The concentration of dissolved Fe(II) is therefore a primary determinant of the stability of U(IV) solid phases in the presence of ferrihydrite and should be considered when designing site-specific remediation strategies.

Finally, aluminum (Al) impurities were found to enhance the ability of ferrihydrite to oxidize U(IV), which decreased rates of uranium removal during U(VI) bioreduction. Additionally, Al substitution sustained U(IV) oxidation by limiting the consumption of ferrihydrite via microbial reduction and secondary mineralization. Thermodynamic data for pure ferrihydrite were not sufficient to predict the redox behavior of Al-ferrihydrite in the presence of uranium, indicating that Al substitution altered the redox properties of ferrihydrite. These results suggest that natural impurities in ferrihydrite make it a more effective and longer-lived oxidant of U(IV) solid than suggested by previous studies.

Overall, this dissertation identifies for the first time important biogeochemical parameters that are expected to impact the success of U(VI) bioreduction in the presence of iron oxides and proposes a framework to incorporate these parameters into more

advanced reactive transport models. The findings of this study suggest that site-specific implementation of U(VI) bioreduction is needed to ensure the long-term stability of U(IV) solids against oxidative dissolution by reactive Fe(III) oxides and the overall success of this remediation strategy.

CHAPTER 1. INTRODUCTION

1.1 Overview and motivations

The biogeochemical cycling of uranium regulates its transport in the environment and a mechanistic understanding of its transformations is essential to identify uranium reserves for industrial uses and predict the subsurface transport of this environmental contaminant. Since its discovery in 1789, uranium was widely used as a colorant in the glass and ceramic industry (Strahan, 2001) and has found modern use as a high-yield energy source. The demonstration of controlled uranium fission in 1942 set the stage for massive uranium mining operations to support nuclear weapons programs and later the nuclear energy sector (Plant et al., 1999). Following a global shift from nuclear proliferation to nuclear disarmament and years of poor waste disposal practices at nuclear facilities, research interests in uranium have more recently focused on understanding its mobility in the environment as an ecological and human health hazard (Blanchard et al., 1983; Riley et al., 1992). The adverse effects of uranium exposure have been observed in microorganisms (Carvajal et al., 2012; Fortin et al., 2007; Fortin et al., 2004; Konopka et al., 2013; Tapia-Rodriguez et al., 2012; VanEngelen et al., 2010b; VanEngelen et al., 2011), macrofauna (Markich et al., 2000; Tran et al., 2004), and aquaculture (Trenfield et al., 2011), and the public health effects from ingestion of uranium and exposure to its

radioactive decay products (e.g. radium) have been well documented (Blanchard et al., 1983; Hirose and Fawell, 2012). As governments recognize the benefits of shifting away from fossil fuel-based energy sources and look to nuclear energy as an alternative, understanding the biogeochemical cycling of uranium is imperative to ensure safe production of nuclear energy and minimize adverse effects on the environment.

A mechanistic understanding of uranium geochemistry has played a crucial role in identifying uranium reserves (Plant et al., 1999) and utilizing uranium as a powerful tool for dating geologic samples (Condomines et al., 2003; Edwards et al., 2003), tracing oceanic mixing processes (Moore and Shaw, 2008; Santos et al., 2011), and reconstructing the redox environments of early Earth (Tribovillard et al., 2006). The discovery of biological uranium transformations (Lovley et al., 1991) has fundamentally altered our understanding of uranium cycling in the environment and has even lead to the development of biological remediation strategies to address anthropogenic nuclear waste. This area of research has greatly expanded the network of biogeochemical processes regulating the distribution of uranium in subsurface environments and has identified new caveats to the traditional view of uranium cycling which must be considered to accurately predict the fate of this contaminant in the environment.

1.2 Uranium chemistry and geochemical controls of uranium mobility

The actinide uranium is a hard cation and forms strong complexes with hard anions such as oxygen-containing ligands (e.g. OH^-, CO_3^{2-}, PO_4^{3-}) (Clark et al., 1995; Cotton et al., 1999). Natural uranium is primarily comprised of three isotopes (^{238}U, 99.27%; ^{235}U, 0.72%; and ^{234}U, 0.01%), all of which are radioactive and undergo alpha decay with half-

lives on the order of $10^5 – 10^9$ years. Uranium exists in four oxidation states (U(III), U(IV), U(V), and U(VI)), however, most attention has focused on reduced U(IV) and oxidized U(VI) as they are the most prevalent oxidation states observed in nature and are generally recognized as the dominant oxidation states controlling the mobility of uranium in the environment. U(III) is unstable within the stability field of water, thus it is not reported in natural environments (Langmuir, 1978). Likewise, U(V) is commonly described as a transient intermediate during reduction of U(VI) or oxidation of U(IV) due to its propensity for disproportionation over a wide range of conditions. Thermodynamics predict U(V) to be the most stable oxidation state in reducing environments below pH 7 (Langmuir, 1978), however, U(V) readily undergoes acid-mediated disproportionation outside of a narrow pH range around 2 – 2.5 (Ekstrom, 1974; Mougel et al., 2010; Steele and Taylor, 2007) which regenerates the two most stable oxidation states (U(VI) and U(IV)) and helps explain its elusiveness in aqueous environments. Naturally occurring U(V) minerals have been identified (Burns and Finch, 1999) though they are rare and the mechanisms of their formation remains uncertain.

In oxidizing environments, uranium is present as the U(VI) uranyl ion (UO_2^{2+}) which is soluble over a wide range of geochemical conditions and contributes to the mobility of uranium in subsurface environments. The uranyl ion has a linear geometry characterized by double bonds to two axial oxygen atoms which are highly stable and remain intact during sorption to mineral surfaces and complexation with ligands. Equatorial binding sites allow for coordination of a wide variety of ligands depending on pH and solution composition which alters the physical (e.g. size, charge), thermodynamic (e.g. redox potential, solubility), and biochemical (e.g. bioavailability) properties of the

uranyl ion and drastically affects how U(VI) interacts with its immediate surroundings. In pure water, the uranyl ion is mainly hydrated or hydrolyzed and present as monomeric or polymeric uranyl hydroxide species depending on the concentration of U(VI), which may lead to the precipitation of schoepite ($(UO_2)_8O_2(OH)_{12}\bullet 12(H_2O)$) or its derivatives (Bargar et al., 2000; Rai et al., 1990). In most natural aquatic systems, however, uranyl can be complexed by chloride, sulfate, nitrate, and orthophosphates (ΣPO_4^{3-}) at low pH, or hydrolyzed and complexed by carbonates at circumneutral pH (Bernhard et al., 2001; Langmuir, 1997) such that the 'free' hydrated uranyl ion is only present in appreciable amounts in acidic environments (Figure 1.1). When carbonates and alkali earth metal cations (i.e. Ca^{2+}, Mg^{2+}, Sr^{2+}, Ba^{2+}) are present, ternary uranyl carbonate complexes represent the only significant fraction of U(VI) above circumneutral pH (Figure 1.1).

Complexation of the uranyl ion generally enhances the solubility of U(VI) compared to solutions without ligands. Certain ligands, however, decrease the solubility of U(VI) and a variety of U(VI) solids may form depending on local geochemical conditions (e.g. uranyl phosphates, vanadates, and arsenates) (Figure 1.2). Furthermore, U(VI) minerals are also commonly associated with uraninite deposits as alteration products generated as a result of fluctuating redox conditions (for a thorough description of these processes see Finch and Murakami, 1999). In addition, small organic ligands such as citrate, malonate, and oxalate can complex uranyl with different efficiencies (Ganesh et al., 1999; Haas and Northup, 2004; Pasilis and Pemberton, 2003; Robinson et al., 1998). The high number of U(VI) complexes and their variable stoichiometry make the reactivity of U(VI) with reductants, ligands, and solid phases difficult to investigate.

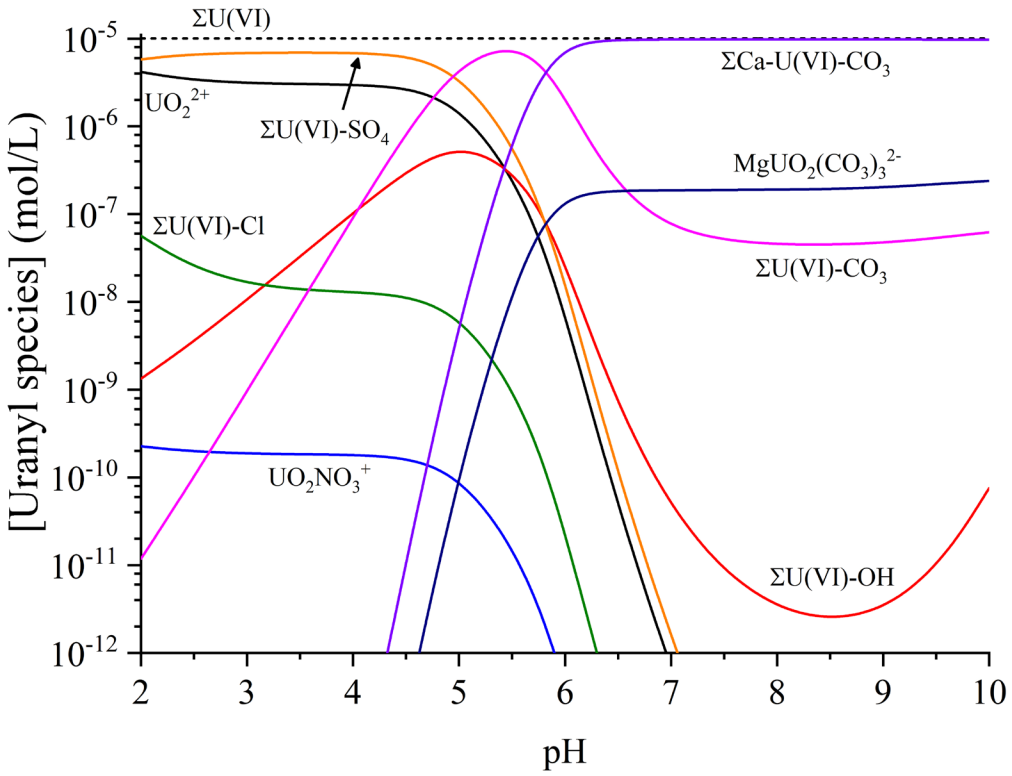

Figure 1.1 Uranyl speciation as a function of pH at the US Department of Energy (DOE) Integrated Field Research Challenge (IFRC) site in Rifle, Colorado. For simplification, uranyl complexes with the same ligand but with different stoichiometries are presented as the summation of those species (ΣU(VI)-OH: UO_2OH^+, $UO_2(OH)_2^0$, $UO_2(OH)_3^-$, $UO_2(OH)_4^{2-}$, $(UO_2)_2OH^{3+}$, $(UO_2)_2(OH)_2^{2+}$, $(UO_2)_3(OH)_4^{2+}$, $(UO_2)_3(OH)_5^+$, $(UO_2)_3(OH)_7^-$, $(UO_2)_4(OH)_7^+$; ΣU(VI)-SO_4: $UO_2SO_4^0$, $UO_2(SO_4)_2^{2-}$, $UO_2(SO_4)_3^{4-}$; ΣU(VI)-Cl: UO_2Cl^+, $UO_2Cl_2^0$; ΣU(VI)-CO_3: $UO_2CO_3^0$, $UO_2(CO_3)_2^{2-}$, $UO_2(CO_3)_3^{4-}$, $(UO_2)_3(CO_3)_6^{6-}$, $(UO_2)_2CO_3(OH)_3^-$, $(UO_2)_3O(OH)_2(HCO_3)^+$, $(UO_2)_{11}(CO_3)_6(OH)_{12}^{2-}$; ΣCa-U(VI)-$CO_3$: $CaUO_2(CO_3)_3^{2-}$, $Ca_2UO_2(CO_3)_3^0$). Uranyl speciation was calculated in PHREEQC, updated with the most recent thermodynamic data for solid and aqueous uranyl species (Dong and Brooks 2006; Guillaumont et al. 2003), for 10 µM U(VI) using measured groundwater composition (3.3 mM DIC, 6.8 mM Na^+, 4.8 mM Ca^{2+}, 4.6 mM Mg^{2+}, 44 mM NH_4^+, 8.4 mM SO_4^{2-}, 2.8 mM Cl^-, 60 µM NO_3^- (Campbell et al. 2011; Zachara et al. 2013)).

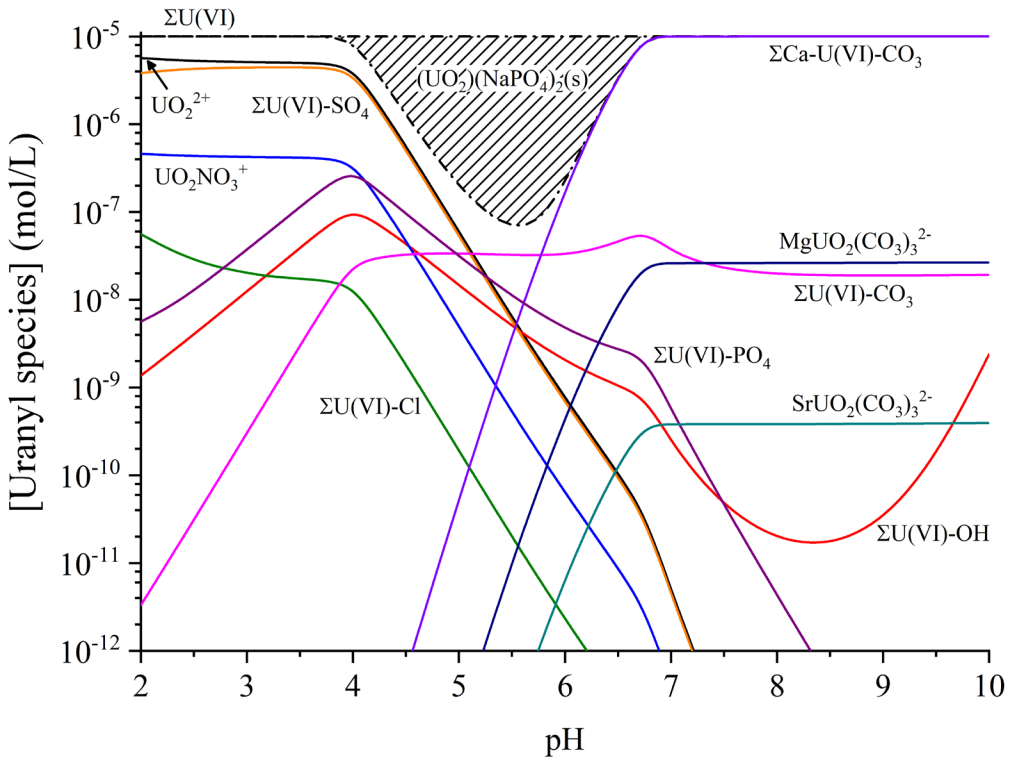

Figure 1.2 Uranyl speciation with dissolved phosphate as a function of pH at the US DOE IFRC site in Oak Ridge, Tennessee. For simplification, uranyl complexes with the same ligand but with different stoichiometries are presented as the summation of those species (ΣU(VI)-OH: UO_2OH^+, $UO_2(OH)_2^0$, $UO_2(OH)_3^-$, $UO_2(OH)_4^{2-}$, $(UO_2)_2OH^{3+}$, $(UO_2)_2(OH)_2^{2+}$, $(UO_2)_3(OH)_4^{2+}$, $(UO_2)_3(OH)_5^+$, $(UO_2)_3(OH)_7^-$, $(UO_2)_4(OH)_7^+$; ΣU(VI)-SO_4: $UO_2SO_4^0$, $UO_2(SO_4)_2^{2-}$, $UO_2(SO_4)_3^{4-}$; ΣU(VI)-Cl: UO_2Cl^+, $UO_2Cl_2^0$; ΣU(VI)-CO_3: $UO_2CO_3^0$, $UO_2(CO_3)_2^{2-}$, $UO_2(CO_3)_3^{4-}$, $(UO_2)_3(CO_3)_6^{6-}$, $(UO_2)_2CO_3(OH)_3^-$, $(UO_2)_3O(OH)_2(HCO_3)^+$, $(UO_2)_{11}(CO_3)_6(OH)_{12}^{2-}$; ΣCa-U(VI)-$CO_3$: $CaUO_2(CO_3)_3^{2-}$, $Ca_2UO_2(CO_3)_3^0$; ΣU(VI)-PO_4: $UO_2PO_4^-$, $UO_2HPO_4^0$, $UO_2H_2PO_4^+$, $UO_2H_3PO_4^{2+}$, $UO_2(H_2PO_4)_2^0$, $UO_2(H_2PO_4)(H_3PO_4)^+$). Uranyl speciation was calculated in PHREEQC, updated with the most recent thermodynamic data for solid and aqueous uranyl species (Dong and Brooks 2006; Guillaumont et al. 2003), for 10 µM U(VI) using 1 mM DIC, 35 µM PO_4^{3-}, and measured groundwater composition (32.9 mM Na^+, 2.4 mM K^+, 25.1 mM Ca^{2+}, 6.8 mM Mg^{2+}, 10 µM Sr^{2+}, 7.3 mM Cl^-, 133 µM NO_3^-, 9.9 mM SO_4^{2-} (Wu et al. 2006a)).

Contrary to U(VI), U(IV) as the uranous ion (U^{4+}) lacks the two axial oxo ligands characteristic of the uranyl ion and is highly insoluble. The uranous ion undergoes hydrolysis above pH 1 and forms aqueous complexes with carbonate ligands at higher pH, however, the number of identified complexes and their equilibrium concentrations are small due to the low solubility of U(IV) (Ciavatta et al., 1983; Clark et al., 1995; Guillaumont et al., 2003; Langmuir, 1978). Uranium(IV) is present in the environment predominantly as reduced U(IV) mineral deposits such as uraninite (UO_2), coffinite ($USiO_4$), and sometimes ningyoite ($CaU(PO_4)_2 \cdot 2H_2O$) (Langmuir, 1978; Plant et al., 1999). Additionally, non-crystalline mononuclear U(IV) complexes and nanocrystalline precipitates have been identified in the environment where U(IV) is associated with organic matter or colloidal aggregates via phosphate and carbonate ligands (Bargar et al., 2013; Bhattacharyya et al., 2017; Wang et al., 2013a). In these environments uranium mobility may be higher than anticipated due to the formation of soluble organic U(IV) complexes with natural and synthetic organic acids (Francis and Dodge, 2008; Ganesh et al., 1997; Haas and Northup, 2004; Suzuki et al., 2010) and humics (Burgos et al., 2007) or U(IV)-associated colloids which may be susceptible to advective transport (Wang et al., 2013a).

1.3 Interactions of uranyl with the mineral-water interface

While the oxidation state of uranium provides insight into the mobility of uranium to a first degree, the strong affinity of the uranyl ion for solid phase minerals exerts an additional control on the transport of uranium in subsurface environments. Uranyl ions can be removed by adsorption onto aluminum (Gu et al., 2003; Guo et al., 2009; Jung et al., 2012; Sylvester et al., 2000; Tao et al., 2000), manganese (Brennecka et al., 2011; Rihs et al., 2014; Wang et al., 2013b; Webb et al., 2006), and iron oxides (Bargar et al., 2000;

Bruno et al., 1995; Cheng et al., 2004; Duff et al., 2002; Gabriel et al., 1998; Hsi and Langmuir, 1985; Lack et al., 2002; Lenhart and Honeyman, 1999; Moyes et al., 2000; Sato et al., 1997; Singh et al., 2012; Tao et al., 2000; Waite et al., 1994) with more efficient sorption onto amorphous than crystallized iron oxide phases (Hsi and Langmuir, 1985; Payne et al., 1996) but less efficient sorption onto biotic than synthesized manganese oxides (Wang et al., 2013b).

In natural waters, U(VI) adsorption typically increases with pH as hydrolysis of the uranyl ion becomes progressively more important and generates negatively charged complexes that are attracted by the positively charged oxohydroxide minerals below the pH of zero point charge (pH_{zpc}). Above the pH_{zpc} of these minerals, however, the mean surface charge of the oxide phases is negative and U(VI) adsorption tends to decrease. As a result, the apex of adsorption of U(VI) onto oxohydroxide minerals, though variable depending on the exact mineral composition, tends to be maximum between pH 6 and 10 for aluminum oxides (Guo et al., 2009; Tao et al., 2000), 4 and 9 for manganese oxides (Wang et al., 2013b), and 7 and 10 for iron (hydr)oxides (Cheng et al., 2004; Hsi and Langmuir, 1985; Tao et al., 2000).

In the presence of carbonates, uranyl adsorption onto iron and manganese oxides is less efficient because uranyl carbonate complexes are weakly sorbed (Hsi and Langmuir, 1985; Lenhart and Honeyman, 1999; Waite et al., 1994; Wang et al., 2013b). This effect is exacerbated by alkali earth metal cations which result in the formation of ternary uranyl carbonate species and further decrease uranyl-surface interactions (Nair and Merkel, 2011; Stewart et al., 2010). If the pH is low enough, however, ternary complexes can form between the manganese or iron oxide, uranyl, carbonate, and sometimes calcium-carbonate

(Bargar et al., 2000; Foerstendorf et al., 2012; Singer et al., 2012a; Wang et al., 2013b). In addition, coprecipitation of carbonate minerals may be significant at pH >8 (Reeder et al., 2000; Reeder et al., 2001).

In the presence of natural organic matter, adsorption onto oxide minerals is enhanced at low pH and decreased at high pH (Lenhart and Honeyman, 1999; Payne et al., 1996; Tao et al., 2000) and may be followed by coprecipitation of schoepite (Bruno et al., 1995; Duff et al., 2002) or other U(VI) minerals (Gu et al., 2003; Sato et al., 1997) if the concentration of uranyl ions in solution and/or the pH are high enough. Uranium can also be removed by adsorption onto clays (Catalano and Brown Jr., 2005; Chisholm-Brause et al., 2001; Krestou et al., 2004; McKinley et al., 1995; Prikryl et al., 2001; Sylvester et al., 2000), or by adsorption to (Drot and Simoni, 1999; Fuller et al., 2003; Rakovan et al., 2002) or coprecipitation with (Arey et al., 1999; Krestou et al., 2004) phosphate minerals, or a combination of both depending on whether the solubility of uranium phosphate minerals is exceeded (Fuller et al., 2002; Ghafar et al., 2002; Simon et al., 2008). Finally, uranium adsorbs to cell membranes mainly via complexation by carboxyl and phosphoryl groups (Fowle et al., 2000; Haas et al., 2001; Hu et al., 1996; Kelly et al., 2002) which may act as nucleation centers for the precipitation of uranium phosphate minerals (Dunham-Cheatham et al., 2011).

1.4 Uranium redox transformations

1.4.1 Chemical redox processes

As discussed earlier, the oxidation state of uranium exerts significant influence over its mobility in the subsurface due to the large range in solubility amongst its reduced and

oxidized forms. Basic thermodynamic calculations demonstrate the versatility of uranium as both an oxidant and reductant to a number of redox active species (Figure 1.3). Calculated Gibbs free energies of reaction (ΔG_r) for the reduction of the 'free' uranyl ion to amorphous uraninite (UO_2(am)) under conditions at the US Department of Energy (DOE) Integrated Field Research Challenge (IFRC) site in Rifle, CO, as an example of a uranium-contaminated subsurface environment, demonstrate the numerous possible redox transformations of uranium. The non-linear relationship between ΔG_r and pH is a result of changes in the concentration of UO_2^{2+} with pH in the presence of ligands (Figure 1.1 and Figure 1.2) and highlights the challenge of determining the fate of uranium in complex, highly heterogeneous subsurface environments. Although thermodynamics provides a good approximation to the mobility of uranium in various redox environments, thermodynamic equilibrium in soils and sediments is rarely achieved due to kinetic limitations, microbial activity, and the effect of transport on microbial and chemical processes.

In anaerobic environments, sulfate-reducing bacteria (SRB) catalyze the production of sulfide, a strong reductant which plays a significant role in the cycling of metals and non-metals, including uranium (Figure 1.3A). When iron oxides are present their reduction by dissolved sulfides (ΣH_2S) produces Fe(II) which readily reacts with excess dissolved sulfides to form amorphous iron sulfide (FeS(am)), mackinawite (FeS), and eventually pyrite (FeS_2), over longer time scales (Rickard and Luther, 1997). Whereas the kinetics of U(VI) reduction by dissolved sulfides is slow (Hua et al., 2006), the kinetics of its reduction by iron sulfides (Hua and Deng, 2008; Hyun et al., 2012; Qafoku et al., 2009; Veeramani et al., 2013; Wersin et al., 1994) and metal sulfides (Wersin et al., 1994) is rapid. Reports

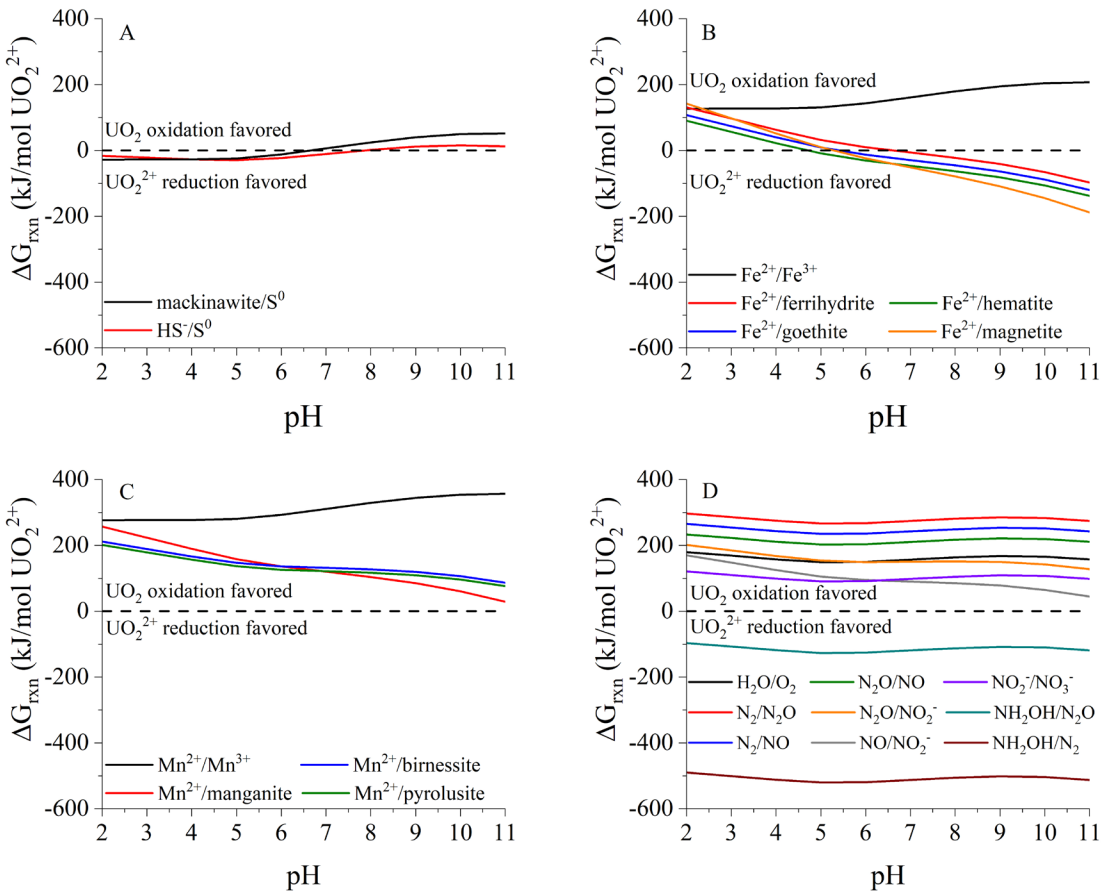

Figure 1.3 Gibbs free energy of reaction (ΔG_r) as a function of pH for the reduction of UO_2^{2+} to UO_2(am) coupled to the oxidation of reduced (A) sulfur, (B) iron, (C) manganese, and (D) nitrogen in a typical uranium-contaminated groundwater (only 1 and 2 e^- transfer reactions were considered). A negative ΔG_r indicates that reduction of UO_2^{2+} is thermodynamically favorable, while a positive ΔG_r indicates that the oxidation of UO_2(am) is thermodynamically favorable. ΔG_r ($\Delta G_r = \Delta G_r^0 + RT\ln(Q)$, where Q is the reaction quotient) was calculated using measured groundwater composition at the US DOE IFRC site in Rifle, Colorado (Campbell et al. 2011; Zachara et al. 2013). 'Free' hydrated UO_2^{2+} concentrations were calculated as a function of pH using PHREEQC, updated with the most recent thermodynamic data for solid and aqueous uranyl species (Dong and Brooks 2006; Guillaumont et al. 2003)). A concentration of 10 µM was used for HS^-, Fe^{3+}, Mn^{3+}, N_2, N_2O, NO, NO_2^-, and NH_2OH.

of oxidation products of iron sulfide minerals by U(VI) vary and include elemental sulfur (S^0) (Hua and Deng, 2008; Hyun et al., 2012), sulfate (SO_4^{2-}) (Veeramani et al., 2013), and polysulfides (S_x^{2-}) (Wersin et al., 1994). Regardless, the reduction of U(VI) by iron sulfide minerals is generally agreed to proceed via adsorption of U(VI) to the iron sulfide surface, release of structural Fe(II) into solution, followed by electron transfer between adsorbed U(VI) and structural sulfide (Hua and Deng, 2008; Hyun et al., 2012; Veeramani et al., 2013).

In anaerobic environments not exposed to sulfate reduction, Fe(II) is usually prevalent as the product of microbial iron reduction and provides a significant source of electrons to enable the reduction of U(VI). Although homogeneous electron transfer between aqueous U(VI) and Fe(II) is thermodynamically favorable above circumneutral pH (Figure 1.3B) (Du et al., 2011), the reaction is only kinetically feasible via the formation of an inner sphere U-Fe complex, which is thermodynamically hindered in an aqueous system (Taylor et al., 2015). Thus, reduction of U(VI) by Fe(II) requires a mineral surface to facilitate the formation of the U-Fe inner sphere complex and promote rapid electron transfer. Changes in the electronic structure of Fe(II) while adsorbed onto iron oxides surfaces, however, may overcome a kinetic or thermodynamic barrier (Wehrli et al., 1989), and surface-catalyzed U(VI) reduction by Fe(II) has been observed on colloidal (Liger et al., 1999) and nanoparticulate (Zeng and Giammar, 2011) hematite (Fe_2O_3), hydrous ferric oxide (Jang et al., 2008), and Fe-bearing clays (Chakraborty et al., 2010; Tsarev et al., 2016). Surface-catalyzed U(VI) reduction may outcompete biological U(VI) reduction under naturally-occurring U(VI) concentrations (Behrends and Van Cappellen, 2005). In this scenario, the primary role of iron-reducing bacteria is to supply electrons indirectly via

production of Fe(II) rather than directly via enzymatic reduction of U(VI) (discussed below). U(VI) surface coverage, the presence of humic acids, Fe(II) speciation, and Fe(III) oxidation products all contribute to the extent of surface-catalyzed U(VI) reduction by Fe(II) (Jang et al., 2008; Zeng and Giammar, 2011).

Heterogeneous reduction of U(VI) by ferrous minerals is not kinetically inhibited and may be a significant abiotic uranium reduction pathway in naturally reduced soils (Latta et al., 2012a). Magnetite (Crane et al., 2011; Huber et al., 2012; Ilton et al., 2010; Latta et al., 2012b; Latta et al., 2014; Latta et al., 2013; Missana et al., 2003b; Singer et al., 2012a, b), green rust (Fe(II)/Fe(III)-hydroxide) (O'Loughlin et al., 2003), ferrous micas (Ilton et al., 2005), siderite ($FeCO_3$) (Ithurbide et al., 2009), and vivianite ($Fe(II)_3(PO_4)_2 \cdot 8(H_2O)$) (Veeramani et al., 2011) all successfully reduce U(VI). Magnetite is a common mixed valence iron oxide mainly formed by secondary mineralization during microbial reduction of more labile iron oxides (Hansel et al., 2003) and is the primary anoxic corrosion product of carbon steel containers used for long-term uranium waste repositories (Duro et al., 2008). The mechanism of uranium immobilization by magnetite is a function of its stoichiometry (Fe^{2+}:Fe^{3+} ratio) (Latta et al., 2012b), the prevalence of structural defects in the magnetite crystal (Singer et al., 2012a), and the uranium surface coverage (Latta et al., 2014) and may proceed via adsorption, reductive precipitation, incorporation in the mineral lattice, or a combination of the three (Huber et al., 2012; Latta et al., 2012b; Latta et al., 2014; Singer et al., 2012a, b). The reduction capacity of magnetite may be recharged upon exposure to Fe(II) which replenishes structural Fe(II) and restores its ability to reduce U(VI) (Latta et al., 2012b). Thus, magnetite may play an important role in maintaining reducing environments and buffering against the oxidation and mobilization

of uranium during brief periods of aerobic conditions. Uraninite is commonly cited as the primary U(IV) mineral product of uranium reduction by magnetite (Latta et al., 2012b; O'Loughlin et al., 2010; Veeramani et al., 2011), however, mononuclear U(IV) species are observed with titanium-doped magnetite (Latta et al., 2013) or when phosphate is pre-sorbed onto the magnetite surface (Veeramani et al., 2011), similar to U(VI) reduction by vivianite, demonstrating the importance of the geochemical conditions and coordination environment on the composition of the final U(IV) mineral product.

Iron oxides are also efficient oxidants of U(IV), primarily below circumneutral pH (Figure 1.3B), but the mineralogy of iron oxides affects the thermodynamics and extent of U(IV) oxidation (Figure 1.3B). Organic chelating agents which solubilize Fe(III) and U(IV) promote homogenous and heterogeneous reactions between Fe(III) and U(IV) and expedite electron transfer (Stewart et al., 2013). As U(IV) is oxidized by iron oxides, however, the accumulation of Fe(II) in solution decreases the thermodynamic driving force of the reaction (Ginder-Vogel et al., 2006) and passivates the oxide surface (Senko et al., 2005) which limits the extent of U(IV) oxidation. Furthermore, Fe(II) eventually induces the ripening and secondary mineralization of ferrihydrite ($Fe(OH)_3$) to more crystalline phases (i.e. goethite (FeOOH) and hematite (Fe_2O_3)) (Hansel et al., 2003) which are less favorable for the oxidation of U(IV) (Figure 1.3B) (Ginder-Vogel et al., 2006). On the other hand, processes that limit the extent of Fe(II) accumulation in solution, such as adsorption or precipitation of Fe(II)-bearing minerals (e.g. siderite, mackinawite, magnetite), maintain the thermodynamic driving force of the reaction and promote the continuous oxidation of U(IV) by iron oxides (Spycher et al., 2011). Similarly, dissolved sulfides (ΣH_2S) produced upon the development of sulfate-reducing conditions may

outcompete U(IV) for oxidation by iron oxides and prevent the oxidation of uranium (Sani et al., 2004; Spycher et al., 2011).

With few exceptions, the vast majority of studies use pure, synthetic iron oxides to study the coupled redox cycling of uranium and iron. Although this approach provides valuable information on the mechanisms involved in electron transfer between uranium and iron, naturally occurring iron oxides typically contain abundant inorganic and organic impurities that alter their biological and chemical reactivity (Cismasu et al., 2011; Cornell and Schwertman, 2003; Jambor and Dutrizac, 1998). During formation, a variety of elements may substitute for Fe^{3+} in the crystal lattice of iron oxides which affects adsorption (Anderson and Benjamin, 1990; Johnston and Chrysochoou, 2016; Masue et al., 2007), microbial reduction kinetics (Ekstrom et al., 2010), chemical reaction kinetics (Gonzalez et al., 2002; Jentzsch and Penn, 2006), and secondary mineralization pathways (Hansel et al., 2011; Vempati and Loeppert, 1989). Furthermore, natural organic matter may co-precipitate with Fe(III) during iron oxide formation and impact microbial reduction kinetics (Amstaetter et al., 2012; Shimizu et al., 2013) and secondary mineralization (Chen et al., 2015; ThomasArrigo et al., 2017). Iron oxide impurities have been shown to limit heterogeneous abiotic U(VI) reduction by Fe(II) (Stewart et al., 2015) and the incorporation of uranium into secondary mineralization products of ferrihydrite (Massey et al., 2014b), however, knowledge of how impurities affect the redox cycling of uranium is severely limited.

Manganese oxides are common in soils and sediments and powerful oxidizing agents for a variety of reduced species, including U(IV) (Figure 1.3C) (Chinni et al., 2008; Fredrickson et al., 2002; Liu et al., 2002b; Wang et al., 2013c). Their prevalence is

attributed to manganese-oxidizing bacteria which catalyze the otherwise kinetically-inhibited abiotic oxidation of Mn(II) by dissolved oxygen (Tebo et al., 2004). In fact, in the presence of Mn(II) and dissolved oxygen, manganese-oxidizing bacteria catalyze the formation of manganese oxides and indirectly oxidize U(IV) at faster rates than with dissolved oxygen alone (Chinni et al., 2008). Microbial manganese reduction (Lin et al., 2012) and oxidation (Butterfield et al., 2013; Webb et al., 2005), however, proceed through formation of a soluble Mn(III) intermediate which readily oxidizes U(IV) at rates much faster than dissolved oxygen under similar concentrations (Wang et al., 2014), suggesting that Mn(IV) oxides may not necessarily be the direct oxidant of U(IV).

While iron and manganese oxides are effective oxidants of U(IV) in laboratory experiments, rates of U(IV) oxidation in subsurface environments may be limited by lack of direct contact between these minerals and solid U(IV). These conditions provide ample opportunity for oxidation of U(IV) by soluble oxidants such as nitrogen species and dissolved oxygen which are highly favorable oxidants of U(IV) across all pH even at low concentrations (Figure 1.3D). Denitrification intermediates produced during dissimilatory nitrate reduction (i.e. nitrite, NO_2^-; nitric oxide, NO; nitrous oxide, N_2O) are effective oxidants of U(IV) (Moon et al., 2007; Senko et al., 2005) though the kinetics and mechanisms of these reactions remain to be determined. Because nitrite can also oxidize Fe(II) (Sorensen and Thorling, 1991; Van Cleemput and Baert, 1983), iron can serve as an electron shuttle between nitrite and U(IV) and effectively oxidize large concentrations of uranium even at low Fe(II) content (Senko et al., 2005). The high reactivity of Fe(II), and to some extent dissolved sulfides, with molecular oxygen compared to denitrification intermediates may make Fe(II) and dissolved sulfides effective redox buffers against

aerobic U(IV) oxidation but may also favor the oxidation of U(IV) by nitrogen species (Bi and Hayes, 2014; Bi et al., 2013; Moon et al., 2007).

1.1.1 Biological redox processes

Select species of bacteria are able to utilize uranium during respiration processes which, in some cases, affords sufficient energy for cell growth (Sanford et al., 2007; Tebo and Obraztsova, 1998; Wade and DiChristina, 2000) and simultaneously alters the oxidation state and, inherently, the mobility of uranium. As uranium is not an essential element and uranium-dependent biochemical processes do not exist, the ability of bacteria to utilize uranium during cellular respiration is surprising, especially given that uranium is toxic to many microorganisms (Carvajal et al., 2012; Konopka et al., 2013; Tapia-Rodriguez et al., 2012; VanEngelen et al., 2010a) by compromising cell membrane integrity (Bencheikh-Latmani and Leckie, 2003) and inhibiting enzymatic functions (Pible et al., 2010; VanEngelen et al., 2011). Yet, select species of metal-reducing bacteria (MRB) (e.g. *Shewanella spp., Geobacter spp., Anaeromyxobacter spp.*) and SRB (e.g. *Desulfotomaculum sp., Desulfovibrio spp.*) couple the reduction of U(VI) to U(IV) with the oxidation of organic carbon and generate sufficient energy for growth (Sanford et al., 2007), even if precipitation of intercellular uranium minerals decreases cell viability (Cologgi et al., 2011). In turn, select lithotrophic bacteria may couple the oxidation of U(IV) to dissimilatory nitrate reduction, although not to support cell growth (Beller, 2005; Finneran et al., 2002; Weber et al., 2011).

The biochemical mechanism and genetic components responsible for the enzymatic reduction of U(VI) remain elusive. Genetic studies with pure-cultures of *Shewanella*

oneidensis strain MR-1, a model MRB, invoke the involvement of outer membrane c-type cytochromes in U(VI) reduction (Marshall et al., 2006). However, MR-1 mutants lacking genes for individual cytochromes (i.e. MtrC, OmcA, MtrC/OmcA) display moderate U(VI) reduction ability compared to wild-type cells, and a complete inability to reduce U(VI) is only observed with a mutant lacking all c-type cytochrome genes (Marshall et al., 2006). Similarly, deletion of genes encoding the 5 most abundant outer membrane c-type cytochromes of *Geobacter sulfurreducens* was required to decrease U(VI) reduction to levels less than 20% of the wild-type, indicating the involvement of outer membrane c-type cytochromes in U(VI) bioreduction (Orellana et al., 2013). The existence of multiple mechanisms of enzymatic uranium reduction is supported by the observation that biogenic uraninite is formed both on the outside of cells and within the periplasmic space (Marshall et al., 2006; Senko et al., 2007; Shao et al., 2014). As a singular terminal reductase to catalyze the reduction of U(VI) has not been identified, it is likely that U(VI) bioreduction involves non-specific outer membrane cytochromes and periplasmic reductases with sufficiently low redox potentials rather than a unique molecular system.

Significantly less is known about lithotrophic U(IV) oxidizing bacteria which utilize U(IV) as an electron donor and couple its oxidation to dissimilatory nitrate-reduction. Nitrate-dependent U(IV) oxidizers are taxonomically diverse and include members of the *Acidobacteria* and *Alpha-*, *Beta-*, *Gamma-*, and *Delta-proteobacteria* (Weber et al., 2011). C-type cytochromes have been identified as potential molecular components of U(IV) oxidation (Beller et al., 2009). Cell growth, however, has not been reported for this metabolism, likely due to the small concentrations of U(IV) oxidized, thus whether U(IV) oxidation is coupled to energy generation remains to be determined (Beller, 2005; Weber

et al., 2011). Regardless, U(IV) oxidizers can liberate sufficient U(VI) to surpass regulatory limits and their presence may impede remediation efforts to sequester uranium as biogenic U(IV) minerals.

1.2 Effects of aqueous speciation on uranium reactivity

The aqueous speciation of uranium is highly complex as all oxidation states of uranium form aqueous complexes with both inorganic and organic ligands present in subsurface environments that are strongly influenced by the pH (Langmuir, 1978). Ligands alter uranium adsorption on mineral surfaces (Stewart et al., 2010; Waite et al., 1994), its bioavailability to microbes (Belli et al., 2014; Brooks et al., 2003; Markich et al., 1996; Ulrich et al., 2011), its reaction kinetics (Behrends and Van Cappellen, 2005; Ginder-Vogel et al., 2010; Hua et al., 2006), and ultimately its mobility. The classic view of uranium geochemistry typically associates U(VI) with high solubility and mobility, U(V) with instability toward disproportionation, and U(IV) with low solubility and mobility. These properties, however, depend on the speciation of uranium and do not necessarily reflect the reactivity of uranium in all environments. As a result, understanding the influence of geochemical speciation on the physical, chemical, and biological processes controlling uranium mobility is crucial to successfully predict the behavior of uranium in diverse environments.

As discussed earlier, adsorption of uranium relies in part on electrostatic attraction between the charged uranyl complex and the charged mineral surface, which are a function of the type of ligand, its concentration, and the pH. Additionally, proper coordination between the uranyl complex and the mineral surface is affected by bulky complexing

ligands (e.g. carbonates, phosphates) (Cheng et al., 2004; Hsi and Langmuir, 1985; Lenhart and Honeyman, 1999; Nair and Merkel, 2011; Stewart et al., 2010; Waite et al., 1994; Wang et al., 2013b). Ligands also impact the redox cycling of uranium by altering the U(VI)/U(IV) redox potential and, in some cases, limiting the kinetics of electron transfer to and from uranium. For example, the potential of the U(VI)/U(IV) redox couple under geochemical conditions at the Rifle site spans 70 mV due to differences in redox potential amongst uranyl species (Figure 1.4). The 'free' hydrated uranyl ion and uranyl hydroxide species typically display the highest redox potential whereas ternary Ca and Mg uranyl carbonate complexes display the lowest. Although this range of potentials is small in comparison to the range of potentials across the suite of TEAs used in microbial respiration (Figure 1.4), speciation dependent changes in the U(VI)/U(IV) potential are significant in that they span the ferrihydrite/Fe(II) potential and may alter iron-uranium-bacteria interactions. As iron is an effective oxidant and reductant of uranium (Figure 1.3B), changes in uranyl speciation which alter its redox potential determine the role of iron in redox transformations of uranium. This effect can be explained in both thermodynamic and mechanistic terms. Thermodynamically, carbonates enhance the effectiveness of ferrihydrite as an oxidant of uraninite by lowering the redox potential of U(VI) relative to other uranyl species (i.e. the 'free' hydrated uranyl ion and uranyl hydroxides) (Figure 1.4) and shifting the equilibrium toward formation of highly soluble uranyl carbonate complexes (Ginder-Vogel et al., 2006). Mechanistically, carbonates enhance the oxidative dissolution of uraninite by promoting the release of U(VI) from the uraninite surface and limiting surface passivation by U(VI) precipitates (Ginder-Vogel et al., 2010; Ulrich et al., 2009). As carbonates thermodynamically promote the oxidation of U(IV) by iron oxides,

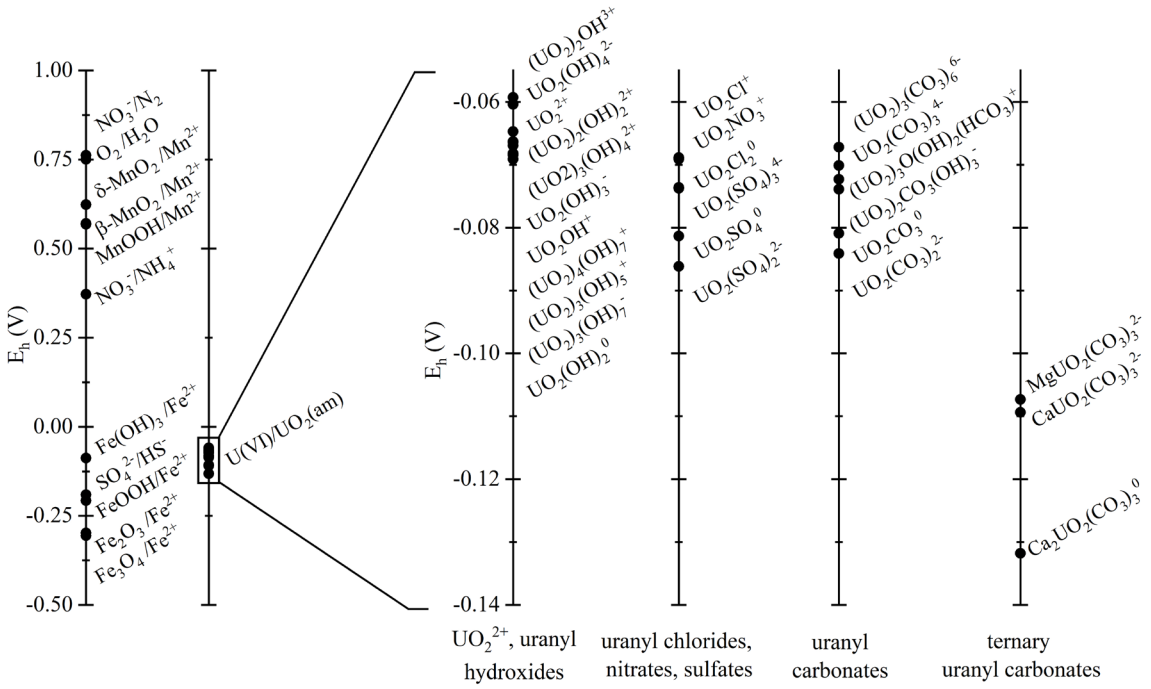

Figure 1.4 Redox potentials (E_h) of terminal electron acceptors for microbial respiration at the US DOE IFRC site in Rifle, Colorado. The right side is an expanded view of E_h for individual uranyl species, demonstrating the influence of uranyl speciation on the U(VI)/UO_2(am) redox potential. E_h was calculated with the Nernst equation ($E_h = E_h^0 - (RT/nF)\ln(Q)$, where Q is the reaction quotient) using groundwater composition at the Rifle site (Campbell et al. 2011; Zachara et al. 2013). Uranyl speciation was calculated as a function of pH using PHREEQC, updated with the most recent thermodynamic data for solid and aqueous uranyl species (Dong and Brooks 2006; Guillaumont et al. 2003). A concentration of 10 µM was used for N_2 and HS^-.

they also hinder the reduction of U(VI) by Fe(II) and other reductants. In fact, rates of abiotic reduction of U(VI) by Fe(II) (Behrends and Van Cappellen, 2005) and dissolved sulfides (Hua et al., 2006) are inversely related to the concentration of carbonates. Simultaneously, the complexation of uranyl by carbonates alters its size and charge which may increase steric hindrance and limit the kinetics of electron transfer (Wander et al., 2006). The combination of these two effects ultimately determines the rate of U(VI) reduction in the presence of carbonates. Although carbonates do not prevent U(VI) reduction by magnetite, reduction is not observed in the presence of Ca^{2+} and carbonates as a result of the formation of ternary Ca uranyl carbonate surface complexes (Singer et al., 2012a, b). Although the mechanism of inhibition remains unclear, Ca^{2+} promotes the formation of ternary uranyl carbonate complexes which have less favorable redox potentials than other uranyl carbonate species (Figure 1.4) and may be below the threshold potential for reduction.

Finally, the speciation of U(VI) greatly impacts its bioavailability and ultimately determines the kinetics of bioreduction by MRB (Brooks et al., 2003; Stewart et al., 2011; Ulrich et al., 2011) and its toxicity to microbial communities (Campbell, 1995; Di Toro et al., 2001; Morel, 1983). For example, conditions which promote the formation of carbonate and ternary carbonate uranyl species (i.e. alkaline pH and high concentrations of carbonates and alkali earth metal cations) decrease the rate of U(VI) bioreduction (Brooks et al., 2003; Stewart et al., 2011; Ulrich et al., 2011). Simultaneously, UO_2^{2+} and UO_2OH^+ have been identified as the uranyl complexes responsible for uranium toxicity to microorganisms (Konopka et al., 2013; Trenfield et al., 2012; VanEngelen et al., 2010a). Because transport of uranium across the outer membrane is likely an active process (Fortin et al., 2007),

adsorption of U(VI) to the outer membrane is an essential first step in the transport of U(VI) into the cell where it may interact with periplasmic reductases, in the case of bioreduction (Marshall et al., 2006; Senko et al., 2007), or inhibit essential enzymes, in the case of toxicity (Pible et al., 2010; VanEngelen et al., 2011). Thus, toxicity may be avoided in alkaline environments where the formation of uranyl carbonate species either decreases the concentration of the toxic uranyl species, prevents sufficient cell-uranyl interactions to induce a toxic response, or a combination of both (Carvajal et al., 2012; Konopka et al., 2013; VanEngelen et al., 2010a). Understanding how the bioavailability and toxicity of U(VI) to MRB act together to control U(VI) bioreduction rates will be necessary to predict the fate of uranium at contaminated sites characterized by diverse geochemical conditions, however, previous studies have only investigated these processes in isolation.

Following reduction of U(VI), ligands continue to play a role in the fate of uranium by altering the stability of U(V) and the solubility of U(IV). Pentavalent U(V) has been implicated as a transient intermediate during U(VI) bioreduction (Renshaw et al., 2005), abiotic reduction of U(VI) by aqueous Fe(II) (Wander et al., 2006), magnetite (Ilton et al., 2010), and ferrous mica (Ilton et al., 2005), and uraninite oxidation (Ulrich et al., 2009). Its stability may therefore constitute the rate-limiting step during redox transformations of uranium. Carbonates retard the disproportionation of U(V) (Ikeda et al., 2007; Morris, 2002) possibly by limiting electron transfer between the two U(V)-carbonate species because of their similar charge and bulky carbonate ligands. Upon disproportionation of U(V) to U(VI) and U(IV), precipitation of insoluble reduced U(IV) species are expected to occur. In the presence of strongly complexing organic acids and soil humics, however, organic U(IV) complexes may form and prevent its precipitation (Burgos et al., 2007;

Francis and Dodge, 2008; Ganesh et al., 1997; Haas and Northup, 2004; Robinson et al., 1998; Sheng et al., 2011; Suzuki et al., 2010). Naturally occurring organic acids and synthetic chelating agents promote the mobilization of uranium by decreasing the bioavailability of uranium to MRB and SRB and increasing the solubility of U(IV) (Francis and Dodge, 2008; Ganesh et al., 1997; Haas and Northup, 2004; Suzuki et al., 2010). Thus, contrary to the classic view of U(IV) as displaying low solubility and low mobility, uranium may remain mobile even under highly reducing conditions under the form of organic complexes.

Figure 1.5 summarizes the biogeochemical processes which control the mobility of uranium in the subsurface. The left side of the figure shows the relative concentrations of redox-active species with depth in an idealized redox-stratified aquifer. Organophosphate hydrolyzing bacteria ($P_{org}HB$) liberate orthophosphate (ΣPO_4^{3-}) from phytogenic organophosphates, which precipitates with oxidized UO_2^{2+} as uranyl phosphate minerals at high P:DIC ratios and may dissolve at lower P:DIC ratios. In addition, UO_2^{2+} may be immobilized via adsorption/incorporation into metal oxides and clays. Uranium(VI) can be reduced abiotically by a number of inorganic reductants or microbially by select species of metal-reducing bacteria (MRB) and sulfate-reducing bacteria (SRB). Uranium(VI) reduction likely proceeds through a pentavalent UO_2^{+} intermediate that may undergo disproportionation, thereby regenerating UO_2^{2+} and producing U^{4+}, or it may be stabilized on certain mineral surfaces as a result of heterogeneous reduction. The kinetics of each of these processes is also influenced by the speciation of U(VI) in solution which enhances the complexity of predicting the rate of U(VI) transformation in sites characterized by diverse geochemical conditions. Uranium(IV) is highly insoluble and may precipitate as

U(IV) minerals or non-crystalline U(IV) complexes in the absence of strongly complexing ligands; however, it may also be stabilized on mineral surfaces as a result of heterogeneous reduction. Uranium(IV) can be oxidized abiotically by common oxidants or microbially by select iron-oxidizing bacteria (FeOB).

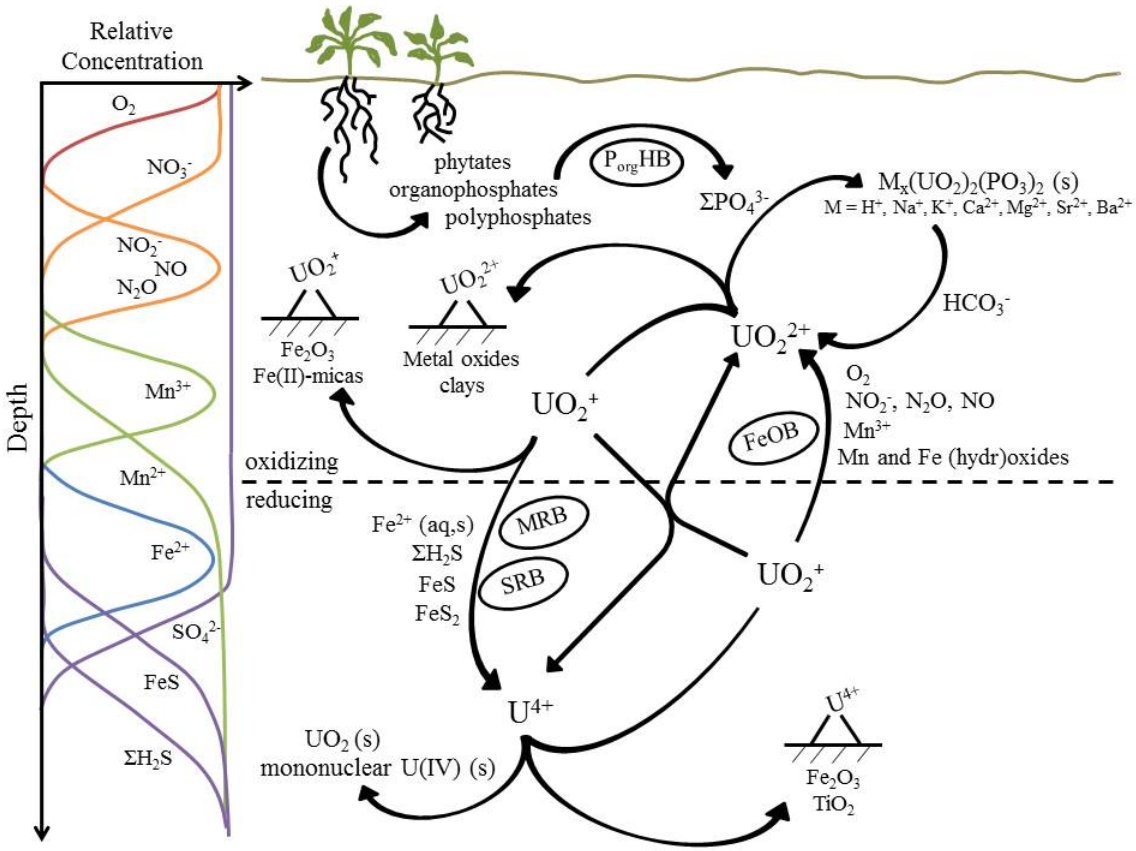

Figure 1.5 Schematic of biogeochemical processes controlling the mobility of uranium in the subsurface. Abbreviations: $P_{org}HB$, organophosphate hydrolyzing bacteria; FeOB, iron-oxidizing bacteria; MRB, metal-reducing bacteria; SRB, sulfate-reducing bacteria.

1.5 Remediation of uranium-contaminated subsurfaces

Humans have dramatically perturbed the global uranium cycle by mining and processing uranium ore to produce nuclear weapons and fuel for nuclear power plants. In addition, vast quantities of uranium-contaminated groundwater and soils have been generated from years of poor waste disposal practices and aging of nuclear waste storage containers (Riley et al., 1992). Much of the current understanding of uranium biogeochemistry stems from the need to predict the fate of uranium in contaminated environments, prevent the mobilization of uranium into pristine aquifers, and devise remediation strategies which utilize the natural processes controlling uranium mobility in the environment. Originally, natural attenuation of uranium-contaminated soils was expected to play a significant role in decreasing uranium concentrations below the Maximum Contaminant Level (MCL) of 0.126 μmol/L tolerated by the US Environmental Protection Agency (EPA) on the time scale of tens of years. The persistence of uranium plumes exceeding regulatory limits, however, highlighted the inability to successfully predict the fate of uranium in subsurface environments. These findings also demonstrated the need for a process-based understanding of uranium biogeochemistry to develop site-specific remediation strategies which exploit the natural biogeochemical and hydrological processes controlling uranium mobility.

1.5.1 Physical remediation strategies

Physical remediation strategies to address uranium contaminations are primarily focused on containment of uranium by erecting impenetrable barriers to restrict surface water infiltration or impede the subsurface transport of the contaminant plume. While

physical remediation strategies are often the most economic approach, they merely contain the contaminant and do not actually mitigate its toxicity to the environment. Indeed, original efforts to contain the uranium plume at the Y-12 Facility in Oak Ridge, TN were unsuccessful in preventing uranium migration following soil capping and the construction of a parking lot above the capped waste ponds (Wu et al., 2006a).

1.5.2 Chemical remediation strategies

Chemical remediation of uranium contamination involves altering the mobility of uranium by promoting changes in its solubility, either through complexation with ligands or reduction/oxidation. Soil washing and pump-and-treat strategies are performed *ex situ* whereby soil or groundwater is removed from the aquifer, treated above ground, and replaced/reinjected into the subsurface (Kerr, 1990; Mackay and Cherry, 1989). During treatment, uranium may be removed from the soil matrix through mechanical separation and from groundwater by flocculation, precipitation, adsorption, ion exchange resins, or reverse osmosis (Dawson and Gilman, 2001; Nimmons, 2007). Because soil washing and pump-and-treat technologies are cost prohibitive on large scales and require the handling of toxic contaminants, *in situ* remediation strategies have been explored (Jardine et al., 2004; Riley et al., 1992). *In situ* chemical strategies include flushing the soil with a suitable chelating agent by injection into the subsurface via a gallery of wells upstream of the contaminant plume to increase the mobility of uranium and allow for extraction via groundwater pumping (Fox et al., 2012; Francis et al., 1998; Shiel et al., 2013). Carbonate and citrate are effective ligands for these applications as they promote the mobility of uranium by forming stable aqueous complexes which are less prone to adsorption (Fox et al., 2012; Francis et al., 1998; Shiel et al., 2013) and, in the case of citrate, may dissolve

potential sorbents (e.g. iron oxides) and release contaminants (Francis et al., 1998; Kantar and Honeyman, 2006). Soil flushing, however, requires high permeability soils and may promote the unwanted mobility of co-contaminants as a variety of ligands non-specifically bind to metals.

Conversely, other *in situ* chemical remediation strategies seek to immobilize uranium by promoting adsorption onto solid phases or formation of insoluble uranium minerals. Various minerals have been investigated for their ability to remove U(VI) from contaminated environments. The most important are zeolites (Krestou et al., 2004), zero-valent iron (Cantrell et al., 1995), calcium carbonates (Meece and Benninger, 1993; Reeder et al., 2000; Reeder et al., 2001) and hydroxyapatites (Fuller et al., 2003; Fuller et al., 2002; Jerden and Sinha, 2003; Krestou et al., 2004). Uranyl phosphate minerals (e.g. autunite/meta-autunite group minerals) are highly insoluble and stable in mildly acidic and neutral pH over long time-scales (Jerden and Sinha, 2003; Kanematsu et al., 2014) and are therefore appealing candidates for long-term uranium remediation efforts. While uranyl phosphates are stable in oxidizing environments, the presence of carbonates prevents their precipitation apparently because carbonates compete with phosphate for uranium (Fuller et al., 2002). pH plays a significant role in determining the stability of uranyl phosphate minerals as it controls the concentration of carbonates in natural waters and simultaneously affects the solubility of uranyl phosphate compounds. Indeed, the complex speciation of U(VI) in carbonate-dominated waters in the presence of hydroxyapatite results in the efficient removal of U(VI) by adsorption in the pH range 6-7, but above circumneutral pH, the pH_{zpc} of hydroxyapatite is exceeded, and U(VI) is under the form of the less negatively charged $(UO_2)_2(CO_3)(OH)_3^-$ which tends to desorb from the solid phase (Wellman et al.,

2008). As a result, uranium phosphate phases such as chernikovite or autunites may precipitate preferentially in these conditions, provided that phosphate is present in significant concentrations in the groundwater compared to carbonates (Jerden and Sinha, 2003).

As inorganic phosphorus is scarce in most soils, *in situ* remediation strategies have included the injection of inorganic phosphates, organophosphates, such as phytate, or even polyphosphates to provide a phosphorus source that would slowly precipitate U(VI) from groundwater (Nash et al., 1998; Seaman et al., 2003; Wellman et al., 2006). However, tests performed with Hanford soils at pH 8 revealed that precipitation of calcium phosphate and calcium phytate decreases the permeability of these soils rapidly, probably precluding their use as a remediation strategy at such a high pH (Wellman et al., 2006). In turn, tripolyphosphate (TPP) does not decrease permeability of these soils, suggesting it could be transported far away from its source and used as a slow source of ΣPO_4^{3-} to immobilize U(VI) (Wellman et al., 2006).

As an alternative to the injection of a reactant, chemical remediation can be achieved using permeable reaction barriers (PRB) – trenches filled with porous, reactive material arranged downstream and perpendicular to groundwater flow such that the contaminant is chemically treated as it flows through the barrier (Dawson and Gilman, 2001). PRBs are suitable for shallow surface contaminations, do not require maintenance, and avoid the handling of contaminants required in *ex situ* remediation strategies. PRBs constructed from zero-valent iron successfully decrease effluent uranium concentrations via reductive precipitation within the barrier coupled to the oxidation of Fe(0) to Fe(II) (Biermann et al., 2006; Gu et al., 1998; Morrison et al., 2001). Successful PRBs made of

apatite have also been used to treat Zn, Pb, and Cd contaminated waters (Conca and Wright, 2006) and have shown promise for treatment of uranium during laboratory studies (Biermann et al., 2006; Simon et al., 2008; Simon et al., 2004). In this treatment, uranium uptake by hydroxyapatite occurs via adsorption at low surface loading and precipitation of uranyl phosphate minerals at higher surface loading (Fuller et al., 2002). Long-term contaminant immobilization by PRBs is limited by the finite amount of surface sites for contaminant adsorption, in the case of hydroxyapatite PRBs, or decreasing permeability due to the buildup of corrosion products with time (i.e. iron oxides), in the case of Fe(0) PRBs (Biermann et al., 2006).

1.5.3 Bioremediation strategies

In situ bioremediation is an attractive alternative to *in situ* chemical approaches as it preserves subsurface hydrology, can be applied over a larger scale compared to PRBs, and is more selective to a specific contaminant than soil flushing. The bioremediation of uranium relies on subsurface microbial communities that transform uranium into a less mobile form either by reductive or non-reductive precipitation. Bioreduction is the most studied uranium bioremediation strategy and relies on the stimulation of subsurface MRB that catalyze the reduction of soluble U(VI) to sparingly soluble U(IV) minerals to decrease groundwater uranium concentrations. Because subsurface microbial communities are typically carbon-limited, an organic carbon substrate which acts as both an electron donor and carbon source is injected into the subsurface upstream of the contaminant plume via a gallery of injection wells to stimulate microorganisms (Anderson et al., 2003; Istok et al., 2004; Senko et al., 2002; Watson et al., 2013; Williams et al., 2011; Wu et al., 2006a; Wu et al., 2006b; Wu et al., 2007). A variety of carbon substrates have been successfully

injected in contaminated subsurfaces to decrease uranium concentrations during large-scale field studies, including acetate (Anderson et al., 2003; Istok et al., 2004; Williams et al., 2011), glucose (Istok et al., 2004), emulsified vegetable oil (EVO) (Watson et al., 2013), and ethanol (Istok et al., 2004).

Although bioreduction is seemingly straightforward, stimulating diverse microbial communities initiates a complex network of enzymatic and abiotic reactions that ultimately affects the fate of uranium. For example, as uranium-contaminated areas are often associated with nitrate contaminations and low pHs as a result of the use of nitric acid to extract uranium from ore, nitrate reduction via denitrification or dissimilatory nitrate reduction to ammonia (DNRA) is readily stimulated following addition of a carbon substrate (Istok et al., 2004; Watson et al., 2013; Wu et al., 2006b). During this phase, uranium concentrations remain elevated as denitrifying bacteria utilize nitrate over U(VI) as a TEA and produce denitrification intermediates which readily oxidize U(IV) (Figure 1.3D). After complete removal of nitrate via denitrification (Senko et al., 2002) or pretreatment of groundwater (Wu et al., 2006a), the growth and activity of MRB are enhanced and associated with the production of Fe(II), Mn(II), and the removal of U(VI) via bioreduction (Anderson et al., 2003; Istok et al., 2004; Watson et al., 2013). In addition to direct enzymatic reduction of U(VI), microorganisms indirectly affect U(VI) reduction via production of reduced metabolites which either adsorb onto minerals and make them better abiotic reductants of U(VI) (i.e. Fe(II)) (Liger et al., 1999; Wehrli et al., 1989), or form iron sulfide minerals (i.e. Fe(II) and ΣH_2S) which abiotically reduce U(VI) and immobilize uranium for long periods of time after biostimulation (Bargar et al., 2013; Williams et al., 2011). In contrast, microorganisms also indirectly affect U(VI) reduction

via remineralization of organic carbon during respiration which increases alkalinity and promotes desorption of U(VI), dissolution of non-uraninite U(IV), and ultimately remobilization of uranium (Anderson et al., 2003; Williams et al., 2011; Wu et al., 2006b).

The success of bioreduction depends on maintaining reducing conditions to prevent the oxidative dissolution of U(IV) solids which is challenging over long time scales given the large number of U(IV) oxidants (Figure 1.3). Indeed, the return of aerobic and nitrate-reducing conditions promotes oxidative dissolution of U(IV) species by dissolved oxygen (Campbell et al., 2011; Watson et al., 2013; Wu et al., 2007) and denitrification intermediates (Istok et al., 2004; Watson et al., 2013). Mackinawite and amorphous FeS formed during biostimulation under iron- and sulfate-reducing conditions may protect the oxidation of U(IV) by preferentially reducing dissolved oxygen during short term oxygenation of the bioreduced zone (Bi and Hayes, 2014; Bi et al., 2013), but are much less effective at preventing U(IV) oxidation by denitrification intermediates (Moon et al., 2009). For this reason, the long-term success of bioreduction is difficult in naturally oxidizing environments without continuous injection of electron donor to maintain reducing conditions. Furthermore, long-term biostimulation may lead to elevated concentrations of carbonates which lower the potential of the U(VI)/U(IV) redox couple and promote oxidative dissolution of uranium by amorphous iron and manganese oxides (Ginder-Vogel et al., 2006; Ginder-Vogel et al., 2010), even under highly reducing conditions when uranium-reducing organisms are present and active (Wan et al., 2005; Wan et al., 2008). Finally, while uraninite is fairly resistant to ligand-promoted dissolution, mononuclear U(IV) compounds may represent a more significant fraction of U(IV) in the field than previously thought (Bargar et al., 2013; Campbell et al., 2012; Kelly et al., 2008;

Latta et al., 2012a; Wang et al., 2013a) and are highly susceptible to dissolution at elevated concentrations of carbonates (Alessi et al., 2012; Cerrato et al., 2013). Non-uraninite U(IV) associated with organic matter colloids has recently been demonstrated to be more mobile than originally thought, challenging the long-standing paradigm of low uranium mobility in reducing environments (Wang et al., 2013a). Thus, more work is needed to understand the mechanism of their formation and their thermodynamic properties.

1.6 Research scope and objectives

The discovery of microbial uranium reduction opened the door for new and innovative ways to address uranium contamination, and U(VI) bioreduction has the potential to be more cost effective, efficient, and sustainable than traditional physical and chemical remediation strategies. The geochemical and mineralogical diversity of uranium-contaminated subsurfaces, combined with the complex network of biotic and abiotic reactions set in motion by biostimulation of the native subsurface microbial community, necessitates a predictive understanding of uranium biogeochemistry to assess: 1) the feasibility of U(VI) bioreduction at a specific site; and 2) the fate of uranium following biostimulation. The overall objective of this body of work is to advance our understanding of the coupled biogeochemical cycling of uranium and iron and incorporate this newfound knowledge into kinetic models able to predict the removal of uranium from solution over a wide range of geochemical conditions in the presence and absence of iron oxides.

Previous studies have separately demonstrated the ability of iron to act as both a reductant and an oxidant of uranium, and factors affecting the extent of reaction between uranium and iron are known to include pH, solution composition, and iron oxide

mineralogy. However, questions remain as to the mechanisms by which these geochemical parameters control uranium removal from solution. Far less is known about the coupled redox cycling of uranium and iron in the presence of metal-reducing bacteria which can utilize both U(VI) and Fe(III) oxides as terminal electron acceptors in anaerobic respiration. The primary goal of this dissertation is to identify the dominant geochemical controls of uranium removal from solution in the presence of iron oxides and metal-reducing bacteria for the express purpose of predicting the success of U(VI) bioreduction as a bioremediation strategy over a wide range of geochemical conditions. Specifically, this dissertation details experiments which seek to test the following hypotheses:

1) The rate of U(VI) bioreduction is controlled by the concentration of non-carbonate uranyl species, which are bioavailable to metal-reducing bacteria yet toxic at high concentrations.
2) Aqueous uranyl speciation alters the U(VI)/U(IV) redox potential and controls whether iron acts either as a reductant or an oxidant of uranium.
3) Aluminum substitution of ferrihydrite decreases uranium removal via U(VI) bioreduction by: enhancing the abiotic oxidative dissolution of U(IV) solids by ferrihydrite; and sustaining U(IV) oxidation by preserving ferrihydrite against consumption via microbial reduction and secondary mineralization.

Pure culture batch incubations with synthetic iron oxide minerals were preferred compared to natural microbial communities and sediments as the experimental approach to study the coupled biogeochemical cycling of uranium and iron in order to develop a mechanistic understanding of uranium-iron cycling under well-defined geochemical conditions. A suite of analytical techniques were employed to monitor aqueous and solid

phase speciation of uranium, iron, and secondary elements over time during bioreduction incubations, and computational techniques were used to calculate equilibrium concentrations of aqueous metal-ligand complexes and to construct kinetic models to reproduce experimental observations. Chapter 2 of this dissertation describes in detail the biological, geochemical, analytical, and computation techniques employed to achieve these objectives.

Aqueous uranyl speciation affects nearly all aspects of uranium biogeochemistry, including the kinetics of U(VI) bioreduction by metal-reducing bacteria and the toxicity of uranium to microorganisms. Thus far, however, the influence of uranium toxicity on microbial uranium reduction remains poorly defined. Chapter 3 sought to deconvolute the roles of solution composition on the kinetics of U(VI) bioreduction in the absence of additional terminal electron acceptors and provide a unifying framework to account for the effects of aqueous uranyl speciation on bioavailability and toxicity to a metal-reducing bacterium. Uranium(VI) bioreduction incubations and viability assays were conducted with *Shewanella putrefaciens* strain 200 over a broad range of aqueous uranyl speciation conditions, and a speciation-dependent kinetic model for U(VI) bioreduction was developed to reproduce observed time series of total dissolved uranium concentration. The proposed model is discussed in the context of biostimulation field studies at uranium-contaminated sites and the challenges associated with transferring knowledge acquired in simple laboratory model systems to real-world applications.

Whereas the bioavailability and toxicity of U(VI) to metal-reducing bacteria represent the dominant controls of U(IV) bioreduction and uranium removal from solution in the absence of other redox active elements, uranium removal from solution in the

presence of iron may be enhanced or hindered depending on the role of iron as either a reductant or an oxidation of uranium. Chapter 4 investigated the geochemical controls of the role of iron in uranium redox cycling. The objectives of this work were to determine the effects of 1) aqueous uranyl and ferrous speciation and 2) secondary mineralization of ferrihydrite on the abiotic reduction or oxidation of uranium by iron. A kinetic model which accounts for the thermodynamic controls of abiotic uranium-iron redox reactions was proposed.

The use of pure, synthesized iron oxides provide the opportunity to understand chemical reaction mechanisms in idealized conditions. Impurities, however, are abundant in natural iron oxides, and these impurities affect their biological and chemical reactivity. Little is known regarding the effect of ferrihydrite impurities on the redox properties of this mineral. Chapter 5 investigated the effect of aluminum- and silica-substituted ferrihydrite on the coupled redox cycling of uranium and iron. The objectives of this work were 1) to identify the effects of Al- and Si-substitution on the ability of ferrihydrite to oxidize U(IV) solids and 2) to identify how changes in the secondary mineralization of Al- and Si-ferrihydrite affect the oxidation of U(IV) solids.

Finally, Chapter 6 synthesizes the results of this dissertation and discusses the implications of this work in the context of bioremediation of uranium-contaminated subsurface environments. New research questions raised by this work are discussed, and recommendations for future work are made.

CHAPTER 2. MATERIALS AND METHODS

2.1 Cell cultures

Shewanella putrefaciens strain 200 (ATCC 51753), a gram-negative metal-reducing gammaproteobacterium, was used for all biotic batch incubations. Originally isolated from a crude oil pipeline (Obuekwe et al., 1981), *S. putrefaciens* is capable of utilizing a suite of terminal electron acceptors for energy generation and growth, including U(VI) and solid Fe(III) oxides (Wade and DiChristina, 2000).

A single freezer stock (-80 °C, 15% glycerol) of *S. putrefaciens* was used to prepare all cell cultures. First, a sterile wire loop was used to plate frozen cells onto lysogeny broth (LB) agar plates (16.3 g/L agar). Following 24 – 48 hours of incubation at 30°C, single colonies were selected using a sterile wire loop and inoculated into sterile glass culture tubes containing 5 mL of LB medium (Table 2.1).

Table 2.1 Lysogeny broth (LB) medium composition

Component	Concentration (g/L)
NaCl	10
Yeast extract	5
Tryptone	10

LB cultures were shaken at 30°C for approximately 8 hours until visibly turbid. 4 – 6 LB cultures were combined into a sterile 50 mL Falcon tube, and cells were harvested

by centrifugation (2500×g for 15 min) then resuspended in 5 mL of M1 growth medium (Table 2.2). An aliquot of LB-grown cells was inoculated into an Erlenmeyer flask containing 1 or 2 liters of M1 growth medium (pH 7.8, 15 mM HEPES buffer) provided with lactate as the electron donor (15 mM) and fumarate as the electron acceptor (60 mM) to achieve an initial cell density of 0.01 OD_{600} (optical density measured at 600 nm on a Beckman Coulter DU720 UV/Vis spectrophotometer). The medium was stirred with a magnetic stir bar and continuously bubbled with N_2 gas to prevent oxygen diffusion from the atmosphere. Cell growth was periodically monitored by OD_{600}, and upon reaching late-log phase (up to approximately 0.08 OD_{600}), the culture was decanted into sterile 50 mL Falcon tubes and cells were harvested by centrifugation (2500×g for 15 min), combined, and washed once with the background M1 medium (i.e., lacking electron donors and acceptors) used for the batch incubations. Finally, a sterile needle and syringe was used to inoculate an aliquot of the concentrated fumarate-grown cell suspension into batch reactors for an initial cell concentration of 2×10^7 cell/mL as determined by OD_{600} using a conversion factor of 2×10^9 cell/mL/AU as determined by direct cell counts.

2.2 Synthesis of iron oxides

2.2.1 2-line ferrihydrite

Two-line ferrihydrite (hereafter referred to as ferrihydrite) was synthesized by dissolving 5.4 g of $FeCl_3\cdot6H_2O$ (Fisher Scientific) in ~100 mL of sterile, 18 MΩ Milli-Q water and titrating the solution to pH 7.5 with 1 N NaOH at a flow rate of 4 mL/min while rapidly stirring the suspension with a magnetic stir bar (Cismasu et al., 2012; Schwertmann and Cornell, 2000). The resulting ferrihydrite suspension was washed three times

Table 2.2 Composition of stock solutions used to prepare M1 growth medium

Solution	Concentration in stock solution	Final concentration in M1 medium[a]
Metal supplement stock solution		
$CoCl_2$	5 mM	5 μM
$NiCl_2$	5 mM	5 μM
NaCl	10 mM	10 μM
Trace element stock solution		
H_3BO_4	56.6 mM	56.6 μM
$ZnSO_4$	1.04 mM	1.04 μM
Na_2MoO_4	3.87 mM	3.87 μM
$MnSO_4 \cdot H_2O$	1.26 mM	1.26 μM
$CuSO_4$	200 mM	200 nM
Basal salt stock solution		
$MgSO_4$	25 mM	1 mM
$FeSO_4$	135 μM	5.4 μM
$CaCl_2$	12.13 mM	485.2 μM
Na_2EDTA	1.68 mM	67.2 μM
Amino acid solution		
L-serine	190.5 mM	381 μM
L-arginine	57.5 mM	115 μM
L-glutamine	68.5 mM	137 μM
Individual stock solutions[b]		
$(NH_4)_2SO_4$	500 mM	50 μM
Na_2SeO_4	15 mM	1.5 μM
$FeCl_3$	100 mM	100 μM
KH_2PO_4	100 mM	100 μM
HEPES	500 mM	20 mM
$NaC_3H_6O_3$ (lactate)	3.57 M (30%)	15 mM

[a]1 L of M1 medium is prepared by combining 910 mL DI H_2O, 100 μL $(NH_4)_2SO_4$ solution, 100 μL Na_2SeO_4 solution, 40 mL basal salt solution, 1 mL trace element solution, 1 mL metal supplement solution, 4.2 mL lactate solution, and 9.6 g sodium fumarate (160.04 g/mol, 60 mM final concentration). Autoclave. Finally, add 2 mL filter-sterilized amino acid solution, 1 mM filter-sterilized $FeCl_3$ solution, 1 mL filter-sterilized KH_2PO_4 solution, and 40 mL filter-sterilized HEPES buffer (pH 8.0). [b]Components are prepared individually

with sterile Milli-Q water, by repeated centrifugation (2500×g for 3 min) and decantation of the supernatant, and stored as a sterile ~200 mM stock solution in a brown glass bottle at room temperature until needed. The total iron concentration of the ferrihydrite stock solution was measured using the ferrozine assay (detailed in section 2.3.4.1) following reduction by hydroxylamine (0.1 M HCl, 0.2 M hydroxylamine). The dry weight of 1 mL of the stock solution was measured after drying overnight at 60°C to determine the concentration in g/L. The average molar weight of the ferrihydrite prepared using this method was 95.5±4.1 g/mol (n=8). Ferrihydrite was prepared no more than 5 days prior to inoculation to avoid transformation to more crystalline phases before use.

2.2.2 Al-substituted 2-line ferrihydrite

Al-substituted 2-line ferrihydrite (hereafter referred to as Al-ferrihydrite) was prepared in a manner analogous to the synthesis of pure ferrihydrite as described above (section 2.2.1). Predetermined amounts of $AlCl_3 \cdot 6H_2O$ (99% pure, Acros Organics) and $FeCl_3 \cdot 6H_2O$ (Fisher Scientific) were dissolved in sterile, 18 MΩ Milli-Q water to give a 0.2 M solution with the desired mol% Al (mol% Al = [Al]/([Al]+[Fe])). The aluminum salt was dissolved completely prior to addition of the iron salt to prevent secondary aluminum precipitation. The solution was rapidly titrated to a final pH of 7.5 with 1 N NaOH at a flow rate of 4 mL/min while rapidly stirring the suspension with a magnetic stir bar (Cismasu et al., 2012). The resulting Al-ferrihydrite suspension was washed three times with sterile 18 MΩ Milli-Q water by repeated centrifugation (2500×g for 3 min) and decantation of the supernatant, and stored as a sterile ~200 mM Fe stock solution in a brown glass bottle at room temperature until needed. The total iron concentration of the Al-

ferrihydrite stock solution was measured using the ferrozine assay (detailed in section 2.3.4.1) following reduction by hydroxylamine (0.1 M HCl, 0.2 M hydroxylamine). The total Al concentration of the Al-ferrihydrite stock solution was confirmed by dissolving an aliquot of the stock solution in 1 M HNO_3 and measuring Al by ICP-MS (detailed in section 2.3.3). This method yielded Al-ferrihydrite within 10% of the desired Al content.

2.3 Analytical techniques

All reagents and dilutions were made with 18 MΩ Milli-Q water, hereafter referred to as DI H_2O.

2.3.1 pH

pH was measured using a double junction semi-micro pH electrode (Orion) calibrated with three low ionic strength commercial buffers (pH 4, 7, and 10, Fisher Scientific, Inc.). All pH measurements were performed on unfiltered aliquots in 1.5 mL microcentrifuge tubes.

2.3.2 Dissolved inorganic carbon (DIC)

Dissolved inorganic carbon (DIC) was measured by flow injection analysis with conductivity detection (Hall and Aller, 1992) using a computer-operated Analytical Instruments Systems, Inc. (AIS, Inc.) LCC100 integrator. The system was operated by a peristaltic pump (Dynamax) at a flow rate of approximately 1.5 mL/min. Samples were injected using a 50 μL sample loop into a 30 mM HCl carrier stream and passed over a gas-permeable Teflon membrane while a 10 mM NaOH receiving stream was pumped in the same direction on the other side of the membrane. DIC present in the sample was

converted into $CO_2(g)$ in the acidic carrier stream which diffused across the gas-permeable membrane into the basic receiver stream where it was converted to CO_3^{2-}. The receiver stream was then pumped to a conductivity detector which processed conductivity measurements every 100 ms. The presence of DIC in a sample was visualized as a negative peak in the conductivity time series with the area of the peak proportional to DIC concentration (Figure 2.1). A semi-automated MATLAB script was used to integrate the data and obtain peak areas (Bristow and Taillefert, 2008). Calibration standards (1 – 20 mM DIC) were prepared with $NaHCO_3$ in DI H_2O immediately prior to analysis.

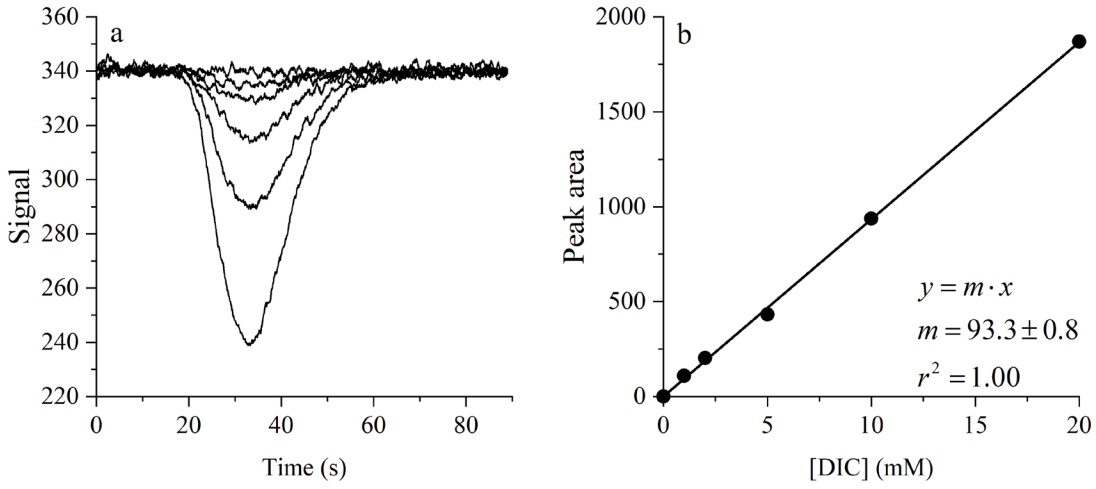

Figure 2.1 Typical (A) signal output (11-point moving average) and (B) calibration curve for dissolved inorganic carbon (DIC) measurements using flow injection analysis with conductivity detection. Note that the blank peak area value has been subtracted from all standards and the slope of the linear regression has been forced through the origin.

2.3.3 Inductively-coupled plasma mass spectrometry (ICP-MS)

Total dissolved magnesium, calcium, aluminum, and uranium were measured by inductively-coupled plasma mass spectrometry (ICP-MS, Agilent 7500a series). Filtered aliquots were diluted in 2% trace metal grade HNO_3 (Fisher Scientific, Inc.) containing scandium, holmium, and bismuth as internal standards to correct for instrument drift (0.5 ppb in auto mode or 5 ppb in analog mode, SPEX CertiPrep). Scandium was used to correct magnesium, calcium, and aluminum counts whereas holmium and bismuth were used to correct uranium counts. Blanks and a calibration standard (0.5 ppb in auto mode or 5 ppb in analog mode) were measured every 6-7 samples as quality controls. Recovery of the

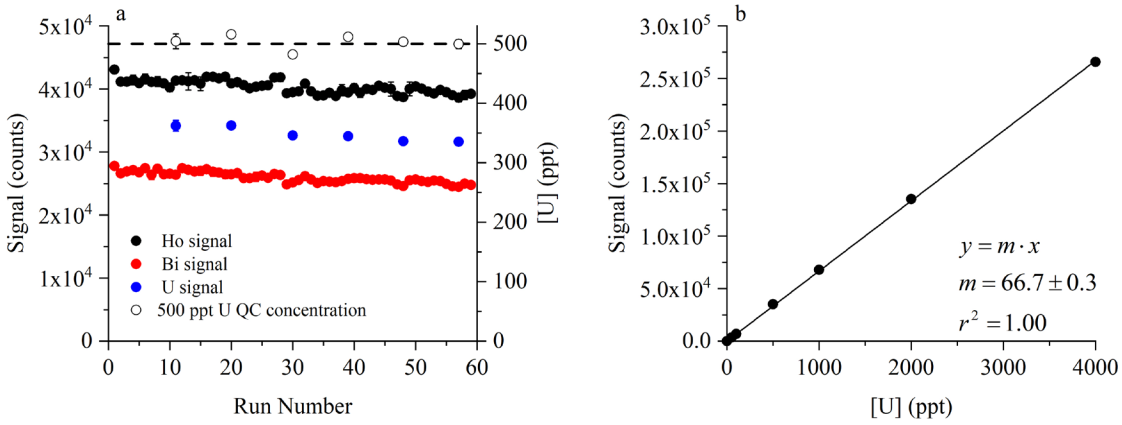

Figure 2.2 Typical (A) signal output and (B) calibration curve for ICP-MS measurements of total dissolved uranium. A 500 ppt U standard (blue) was run periodically as a quality control, and Ho (black) and Bi (red) were used as internal standards to correct the signal for instrument drift. Recovery of the quality control (open circles) was 96 – 103% for the data shown. Note that the blank signal value has been subtracted from all standards and the slope of the linear regression has been forced through the origin. Symbols and error bars represent the mean and instrument precision (n=3), respectively.

calibration standard was typically 95 – 105% (Figure 2.2A). Calibration standards for magnesium (50 – 200 ppb), calcium (20 – 200 ppb), aluminum (low range: 5 – 25 ppb; high range: 50 – 100 ppb), and uranium (low range: 0.05 – 4; high range: 0.5 – 40 ppb) were prepared with certified stock solutions (U and Al, SPEX CertiPREP; Ca and Mg, Ricca Chemical Company) in 2% HNO_3 containing the internal standards and measured approximately every 25-30 samples (Figure 2.2B).

2.3.4 Colorimetry

2.3.4.1 Iron

The ferrozine assay was used to measure aqueous and solid-phase iron speciation (Stookey, 1970). Briefly, the ferrozine reagent reacts with ferrous iron to form a ferrozine-iron(II) complex which absorbs light at 562 nm proportionally to the concentration of the complex. Following pretreatment with either acid or reductant, an aliquot was added to 500 µL of 1 g/L ferrozine (buffered with 2 M ammonium acetate) and diluted with DI H_2O to a final volume of 1 mL. Total Fe(II) ($Fe(II)_T$) was quantified by dissolving an unfiltered subsample in 1 M HCl for 24 hours in the dark under the anaerobic chamber atmosphere and measuring Fe(II) by the ferrozine assay. Dissolved Fe(II) ($Fe(II)_d$) was measured in filtered subsamples by the ferrozine assay, whereas total initial iron ($Fe_{T,0}$) and total dissolved iron (Fe_{Td}) were measured in unfiltered and filtered subsamples by the ferrozine assay following reduction with hydroxylamine (0.2 M hydroxylamine, 0.1 M HCl). Dissolved Fe(III) ($Fe(III)_d$) was calculated by difference from measurements of Fe_{Td} and $Fe(II)_d$ (Viollier et al., 2000). Calibration standards (1 – 60 µM) were prepared with a ferrous ammonium sulfate salt ($Fe(NH_4)_2(SO_4)2{\cdot}6H_2O$, Fisher) in acidified (10 mM HCl)

DI H_2O. Both samples and calibration standards used a ferrozine:total volume ratio of 1:2. Absorbance at 562 nm was measured on a Beckman Coulter DU720 UV/Vis spectrophotometer.

2.3.4.2 Silica

Total dissolved silica was measured in filtered subsamples (0.22 μm) using the molybdenum-blue colorimetric method. Briefly, silica in the sample is mixed with an acidic ammonium molybdate solution to form a yellow beta-molybdosilicic acid complex, which is then reduced by a metol-oxalic acid solution to form a heteropolymolybdous-blue complex that absorbs light at 810 nm proportionally to the concentration of the complex. The following reagents were prepared in DI H_2O:

Ammonium molybdate solution: 1 g of $(NH_4)_6Mo_7O_{24}\cdot 4H_2O$ (Fisher) was dissolved in 100 mL water, and the solution was acidified by the addition of 3 mL concentrated trace metal grade HCl (Fisher). The solution was stored in a polyethylene bottle at room temperature in the dark. This solution was remade periodically to avoid the formation of a white precipitate on the sides of the bottle.

Metol-sulfite solution: 1.2 g Na_2SO_3 (Fisher) was dissolved in 100 mL water. Next, 2.0 g Metol (*p*-methylamino-phenol sulfate, Kodak) was added and dissolved. The solution was filtered (0.22 μm) and stored at room temperature in a brown glass bottle. This solution was remade every few months to avoid the formation of an amber precipitate.

Sulfuric acid solution: A 50% (v/v) H_2SO_4 solution was prepared from concentrated trace metal grade H_2SO_4 (Fisher) and stored at room temperature in a brown glass bottle.

Oxalic acid solution: 10 g $C_2H_2O_4$ (Acros Organics) was dissolved in 100 mL water and stored at room temperature in a brown glass bottle.

Mixed reducing reagent: 10 mL metol-sulfite solution, 6 mL oxalic acid solution, 6 mL sulfuric acid solution, and 8 mL water were combined in a 50 mL centrifuge tube. This reagent was prepared fresh prior to each batch of analyses.

A filtered aliquot was added to 0.2 mL ammonium molybdate solution and diluted up to a final volume of 0.7 mL. The yellow beta-molybdosilicic acid complex was allowed to develop for at least 15 minutes. Next, 0.3 mL mixed reducing agent was added, and the molybdous-blue complex was allowed to develop for at least 2.5 hours. Calibration standards (4 – 60 μM) were made with a certified silica stock solution (Fisher) in the same reagent ratios as the samples. Finally, absorbance at 810 nm was measured on a Beckman Coulter DU720 UV/Vis spectrophotometer within 24 hours of adding the reducing agent.

2.3.5 Adenosine triphosphate (ATP) assay

The presence iron and uranium solids in batch incubations with *S. putrefaciens* hinders the use of conventional techniques to measure cell growth. *Shewanella spp.* are known to attach to mineral surfaces (Zhang et al., 2010) which allows them to evade visual counting. Reductive dissolution of iron oxides prior to cell counting has been used to address this issue, however, when uranium and iron are included together in incubations, chemical reduction leads to the precipitation of U(IV) solids which also interfere with

visual counting. Protein concentration can be used as a proxy for biomass concentration, however, preliminary results demonstrate that U(VI) interferes with the Bradford protein assay (data not shown). Molecular techniques such as qPCR relate the 16S rRNA copy number to cell number (Sanford et al., 2007), however, this technique does not differentiate live and dead cells which might be substantial in the presence of uranium.

To avoid issues associated with conventional techniques, intracellular adenosine triphosphate (ATP) was measured as a proxy for cell growth. This approach assumes 1) cells contain the same concentration of intracellular ATP under similar growth conditions and 2) an increase in intracellular ATP is proportional to an increase in viable cells. Preliminary experiments have demonstrated the correlation between cell counts, OD_{600}, and intracellular ATP during growth of *S. oneidensis* on fumarate (personal communication with Christina Smeaton). Dead cells are not expected to contribute to the measurement of intracellular ATP, and extracellular ATP can also be measured as an indication of cell death (Smeaton et al., 2012).

Total ATP and extracellular ATP were measured in unfiltered and filtered aliquots, respectively, using the Promega BacTiter-Glo™ Microbial Cell Viability Assay following the manufacturer instructions. Briefly, 100 µL sample aliquots were pipetted into an opaque, flat-bottom, white 96-well plate (Thermo Scientific). Wells used for measurement were spaced horizontally and vertically to avoid cross talk between wells. The BacTiter-Glo™ reagent was prepared according to manufacturer instructions and stored as 2.5 mL aliquots in 5 mL Falcon tubes at -20°C prior to use. 100 µL of the thawed BacTiter-Glo™ reagent was added to the measurement wells and mixed by triturating the solution with a multi-channel pipette. Following 5 minutes of incubation at room temperature,

luminescence measurements were made on a Hidex Sense microplate reader. ATP measurements were made immediately after sampling incubations, and luminescence measurements were made within 15 minutes of adding the BacTiter-Glo™ reagent. 10 mL ATP standards (0.1 – 100 nM) were prepared by serial dilution in M1 growth medium from a 10 mM ATP stock solution (Promega) and stored as 1 mL aliquots in 1.5 mL microcentrifuge tubes at -20°C. Standards and a blank were prepared in the same manner as the samples and measured with each plate (Figure 2.3). Intracellular ATP was calculated as the difference between total and extracellular ATP concentrations.

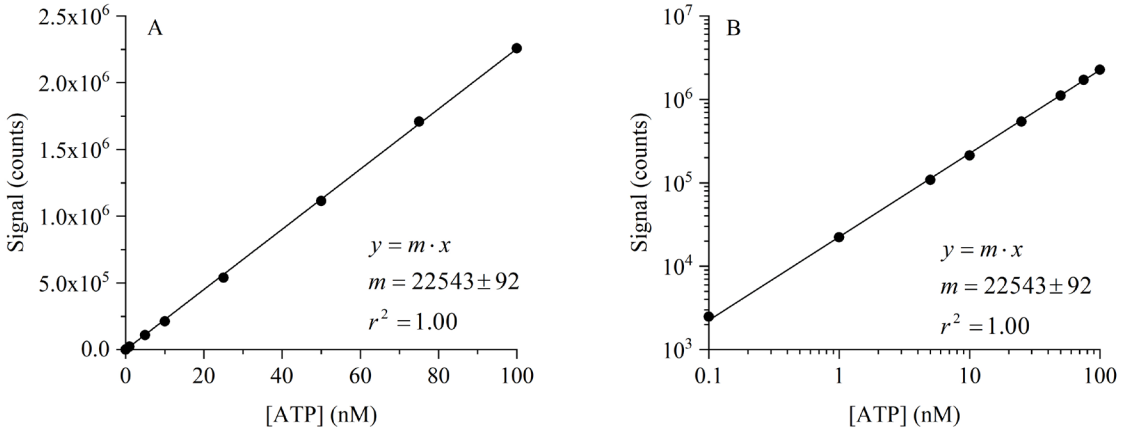

Figure 2.3 Typical calibration curve for ATP using the Promega BacTiter-Glo™ Microbial Cell Viability Assay. The same calibration curve is represented on a (A) linear and (B) logarithmic scale to demonstrate the linearity of the signal over a large range of ATP concentration. Note that the blank signal value has been subtracted from all standards and the slope of the linear regression has been forced through the origin.

2.3.6 Solid phase analyses

2.3.6.1 Solid phase extractions

Unfiltered aliquots of 200 µL were pelleted in 1.5 mL centrifuge tubes via centrifugation (9000×g for 10 minutes) and the supernatants were discarded using a 100 µL pipette. An ascorbate extractant (170 mM sodium citrate, 60 mM $NaHCO_3$, and 114 mM ascorbic acid adjusted to pH 8) was used to selectively extract amorphous solid-phase iron (Kostka and Luther, 1994). The pellet was resuspended in 1 mL of extractant and mixed by placing up to six 1.5 mL centrifuge tubes in a 50 mL centrifuge tube and attaching them to a rotary wheel. Following 24 hours of extraction, the sample was pelleted via centrifugation and Fe(II) in the supernatant was measured using the ferrozine assay as described in section 2.3.4.1.

2.3.6.2 Powder X-Ray Diffraction (XRD)

A hand-operated vacuum filtration unit was used to collect the solid phase on a 0.22 µm PES filter (Millipore). The samples were rinsed once with anoxic DI H_2O and dried inside an anaerobic chamber (5% H_2, 95% N_2 atmosphere). Finally, the solids were removed from the anaerobic chamber, scraped from the filter, and finely ground using a mortar and pestle prior to analysis. Diffraction data of samples mounted on a zero background holder were collected on a PANalytical Empyrean diffractometer (Cu Kα radiation) at the IEN/IMat Materials Characterization Facility at Georgia Tech. Phase identification was performed with the HighScore Plus software package using reference diffraction patterns from the PDF-4+ database (ICDD, 2015).

2.3.7 Voltammetry

Voltammetry is a powerful analytical technique because it provides accurate, reproducible, real-time measurements of multiple electrochemically active chemical species in a single measurement. In addition to quantitative measurements, voltammetry also provides specific information regarding the redox characteristics (i.e. redox potential) and the reduction/oxidation mechanism of a given chemical species. In voltammetry, a range of potentials is applied as a function of time between a working and a reference electrode. When the redox potential of an electrochemically active species is reached, the reduction or oxidation of the species at the surface of the working electrode generates a current measured between the working electrode and the counter electrode which is proportional to the concentration of the species in solution (Taillefert et al., 2000). Analytical chemists have used voltammetry to characterize the interaction between uranyl and various ligands (Djogic and Branica, 1995b; Suzuki et al., 2007; Suzuki et al., 2006), quantify trace amounts of dissolved uranium in natural samples (Djogic and Branica, 1995a; Djogic et al., 2001; Van Den Berg and Nimmo, 1987), and evaluate uranyl speciation in natural samples (Djogic et al., 1986), but this technique has never been applied to studying microbial uranium reduction.

2.3.7.1 Hanging mercury drop electrode (HMDE)

To determine electrochemically active uranyl species, 15 samples (100 μM uranyl acetate, 10 mM $NaHCO_3$, 0.1 M KNO_3) were adjusted to pH ranging from 3 to 10 with NaOH and HNO_3. A U(VI):DIC ratio of 1:100 was chosen to minimize the number of uranyl species over the chosen pH range and focus on uranyl carbonate species, which are

the dominant uranyl species in natural environments around circumneutral pH (Langmuir, 1978). After 24 hours of equilibration, samples were filtered (0.22 μm, Millipore) and measured for pH, U(VI) speciation by voltammetry, and total dissolved uranium by ICP-MS. Voltammetric analyses were conducted with a Metrohm VA-633 hanging mercury drop electrode (HMDE) connected to a PGSTAT12 potentiostat (Autolab). The three-electrode cell included a mercury drop working electrode, Pt counter electrode, and saturated Ag/AgCl (KCl) reference electrode. Samples were degassed with ultra-high purity N_2 and maintained under a N_2 atmosphere during measurements. Differential pulse and square wave methods were used for scanning the potential range. Method parameters are listed in Table 3. Voltammograms were analyzed using Voltint, a semi-automated MATLAB script (Bristow and Taillefert, 2008). Peak surface areas were normalized to the maximum surface area of each unique peak for comparison with uranyl speciation calculations. Uranyl speciation for each sample was calculated in MINEQL using pH and sample composition and compared to the normalized peak surface areas as a function of pH to identify electrochemically active uranyl species.

Table 2.3 Method parameters for HMDE measurements

Method	Differential Pulse	Square Wave
Purge Time	30 s	0 s
Equilibrium Time	10 s at 0.0 V	0 s
Potential Scan	Cathodic (0.0 V to -1.5 V) at 80 mV/s	Cathodic (-0.1 V to -1.85 V) at 50 mV/s

Three distinct voltammetric peaks were identified at -0.2, -0.6, and -1.2 V vs. Ag/AgCl (Figure 2.4A). The three voltammetric signals correlate well with speciation data indicating that the peaks at -0.2, -0.6, and -1.2 V most likely correspond to UO_2^{2+}, $UO_2(CO_3)_2^{2-}$, and $UO_2(CO_3)_3^{4-}$, respectively (Figure 2.4B).

Attempts were made to calibrate the three electrochemically active uranyl complexes. UO_2^{2+} was calibrated using uranyl acetate in 30 mM $NaHCO_3$ (pH 2.6, adjusted with H_2SO_4). The voltammetric response was linear from 0-100 µM using peak surface area (Figure 2.5A). The limit of detection (LOD) was determined to be 1.2 µM (3σ of the blank). $UO_2(CO_3)_3^{4-}$ was calibrated using uranyl acetate in 30 mM $NaHCO_3$ (pH 8.92,

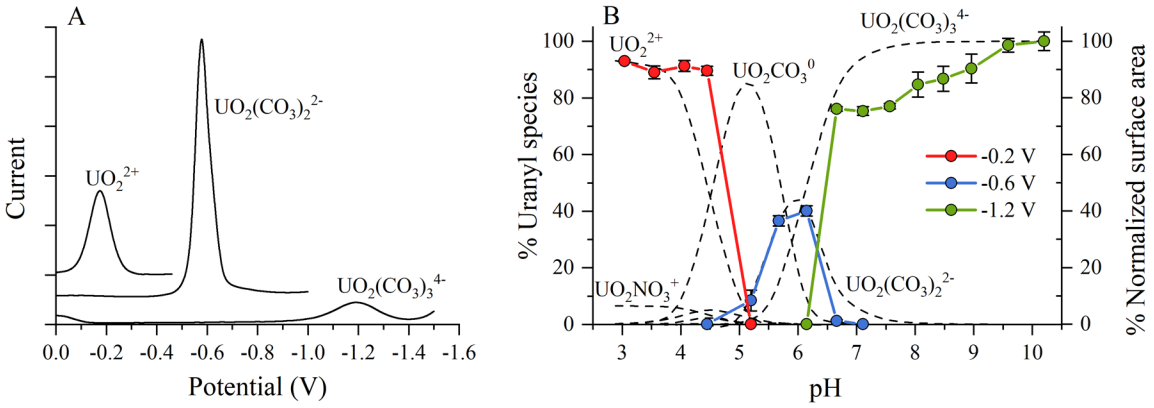

Figure 2.4 A) Voltammograms showing the appearance of three distinct peaks at pH 2 (-0.2 V), 6 (-0.6 V), and 9 (-1.2 V) in a solution of 100 µM uranyl acetate and 10 mM $NaHCO_3$. B) Percent normalized peak surface area was compared to percent uranyl speciation to identify the peaks at -0.2, -0.6, and -1.2 V as UO_2^{2+}, $UO_2(CO_3)_2^{3-}$, and $UO_2(CO_3)_3^{4-}$, respectively.

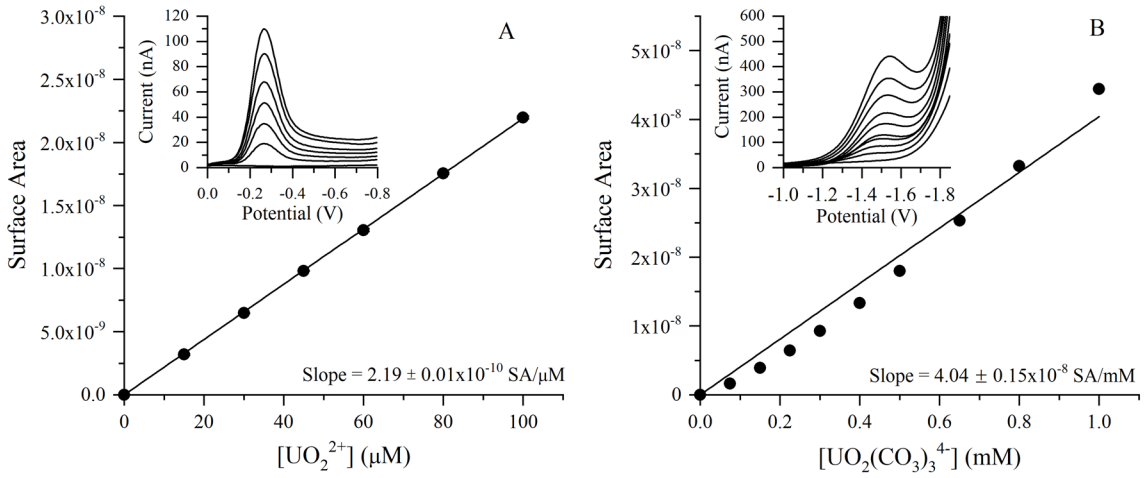

Figure 2.5 A) Calibration curve for UO_2^{2+} in 30 mM $NaHCO_3$ (pH 2.6). B) Calibration curve for $UO_2(CO_3)_3^{4-}$ in 30 mM NaHCO3 (pH 8.92). Inset figures show voltammograms for each calibration standard.

adjusted with NaOH). The voltammetric response was linear from 0-1 mM using peak surface area (Figure 2.5B), and the LOD was determined to be 1.9 μM. Attempts to calibrate $UO_2(CO_3)_2^{2-}$ were complicated by the inability to obtain a pure $UO_2(CO_3)_2^{2-}$ solution. Additionally, the voltammetric peak for $UO_2(CO_3)_2^{2-}$ appeared convoluted with two smaller adjacent peaks during calibration attempts (data not shown). These preliminary results merit additional work to identify the two smaller peaks before a robust calibration procedure for $UO_2(CO_3)_2^{2-}$ can be designed.

2.3.7.2 Au/Hg amalgam microelectrodes

Voltammetric uranyl speciation measurements during U(VI) bioreduction incubations were conducted with Au/Hg amalgam solid-state microelectrodes (Brendel and Luther, 1995) connected to a Model DLK-100 potentiostat (Analytical Instrument

Systems). Method parameters are listed in Table 2.4. A Pt wire and a saturated Ag/AgCl (KCl) electrode served as the counter and reference electrodes, respectively. Microelectrodes provide the benefit of small sample size, thus they were selected over a HMDE for uranyl speciation measurements during biotic incubations. $UO_2(CO_3)_3^{4-}$ was calibrated in the incubation media (Table 2.2) from 0 to 2 mM using uranyl acetate. No interferences from the incubation media were observed.

Table 2.4 Method parameters for Au/Hg microelectrode measurements

Method	Square Wave
Purge Time	60 s
Conditioning	-0.8 V for 60 s
Depositing	0.0 V for 45 s
Potential Scan	Cathodic (-0.1 V to -1.75 V) at 200 mV/s

To validate the measurement of U(VI) by voltammetry, U(VI) bioreduction incubations with *S. putrefaciens* were conducted in a media containing almost entirely $UO_2(CO_3)_3^{4-}$ species (>99%, MINEQL). *S. putrefaciens* reductively precipitated 1.95 mM U(VI) from solution after 218 hr in duplicate incubations while the abiotic control showed no significant U(VI) removal (Figure 2.6). Au/Hg microelectrode measurements of $UO_2(CO_3)_3^{4-}$ correlated with total dissolved uranium measurements by ICP-MS ($R^2 = 0.99$) thereby validating the newly developed voltammetric technique for quantifying uranyl speciation during U(VI) bioreduction incubations.

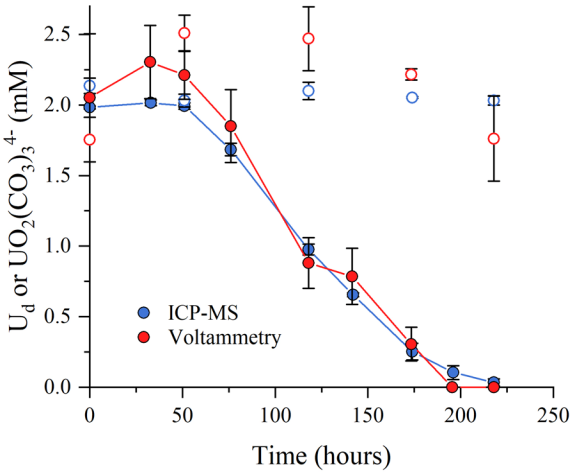

Figure 2.6 Times series of total dissolved uranium (U_d, by ICP-MS) and $UO_2(CO_3)_3^{4-}$ (by voltammetry) and concentrations in U(VI) bioreduction incubations with *S. putrefaciens* correlate strongly ($R^2 = 0.99$), thus validating the newly developed technique. Closed symbols represent biotic incubations whereas open symbols represent abiotic controls. Error bars represent the standard deviation from duplicate incubations.

Considerations should be made when deciding if voltammetry is suitable for measuring U(VI) under certain experimental conditions. Voltammetric measurements of U(VI) will not be accurate when aqueous U(IV) is present (e.g., in the presence of organics or humics which complex U(IV)). During the potential scan under these conditions, U(VI) will be produced via oxidation of U(IV) at the electrode surface while the electrode potential is more positive than the reduction potential of U(VI). U(VI) artificially produced by the electrode will then be reduced along with the U(VI) already in solution once the electrode potential reaches the reduction potential of U(VI), thereby artificially increasing the U(VI) signal. Increasing the potential scan rate and/or limiting the potential range to

lower potentials may alleviate this analytical artifact, but further optimization will be required to address this issue.

2.4 Computational techniques

2.4.1 Geochemical equilibrium modeling using PHREEQC

The modeling software PHREEQC (Version 3.3.9, USGS, http://wwwbrr.cr.usgs.gov/projects/GWC_coupled) was used to perform all geochemical equilibrium and kinetic calculations. PHREEQC is capable of performing equilibrium calculations of aqueous solutions interacting with solid phase minerals, gasses, and sorption surfaces. Additionally, PHREEQC can model kinetic reactions with user-defined rate laws. The ability of PHREEQC to interconnect equilibrium and kinetic modeling calculations enables rate laws to be expressed as equilibrium concentrations of aqueous, surface, and solid species. The PHREEQC User's Guide (Parkhurst and Appelo, 2013) provides detailed descriptions of model input and relevant examples which cover the full functionality of PHREEQC. Specifics of model input as they relate to the research presented in this dissertation are provided in the following sections.

2.4.1.1 PHREEQC database

The PHREEQC software package includes several databases which are used to define complexation constants, redox equilibrium constants, and solubility products for included aqueous and solid-phase species. The default PHREEQC database (*phreeqc.dat*) was used as a starting point and was amended to disable redox equilibrium amongst oxidation states of the same element, which PHREEQC assumes is achieved in all

calculations. For example, if sulfate (i.e., S(VI)) is provided in the input solution, the total concentration of sulfur will be partitioned amongst all possible oxidation states in accordance with the redox equilibrium of the system, regardless if oxidation states other than S(VI) are included in the input solution. This approach neglects the kinetics of the redox reactions involved and assumes that equilibrium is established instantaneously. As the modeling exercises conducted herein are primarily concerned with the kinetics of redox reactions, redox equilibrium was disabled to allow transformations amongst oxidation states to be kinetically controlled by prescribed rate laws.

To disable redox equilibrium, undesired redox reactions (e.g., SO_4^{2-}/H_2S, NH_4/NO_3^-, Fe^{3+}/Fe^{2+}) listed under the SOLUTION_SPECIES data block in the database file were removed from the included database. Next, the database was updated to include individual elements for U(VI), U(IV), $Fe(III)_{ferrihydrite}$, $Fe(III)_{goethite}$, $Fe(III)_{magnetite}$, $Fe(II)_{magnetite}$, $Fe(II)_{siderite}$, and $Fe(II)_{aq}$ under the SOLUTION_MASTER_SPECIES data block. As these oxidation states were input as elements rather than master species of the same element, transformation between the oxidation states could be controlled by prescribed kinetic rate laws. Three elements for Fe(II) and three elements for Fe(III) were required to describe transformations between solid and aqueous Fe(II) and Fe(III) using kinetic reactions rather than redox equilibrium. This approach is modeled after Example 9 in the PHREEQC Version 3 User's Guide (Parkhurst and Appelo, 2013).

Finally, the included PHREEQC database was updated with the most recently published thermodynamic data for aqueous, adsorbed, and solid U(VI), U(IV), Fe(III), Fe(II), and secondary element complexes. A complete list of complexation constants,

adsorption formation constants, and mineral solubility products added to the database can be found in Appendix A.

2.4.2 Model parameter estimation using PEST

The parameter estimation program PEST Version 13.0 (Watermark Numerical Computing http://www.pesthomepage.org/) was used to optimize model parameters to best fit the model-predicted time series to the measured concentrations using a Gauss-Marquardt–Levenberg nonlinear estimation algorithm. PEST calls PHREEQC which executes the model using initial guesses for the model parameters. Once the first model run is complete, PEST linearizes the relationship between model parameters and model output and solves for a new set of parameters, which PHREEQC uses to execute the model again. This procedure is repeated until the change in goodness of fit between parameter sets drops below a threshold tolerance. PEST provides uncertainty estimates for the optimized parameter values along with additional statistical information regarding the goodness of fit between the model output and the measured data.

The implementation of PEST was based on the work of Bachmaf and Broder (2011) which details the installation, setup, and operation of PEST in combination with PHREEQC. The 4 files needed to run PEST are briefly described below:

Template file (*filename.tpl*): The Template file is a modified PHREEQC input file in which PEST modifies the model parameters for each optimization model run. A symbol (e.g., @) is placed on either side of the variable name to denote the location where PEST will insert the parameter value.

Control file (*filename.pst*): The Control file contains program parameters, the variable names of the model parameters to be optimized, initial guesses for the model parameters, upper and lower bounds for each variable, measured values to be compared to model output, and file names of the PHREEQC database, PHREEQC input file, PHREEQC output file.

Instruction file (*filename.ins*): The Instruction file tells PEST how to search the PHREEQC output file for values to be compared to measured values listed in the Control file.

Batch file (*filename.bat*): The Batch file is used to execute PEST. Running the Batch file from the Windows Command Prompt will begin the parameter estimation process.

At the end of the optimization, PEST calculates the upper and lower bound 95% confidence intervals of the optimized parameters values. Highly correlated model parameters will lead to large confidence intervals which may even include negative values. In this case, the "best" parameter value is highly uncertain, and a large range of values for each parameter give equally good fits of the model to the measured data. If unique optimized values were found for the model parameters (i.e., non-overlapping 95% confidence intervals), the optimized values and the confidence intervals were reported. If, however, PEST was unable to optimize the model with unique parameter values (i.e., 95% confidence intervals of multiple parameters overlap), then the model parameters were optimized by hand to minimize the sum of the squared weighted residuals between the model output and the measured values (i.e., the objective function, Φ) calculated by PEST.

CHAPTER 3. EFFECTS OF AQUEOUS URANYL SPECIATION ON THE KINETICS OF MICROBIAL URANIUM REDUCTION

3.1 Abstract

The ability to predict the success of the microbial reduction of soluble U(VI) to highly insoluble U(IV) as an *in situ* bioremediation strategy is complicated by the wide range of geochemical conditions at contaminated sites and the strong influence of aqueous uranyl speciation on the bioavailability and toxicity of U(VI) to metal-reducing bacteria. To determine the effects of aqueous uranyl speciation on uranium bioreduction kinetics, incubations and viability assays with *Shewanella putrefaciens* strain 200 were conducted over a range of pH and dissolved inorganic carbon (DIC), Ca^{2+}, and Mg^{2+} concentrations. A speciation-dependent kinetic model was developed to reproduce the observed time series of total dissolved uranium concentration over the range of geochemical conditions tested. The kinetic model yielded the highest rate constant for the reduction of uranyl non-carbonate species (i.e., the 'free' hydrated uranyl ion, uranyl hydroxides, and other minor uranyl complexes), indicating that they represent the most readily reducible fraction of U(VI) despite being the least abundant uranyl species in solution. The presence of DIC, Ca^{2+}, and Mg^{2+} suppressed the formation of more bioavailable uranyl non-carbonate species and resulted in slower bioreduction rates. At high concentrations of bioavailable

U(VI), however, uranium toxicity to *S. putrefaciens* inhibited bioreduction, and viability assays confirmed that the concentration of non-carbonate uranyl species best predicts the degree of toxicity. The effect of uranium toxicity was accounted for by incorporating the free ion activity model of metal toxicity into the bioreduction rate law. Overall, these results demonstrate that, in the absence of competing terminal electron acceptors, uranium bioreduction kinetics can be predicted over a wide range of geochemical conditions based on the bioavailability and toxicity imparted on U(VI) by solution composition. These findings also imply that the concentration of uranyl non-carbonate species, despite being extremely low, is a determining factor controlling uranium bioreduction at contaminated sites.

3.2 Introduction

The need for a mechanistic understanding of uranium biogeochemistry is driven by ongoing efforts to control, contain, and predict the fate of this contaminant at nuclear processing facilities, where poor waste disposal practices have resulted in an extensive legacy of uranium contamination (Riley et al., 1992). Speciation (i.e., oxidation state and aqueous complexation) regulates the physical and chemical processes that determine the mobility of uranium in the subsurface. In oxidizing environments, uranium is predominantly under the form of the U(VI) uranyl ion (UO_2^{2+}), which is soluble over a wide range of geochemical conditions (Langmuir, 1978). Uranium(VI) may be reduced abiotically or microbially to the U(IV) uranous ion (U^{4+}), which is highly insoluble and readily precipitates from solution as uraninite (UO_2) (Burgos et al., 2008; Schofield et al., 2008) or other non-uraninite U(IV) compounds (Bernier-Latmani et al., 2010; Boyanov et al., 2011).

Uranium(VI) bioreduction is a promising *in situ* bioremediation strategy which exploits the large differences in solubility among uranium oxidation states with the goal of immobilizing uranium in the subsurface as insoluble U(IV) minerals. Large-scale field studies have demonstrated that U(VI) bioreduction by metal-reducing bacteria is stimulated by injection of organic carbon substrates upstream of the contaminant plume (Anderson et al., 2003; Watson et al., 2013; Williams et al., 2011; Wu et al., 2006b). The broad range of geochemical conditions at uranium-contaminated sites, however, complicates the implementation of U(VI) bioreduction due, in part, to the impact of solution composition on the biogeochemical transformations of uranium. Changes in the physical (e.g., size and charge) and thermodynamic (e.g., redox potential and solubility) properties of the uranyl ion upon complexation by ligands alter U(VI) reactivity in the subsurface. For instance, the formation of uranyl carbonate and ternary uranyl carbonate complexes decreases uranyl adsorption to mineral surfaces (Nair and Merkel, 2011; Stewart et al., 2010; Waite et al., 1994; Wang et al., 2013b), lowers the U(VI)/U(IV) redox potential (Du et al., 2011; Ginder-Vogel et al., 2006), and retards the kinetics of chemical (Behrends and Van Cappellen, 2005; Hua et al., 2006) and biological (Brooks et al., 2003; Sheng and Fein, 2014; Sheng et al., 2011; Ulrich et al., 2011) U(VI) reduction. Following reduction, solution composition (Bernier-Latmani et al., 2010; Boyanov et al., 2011) and the local coordination environment of U^{4+} (Bargar et al., 2013; Latta et al., 2014) affect the formation of U(IV) mineral products and ultimately the long-term stability of uranium against mobilization (Alessi et al., 2012; Cerrato et al., 2013).

The kinetics of microbial U(VI) reduction is highly dependent on aqueous uranyl speciation, and labile uranyl complexes (e.g., the ‘free’ hydrated, hydroxide, and organic

uranyl species) have been proposed to represent the bioavailable fraction of U(VI) (Ulrich et al., 2011). Decreased bioreduction rates in the presence of dissolved inorganic carbon (DIC) and Ca^{2+} are attributed to the formation of stable uranyl carbonate and ternary Ca uranyl carbonate complexes which are less thermodynamically favorable for reduction and may be inaccessible to bacteria due to steric hindrance or poor affinity for adsorption to the cell membrane (Brooks et al., 2003; Sheng and Fein, 2014; Sheng et al., 2011; Stewart et al., 2011; Ulrich et al., 2011). Similarly, low molecular weight organic acids (Francis and Dodge, 2008; Haas and Northup, 2004; Sheng et al., 2011; Suzuki et al., 2010) and soil humics (Burgos et al., 2007; Gu et al., 2005) may prevent microbial reductive precipitation of uranium by decreasing the bioavailability of U(VI) (e.g., imparting steric hindrance) and/or increasing the solubility of U(IV).

Although select species of bacteria are able to support cell growth using U(VI) as a terminal electron acceptor (TEA) during anaerobic respiration (Lovley et al., 1991; Sanford et al., 2007; Tebo and Obraztsova, 1998; Wade and DiChristina, 2000), uranium is also toxic to many microorganisms (Konopka et al., 2013; Tapia-Rodriguez et al., 2012). As metal toxicity is a function of aqueous metal speciation rather than the total dissolved metal concentration (Campbell, 1995; Morel, 1983), the toxicity of uranium to aquatic organisms has been linked to the aqueous concentrations of UO_2^{2+} and UO_2OH^+ (Markich et al., 1996; Markich et al., 2000; Trenfield et al., 2011). Ligands such as carbonate (Carvajal et al., 2012; Markich et al., 1996; VanEngelen et al., 2010b), phosphate (Fortin et al., 2004), sulfate (Markich et al., 1996), and dissolved organic carbon (DOC) (Trenfield et al., 2011) lessen uranium toxicity by decreasing the concentrations of UO_2^{2+} and UO_2OH^+, while cations such as Ca^{2+}, Mg^{2+}, and H^+ decrease uranium toxicity by competing with uranyl

complexes for biotic ligand binding sites (Charles et al., 2002). Thus far, however, the influence of uranium toxicity on microbial uranium reduction remains poorly defined.

Given the multiple effects of aqueous uranyl speciation, the main objective of this study was to deconvolute the roles of solution composition on the kinetics of U(VI) bioreduction and, hence, provide a unifying framework to account for the effects of bioavailability and toxicity. Uranium(VI) bioreduction incubations and viability assays were conducted with *Shewanella putrefaciens* strain 200 over a broad range of aqueous uranyl speciation conditions, and a speciation-dependent kinetic model for U(VI) bioreduction was developed to reproduce observed time series of total dissolved uranium concentrations. The proposed model is discussed in the context of biostimulation field studies at uranium-contaminated sites and the challenges associated with transferring knowledge acquired in simple laboratory model systems to real-world applications.

3.3 Materials and Methods

3.3.1 Cell cultures

All biotic experiments were conducted with *Shewanella putrefaciens* strain 200 (ATCC 51753), a model uranium-reducing bacteria capable of growth using U(VI) as its sole terminal electron acceptor (TEA) during anaerobic respiration (Wade and DiChristina, 2000). Prior to all biotic experiments, *S. putrefaciens* was grown anaerobically on a defined growth medium (M1) (Myers and Nealson, 1988) modified to decrease the concentrations of NH_4^+, ΣPO_4^{3-}, and Mg^{2+} to 100 μM, buffered at pH 8.0 with 10 mM HEPES, and amended with 100 μM $FeCl_3$. Lactate (15 mM) was supplied as the electron donor and carbon source, and fumarate (60 mM) was supplied as the TEA. Cells were collected during

late-log phase by centrifugation and harvested and washed once with growth medium prior to inoculation.

3.3.2 Bioreduction incubations

Uranium(VI) bioreduction batch incubations with *S. putrefaciens* were conducted in duplicate in 100 mL serum bottles containing M1 medium (modified to remove Na_2EDTA, $CaCl_2$, and $FeCl_3$) and continuously mixed with magnetic stir bars (290 rpm). Lactate (15 mM) was provided as the sole electron donor and U(VI) (800 μM uranyl acetate, Spectrum) as the sole TEA. Autoclaved M1 medium was purged with N_2 to remove dissolved oxygen prior to assembling the incubations. The serum bottles were placed inside an anaerobic chamber (5% H_2, 95% N_2 atmosphere) where U(VI) (800 μM uranyl acetate), DIC (15, 20, 25, 30, or 45 mM $NaHCO_3$), Ca^{2+} (0.0, 0.5, 1.0, or 4.9 mM $CaCl_2$), Mg^{2+} (0.0, 1.0, or 5.1 mM $MgSO_4$), and PIPES buffer (15 mM, adjusted to pH 6.5±0.1, 7.5±0.2, or 8.1±0.1) were added from filter sterilized stock solutions. Overall, 15 incubation conditions were considered. The M1 medium included a background Mg^{2+} concentration of 100 μM in all incubations except those conducted in the presence of Ca^{2+}, which contained no Mg^{2+}. The serum bottles were capped with butyl rubber stoppers and aluminum crimps to avoid exposure to the atmosphere, and all incubations were allowed to equilibrate for approximately one week prior to inoculation. During this time, minor pH adjustments were performed by addition of 1 M NaOH or HCl. Measured initial DIC concentrations were within 13% of predicted values assuming thermodynamic equilibrium (calculations performed with PHREEQC, data not shown), indicating that equilibration was closely achieved prior to inoculation. Incubations were inoculated with an initial cell concentration

of approximately $5x10^7$ cells/mL, determined using optical density at 600 nm (OD_{600}) and a conversion factor of $2x10^9$ cell/mL/Abs. unit.

Small aliquots were collected periodically with a needle and syringe flushed with the anaerobic chamber atmosphere. An unfiltered subsample was processed to measure pH and DIC: pH was measured using a double junction semi-micro pH electrode (Orion) calibrated with three low ionic strength commercial buffers (pH 4, 7, and 10, Fisher Scientific, Inc.), and DIC was measured by a flow injection analysis system with conductivity detection (Analytical Instruments Systems, Inc. LCC100 integrator) (Hall and Aller, 1992). The remaining subsample was filtered (0.22 µm nitrocellulose, Millipore) and used to measure total dissolved uranium by inductively coupled plasma mass spectrometry (ICP-MS, Agilent 7500a series). Filtered aliquots were diluted in 2% trace metal grade HNO_3 (Fisher Scientific, Inc.) containing 5 ppb holmium and bismuth as internal standards (SPEX CertiPrep) to correct for instrument drift. All total dissolved uranium measurements were conducted in duplicate. Calibration standards were prepared with a certified uranium stock solution (SPEX CertiPrep) in 2% HNO_3 containing the internal standards and measured approximately every 25-30 samples. Blanks and a calibration standard were measured every 6-7 samples as quality controls.

The averaged, time-corrected data sets from duplicate incubations (discussed in Section 3.4.1) were used in all kinetic analyses and modeling exercises. Lag phases were defined as the time of inoculation (t = 0) up to the last measurement of a total dissolved uranium concentration within 1 standard deviation of the average concentration of previous measurements within the lag phase. The experimental, overall pseudo-first order bioreduction rate constant (k_{obs}) was determined for each experimental condition from the

slope of the linearized, integrated equation of total dissolved uranium concentration *[U]* versus time *t* (Equation 3.1, where X is biomass) over the time interval following the lag phase that yielded the largest k_{obs} and conformed to the pseudo-first order rate law (i.e., smallest standard deviation of the linear regression of the data represented using Equation 3.1). The overall U(VI) bioreduction rate was determined by fitting a linear regression to measured total dissolved uranium concentrations over the same time interval used in the calculation of kobs.

$$ln\frac{[U]}{[U]_0} = -k_{obs}[X]t \tag{3.1}$$

3.3.3 Cell viability assays

The effects of uranyl speciation on uranium toxicity to *S. putrefaciens* were determined in viability assays similar to those used to study the effects of uranyl speciation on cell viability during U(VI) biosorption (Carvajal et al., 2012) and bioreduction (Cologgi et al., 2011). The assays were conducted over a range of DIC, Ca^{2+}, and Mg^{2+} concentrations. *S. putrefaciens* was grown anaerobically to late-log phase on fumarate (60 mM) in M1 medium. Cells were harvested by centrifugation and resuspended in 50 mL Falcon tubes under aerobic, non-growth conditions in solutions of uranyl acetate (1 mM), PIPES buffer (20 mM, pH 7.2 ± 0.2), $NaHCO_3$ (10, 30, or 50 mM), and $CaCl_2$ or $MgSO_4$ (0, 1, or 5 mM) and mixed on a rotary wheel for 6 hours. Control cells were resuspended in a solution of PIPES buffer (20 mM) and $NaHCO_3$ (10 mM) without uranyl acetate. Following uranium exposure, cells were harvested by centrifugation, washed twice with M1 medium, and inoculated into anaerobic culture tubes (Chemglass Life Sciences) to an

initial OD_{600} of ~0.01 and regrown anaerobically on fumarate in fresh, N_2-purged, uranium-free M1 medium. Cell growth was monitored by OD_{600} (Beckman Coulter DU720 UV/Vis spectrophotometer) and growth curves were conducted in duplicate.

The log-phase region of growth curves was used to calculate survival rates of *S. putrefaciens* following exposure to uranium. This approach assumes that after uranium exposure, only a certain percentage of cells is viable and capable of cell division, which results in a lag phase in the growth curve before exponential growth is observed. A first-order rate law with respect to the concentration of cells (X in Equation 3.2) was integrated and fitted to the exponential region of the growth curves to obtain a rate constant k for each uranium exposure condition. As the cell concentration at the end of the inherent lag phase (i.e., the lag phase of the control cells not exposed to uranium) represents the concentration of viable cells at the time of inoculation, the rate law (Equation 3.2) was integrated and used with the rate constant k determined for each uranium exposure condition to calculate the concentration of viable cells at the time of inoculation. The survival rate was then determined for each exposure condition by dividing the calculated concentration of viable cells by the measured initial total concentration of cells.

$$\frac{d[X]}{dt} = k[X] \tag{3.2}$$

3.3.4 Speciation-dependent biogeochemical kinetic model

S. putrefaciens couples the oxidation of lactate to acetate and DIC to the reduction of U(VI) to U(IV) (Equation 3.3), which spontaneously precipitates from solution as biogenic U(IV) minerals (uraninite in Equation 3.4) or forms various non-crystalline

complexes depending on bacterial strain and solution composition (Bernier-Latmani et al., 2010; Boyanov et al., 2011).

$$2UO_2^{2+} + Lactate^- + 3H^+ \rightarrow 2U^{4+} + Acetate^- + HCO_3^- + 2H_2O \quad (3.3)$$

$$U^{4+} + 2H_2O \rightarrow UO_2(am) + 4H^+ \quad (3.4)$$

The rate law for U(VI) bioreduction is based on Michaelis-Menten kinetics (Equation 3.5), where k is the rate constant, $[X]$ the concentration of biomass, $[Lac^-]$ the concentration of electron donor, $[U(VI)]$ the concentration of U(VI), and K_{Lac} and K_U the half-saturation constants for lactate and U(VI), respectively.

$$\frac{d[U(VI)]}{dt} = -k[X]\frac{[Lac^-]}{K_{Lac} + [Lac^-]}\frac{[U(VI)]}{K_U + [U(VI)]} \quad (3.5)$$

Equation 3.5 was further modified to account for aqueous uranyl speciation by assuming that the kinetics of enzymatic electron transfer to U(VI) depend on the type of ligand(s) surrounding U(VI). In addition, as lactate concentration (15 mM) was provided in excess of K_{Lac} (Liu et al., 2001), the Michaelis-Menten term for lactate approaches unity. As a result, the overall rate law under the experimental conditions can be expressed as Equation 3.6, where i represents an individual uranyl complex and n is the total number of uranyl complexes considered.

$$\frac{d[U(VI)]}{dt} = -[X]\sum_{i=1}^{n}\frac{k_i[U(VI)_i]}{K_{Ui} + [U(VI)_i]} \quad (3.6)$$

Due to the large number of uranyl species, Equation 3.6 was simplified by grouping species based on the type of ligand, as done in previous studies (Stewart et al., 2011; Ulrich et al., 2011). Three groups of uranyl species were considered in our model: non-carbonate, carbonate, and ternary-carbonate (Equation 3.7). The uranyl non-carbonate species include the 'free' hydrated uranyl ion and hydroxide, chloride, sulfate, phosphate, lactate, and acetate uranyl complexes formed in the presence of ligands present in the growth medium. The uranyl carbonate species include carbonate and hydroxide-carbonate complexes, while the ternary uranyl carbonate species include Ca and Mg uranyl carbonate complexes. Assuming that the uranyl species in each group have comparable chemical properties, each group of uranyl species is assigned a single rate constant and half-saturation constant.

$$\frac{d[U(VI)]}{dt} = -[X]\left(\frac{k_1\left[U(VI)_{non-CO_3}\right]}{K_{U1} + \left[U(VI)_{non-CO_3}\right]} + \frac{k_2\left[U(VI)_{CO_3}\right]}{K_{U2} + \left[U(VI)_{CO_3}\right]} + \frac{k_3\left[U(VI)_{ternary-CO_3}\right]}{K_{U3} + \left[U(VI)_{ternary-CO_3}\right]}\right) \quad (3.7)$$

Initial modeling efforts with the full Michaelis-Menten terms in Equation 3.7 revealed that the optimized half-saturation constant concentrations (i.e., K_{U1}, K_{U2}, K_{U3}) were orders of magnitude larger than the corresponding concentrations, such that the Michaelis-Menten terms could be approximated by first order expressions with respect to the concentrations of each group of uranyl species (Equation 3.8). This approach is consistent with past studies (Liu et al., 2002a; Ulrich et al., 2011) and decreases the number of model parameters. Finally, because uranium is toxic to bacteria above a strain-specific threshold level (Katsenovich et al., 2013), an inhibition term was added to the bioreduction rate law to account for the inhibition of anaerobic respiration in the presence of elevated

'free' uranyl ion concentrations, in accordance with the free ion activity model of metal toxicity (Campbell, 1995; Morel, 1983). A two-parameter logistic function was used as the concentration-response toxic inhibition factor F_{toxic} (Equation 3.9), similar to previous approaches describing the toxicity of uranium to aquatic organisms (Markich et al., 1996; Markich et al., 2000). The inhibition factor varies between 0 and 1 as a function of the 'free' uranyl ion concentration; the parameters are the concentration of UO_2^{2+} at 50% inhibition IC_{50}, and p which characterizes the slope of the curve at the 50% inhibition inflection point.

$$\frac{d[U(VI)]}{dt} = -F_{toxic} \cdot [X] \cdot \left(k_1\left[U(VI)_{non-CO_3}\right] + k_2\left[U(VI)_{CO_3}\right] + k_3\left[U(VI)_{ternary-CO_3}\right]\right) \tag{3.8}$$

$$F_{toxic} = \frac{1}{1 + \left(\frac{[UO_2^{2+}]}{IC_{50}}\right)^p} \tag{3.9}$$

The biogeochemical kinetic model was fitted to the averaged, time-corrected total dissolved uranium concentration time series obtained after the initial lag phase, beginning at the first measurement used to calculate k_{obs} and the overall U(VI) bioreduction rate. The speciation-dependent bioreduction rate law (Equation 3.8) was integrated using the geochemical modeling software PHREEQC Version 3.1.1 (USGS, http://wwwbrr.cr.usgs.gov/projects/GWC_coupled). The thermodynamic database in PHREEQC 3.1.1 was updated with the most recently published thermodynamic data for aqueous and solid U(VI) and U(IV) compounds (Dong and Brooks, 2006; Guillaumont et

al., 2003; Gustafsson, 2012). All 15 experimental conditions were analyzed together in a single PHREEQC model with the same bioreduction rate law and a single set of parameters. For each experimental condition, the measured initial total dissolved uranium concentration, measured average pH during the bioreduction period, measured initial DIC concentration, and medium composition were provided as model inputs, and the model was run with a time step of 6 hours. PHREEQC executes a Runge-Kutta algorithm to integrate the bioreduction rate law (Equation 3.8) using the calculated uranyl speciation at each time step, assuming internal thermodynamic equilibrium, and adjusts the solution composition in accordance with the stoichiometry of Equation 3.3. The solution was further assumed to be in instantaneous equilibrium with amorphous uraninite, that is, U(IV) was allowed to precipitate from solution (Equation 3.4) when the solubility product of uraninite was exceeded.

The biogeochemical model includes a total of five adjustable parameters: three bioreduction rate constants (i.e., k_1, k_2, and k_3, one for each group of uranyl species) and two parameters for the concentration-response toxic inhibition factor (i.e., p and IC_{50}). The parameter estimation program PEST Version 13.0 (Watermark Numerical Computing http://www.pesthomepage.org/) was used to optimize the model parameters to best fit the model-predicted time series of total dissolved uranium to the measured concentrations using a Gauss-Marquardt-Levenberg nonlinear estimation algorithm. PEST calls PHREEQC which executes the model using initial guesses for the model parameters. Once the first model run is complete, PEST linearizes the relationship between model parameters and model output and solves for a new set of parameters, which PHREEQC uses to execute the model again. This procedure is repeated until the change in goodness of fit between

parameter sets drops below a threshold tolerance. The five parameters were optimized to simultaneously maximize the fit between measured and modeled total dissolved uranium concentrations for all 15 experimental conditions. Finally, to compare measured bioreduction rates for each condition with the rates predicted by the model, overall pseudo-first order rate constants k_{obs} were derived from Equation 3.1 using the time series of total dissolved uranium obtained with the model over the same time period as the experimental data.

3.4 Results

3.4.1 Effect of uranyl speciation on U(VI) bioreduction rates

Bioreduction incubations were conducted from pH 6.5 to 8.1 and over a range of concentrations of DIC, Ca^{2+}, and Mg^{2+}, in order to relate aqueous uranyl speciation to uranium bioreduction kinetics (Figure 3.1). Uranyl carbonate species dominated uranyl speciation at all pH and DIC conditions without added Ca^{2+} or Mg^{2+} (Table 3.1): 95±1% of U(VI) was present as uranyl carbonate species and 5±1% of U(VI) was present as the ternary Mg uranyl carbonate complex $MgUO_2(CO_3)_3^{2-}$ (due to the 100 μM Mg^{2+} background in the growth medium). The remaining fraction of U(VI) (< 0.1%) was composed of uranyl non-carbonate species. While the concentration of the most abundant uranyl species was similar across all pH and DIC conditions without added Ca^{2+} or Mg^{2+}, the concentration of the uranyl non-carbonate species, the least abundant species in solution, spanned four orders of magnitude, ranging from 38 pM (pH 8.1 incubation containing 39 mM DIC) to 562 nM (pH 6.5 incubation containing 23 mM DIC).

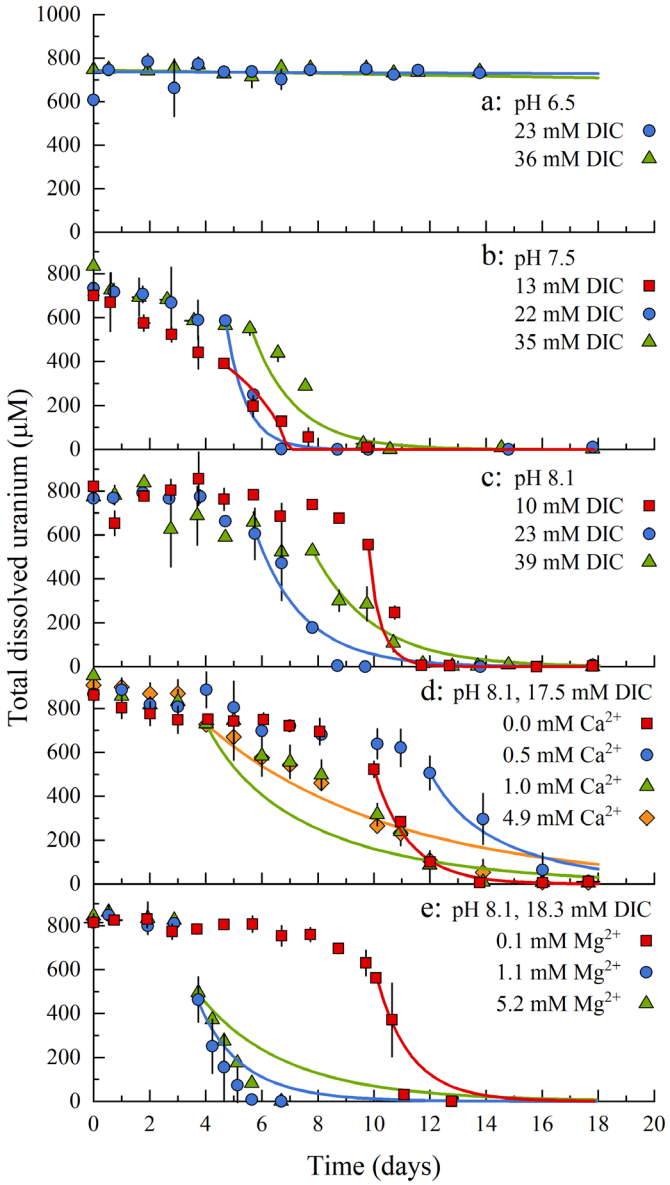

Figure 3.1 Averaged, time-corrected total dissolved uranium concentration time series in duplicate bioreduction incubations conducted without added Ca^{2+} and Mg^{2+} at pH (A) 6.5, (B) 7.5, and (C) 8.1 in the presence of various concentrations of DIC, and amended with various concentrations of (D) Ca^{2+} and (E) Mg^{2+} at pH 8.1 in the presence of a constant DIC concentration. Symbols represent measured values and solid lines represent optimized model outputs. Error bars represent duplicate incubations.

Table 3.1 Uranium bioreduction incubations: Solution composition, initial aqueous U(VI) speciation assuming thermodynamic equilibrium, and measured overall U(VI) bioreduction rates.

pH	[DIC][a] (mM)	[Ca^{2+}] (mM)	[Mg^{2+}] (mM)	[UO_2^{2+}] (pM)	Σ[non-carb][b] (nM)	Σ[carb] (μM)	Σ[Ca-carb] (μM)	Σ[Mg-carb] (μM)	overall rate[c] (mol/cell/day)
6.5	23±0.2		0.1	1883	562	686		27.4	$1.41\pm5.63\times10^{-17}$
	36±0.2		0.1	210	74.2	716		26.6	$2.33\pm3.31\times10^{-17}$
7.5	13±0.3		0.1	23.9	64.5	366		25.5	$2.44\pm0.46\times10^{-15}$
	22±0.3		0.1	0.295	2.31	561		28.2	$7.02\pm0.58\times10^{-15}$
	35±1.2		0.1	0.06	0.404	531		21.6	$3.16\pm0.29\times10^{-15}$
8.1	10±0.8		0.1	0.089	4.45	523		34.4	$6.58\pm0.48\times10^{-15}$
	23±2.3		0.1	0.01	0.317	576		27.8	$5.00\pm0.87\times10^{-15}$
	39±0.6		0.1	0.001	0.038	510		19.4	$3.12\pm0.70\times10^{-15}$
8.1	19±0.1			0.004	0.328	525			$3.90\pm0.43\times10^{-15}$
	17±0.4	0.5		0.005	0.221	199	309		$1.68\pm0.23\times10^{-15}$
	17±1.3	1.0		0.004	0.206	163	569		$1.36\pm0.11\times10^{-15}$
	17±0.1	4.9		0.0003	0.01	8.87	720		$1.24\pm0.08\times10^{-15}$
8.1	19±0.1		0.1	0.024	0.742	535		30.2	$1.19\pm0.28\times10^{-14}$
	18±0.0		1.1	0.028	0.548	275		191	$7.72\pm1.26\times10^{-15}$
	18±0.1		5.2	0.019	0.222	138		359	$5.74\pm0.09\times10^{-15}$

[a] Errors are associated with measurements of initial DIC concentrations in duplicate incubations. [b] Uranyl non-carbonate species include the 'free' hydrated uranyl ion and hydroxide, chloride, sulfate, phosphate, lactate, and acetate uranyl complexes. [c] Standard deviations of the linear slopes used to obtain bioreduction rates from the averaged, duplicate time series of total dissolved uranium concentration ($n \geq 3$).

As a result of the accompanying changes in aqueous uranyl speciation, the pH and DIC concentrations affected bioreduction rates significantly (Table 3.1). Uranium bioreduction was negligible in incubations at pH 6.5 (Figure 3.1A) which included the highest concentrations of uranyl non-carbonate species (Table 3.1). Interestingly, in incubations at pH 7.5 (Figure 3.1B), the maximum bioreduction rate was observed in the presence of 22 mM DIC whereas bioreduction rates were slower in the incubations containing both higher (35 mM) and lower (13 mM) DIC concentrations (Table 3.1). In contrast, incubations conducted at pH 8.1 (Figure 3.1C) generally exhibited an inverse correlation between the DIC concentration and the bioreduction rate (Table 3.1). Across all incubation conditions, the pH remained stable (±0.1 pH units) during the period of bioreduction (data not shown).

The addition of Ca^{2+} and Mg^{2+} led to the formation of ternary uranyl carbonate species, which decreased the concentration of carbonate and non-carbonate species and affected uranium bioreduction rates (Table 3.1): bioreduction rates were inversely proportional to the Ca^{2+} and Mg^{2+} concentrations, though Ca^{2+} led to a larger relative decrease in bioreduction rate than Mg^{2+} for the same concentration (Table 3.1). An inverse correlation was observed between the lag phase in uranium bioreduction and the concentrations of Ca^{2+} and Mg^{2+} (Figure 3.1D and Figure 3.1E). Incubations containing 1.0 and 4.9 mM Ca^{2+} exhibited shorter lag phases compared to incubations without Ca^{2+} (Figure 3.1D). Similarly, the addition of 1.0 and 5.1 mM Mg^{2+} resulted in shorter lag phases compared to incubations conducted in the presence of the background Mg^{2+} concentration (Figure 3.1E). The reproducibility of the lag phases in replicate incubations for all conditions was also affected by the concentrations of Ca^{2+} and Mg^{2+} (data not shown):

below 0.5 mM Ca^{2+} and Mg^{2+}, lag phases were quite variable, differing in length between 1 to 7 days in duplicate incubations, whereas for Ca^{2+} and Mg^{2+} concentrations above 0.5 mM, lag phases were mostly reproducible. When significant inter-duplicate variability in lag phase occurred, the time series data were shifted in time relative to one another until the time intervals of maximum bioreduction in the duplicate experiments coincided. Following time adjustments, the total dissolved uranium measurements from duplicate incubations were averaged and the resulting time series was then used for all subsequent kinetic analyses and modeling exercises. Despite significant variations in the lag phase at low concentrations of Ca^{2+} and Mg^{2+}, bioreduction rates were highly reproducible between duplicate incubations and did not correlate with lag phase duration across all incubation conditions (R^2 = 0.02, data not shown). These observations suggest that variability in metabolic performance or adaptation during the lag phase did not affect uranium bioreduction rates significantly.

3.4.2 Effect of uranyl speciation on cell viability

In viability assays without Ca^{2+} or Mg^{2+}, uranyl carbonate species accounted for >99% of U(VI) while the remaining fraction consisted of uranyl non-carbonate species (i.e., 'free' hydrated, hydroxide, and acetate species) (Table 3.2). Whereas the concentration of uranyl carbonate species was nearly the same across the different DIC concentrations in these assays, the concentration of uranyl non-carbonate species spanned three orders of magnitude, from 42 pM to 46 nM, and correlated inversely with the DIC concentration (Table 3.2). After 6 hours of exposure to 1 mM uranyl acetate (pH 7.2±0.2) in the presence of 30 and 50 mM DIC, the bacteria recovered rapidly and displayed exponential growth after a relatively brief 5 hour lag phase, similar to control cells not

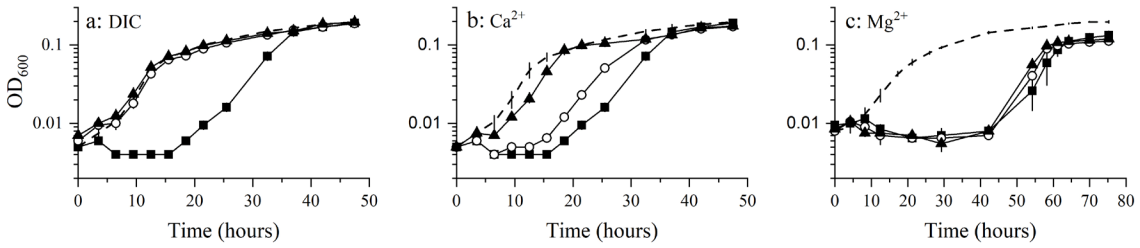

Figure 3.2 Viability assays of *S. putrefaciens* following 6 hours of exposure to 1 mM U(VI) at pH 7.2±0.2 with various concentrations of DIC, Ca^{2+}, and Mg^{2+}. Shown is cell density as a function of time (growth curves) in the presence of (A) 10 mM (■), 30 mM (○), and 50 mM (▲) DIC; (B) 10 mM DIC and 0 mM (■), 1 mM (○), and 5 mM (▲) Ca^{2+}; and (C) 10 mM DIC and 0 mM (■), 1 mM (○), and 5 mM (▲) Mg^{2+}. Dashed lines represent cell density as a function of time for control cells not exposed to U(VI). Error bars represent duplicate assays. Cells were grown anaerobically on fumarate as TEA and lactate as electron donor in M1 medium.

exposed to uranium (Figure 3.2A). In the presence of 10 mM DIC, however, exposure to uranium resulted in a 15 hour lag phase before cell growth was detected (Figure 3.2A).

The addition of 1 and 5 mM Ca^{2+} to incubations conducted in the presence of 10 mM DIC led to the formation of ternary Ca uranyl carbonate complexes which dominated uranyl speciation (77% and >99% of U(VI), respectively) and decreased the concentration of carbonate and non-carbonate uranyl species (Table 3.2). As observed with the increase in DIC concentration, the increase in Ca^{2+} concentration from 1 to 5 mM decreased the lag phase to 14 and 6 hours, respectively, compared to the 15 hours observed in the incubations conducted without Ca^{2+} (Figure 3.2B). Addition of Mg^{2+} also altered the speciation of U(VI) via formation of the ternary Mg uranyl carbonate complex, but this complex only accounted for 44% and 78% of U(VI) in the presence of 1 and 5 mM Mg^{2+}, respectively,

Table 3.2 Viability assays: Solution composition, aqueous U(VI) speciation assuming thermodynamic equilibrium, and survival rate.

pH	[DIC] (mM)	[Ca^{2+}] (mM)	[Mg^{2+}] (mM)	[UO_2^{2+}] (pM)	Σ[non-carb][b] (nM)	Σ[carb] (μM)	Σ[Ca-carb] (μM)	Σ[Mg-carb] (μM)	Survival rate[c] (percent)
7.2	10			210	45.5	937			17.0±1.4
7.3	30			1.76	0.488	1000			76.6±24.0
7.5	50			0.088	0.042	1000			90.9±16.3
7.2	10	1.0		80	15.5	226	769		13.5±1.1
7.1	10	5.0		2.98	0.358	4.34	997		71.0±10.0
7.1	10			521	65.2	900			0.1±0.1
7.0	10		1.0	521	50.8	529		421	0.0±0.0
7.0	10		5.0	298	22.7	219		774	0.4±0.2

[a] Total U(VI) is 1 mM for all conditions. Note that concentrations of each group of uranyl species may not sum to 1 mM due to the formation of polymeric uranyl complexes.
[b] Uranyl non-carbonate species include the 'free' hydrated uranyl ion and hydroxide and acetate uranyl complexes.
[c] Standard deviations represent propagated error from fitting the exponential region of growth curves.

whereas the remaining fraction of U(VI) consisted predominantly of carbonate species (Table 3.2). Concentrations of uranyl non-carbonate species were within the same order of magnitude regardless of the Mg^{2+} concentration, in line with the absence of a significant effect of Mg^{2+} additions on the duration of the lag phase (Figure 3.2C). The addition of 1 and 5 mM Mg^{2+} with 10 mM DIC yielded only marginally shorter lag phases (45 and 39 hours, respectively) compared to cells exposed to uranium and 10 mM DIC without Mg^{2+} (45 hours).

To compare viability assays across all geochemical conditions, survival rates were calculated from growth curve data and represented as a function of the calculated aqueous uranyl speciation during uranium exposure. A two-parameter logistic function (Equation 3.9) was fitted to the data, and the strongest negative concentration-response relationships across all viability assay conditions were observed between the survival rate of the bacteria after exposure to uranium and the sum of the concentrations of all uranyl non-carbonate species (R^2 = 0.97, Figure 3.3) as well as concentrations of individual uranyl complexes such as the 'free' hydrated uranyl ion UO_2^{2+} (R^2 = 0.98, Figure B.1A) and the hydroxide complexes UO_2OH^+ (R^2 = 0.98, Figure B.1B) and $(UO_2)_2OH^{3+}$ (R^2 = 0.98, Figure B.1C). Interestingly, a strong positive concentration-response relationship was observed between survival rate and the sum of the concentrations of ternary uranyl carbonate species (R^2 = 0.97, Figure B.1D). In contrast, no significant relationship between survival rate and the sum of the concentrations of uranyl carbonate species was observed (R^2 = 0.04, Figure B.1E).

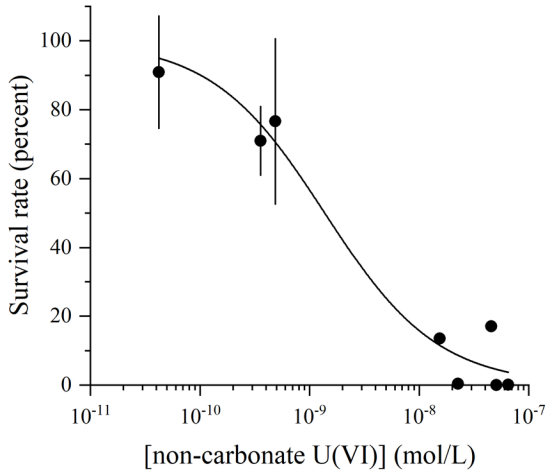

Figure 3.3 Correlation between survival rate of *S. putrefaciens* and the concentration of the sum of all uranyl non-carbonate species in viability assays of cells exposed to 1 mM U(VI) at pH 7.2±0.2 in the presence of various concentrations of DIC, Ca^{2+}, and Mg^{2+}. A two-parameter logistic function (Equation 3.9) was fitted to the data (R^2 = 0.97). Nearly identical correlations are observed between survival rate and concentrations of select individual uranyl non-carbonate complexes (e.g. UO_2^{2+}, UO_2OH^+, $(UO_2)_2OH_3^+$). Standard deviations represent propagated error from fitting the exponential region of growth curves.

3.4.3 Biogeochemical kinetic model

Overall, the optimized speciation-dependent biogeochemical model captured the range of bioreduction rates and reproduced the post-lag phase time series of total dissolved uranium concentration across nearly all incubation conditions (Figure 3.1). The notable exceptions are the pH 8.1 incubations containing 1.0 mM Ca^{2+} (Figure 3.1D) and 5.2 mM Mg^{2+} (Figure 3.1E) for which the modeled time series of total dissolved uranium concentration significantly deviated from measured values. The relatively good correlation between measured and modeled overall pseudo-first order rate constants k_{obs} (R^2 = 0.69, Figure B.2) across a wide range of geochemical conditions supports the conceptual

framework of the model, in particular the distribution of the uranyl species into three groups, each represented by a single rate constant. Discrepancies between measured and modeled k_{obs} values generally resulted from underpredicted values by the model, especially for incubations with the largest measured k_{obs}, which also exhibited the largest uncertainties (Figure B.2).

Unlike the incubations conducted at pH 8.1, bioreduction rates obtained in the incubations conducted at pH 6.5 and 7.5 were not proportional to the concentration of uranyl non-carbonate species (Table 3.1), and the corresponding time series data could not be reproduced by a first order rate law alone (data not shown). Including the toxic inhibition factor F_{toxic} in the rate law (Equation 3.8) greatly improved the model fit and was necessary to reproduce the lack of bioreduction observed in incubations at pH 6.5, as well as the decreased bioreduction rates observed in incubations at pH 7.5 with 13 and 22 mM DIC. By optimizing the kinetic parameters to all 15 experimental conditions simultaneously, the speciation-dependent kinetic model yielded a rate constant of bioreduction for uranyl non-carbonate species that was six orders of magnitude larger than those of uranyl carbonate and ternary uranyl carbonate species (Table 3.3). The rate constants of bioreduction for the uranyl carbonate and ternary uranyl carbonate species were nearly the same within experimental error.

3.5 Discussion

3.5.1 Lag phases

Lag phases of up to 11 days precede the onset of uranium reductive precipitation in the incubations (Figure 3.1). Lag phases have been observed in previous uranium

Table 3.3 Optimized rate constants, toxic inhibition factor (F_{toxic}) parameters, and their 95% confidence limits for the speciation-dependent U(VI) bioreduction rate law.

Parameter	Value	95% Confidence limits	
		Lower	Upper
k_1 (non-carbonate) (L/cell/day)	3.42×10^{-6}	1.81×10^{-6}	6.47×10^{-6}
k_2 (carbonate) (L/cell/day)	5.40×10^{-12}	3.79×10^{-12}	7.70×10^{-12}
k_3 (ternary carbonate) (L/cell/day)	1.37×10^{-12}	1.09×10^{-12}	1.71×10^{-12}
IC_{50} (pM UO_2^{2+})	1.02	0.19	5.59
p	1.68	0.95	3.00

bioreduction studies (Brooks et al., 2003; Nyman et al., 2007; Ray et al., 2011; Sani et al., 2006; Sivaswamy et al., 2011; Spear et al., 1999) and may be inversely correlated to biomass concentration (Spear et al., 1999), though such a relationship was not observed in the present incubations. Instead, the duration and inter-duplicate variability of the lag phases correlate inversely with the concentrations of Ca^{2+} and Mg^{2+}, possibly reflecting the limited concentrations of these essential cations in the growth medium. Indeed, preliminary experiments revealed that Mg^{2+} is necessary to sustain the growth of *S. putrefaciens* on fumarate, and for this reason, a background Mg^{2+} concentration of 100 μM was chosen to minimize the duration of the lag phase while avoiding excessive formation of Mg uranyl carbonate complexes.

3.5.2 Effect of DIC, Ca^{2+}, and Mg^{2+} on U(VI) bioreduction rates

Following the lag phases, uranium bioreduction proceeds at rates highly dependent on the aqueous uranyl speciation. Increasing concentrations of DIC at pH 8.1 result in the formation of uranyl carbonates, lower concentrations of uranyl non-carbonate species, and

slower bioreduction rates (Table 3.1). These results are consistent with earlier studies showing that DIC inhibits microbial U(VI) reduction (Behrends and Van Cappellen, 2005; Sheng and Fein, 2014; Ulrich et al., 2011), as well as abiotic U(VI) reduction by Fe(II) (Behrends and Van Cappellen, 2005) and ΣH_2S (Hua et al., 2006). Similarly, increasing concentrations of Ca^{2+} and Mg^{2+} at pH 8.1 decrease bioreduction rates, albeit to different extents, consistent with previous U(VI) bioreduction studies with Ca^{2+} (Brooks et al., 2003; Sheng et al., 2011; Stewart et al., 2011).

Both thermodynamic and kinetic explanations have been proposed to address the speciation-dependence of uranium bioreduction kinetics (Brooks et al., 2003; Stewart et al., 2011; Ulrich et al., 2011). Existing models primarily focus on the inhibition of bioreduction by Ca^{2+}, which forms ternary Ca uranyl carbonate complexes ($CaUO_2(CO_3)_3^{2-}$ and $Ca_2UO_2(CO_3)_3^{0}$) (Dong and Brooks, 2006) that consequently decrease the concentrations of uranyl carbonate species in solution. Uranyl carbonate complexes generally display higher redox potentials than ternary Ca uranyl carbonate complexes, supporting the hypothesis that the decrease of the most abundant and thermodynamically more favorable species in the presence of Ca^{2+} is responsible for the inhibition of uranium bioreduction (Brooks et al., 2003). The redox potential of the most favorable uranyl carbonate complex, $UO_2(CO_3)_3^{4-}$, however, is on the order of 46 mV larger than the most favorable ternary uranyl carbonate complexes, $CaUO_2(CO_3)_3^{2-}$ and $MgUO_2(CO_3)_3^{2-}$ (Table 3.4), even in incubations with 4.9 mM Ca^{2+} or 5.2 mM Mg^{2+}, when ternary uranyl carbonate species represent the dominant fraction of U(VI) (Table 3.1). In addition, the Gibbs free energies of reaction (ΔG_r) for the reduction of the carbonate and ternary carbonate complexes are all highly favorable and differ by less than 14% (Table 3.4), consistent with

Table 3.4 Solution composition, overall pseudo-first order rate constant (k_{obs}), toxic inhibition factor (F_{toxic}), and calculated thermodynamic parameters for bioreduction incubations over a range of U(VI) bioavailability.

		Bioavailability of U(VI)[a]		
		low	medium	high
pH		8.1	8.1	6.5
[DIC] (mM)		17	18	23
[Mg^{2+}] (mM)		0.0	5.2	0.1
[Ca^{2+}] (mM)		4.9	0.0	0.0
Measured k_{obs} (L/cell/day)		$2.05\pm0.08\times10^{-12}$	$1.50\pm0.05\times10^{-11}$	$4.23\pm4.10\times10^{-14}$
Toxic inhibition factor (F_{toxic})[b]		1.00	1.00	3.14×10^{-6}
UO_2^{2+}	E_h (mV)[c]	-237	-184	-36
	ΔG_r (kJ/mol)[d]	-124	-136	-153
UO_2OH^+	E_h (mV)[c]	-245	-191	-43
	ΔG_r (kJ/mol)[d]	-121	-133	-151
$(UO_2)_2OH^{3+}$	E_h (mV)[c]	-236	-182	-35
	ΔG_r (kJ/mol)[d]	-124	-137	-154
$UO_2(CO_3)_3^{4-}$	E_h (mV)[c]	-224	-166	-37
	ΔG_r (kJ/mol)[d]	-129	-143	-153
$CaUO_2(CO_3)_3^{2-}$	E_h (mV)[c]	-271		
	ΔG_r (kJ/mol)[d]	-111		
$MgUO_2(CO_3)_3^{2-}$	E_h (mV)[c]		-211	-81
	ΔG_r (kJ/mol)[d]		-126	-136

[a] Assuming uranyl non-carbonate species represent the bioavailable fraction of U(VI)
[b] Calculated using Equation 3.9 with the concentration of UO_2^{2+} (Table 3.1) and optimized values of IC_{50} and p (Table 3.3)
[c] Calculated for the U(VI)/UO_2(am) half-reaction redox couple with the Nernst equation using solution composition and calculated concentrations of each uranyl complex.
[d] Calculated for the reduction of each uranyl species to UO_2(am) coupled with lactate oxidation to acetate and bicarbonate using solution composition and the calculated concentration of each uranyl complex. Values are reported per mol lactate.

previously reported findings (Stewart et al., 2011; Ulrich et al., 2011). The small energetic differences between respiration of uranyl carbonates and ternary uranyl carbonates are therefore unlikely to explain the decreases in bioreduction rate in the presence of 4.9 mM Ca^{2+} (14±2 % per mM Ca^{2+}) and 5.2 mM Mg^{2+} (10±2 % per mM Mg^{2+}) (Table 3.1). Alternatively, ternary Ca uranyl carbonates may be less readily reducible by metal-reducing bacteria as a result of steric hindrance or poor molecular orbital overlap between the U(VI) center and the U(VI) terminal reductase (Sheng et al., 2011; Stewart et al., 2011). A similar explanation may apply to Mg^{2+}, which forms a single ternary carbonate complex with the uranyl ion ($MgUO_2(CO_3)_3^{2-}$) (Dong and Brooks, 2008; Geipel et al., 2008). Thus, the formation of ternary uranyl carbonate complexes in the presence of Ca^{2+} and Mg^{2+} may limit uranium bioavailability and prevent electron transfer to U(VI).

3.5.3 Effect of non-carbonate uranyl species on U(VI) bioreduction rates

Despite the multiple effects of pH and concentrations of DIC, Ca^{2+}, and Mg^{2+} on U(VI) bioreduction rates, the speciation-dependent kinetic model reproduces the bioreduction of uranium as a function of time across nearly all solution compositions tested (Figure 3.1). In the model, the bioavailability of uranyl non-carbonate species to *S. putrefaciens* explains the dependence of the bioreduction rates on solution composition. Several uranyl non-carbonate species, including the 'free' uranyl ion and some of the hydroxide complexes, have redox potentials comparable to $UO_2(CO_3)_3^{4-}$ under the experimental conditions (Table 3.4), despite consistently representing the least abundant species in solution (Table 3.1). Simultaneously, the rate constant for the reduction of uranyl non-carbonate species is six orders of magnitude larger than that of the other species (Table 3.3). Significant differences in bioreduction rate constants among U(VI) species are not

unexpected; they are consistent with the recent findings that rate constants for the bioreduction of uranyl hydroxide and organic uranyl species by *S. oneidensis* strain MR-1 are an order of magnitude larger than those determined for uranyl carbonate species and two orders of magnitude larger than Ca uranyl carbonate species (Ulrich et al., 2011).

Attributing the bioavailability of U(VI) to uranyl non-carbonate species explains the decrease in bioreduction rates with increasing concentrations of DIC in the pH 8.1 incubations, as well as the more significant deceleration of bioreduction in the presence of Ca^{2+} compared to Mg^{2+} (Table 3.1). The apparent inhibition of uranium bioreduction by Ca^{2+} can be attributed to its ability to significantly decrease the concentration of the more bioavailable uranyl non-carbonate species due to the large formation constants of the two Ca uranyl carbonate complexes ($CaUO_2(CO_3)_3^{2-}$, $\beta_{1,1,3}$ = 27.18 and $Ca_2UO_2(CO_3)_3^0$, $\beta_{2,1,3}$ = 30.70 (Dong and Brooks, 2006)). Simultaneously, the smaller decrease in bioreduction rate in the presence of Mg^{2+} is explained by the lower formation constant of the single Mg uranyl carbonate complex ($MgUO_2(CO_3)_3^{2-}$, $\beta_{1,1,3}$ = 26.11 (Dong and Brooks, 2006)) and, hence, the smaller decrease in the concentration of uranyl non-carbonate species. Taken together, the kinetic results presented in this study support the hypothesis that the concentration of uranyl non-carbonate species, rather than uranyl carbonate species, controls U(VI) bioreduction rates (Ulrich et al., 2011).

3.5.4 Uranium toxicity

Regardless of the DIC concentration, uranium bioreduction is negligible in the pH 6.5 incubations (Figure 3.1A), even though these incubations exhibit the highest concentrations of bioavailable uranyl non-carbonate species (Table 3.1). Similarly,

bioreduction rates in the pH 7.5 incubations containing 13 and 22 mM DIC are also lower than expected given the calculated aqueous uranyl speciation. As the pH does not significantly affect the kinetics of Fe(III) reduction by *S. putrefaciens* between pH 6.5 and 7.5 (Arnold et al., 1986), the metabolic potential of *S. putrefaciens* (i.e. growth and respiration rate) can be assumed to be the same across the range of pH conditions employed in the uranium bioreduction incubations. Thus, changes in U(VI) bioreduction kinetics across different pH and medium compositions used in the current study are attributed to changes in uranyl speciation, and any background effects of experimental conditions on cell activity are assumed to be minimal. As a result, uranium toxicity to *S. putrefaciens* is able to explain the inhibition of bioreduction under conditions which U(VI) bioavailability is predicted to be the highest. The viability assays confirm that uranium toxicity to *S. putrefaciens* is also a function of uranyl speciation rather than the total dissolved uranium concentration alone. In other words, uranium toxicity can be predicted by knowing the aqueous uranyl speciation only, whereas knowledge of the total dissolved uranium concentration alone is not sufficient to predict its toxicity. The viability assays further identify the concentration of uranyl non-carbonate species as the best predictor of toxicity across all conditions (Figure 3.3), in line with the observed inhibition of bioreduction under incubation conditions containing the highest concentration of uranyl non-carbonate species (Table 3.1). Under these conditions, accounting for uranium toxicity in the model was required to reproduce the data accurately. Taken together, the combined results of the viability assays and bioreduction incubations therefore indicate that uranium toxicity is primarily responsible for the lack of bioreduction in incubations with the highest concentrations of bioavailable uranyl non-carbonate species. Additionally, the positive

concentration-response relationship observed between survival rate and the concentration of ternary uranyl carbonate species (Figure B.1D) demonstrates that Ca^{2+} prevents uranium toxicity to *S. putrefaciens* by decreasing the concentration of uranyl non-carbonate species via the formation of Ca uranyl carbonate complexes.

Uranium toxicity has been shown to inhibit respiratory processes relevant to contaminated sediments, including denitrification (Tapia-Rodriguez et al., 2012), sulfate reduction (Nyman et al., 2007), and methanogenesis (Tapia-Rodriguez et al., 2012). In addition, the metabolic activity of uranium-reducing microorganisms is inhibited above a threshold concentration of total dissolved uranium (Khijniak et al., 2005; Sani et al., 2006; Wade and DiChristina, 2000), as also observed for other contaminants that undergo biological transformations, such as phenol (Christen et al., 2012), arsenic (Soda et al., 2006), and technetium (Khijniak et al., 2003). As the viability assays were conducted at a single pH, it is impossible to attribute uranium toxicity to *S. putrefaciens* to a specific uranyl complex (Markich et al., 2000). Nonetheless, upon attributing the inhibition of bioreduction to the 'free' uranyl ion (Equation 3.9), in accordance with the free ion activity model of metal toxicity (Campbell, 1995; Morel, 1983), the model is able to reproduce the entire set of bioreduction incubations, including those obtained at pH 6.5 (Figure 3.1A) and 7.5 (Figure 3.1B) where toxicity is significant. The 50% lethal concentration (LC_{50}) of 8.5±1.9 pM UO_2^{2+} derived from the viability assay concentration-response relationship (Figure B.1A) and the IC_{50} determined by the optimized kinetic model (Table 3.3) are both relatively low compared to the total dissolved uranium concentrations added to the incubations. The LC_{50} and IC_{50} values indicate that *S. putrefaciens* strain 200 is highly

sensitive to the 'free' uranyl ion and may experience uranium toxicity even at low concentrations of total dissolved uranium.

3.5.5 Mechanism of speciation-dependent U(VI) bioreduction

Existing mechanisms to explain the toxicity of U(VI) to bacteria invoke the interaction of the uranyl ion with the outer membrane, followed by destabilization of membrane integrity (Bencheikh-Latmani and Leckie, 2003); the transport of uranyl into the periplasm or cytoplasm, followed by reduction and intracellular precipitation of U(IV) minerals (Cologgi et al., 2011); the competitive binding of uranyl to an essential enzyme (Pible et al., 2010; VanEngelen et al., 2011); or the hydrolysis of DNA by intracellular uranyl (Yazzie et al., 2003). Some of these mechanisms resemble those proposed for U(VI) bioreduction by *Shewanella* spp. Uranium(VI) bioreduction is commonly attributed to the interaction of U(VI) with outer membrane cytochromes (Marshall et al., 2006) or with periplasmic reductases that require transport of U(VI) across the outer membrane (Senko et al., 2007). The present incubations reveal that uranium toxicity and uranium bioreduction kinetics are highly correlated with the concentration of uranyl non-carbonate species across a broad range of geochemical conditions, which points to a common mechanism between U(VI) toxicity and U(VI) bioreduction, or at least closely related mechanisms. According to the kinetic model developed in the present study, DIC, Ca^{2+}, and Mg^{2+} decrease uranium bioreduction rates by forming uranyl complexes that are less bioavailable and by simultaneously decreasing the concentration of more bioavailable uranyl non-carbonate species. Thus, bioavailability, rather than thermodynamics alone, accounts for the speciation-dependence of uranium bioreduction kinetics over the wide range of uranyl non-carbonate concentrations covered in this study. Whereas uranyl non-carbonate complexes

are small (U-O_{OH} bond length for uranyl hydroxides, ~2.2 Å (Clark et al., 1999)) and generally positively charged, which enhances attraction to the negatively charged outer membrane (Haas et al., 2001; VanEngelen et al., 2010b), uranyl carbonate complexes are bulky (bond length of U-$O_{distant}$ in ternary Ca uranyl carbonates, ~4.1 Å (Kelly et al., 2007)) and negatively charged, which may hinder interactions between the U(VI) center and U(VI)-reducing enzymes (Sheng and Fein, 2013, 2014). Furthermore, electrostatic repulsion between the cell surface and uranyl carbonate complexes may interfere with transport across the outer membrane and, hence, prevent U(VI) from interacting with the intracellular metabolic machinery (in the case of toxicity) or periplasmic reductases (in the case of bioreduction).

As uranyl non-carbonate species are consumed by bioreduction, they are replenished via re-equilibration of the solution. The slow release of strongly bound carbonate ligands may therefore limit the rate of bioreduction. This mechanism does not appear to play a significant role in controlling U(VI) bioreduction rates in the present study, as the speciation-dependent model reproduces bioreduction time series across a broad range of uranyl speciation while assuming thermodynamic equilibrium is achieved at each time step. Thus, electron transfer to U(VI), rather than slow equilibration among uranyl complexes, more likely constitutes the rate-determining step in the bioreduction of U(VI). Even though solution composition alters the U(VI)/UO_2(am) redox potential and the Gibbs free energy of reaction (ΔG_r) of U(VI) respiration (Table 3.4), the primary role played by solution composition in uranium bioreduction kinetics is through the effect on aqueous uranyl speciation which, in turn, affects the bioavailability of U(VI) to *S. putrefaciens*. The combined effect of bioavailability and toxicity is observed by comparing overall pseudo-

first order rate constants k_{obs} to the aqueous speciation of U(VI) at the onset of reduction across all bioreduction conditions (Figure 3.4). The k_{obs} for U(VI) bioreduction display a clear increase with increasing concentration of uranyl non-carbonate species (Figure 3.4A). Above a concentration of approximately 4 nM, however, the rate constant decreases with a further increase in the concentration of uranyl non-carbonate species due to the onset of uranium toxicity. Simultaneously, the largest uncertainties in measured k_{obs} values, which also coincide with the largest discrepancies between measured and modeled k_{obs} values (Figure B.2), are found at the onset of uranium toxicity, where U(VI) bioreduction kinetics transitions from being controlled by bioavailability to being controlled by toxicity. In contrast, when represented against the concentration of the uranyl carbonate (Figure 3.4B) and ternary uranyl carbonate species (Figure 3.4C), almost all the variability of k_{obs} occurs within a very narrow range of concentration, implying that bioreduction kinetics are largely independent of the concentration of these species. These findings are confirmed by the rate constants predicted by the model for uranyl carbonate and ternary uranyl carbonate species, which are orders of magnitude smaller than the rate constant determined for uranyl non-carbonate species (Table 3.3).

3.5.6 Implications for bioremediation

As geochemical conditions at uranium-contaminated sites are diverse, understanding the effects of aqueous uranyl speciation on bioreduction kinetics is crucial for predicting the fate and transport of uranium. Although the bioreduction incubations and viability assays of the present study were conducted at high concentrations of U(VI) relative to most contaminated subsurface environments, the finding that uranium toxicity is controlled by the concentration of uranyl non-carbonate species, rather than by the

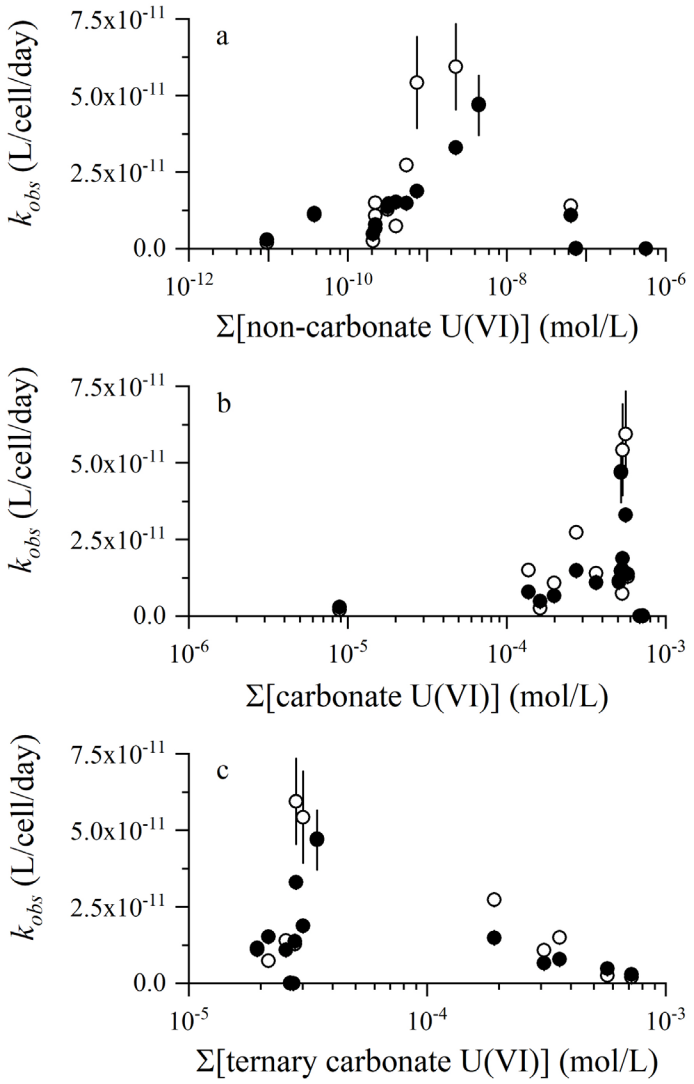

Figure 3.4 Measured (○) and modeled (●) overall pseudo-first order rate constants (k_{obs}) versus the sum of the concentrations of (A) non-carbonate, (B) carbonate, and (C) ternary carbonate U(VI) species for all incubation conditions. Error bars represent the standard deviation of the slope of the linear regression used to obtain k_{obs} from averaged duplicate incubations or model output.

concentration of total dissolved uranium, suggests that groundwater composition may affect uranium bioreduction rates even at low total U(VI) levels. At the three Department of Energy (DOE) Integrated Field Research Challenge (IFRC) sites in the United States, where large-scale bioreduction experiments have been conducted (Hanford, Washington; Rifle, Colorado; and Oak Ridge, Tennessee), distinct waste disposal histories and groundwater compositions (Table B.1) affect the implementation of uranium bioreduction as a bioremediation strategy. At all three sites, ternary uranyl carbonate species represent the main fraction of U(VI) above pH 6.5 due to the prevalence of Ca^{2+} and Mg^{2+} (Figure 3.5). At the Hanford site (Figure 3.5A), a local minimum in bioreduction rate is predicted at pH 8.8, which corresponds to the minimum concentration of bioavailable uranyl non-carbonate species. Below or above this pH, bioreduction rates are predicted to increase, mirroring changes in the concentration of uranyl non-carbonate species. The pH of Hanford groundwater, however, ranges from 7.1 to 8.7 (Zachara et al., 2013) which includes the critical pH window from 7.5 to 8.1 where, according to the model, bioreduction rates decrease abruptly with decreasing pH even as the concentration of bioavailable uranyl non-carbonate species increases. Over this pH range, uranium toxicity apparently overcomes the increase in bioavailability of U(VI) as a result of the increase in concentration of the 'free' uranyl ion (Figure 3.5A). Under these conditions, bioreduction rates are highly sensitive to pH, and bioreduction may be promoted by a slight increase in pH, which decreases the concentration of the toxic 'free' uranyl ion despite simultaneously decreasing the bioavailability of U(VI). In turn, Rifle groundwater pH varies from 6.6 to 7.4 (Zachara et al., 2013), a range over which bioreduction rates are inhibited by uranium toxicity (Figure 3.5B). The model therefore predicts that the pH of Rifle groundwater should be

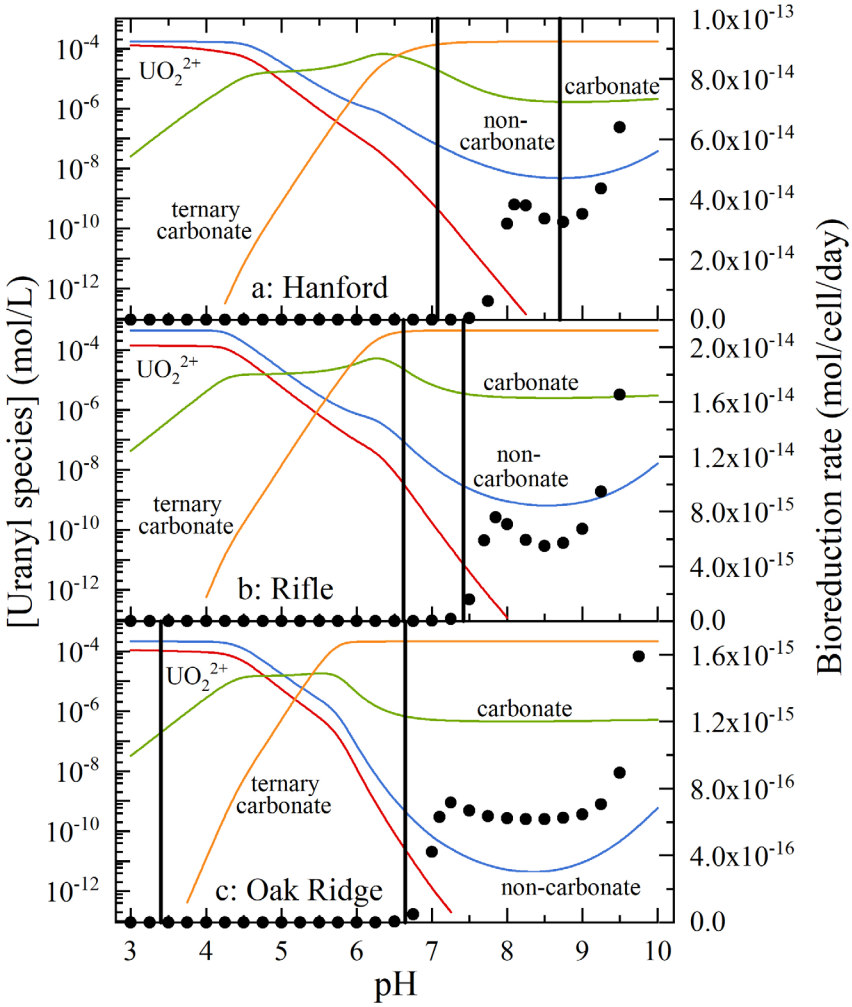

Figure 3.5 Calculated aqueous uranyl speciation (lines) and bioreduction rate (●) as a function of pH using background groundwater composition at the (A) Hanford, (B) Rifle, and (C) Oak Ridge US Department of Energy (DOE) Integrated Field Research Challenge (IFRC) sites (Table B.1), assuming a 3 mM acetate injection to stimulate metal-reducing bacteria. Solid vertical lines represent the minimum and maximum measured pH at each site. Bioreduction rates were calculated using the proposed biogeochemical kinetic model and the optimized model parameters (Table 3.3).

raised to promote bioreduction. Although the kinetic model predicts similar trends in bioreduction rate above pH ~8 at the Hanford (Figure 3.5A) and Rifle (Figure 3.5B) sites, bioreduction rates at Hanford are predicted to be ~5 times greater due to the larger concentration of bioavailable uranyl non-carbonate species. Finally, as most metal-reducing bacteria are naturally inhibited under low pH conditions (Edwards et al., 2007; Petrie et al., 2003), uranium bioreduction is not feasible in the most contaminated zones of the Oak Ridge site (Figure 3.5C) where the groundwater is highly acidic (pH ~3.5) due to the presence of nitric acid in spent uranium wastes. Correspondingly, substantial treatment of the groundwater was found to be necessary to increase pH, decrease Ca^{2+} concentrations, and promote uranium bioreduction at this site (Wu et al., 2006a; Wu et al., 2006b). Interestingly, the model predicts that uranium bioreduction can be extended to a lower pH at the Oak Ridge site (pH 6.8) compared to the Hanford (pH 7.3) and Rifle (pH 7.3) sites due to higher concentrations of DIC, Ca^{2+}, and Mg^{2+} (Table B.1) which decrease the toxicity of uranium and promote bioreduction.

These results indicate that efforts to increase uranium immobilization via bioreduction by promoting the formation of bioavailable uranyl non-carbonate species may ultimately be limited by the toxicity of uranium to indigenous metal-reducing bacteria. Additionally, these findings may explain, in part, the rebound in dissolved uranium concentration observed after extended periods of biostimulation at uranium contaminated sites (Bargar et al., 2013; Williams et al., 2011). The increase in dissolved uranium coincides with an increase in DIC concentration from enhanced electron donor consumption during sulfate reduction. A large DIC:U ratio favors the formation of uranyl carbonate species and promotes desorption of U(VI) from mineral surfaces (Waite et al.,

1994) and oxidation of U(IV) by Fe(III)-oxides (Ginder-Vogel et al., 2006), which increase dissolved uranium concentrations. The results presented in this study indicate that large DIC:U ratios will also decrease the concentration of bioavailable uranyl non-carbonate species and retard U(VI) bioreduction, thereby decreasing the net rate of removal of dissolved uranium from the groundwater.

Although the geochemical kinetic model developed in the present study is suitable to describe U(VI) bioreduction rates by a model metal-reducing microorganism across a wide range of geochemical conditions, the challenges associated with implementing this model to predict rates of U(VI) bioreduction by subsurface microbial communities should not be understated. Bioreduction rates presented in Figure 3.5 primarily serve to illustrate the importance of taking into account aqueous uranyl speciation in the design and implementation of bioreduction-based remediation strategies. These predicted U(VI) bioreduction rates do not consider the background effect of pH on cell activity as the model does not account for the anticipated decrease in respiration rate outside of the habitable pH range of *S. putrefaciens* (e.g., the model erroneously predicts that U(VI) bioreduction rates increase indefinitely above pH 9). Native microbial communities at contaminated sites likely display a higher tolerance to uranium than *S. putrefaciens* as a result of prolonged uranium exposure (Mukherjee et al., 2012). Similarly, the pH range of optimal metabolic activity likely varies between sites depending on the resident microbial community, and site-specific model parameterization may be necessary (Jin et al., 2013). Furthermore, efforts to increase the concentration of bioavailable uranyl species may also enhance the toxicity of metal co-contaminants commonly associated with uranium contamination (e.g., technetium, arsenic, vanadium, copper, nickel) (Ganesh et al., 1999), which needs to be

considered when modeling U(VI) bioreduction rates. Lastly, while significant attention has been given to the effects of inorganic uranyl speciation on U(VI) bioreduction kinetics (Brooks et al., 2003; Sheng and Fein, 2014; Stewart et al., 2011; Ulrich et al., 2011), the roles of organic ligands (Ganesh et al., 1997; Haas and Northup, 2004) and soil humics (Burgos et al., 2007; Gu et al., 2005) in controlling U(VI) bioavailability, toxicity, and solubility remain poorly defined. Quantifying the contribution of natural organic matter to U(VI) complexation will be essential for the development of speciation dependent reactive-transport models able to reproduce the consequences of large-scale biostimulation on uranium mobility.

3.6 Conclusions

Uranyl bioavailability appears to be the primary mechanism responsible for controlling the speciation-dependence of U(VI) bioreduction kinetics by *S. putrefaciens* in the absence of additional TEAs. Although uranyl carbonate species are thermodynamically favorable electron acceptors, they are not bioavailable to *S. putrefaciens*, most likely because of steric hindrance or poor molecular orbital overlap with the terminal reductase. Often overlooked, uranyl non-carbonate species are both bioavailable and thermodynamically favorable for reduction. Indeed, their concentration is best able to predict bioreduction rates over a wide range of solution composition. The results of the present study suggest that any changes in solution composition that significantly alter the concentration of uranyl non-carbonate species should have an impact on uranium bioreduction kinetics. At low concentrations of uranyl non-carbonate species, changes in solution composition that promote their formation increase bioreduction rates. Above a threshold concentration, however, the toxicity of uranyl non-carbonate species to metal-

reducing bacteria decreases rates of bioreduction. Changes in solution composition above this threshold that decrease the concentration of uranyl non-carbonate species should therefore diminish uranium toxicity to metal-reducing bacteria and accelerate uranium bioreduction.

Although native microbial communities in uranium-contaminated aquifers are likely to display a higher tolerance to uranium than the model organism used here, a uranium toxicity threshold is expected to exist even for the most tolerant microorganisms. The implementation of uranium bioreduction as a bioremediation strategy therefore depends on the adaptation of the microbial community to uranium exposure at a given contaminated site. These results highlight the complex, counteracting ways in which aqueous uranyl speciation affects the kinetics of uranium bioreduction and demonstrate the importance of incorporating aqueous uranyl speciation into future reactive transport modeling efforts. Understanding the effects of the bioavailability and toxicity of U(VI) in subsurface environments is imperative to develop bioreduction-based bioremediation strategies for uranium immobilization.

3.7 Acknowledgments

This research was supported by the US Department of Energy Subsurface Biogeochemical Research (SBR) program Grant No. DE-SC0005520. We would like to thank Raoul-Marie Couture for guidance with implementing the PEST and PHREEQC software and the Associate Editor and three anonymous reviewers for providing insightful comments that significantly improved our manuscript.

CHAPTER 4. GEOCHEMICAL CONTROLS OF THE MICROBIALLY MEDIATED REDOX CYCLING OF URANIUM AND IRON

4.1 Abstract

As oxidation state is a primary determinant of the mobility of uranium in subsurface environments, a comprehensive understanding of the redox cycling of uranium is essential to predict the fate of this contaminant. The potential of iron to serve as both a reductant and an oxidant of uranium suggests that remediation strategies which primarily rely on the reduction of the uranyl ion (U(VI)) to the poorly soluble uranous ion (U(IV)) to immobilize uranium in the solid phase may be either enhanced or hindered depending on the biogeochemical transformations of iron. To identify the geochemical controls of both uranium and iron redox cycling, batch incubations with the model metal-reducing bacterium *Shewanella putrefaciens* were conducted with either U(VI), ferrihydrite, or both as terminal electron acceptors, and concentrations of dissolved inorganic carbon (DIC), calcium, and silica were varied to alter aqueous uranyl speciation and secondary mineralization pathways of ferrihydrite. The presence of ferrihydrite increased the pseudo-first order rate constant of initial uranium removal in nearly all conditions compared to uranium-only controls due to a combination of abiotic U(VI) reduction by Fe(II) and solid-phase association with secondary mineralization products of ferrihydrite. Following an initial period of uranium reduction, U(IV) was oxidized by ferrihydrite which led to a rebound in dissolved uranium. Once ferrihydrite was completely consumed by microbial respiration and secondary mineralization, uranium was again removed from solution via

reductive precipitation and association with secondary mineralization products. DIC and calcium enhanced the oxidative dissolution of U(IV) solids but did not affect the redox potential of the U(VI)/U(IV) redox couple despite the formation of aqueous uranyl carbonate and calcium-uranyl carbonate species. Instead, removal of dissolved Fe(II) from solution and the accompanied shift in the potential of the Fe(III)/Fe(II) redox couple was responsible for the abrupt shift in iron acting as a reductant of U(VI) to an oxidant of U(IV). The removal of dissolved Fe(II) via siderite precipitation at the highest DIC concentration and in the presence of calcium enhanced the oxidation of U(IV), and the presence of silica limited the conversion of ferrihydrite to magnetite and sustained U(IV) oxidation. A kinetic model was developed which could reproduce incubation time series of uranium and iron speciation provided the thermodynamic favorability of abiotic uranium-iron redox cycling was accounted for. The modeling exercise revealed that the non-uraninite U(IV) solids formed in the incubations have a redox potential approximately 84 mV lower than that of amorphous uraninite, highlighting the need for a thermodynamic characterization of non-uraninite U(IV) solids. The results of this study identify the dissolved Fe(II) concentration as the primary geochemical control of the role of iron in uranium redox cycling at moderate to high DIC concentrations and emphasize the importance of considering this parameter when designing site-specific, *in situ* bioremediation strategies.

4.2 Introduction

Decades of uranium mining and processing at nuclear facilities, followed by nuclear waste containment failures, have resulted in tremendous quantities of uranium-contaminated groundwater in excess of the US EPA maximum contaminant level of 0.126 μM across the United States (Department of Energy, 1997; Riley et al., 1992). In most

systems, oxidation state is an important control on the mobility of uranium in the subsurface. Reduction of U(VI) (as the uranyl ion, UO_2^{2+}) to U(IV) (as the uranous ion, U^{4+}) by metal-reducing bacteria (MRB) or by common abiotic reductants, such as Fe(II), leads to the precipitation of sparingly soluble U(IV) solid phases (Boyanov et al., 2011; Stylo et al., 2013) and has been proposed as a remediation strategy to address subsurface uranium contamination (Bargar et al., 2013; Long et al., 2015; Williams et al., 2011). Oxidative dissolution of U(IV) solids by common abiotic oxidants, such as Fe(III) oxides, poses a challenge to remediation efforts that rely on maintaining uranium in the tetravalent oxidation state. Thus, the ability to predict the rate and extent of uranium redox transformations over a broad range of geochemical conditions is imperative to designing appropriate, site-specific strategies to address this threat to the environment and human health.

The biogeochemical cycling of uranium is tightly coupled to that of iron due, in part, to the overlapping potentials of the U(VI)/U(IV) and Fe(III)/Fe(II) redox couples (Belli and Taillefert, 2016; Ginder-Vogel et al., 2006; Stewart et al., 2011). Microbial reduction of Fe(III) oxides and U(VI) by iron-reducing bacteria occurs simultaneously in pure culture incubations (Stewart et al., 2011; Wielinga et al., 2000), and the decrease in concentration of dissolved uranium in biostimulated aquifers often coincides with the production of Fe(II) as a result of the microbial respiration of Fe(III) oxides and clays (Anderson et al., 2003; Williams et al., 2011). Uranium isotopic measurements identify microbial reduction as the dominant U(VI) reduction mechanism during field biostimulation studies (Shiel et al., 2016), however, evidence of abiotic reduction of U(VI)

has also been found (Bargar et al., 2013; Fox et al., 2013; Latta et al., 2012a), suggesting that it plays a complimentary role in the removal of uranium from solution.

Although homogeneous electron transfer between aqueous U(VI) and Fe(II) is thermodynamically favorable above circumneutral pH, the reaction is only kinetically feasible via formation of inner sphere U-Fe complexes, which is thermodynamically hindered in aqueous solutions (Taylor et al., 2015). Thus, reduction of U(VI) by Fe(II) requires a mineral surface to facilitate the formation of U-Fe inner sphere complexes and promote rapid electron transfer (Jang et al., 2008; Liger et al., 1999). Both Fe(II) adsorbed on mineral surfaces (Behrends and Van Cappellen, 2005; Jang et al., 2008; Liger et al., 1999) and Fe(II)-bearing minerals (e.g., magnetite, siderite, vivianite, green rust, mackinawite) (Hyun et al., 2012; O'Loughlin et al., 2003; O'Loughlin et al., 2010; Singer et al., 2012a; Veeramani et al., 2011; Veeramani et al., 2013) have the capacity to reduce U(VI) and may enhance the immobilization of uranium as U(IV) solids. The rate and extent of U(VI) reduction by adsorbed and solid phase Fe(II) is a function of Fe(II) mineral content (Latta et al., 2012b), mineral purity (Latta et al., 2013), U(VI) and Fe(II) surface coverage (Jang et al., 2008; Latta et al., 2014), mineral surface defects (Singer et al., 2012a), and solution composition (Behrends and Van Cappellen, 2005; Singer et al., 2012a, b), which may account for the variable importance of this reaction on U(VI) reduction.

In turn, Fe(III) oxides and Fe(III)-bearing clays may serve as effective oxidants of U(IV) solids, leading to oxidative dissolution and remobilization of uranium (Ginder-Vogel et al., 2006; Ginder-Vogel et al., 2010; Luan et al., 2014; Sani et al., 2005; Senko et al., 2005). The rate and extent of U(IV) oxidation by Fe(III) oxides is a function of Fe(III) oxide crystallinity, surface area, solution composition, and pH (Ginder-Vogel et al., 2006;

Ginder-Vogel et al., 2010; Senko et al., 2005). As U(IV) oxidation proceeds, the accumulation of Fe(II) and U(VI) in solution limits the thermodynamic drive of the reaction (Ginder-Vogel et al., 2006; Senko et al., 2005), and adsorption and surface precipitation of reaction products may impede electron transfer by passivating the Fe(III) and U(IV) mineral surfaces (Ginder-Vogel et al., 2010; Ulrich et al., 2009; Ulrich et al., 2008). The remobilization of uranium by Fe(III) solids, however, has proven significant in flow-through systems with natural sediments, even under sustained reducing conditions (Tokunaga et al., 2008; Wan et al., 2005; Wan et al., 2008), highlighting the importance of characterizing the geochemical controls of this reaction.

The behavior of iron as a reductant or an oxidant of uranium is controlled by the potentials of both the Fe(III)/Fe(II) and U(VI)/U(IV) redox couples. In particular, the uranyl ion forms numerous aqueous complexes with inorganic and organic ligands in solution, and aqueous uranyl speciation affects all aspects of uranium biogeochemistry, including the solubility of U(VI) (Langmuir, 1978), the extent of adsorption to mineral surfaces (Fox et al., 2006; Nair and Merkel, 2011; Stewart et al., 2010), the rate of microbial uranium reduction (Belli et al., 2015; Brooks et al., 2003; Sheng and Fein, 2014; Stewart et al., 2011; Ulrich et al., 2011), and the U(VI)/U(IV) redox potential (Ginder-Vogel et al., 2006). The presence of dissolved inorganic carbon (DIC) leads to the formation of large, negatively charged, and sterically hindered uranyl carbonate complexes which decrease adsorption of U(VI) to mineral surfaces (Waite et al., 1994), the bioavailability of U(VI) to MRB (Belli et al., 2015; Ulrich et al., 2011), the rate of abiotic U(VI) reduction (Behrends and Van Cappellen, 2005; Hua et al., 2006), and the redox potential of the U(VI)/U(IV) redox couple (Ginder-Vogel et al., 2006). These effects are exacerbated in

the presence of calcium as highly stable ternary calcium-uranyl-carbonate complexes dominate aqueous uranyl speciation (Brooks et al., 2003; Singer et al., 2012b; Stewart et al., 2011; Stewart et al., 2010). Due to the similar potentials of the U(VI)/U(IV) and Fe(III)/Fe(II) redox couples (Belli and Taillefert, 2016), slight changes in pH and solution composition may alter the role of iron in uranium redox cycling. For instance, the abiotic reduction of U(VI) by adsorbed Fe(II) and Fe(II)-bearing minerals is more favorable above circumneutral pH and at low DIC and calcium concentrations (Behrends and Van Cappellen, 2005; Singer et al., 2012b), and a decrease in pH or an increase in DIC concentration may favor the oxidative dissolution of U(IV) solid phases by Fe(III) oxides and clays (Ginder-Vogel et al., 2006; Ginder-Vogel et al., 2010).

Sustained U(IV) oxidation by Fe(III) oxides may be limited under iron-reducing conditions due to the consumption of ferrihydrite by Fe(II)-induced secondary mineralization to more crystalline phases. Relative abundances of secondary mineralization products are the result of competing reaction pathways whose rates are largely a function of Fe(II) concentration or production rate, pH, and solution composition (Boland et al., 2014b; Fredrickson et al., 2003; Hansel et al., 2005; Zachara et al., 2002). For instance, low Fe(II)/Fe(III) ratios favor the production of goethite and lepidocrocite (Boland et al., 2014b; Yang et al., 2010), which have a lower sorption capacity and are less favorable oxidants of U(IV) than ferrihydrite. In contrast, high Fe(II)/Fe(III) ratios lead to the formation of magnetite which can then reduce U(VI) (Hansel et al., 2005; Yang et al., 2010). Additionally, adsorbed U(VI) can be reduced and/or incorporated into the crystal lattice of secondary mineralization products (Boland et al., 2014a; Marshall et al., 2015; Massey et al., 2014a; Nico et al., 2009; Roberts et al., 2017) where it may be stabilized

against remobilization under both oxidizing and reducing conditions (Stewart et al., 2009). Common anions such as carbonate, orthophosphate, and silicate limit interactions between Fe(II) and the ferrihydrite surface through complexation, competitive adsorption, and/or precipitation and therefore affect ferrihydrite transformation (Jones et al., 2009; Zachara et al., 2002). Whereas previous studies have primarily focused on the effect of these anions on aqueous U(VI) and solid U(IV) speciation, they are also expected to influence the role of iron in uranium redox cycling by altering the secondary mineralization of ferrihydrite.

The potential of iron to serve as both a reductant and an oxidant of uranium suggests that in iron-rich environments, the reduction of U(VI) may be either enhanced or hindered depending on the biogeochemical transformations of iron in these systems. Furthermore, the role of iron is likely to change throughout the biostimulation period as solution composition and iron mineralogy evolve to reflect the transition from oxidizing to reducing conditions. Although uranium reduction by Fe(II) and oxidation by Fe(III) have been studied in isolation, the geochemical conditions which delineate the role of iron in uranium redox cycling remain poorly defined, particularly in biotic systems. In this study, batch incubations with the model MRB *Shewanella putrefaciens* strain 200 were conducted with either U(VI), 2-line ferrihydrite, or a combination of both as terminal electron acceptors (TEAs) to identify the primary geochemical controls of uranium-iron redox cycling and their effect on the removal of uranium from solution. The initial concentrations of DIC, calcium, and silica were varied to assess the roles of aqueous uranyl speciation and secondary mineralization pathways of ferrihydrite on uranium redox cycling.

4.3 Materials and methods

4.3.1 Cell cultures

Batch incubations were conducted with *Shewanella putrefaciens* strain 200 (ATCC 51753), a model MRB capable of utilizing U(VI) (Wade and DiChristina, 2000) and solid Fe(III) oxides (DiChristina and Delong, 1994) as TEAs. Prior to all bioreduction incubations, *S. putrefaciens* was grown anaerobically on a defined salt medium (M1 medium) (Myers and Nealson, 1988), modified to decrease the concentrations of ΣPO_4^{3-} and NH_4^+ to 100 μM, buffered at pH 7.8 with 20 mM HEPES, and amended with 100 μM $FeCl_3$. Lactate (15 mM) served as the electron donor and fumarate (60 mM) as the electron acceptor. Cells were harvested during late-log phase by centrifugation (2500×g for 15 min) and washed once with growth medium prior to inoculation.

4.3.2 Synthesis of 2-line ferrihydrite

Two-line ferrihydrite (hereafter referred to as ferrihydrite) was synthesized by rapidly titrating a sterile solution of $FeCl_3 \cdot 6H_2O$ (Fisher Scientific) to pH 7.5 with 1 N NaOH (4 mL/min) (Cismasu et al., 2012). The resulting ferrihydrite suspension was washed three times with sterile Milli-Q water by repeated centrifugation (2500×g for 5 min) and decantation of the supernatant. The sterile ~200 mM stock suspension was stored in a brown glass bottle at room temperature for no more than 5 days prior to inoculation, and its purity was confirmed by X-ray diffraction (described below).

4.3.3 Bioreduction Experiments

Batch incubations with *S. putrefaciens* were conducted in triplicate in 160 mL serum bottles containing 120 mL total volume of the same M1 medium used for cell cultivation,

but further modified to remove Na_2EDTA, $CaCl_2$, and $FeCl_3$. Dissolved U(VI) (180 μM uranyl acetate, Spectrum) and/or ferrihydrite (5 mM) were supplied as TEAs and lactate (15 mM) served as the electron donor for all incubations. Incubations were conducted under two DIC concentrations (20 and 40 mM $NaHCO_3$) with and without added calcium (800 μM $CaCl_2$) and silica (300 μM $Na_2O_3Si{\cdot}9H_2O$), and the solution pH was buffered with 15 mM PIPES. Components were mixed for at least 24 hours prior to inoculation at t=0 with an initial cell concentration of approximately 2×10^7 cell/mL, determined using optical density at 600 nm and a conversion factor of 2×10^9 cell/mL/AU obtained via direct cell counts. Minor pH adjustments were made by addition of small amounts (<100 μL) of 1 M HCl or NaOH. As a result, the average pH over the course of the incubation period was pH 8.0±0.1. Serum bottles were individually wrapped in aluminum foil to prevent photochemical reactions, continually mixed with magnetic stir bars (290 rpm), and kept inside an anaerobic chamber (26°C; 5% H_2, 95% N_2 atmosphere) where all sampling and oxygen-sensitive analyses took place. Small aliquots were collected periodically using a sterile needle and syringe. Unfiltered subsamples were used to measure pH, DIC, total Fe(II), and ascorbate-extractable solid-phase iron. The remaining subsamples were filtered (0.22 μm PES membrane, Tisch Scientific) to measure dissolved Fe(II) and total dissolved uranium, iron, calcium, magnesium, and silica.

4.3.4 Analytical techniques

The pH was measured using a double-junction pH electrode (Orion) calibrated with three low ionic strength buffers (pH 4, 7, and 10, Fisher Scientific). Initial DIC concentration was measured by flow injection analysis with conductivity detection (Hall and Aller, 1992) using a computer-operated Analytical Instruments Systems, Inc. (AIS,

Inc.) LCC-100 integrator. Uranium, calcium, and magnesium were measured by inductively coupled plasma mass spectrometry (ICP-MS, Agilent 7500a series). Filtered subsamples were diluted in 2% trace metal grade HNO_3 (Fisher Scientific, Inc.) containing scandium, holmium, and bismuth as internal standards. Calibration standards were prepared from certified stock solutions (U, CertiPREP; Ca and Mg, Ricca Chemical Company). Total Fe(II) ($Fe(II)_T$) was quantified by dissolving an unfiltered subsample in 1 M HCl for 24 hours in the dark under the anaerobic chamber atmosphere and measuring Fe(II) by the ferrozine assay (Stookey, 1970) using a Beckman Coulter DU720 UV/Vis spectrophotometer. Dissolved Fe(II) ($Fe(II)_d$) was measured in filtered subsamples by the ferrozine assay, whereas total initial iron ($Fe_{T,0}$) and total dissolved iron (Fe_{Td}) were measured in unfiltered and filtered subsamples by the ferrozine assay following reduction with hydroxylamine (0.2 M hydroxylamine, 0.1 M HCl). Dissolved Fe(III) ($Fe(III)_d$) was calculated by difference from measurements of Fe_{Td} and $Fe(II)_d$ (Viollier et al., 2000).

Preliminary experiments demonstrated that $Fe(II)_T$ measurements of incubations containing both iron and uranium were artificially high due to the reduction of Fe(III) by U(IV) during acidification of the unfiltered subsample as previously observed (Luan and Burgos, 2012). To overcome this issue, $Fe(II)_T$ concentrations of incubations containing both iron and uranium were corrected to account for Fe(II) produced during the acidification step using Equation 4.1,

$$[Fe(II)_T]_t = \left[Fe(II)_{T,m}\right]_t - 2 \cdot ([U_d]_0 - [U_d]_t) \quad (4.1)$$

where $[Fe(II)_T]_t$ is the corrected total Fe(II) concentration at time *t*, $[Fe(II)_{T,m}]_t$ is the measured total Fe(II) concentration in the acidified, unfiltered subsample at time *t*, $[U_d]_0$ is

the initial (t=0) dissolved uranium concentration in the filtered subsample, and $[U_d]_t$ is the dissolved uranium concentration in the filtered subsample at time *t*. This approach assumes that the concentration of U(IV) that reacts with Fe(III) in the acidified sample at each time point is equal to the decrease in dissolved uranium from the initial concentration. Although Equation 4.1 does not account for U(IV) produced by reduction of U(VI) initially adsorbed to ferrihydrite (between 9 and 40 μM), the effect on total Fe(II) measurements is substantially less (≤80 μM) than measured total Fe(II) concentrations such that it can be ignored.

Solid-phase extractions were performed to quantify the transformation of ferrihydrite to more crystalline phases over the course of the incubations. Unfiltered aliquots of 200 μL were pelleted via centrifugation (9000×g for 15 minutes) and the supernatants were discarded. Amorphous solid-phase iron, which included ferrihydrite and biogenic magnetite, was selectively extracted by a citrate-ascorbate solution for 24 hours in the dark and quantified by detection of Fe(II) in the supernatant using the ferrozine assay (Kostka and Luther, 1994).

The final solid phase products were identified by powder X-ray diffraction (XRD) and the elemental composition was determined by wet chemical digestion. A hand-operated vacuum filtration unit was used to collect the solid phase on a 0.22 μm PES filter (Millipore) under the anaerobic chamber atmosphere. The samples were rinsed once with anoxic deionized water and dried inside the anaerobic chamber. The solids were then scraped from the filter and finely ground using a mortar and pestle. Diffraction data of samples mounted on a zero background holder were collected on a PANalytical Empyrean diffractometer (Cu Kα radiation). Phase identification was performed with the HighScore

Plus software package using reference diffraction patterns from the PDF-4+ database (ICDD, 2015). To determine U:Fe molar ratios of the final solid phase, 10 mg of the powdered solid was extracted with oxic 1 M $NaHCO_3$ (pH 8.7) on a rotary wheel for 48 hours and washed twice with oxic 0.1 M $NaHCO_3$ to remove solid and adsorbed uranium (Alessi et al., 2012; Cerrato et al., 2013). The washed pellet was digested in 4 M HNO_3 and analyzed for total Fe and U as described above.

4.3.5 Pseudo-first order rate constant calculations

The initial rates of U_d removal and $Fe(II)_T$ production are the summation of a suite of parallel reactions which are first order with respect to the concentrations of U(VI) (dissolved or adsorbed) and ferrihydrite and can be represented by pseudo-first order rate laws. Pseudo-first order rate constants (k_{obs}) of U_d removal and $Fe(II)_T$ production were determined from the slope of the linearized, integrated first-order rate equation of consumption of U(VI) and Fe(III) oxides (Equation 4.2, where $[S]_0$ and $[S]_t$ are the concentration of either U_d or total Fe(III) ($Fe_{T,0} – Fe(II)_{T,t}$) at t=0 and time *t*, respectively) over the time interval following the lag phase that yielded the largest k_{obs} and conformed to the pseudo-first order rate law (i.e., the smallest R^2 value of the linear regression of the data represented using Equation 4.2). The average k_{obs} for each condition was calculated from the individual k_{obs} determined for triplicate incubations.

$$\ln\left(\frac{[S]_t}{[S]_0}\right) = -k_{obs} \cdot t \tag{4.2}$$

4.3.6 Thermodynamic calculations

The Gibbs free energy of reaction (ΔG_r) for the oxidation of U(IV) by Fe(III) was calculated at each time point to assess the thermodynamic viability of the reaction throughout the incubation. First, reduction potentials (E_h) were calculated for the half-reactions of U(VI) reduction to amorphous uraninite (U(VI) as $UO_2(CO_3)_3^{4-}$ in Equation 4.3) and ferrihydrite reduction to Fe(II) (Fe(II) as $FeHCO_3^+$ in Equation 4.4) using Equation 4.5,

$$UO_2(CO_3)_3^{4-} + 3H^+ + 2e^- \rightarrow UO_2(am) + 3HCO_3^- \quad (4.3)$$

$$Fe(OH)_3(s) + HCO_3^- + 3H^+ + e^- \rightarrow FeHCO_3^+ + 3H_2O \quad (4.4)$$

$$E_h = E_h^0 - \frac{RT}{nF} \ln Q \quad (4.5)$$

where E_h^0 is the standard state reduction potential (listed in Table C.1), R is the ideal gas constant, T is temperature, n is the number of electrons transferred, F is Faraday's constant, and Q is the reaction quotient. Q was calculated using concentrations of individual aqueous U(VI) and Fe(II) complexes calculated in PHREEQC using pH and measured solution composition as inputs (details in Appendix C). The included PHREEQC database was updated with the most recently published thermodynamic data for aqueous and solid-phase U(VI), U(IV), Fe(III), and Fe(II) compounds (Dong and Brooks, 2006; Guillaumont et al., 2003; Gustafsson, 2012). Lack of thermodynamic data on monomeric U(IV) solids prohibited their inclusion in the calculations.

The potentials of the U(VI)/UO_2(am) and $Fe(OH)_3$/Fe(II) redox couples vary amongst individual aqueous U(VI) and Fe(II) complexes, therefore a Monte Carlo

approach was used to calculate the overall U(VI)/UO_2(am) and $Fe(OH)_3$/Fe(II) reduction potentials while accounting for aqueous U(VI) and Fe(II) speciation. Reduction potentials of the most abundant individual aqueous U(VI) and Fe(II) complexes as products of uraninite oxidation by ferrihydrite, which accounted for >99% of total dissolved U(VI) and Fe(II), were calculated at each time point, and 10,000 Monte Carlo sampled E_h values were used to calculate the average and standard deviation of the overall potential of each redox couple. Discrete sampling probabilities were prescribed to the E_h of each aqueous U(VI) and Fe(II) complex at each time point based on the normalized equilibrium concentration of the complex to the total dissolved concentration of U(VI) and Fe(II). The ΔG_r of uraninite oxidation by ferrihydrite was calculated in a similar manner from 10,000 Monte Carlo sampled pairs of E_h values for each redox couple according to Equation 4.6,

$$\Delta G_r = -n \cdot F \cdot \left(E_{h,ox} - E_{h,red}\right) \tag{4.6}$$

where $E_{h,ox}$ and $E_{h,red}$ represent the $Fe(OH)_3$/Fe(II) and U(VI)/UO_2(am) half-reactions, respectively.

4.3.7 Biogeochemical kinetic model

A kinetic model was developed in PHREEQC to identify the dominant processes controlling uranium removal in batch incubations with *S. putrefaciens* (Table 4.1). The model includes kinetic rate laws for microbial respiration of U(VI) and ferrihydrite, secondary mineralization of ferrihydrite to magnetite, incorporation of uranium into magnetite, precipitation of siderite, and abiotic redox reactions between uranium and iron (Table 4.2). Uranium respiration was described using a speciation-dependent rate law which includes two rate constants, one for uranyl non-carbonate species and one for uranyl

Table 4.1 Reactions and equations included in the PHREEQC kinetic model

Reaction	Equation	#
Microbial respiration		
U(VI) respiration	$2UO_2^{2+} + lactate^- + 2H_2O \rightarrow 2UO_2(am) + acetate^- + HCO_3^- + 5H^+$	R1
Fe(III) respiration	$4Fe(OH)_3(s) + lactate^- + 3HCO_3^- + 7H^+ \rightarrow 4FeHCO_3^+ + acetate^- + 10H_2O$	R2
Solid phase reactions		
Magnetite formation	$2Fe(OH)_3(s) + Fe(II)_{ads} \rightarrow Fe_3O_4(s)$	R3
Uranium incorporation	$U(VI)_{ads} \rightarrow U(VI)_{incorp}$	R4
Siderite precipitation	$Fe^{2+} + CO_3^{2-} \rightarrow FeCO_3(s)$	R5
Abiotic redox reactions		
U(IV) oxidation by ferrihydrite	$UO_2(am) + 2Fe(OH)_3(s) + 5HCO_3^- + 3H^+ \rightarrow UO_2(CO_3)_3^{4-} + 2FeHCO_3^+ + 6H_2O$	R6
U(VI) reduction by adsorbed Fe(II)	$U(VI)_{ads} + 2Fe(II)_{ads} \rightarrow UO_2(am) + 2Fe(OH)_3(s)$	R7

Table 4.2 Rate laws included in the kinetic model for the reactions listed in Table 4.1

#	Rate law	Reference
R1[a]	$Rate_{R1} = (k_{U1} \cdot [U(VI)_{non-carb}] + k_{U2} \cdot [U(VI)_{carb}]) \cdot [X] \cdot F_T \cdot F_{tox}$ where $F_T = 1 - e^{\left(\frac{\Delta G_r - \Delta G_C}{\chi \cdot R \cdot T}\right)}$ and $F_{tox} = \frac{1}{1+\left(\frac{[UO_2^{2+}]}{IC_{50}}\right)^p}$	(Belli et al., 2015)
R2	$Rate_{R2} = k_{Fe} \cdot [Fe(OH)_3] \cdot [X] \cdot F_T$	(Roden and Zachara, 1996)
R3	$Rate_{R3} = k_{mag} \cdot \frac{[Fe(II)_{ads}]}{[Fe(OH)_3]}$	(Boland et al., 2014b)
R4	$Rate_{R4} = k_{incorp} \cdot [U(VI)_{ads}] \cdot \frac{[Fe(II)_{ads}]}{[Fe(OH)_3]}$	
R5	$Rate_{R5} = k_{sid} \cdot \left(\frac{[Fe^{2+}] \cdot [CO_3^{2-}]}{K_{sp}} - 1\right)$	(Liu et al., 2001)
R6	$Rate_{R6} = k_{Uox} \cdot [UO_2(am)] \cdot [Fe(OH)_3]$ for $[Fe(OH)_3] \leq 0.63$ mM $Rate_{R6} = 0.00063 \cdot k_{Uox} \cdot [UO_2(am)]$ for $[Fe(OH)_3] > 0.63$ mM if ΔG_r of Equation R6 is ≥ 0, then R6 = 0	(Ginder-Vogel et al., 2010)
R7	$Rate_{R7} = k_{Ured} \cdot [\equiv OFeOH] \cdot [U(VI)_{ads}]$ if ΔG_r of Equation R6 is ≤ 0, then R7 = 0	(Liger et al., 1999)

[a]R is the ideal gas constant. T is temperature. ΔG_r is the Gibbs energy available through respiration. The Gibbs energy conserved by the formation of ATP (ΔG_C, -67.5 kJ/mol) and the average stoichiometric number (χ, 3) were determined for lactate oxidation coupled to Fe(III) respiration and assumed to be the same for U(VI) respiration (Jin, 2012).

carbonate species, and a 2-parameter toxicity function to account for the effect of uranyl toxicity on U(VI) bioreduction rates by *S. putrefaciens* (Belli et al., 2015). Respiration of ferrihydrite was included using a first-order rate law with respect to the concentration of ferrihydrite (Roden and Zachara, 1996). As lactate was provided in excess (15 mM), respiration rates were independent of lactate concentration. Uranium(VI) and Fe(III) respiration rate laws included the biomass concentration and the thermodynamic driving force F_T, which accounts for the effects of microbial respiration energetics on the rate of uranium and iron bioreduction (Jin and Bethke, 2003).

New master species were defined in PHREEQC for Fe(II) and Fe(III) in siderite and magnetite, which allowed solid-phase iron speciation to be controlled by kinetic rate expressions, rather than thermodynamic equilibrium (Parkhurst and Appelo, 1999). The rate of secondary mineralization of ferrihydrite to magnetite was proportional to the concentration of adsorbed Fe(II) normalized to the concentration of ferrihydrite (Boland et al., 2014b). Uranium incorporation into magnetite was proportional to the concentration of U(VI) adsorbed to ferrihydrite and the rate of magnetite formation. A previously established rate law for siderite precipitation was used (Liu et al., 2001). Equilibrium with respect to siderite solubility was not achieved due to slow precipitation kinetics (Jensen et al., 2002), thus the apparent K_{sp} of siderite ($10^{-8.1}$) was calculated from the steady state equilibrium concentrations of CO_3^{2-} and Fe^{2+}. Two rate constants were used to describe the rate of siderite precipitation, one before and one after the maximum concentration of dissolved Fe(II) was reached.

A previously defined rate law and its optimized rate constant (Liger et al., 1999) were included to describe the kinetics of abiotic U(VI) reduction by adsorbed Fe(II) on

ferrihydrite and magnetite surfaces. The rate of U(IV) oxidation (as uraninite) by ferrihydrite was defined as first order with respect to concentrations of uraninite and either first or zero order with respect to ferrihydrite below or above 0.63 mM ferrihydrite, respectively (Ginder-Vogel et al., 2010). The ΔG_r for the abiotic oxidation of uraninite by ferrihydrite was calculated at each time point with the most abundant aqueous U(VI) and Fe(II) complexes as products. The rate of uraninite oxidation was set to 0 if ΔG_r was ≥ 0, and the rate of U(VI) reduction was set to 0 if ΔG_r was ≤ 0.

The model was run with a time step of 6 hours beginning at the first time point used in the calculation of k_{obs} from the experimental data. Medium composition, the average measured pH for the entire incubation, initial measured DIC concentration, and measured concentrations of total Fe(II) and dissolved uranium, calcium, and silica at the first modeled time point were used as initial conditions. Model input concentrations of ferrihydrite were calculated from the difference between $Fe_{T,0}$ and $Fe(II)_T$ at the first modeled time point. The pH was held constant throughout the simulations, and equilibrium with respect to adsorption and aqueous complexation was assumed at each time point. Complete lists of surface complexation constants and mineral surface properties are found in Tables C.2 and C.3 of Appendix C.

Rate law parameters for microbial uranium respiration were calibrated with the dissolved uranium time series from the uranium-only incubations using the parameter estimation program PEST Version 13.0 (Watermark Numerical Computing http://www.pesthomepage.org/). PEST minimizes the sum of squared residuals between the measured and model-predicted time series using a Gauss-Marquardt–Levenberg nonlinear estimation algorithm. These parameters were then applied to the model

simulations of incubations containing both U(VI) and ferrihydrite, and the remaining parameters were optimized in a self-consistent manner across the different incubation conditions. Ferrihydrite-only incubations were not used to calibrate rate law parameters involving iron as the data indicated that uranium altered the secondary mineralization of ferrihydrite and likely the bioavailability of iron in the calcium-amended incubations. PEST was unable to optimize the model parameters for the incubations containing U(VI) and ferrihydrite due to highly correlated parameters for iron respiration and secondary mineralization. Therefore, model parameters were optimized by fixing the rate constant of ferrihydrite respiration while rate constants of siderite precipitation were adjusted to fit the dissolved Fe(II) data and the remaining parameters were adjusted to fit the time series data of dissolved uranium, total Fe(II), and ascorbate-extractable solid phase iron. The same rate constants of U(VI) bioreduction, abiotic U(VI) reduction, and abiotic U(IV) oxidation were applied to all incubations.

4.4 Results

4.4.1 Batch incubations with either U(VI) or ferrihydrite as the sole terminal electron acceptor

4.4.1.1 U(VI) as the sole terminal electron acceptor

Batch incubations with *S. putrefaciens* were conducted with U(VI) as the sole TEA to determine the effect of solution composition on the rate of uranium removal in the absence of ferrihydrite (blue lines, Figure 4.1A-C). Aqueous uranyl speciation varied considerably across the different incubation conditions depending on the concentrations of DIC, calcium, and silica. Aqueous uranyl speciation was primarily composed of uranyl

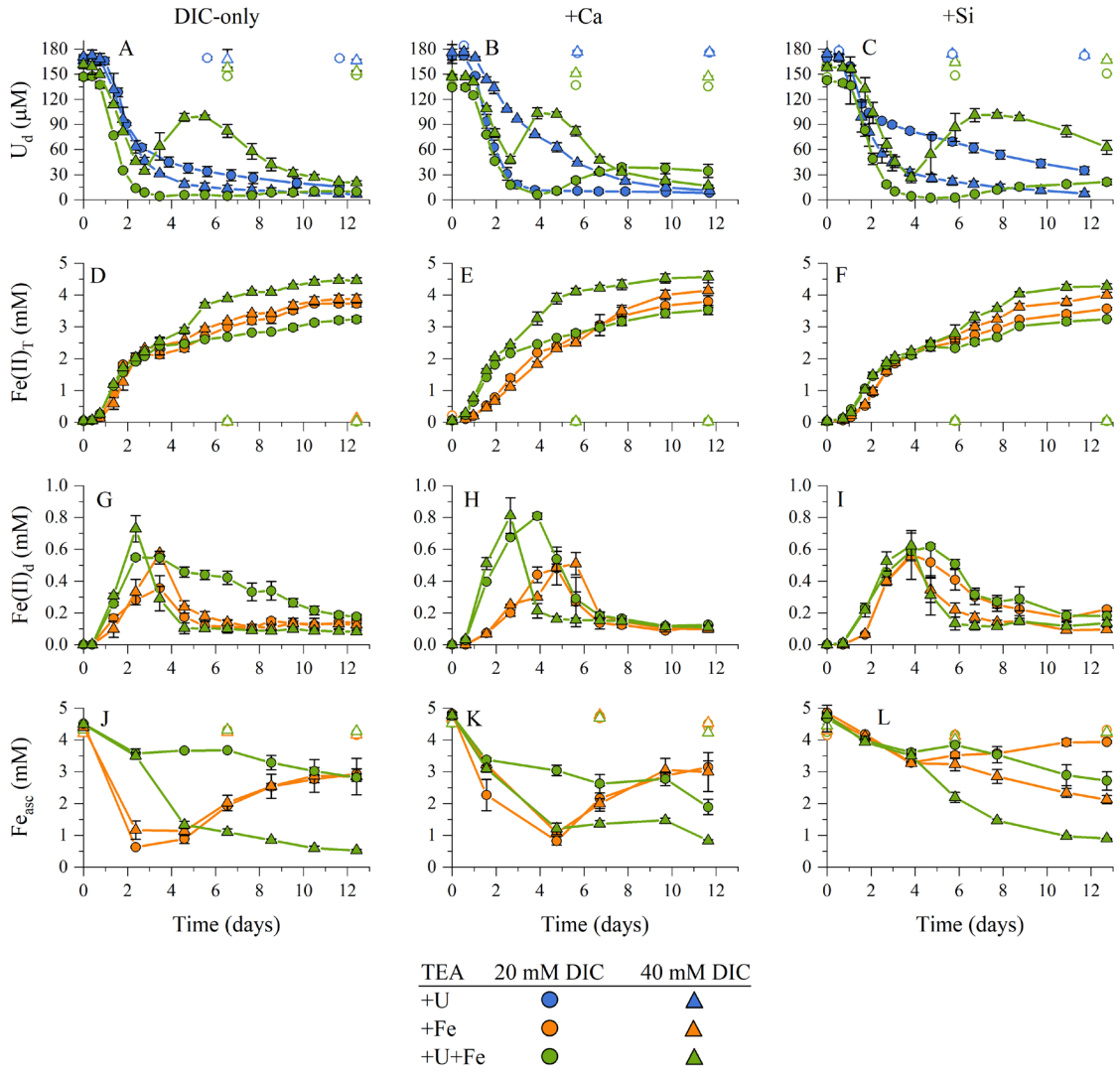

Figure 4.1 Time series of (A-C) dissolved uranium (U_d), (D-F) total Fe(II) ($Fe(II)_T$), (G-I) dissolved Fe(II) ($Fe(II)_d$), and (J-L) ascorbate-extractable solid phase iron (Fe_{asc}) in incubations amended with either 180 μM U(VI) (blue), 5 mM ferrihydrite (orange), or both (green) as terminal electron acceptors, and either 20 mM (circles) or 40 mM (triangles) DIC only (left), DIC and 800 μM calcium (center), or DIC and 300 μM silica (right). Filled symbols and lines represent biotic incubations with *S. putrefaciens* (inoculated at t=0) whereas open symbols represent abiotic controls. Symbols and error bars represent the average and standard deviation from triplicate incubations.

carbonate and ternary uranyl carbonate species (Table C.4) due to the high DIC concentrations used and the background magnesium present in the growth medium. Uranyl non-carbonate species (i.e., the 'free' hydrated uranyl ion and uranyl hydroxide, sulfate, phosphate, and silicate species) represented < 1% of initial U(VI) yet showed the largest range in concentration across the different experimental conditions. Amending incubations with silica had a negligible effect on aqueous uranyl speciation due to the small formation constant of the singular uranyl silicate complex ($UO_2H_3SiO_4^+$, logβ = -1.91), however, the presence of calcium resulted in the formation of highly stable calcium-uranyl carbonate species and decreased the fraction of carbonate and non-carbonate uranyl species.

Initial concentrations of total dissolved uranium were identical in uranium-only incubations inoculated with *S. putrefaciens* and abiotic controls, indicating that adsorption of U(VI) to the bacterial cell surface was negligible across all incubation conditions (Figure 4.1A-C). After around 12 days of incubation, between 79 and 96% of uranium was removed from solution in biotic incubations, whereas minimal (<5%) uranium removal occurred in abiotic controls (Figure 4.1A-C). The concentration of dissolved calcium remained relatively constant in the incubations amended with calcium and 20 mM DIC but decreased to around 100 μM after 3 days in the incubations amended with the same concentration of calcium and 40 mM DIC (Figure C.1A). In contrast, magnesium, which was included in the growth medium, remained in solution in the incubations at both DIC concentrations (Figure C.1B). In incubations amended with silica, the concentration of dissolved silica remained constant at the initial concentration throughout the incubation period regardless of the DIC concentration (Figure C.2).

In the DIC-only and Si-amended incubations, an initial period of rapid uranium removal was followed by a second period beginning at day 2 and characterized by a rate of removal between 2 and 10% of the initial rate (Figure 4.1A and Figure 4.1C). After 4 days, the removal of uranium was greater in incubations amended with 40 mM DIC relative to those amended with 20 mM DIC (Figure 4.1A and Figure 4.1C). This trend was reversed in the presence of calcium, with more uranium removed in incubations amended with 20 mM DIC than with 40 mM DIC, and an abrupt change in the rate of uranium removal was not observed regardless of DIC concentration (Figure 4.1B). Across all conditions, the initial period of uranium removal followed pseudo-first order reaction kinetics with respect to dissolved uranium concentration. Neither DIC concentration nor the presence of silica had a significant effect on the pseudo-first order rate constant of uranium removal (k_{obs}) in the DIC-only and silica-amended incubations (Figure 4.2A). In contrast, the k_{obs} of uranium removal in incubations amended with calcium was substantially higher in the 20 mM DIC incubation and substantially lower in the 40 mM DIC incubation (Figure 4.2A).

4.4.1.2 Ferrihydrite as the sole terminal electron acceptor

After an initial lag phase of less than 24 hours, total Fe(II) in ferrihydrite-only incubations was produced at a rapid rate for the first day, then at a slower rate after 2 to 5 days (orange lines, Figure 4.1D-F). Dissolved Fe(II) increased over time to maximum concentrations ranging from 350 to 575 μM depending on the incubation condition, after which the concentration decreased to between 90 and 180 μM at steady-state (Figure 4.1G-I). Similar trends in dissolved Fe(II) concentration were observed at both DIC concentrations, though the maximum dissolved Fe(II) concentration in the DIC-only incubations (Figure 4.1G), the amount of time before Fe(II) was removed from solution in

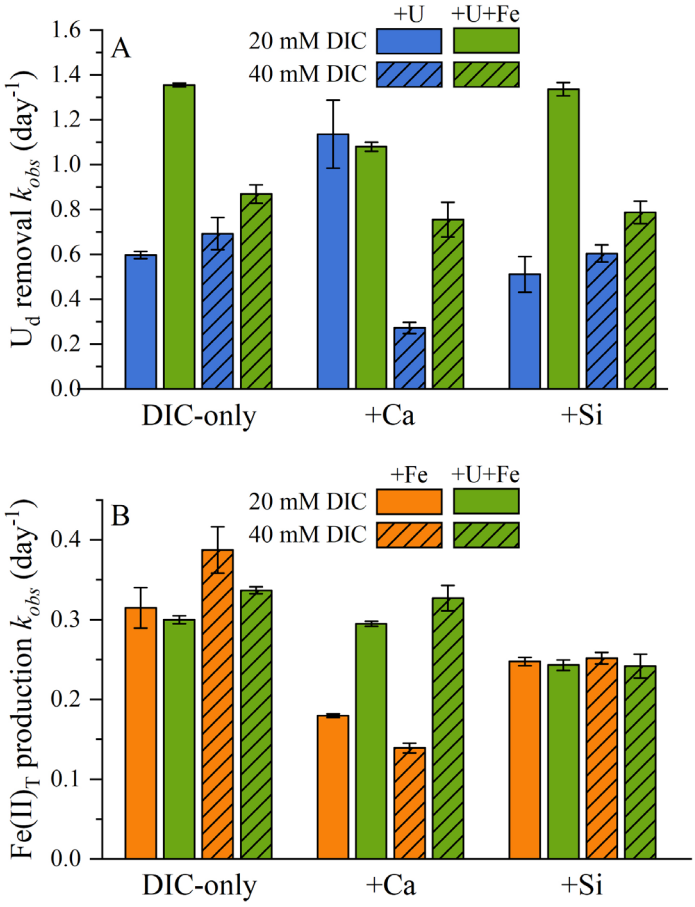

Figure 4.2 Pseudo-first order rate constants (k_{obs}) of the initial (A) removal of dissolved uranium (U_d) and (B) production of total Fe(II) ($Fe(II)_T$) in incubations of *S. putrefaciens* amended with either 180 µM U(VI) (blue), 5 mM ferrihydrite (orange), or both (green) as terminal electron acceptors, and either 20 mM (solid bars) or 40 mM (hashed bars) DIC only, DIC and 800 µM calcium (+Ca), or DIC and 300 µM silica (+Si). Values of k_{obs} were calculated for individual incubations and presented as the average and standard deviation for each condition (n=3).

the calcium-amended incubations (Fig. 1H), and the rate of dissolved Fe(II) removal in the silica-amended incubations (Figure 4.1I) all increased at the higher DIC concentration. As the proportion of dissolved Fe(II) was always below 40% of total Fe(II) over the course of the incubations (Figure C.3), the majority of Fe(II) produced was associated with the solid phase, either adsorbed to mineral surfaces or present as Fe(II)-bearing solids. Less than 12% of calcium added to the calcium-only incubations remained in solution (Figure C.1A), whereas magnesium remained in solution throughout the incubation period (Figure C.1B). In turn, roughly two-thirds of the dissolved silica added to the incubations was initially adsorbed to ferrihydrite, and the dissolved fraction of silica increased over time (Figure C.2). Generally, dissolved Fe(III) (<0.22 μm) was produced in the ferrihydrite incubations up to a maximum concentration of 30-40 μM by day 4 and then consumed by the end of the incubation period (Figure C.4). Although the concentrations of dissolved Fe(III) were slightly higher in the DIC-only incubations (Figure C.4A-B) compared to incubations amended with calcium (Figure C.4C-D) or silica (Figure C.4E-F), the concentration of DIC did not affect dissolved Fe(III) concentrations.

Concentrations of ascorbate-extractable (i.e., amorphous) solid phase iron (Fe_{asc}) remained constant in abiotic control incubations across all conditions, whereas the concentration of Fe_{asc} varied as a function of time according to the treatment and DIC concentration (Figure 4.1J-L). In the DIC-only incubations, Fe_{asc} first decreased to a minimum concentration around 1 mM after two days, then gradually increased to around 3 mM by the end of the incubation period (Figure 4.1J). A similar trend was observed for incubations amended with calcium, though the minimum was reached after 5 days (Figure 4.1K). DIC concentration had no effect on Fe_{asc} concentrations in the DIC-only and

calcium-amended incubations. Iron mass balance calculations indicated that regardless of the presence of calcium, the initial decrease in Fe_{asc} was due to the formation of crystalline Fe(III) solids (i.e., non-ascorbate-extractable solid Fe(III)), and the subsequent increase in Fe_{asc} was due to consumption of the crystalline Fe(III) solids and formation of amorphous Fe(II)-bearing solids (i.e., ascorbate-extractable solid Fe(II)) (Figure C.5A-B). In contrast, silica-amended incubations showed a gradual decrease in Fe_{asc} which was more significant at the higher DIC concentration (Figure 4.1L), reflecting the absence of crystalline Fe(III) solids and the gradual production of ascorbate-extractable Fe(II)-bearing solids (Figure C.5C).

Initial pseudo-first order rate constants for Fe(II) production (k_{obs}) increased with increasing DIC concentration in the DIC-only incubations (Figure 4.2B), whereas the amendment of calcium significantly decreased the k_{obs}, especially at the higher DIC concentration (Figure 4.2B). Finally, silica amendment slightly decreased the k_{obs} of Fe(II) production compared to the DIC-only incubations and minimized the effect of the DIC concentration (Figure 4.2B).

4.4.2 Batch incubations with U(VI) and ferrihydrite provided simultaneously as terminal electron acceptors

4.4.2.1 Uranium removal in the presence of ferrihydrite

When ferrihydrite and U(VI) were included together in incubations with *S. putrefaciens*, adsorption of U(VI) onto the ferrihydrite surface removed between 5 and 22% of dissolved uranium prior to inoculation (green lines, Figure 4.1A-C). Abiotic controls indicate that equilibrium with respect to adsorption was reached prior to t=0 and

that adsorbed uranium was highest in the 20 mM DIC incubations and in the presence of calcium (Figure 4.1A-C, Table C.5). In incubations with 20 mM DIC, the rate and extent of uranium removal in the presence of ferrihydrite either increased (DIC-only and silica-amended) or remained the same (calcium-amended) compared to the uranium-only incubations in the same conditions (Figure 4.1A-C). Maximum uranium removal was achieved between day 3 and 5, after which rebounds in dissolved uranium were observed (Figure 4.1A-C). A modest rebound of up to 29±2% of the initial dissolved uranium concentration was observed in the presence of calcium (Figure 4.1B), whereas silica (Figure 4.1C) only slightly enhanced the minor rebound in dissolved uranium (7±1% of the initial concentration) observed in the 20 mM DIC-only incubation (Figure 4.1A). When ferrihydrite was included with uranium in incubations amended with 40 mM DIC, the initial period of uranium removal was followed by a large rebound in dissolved uranium concentration which was not observed in otherwise identical incubations without ferrihydrite (Figure 4.1A-C). Beginning around day 3 in the 40 mM DIC-only incubation, dissolved uranium increased up to 62±1% of the initial concentration before decreasing again to a final concentration of 20.5±2.3 μM (Figure 4.1A). Similar trends in dissolved uranium time series were observed in 40 mM DIC incubations amended with calcium (Figure 4.1B) and silica (Figure 4.1C), although silica decreased the final extent of uranium removal compared to the other incubations.

Across nearly all incubation conditions, the presence of ferrihydrite increased the pseudo-first order rate constant of uranium removal (k_{obs}) compared to the uranium-only incubations (Figure 4.2A). The only exception was the incubation amended with calcium and 20 mM DIC which displayed a similar k_{obs} of uranium removal regardless of the

presence of ferrihydrite. Larger k_{obs} of uranium removal were observed in incubations amended with ferrihydrite and 20 mM DIC than with 40 mM DIC, regardless of the presence of calcium or silica (Figure 4.2A).

4.4.2.2 Effect of uranium on rates of Fe(II) production and iron speciation

Uranium enhanced the extent of total Fe(II) production in the 40 mM DIC incubations whereas it decreased the extent of total Fe(II) production in the 20 mM DIC incubations relative to otherwise identical incubations without uranium (green lines, Figure 4.1D-F). Pseudo-first order rate constants for the production of Fe(II) (k_{obs}) in the DIC-only and silica-amended incubations were mostly unaffected by the presence of uranium except for a 13±1% decrease in the DIC-only incubation amended with 40 mM DIC (Figure 4.2B). In contrast, uranium increased the pseudo-first order rate constants of Fe(II) production in the calcium-amended incubations by 64±1% and 135±9% in the presence of 20 and 40 mM DIC, respectively.

In addition, the speciation of iron between solid and dissolved phases was significantly affected by the presence of uranium. Regardless of the DIC concentrations and the presence of calcium, uranium increased the maximum dissolved Fe(II) concentration (Figure 4.1G-H) and the percentage of Fe(II) in the dissolved phase (Figure C.3A-B) compared to iron-only incubations. After initial production of dissolved Fe(II) in the DIC-only incubations, dissolved Fe(II) concentrations decreased rapidly in the 40 mM DIC incubations irrespective of the presence of uranium (Figure 4.1G). Although dissolved Fe(II) also decreased rapidly in the absence of uranium in the 20 mM DIC incubations, it only gradually decreased in the presence of uranium (Figure 4.1G). In incubations amended

with calcium, dissolved Fe(II) concentrations decreased rapidly regardless of the DIC concentration and the presence of uranium (Figure 4.1H). In turn, trends in dissolved Fe(II) concentration were largely unaffected by the presence of uranium in the silica-amended incubations regardless of DIC concentration (Figure 4.1I and Figure C.3C). Similarly, time series of dissolved Fe(III) were mostly unaffected by the presence of uranium across all incubation conditions, though initial production rates were slightly lower in the presence of calcium and silica (Figure C.4).

Finally, the crystallinity of solid phase iron was significantly affected by the presence of uranium. The rebound in Fe_{asc} concentration observed in the DIC-only and calcium-amended incubations without uranium was not evident when uranium was present (Figure 4.1J-K). Instead, Fe_{asc} concentrations in the incubations amended with 20 mM DIC never fell below 2 mM whereas those conducted with 40 mM DIC decreased to around 1 mM after day 5, regardless of the presence of calcium (Figure 4.1J-K). In incubations amended with silica, lower concentrations of Fe_{asc} were observed in the presence of uranium under both DIC concentrations relative to otherwise identical incubations without uranium (Figure 4.1L). Simultaneously, production of crystalline Fe(III)-bearing solids was never observed in the presence of uranium based on iron mass balance calculations, and a moderate fraction of Fe(II)-bearing solids was only found in the 20 mM DIC incubations containing uranium, irrespective of the addition of calcium or silica (Figure C.5).

4.4.3 Characterization of the final iron solid phases

Unaltered 2-line ferrihydrite was identified as the final solid-phase product in all abiotic control incubations, in contrast to more crystalline iron minerals identified in incubations inoculated with *S. putrefaciens* (Figure 4.3). Magnetite was the primary product identified in the ferrihydrite-only incubations amended with 20 mM DIC along with peaks of smaller magnitude assigned to lepidocrocite (Figure 4.3A). When uranium was present under the same conditions, siderite was the sole mineral identified in the final solid phase (Figure 4.3B). In the ferrihydrite-only incubation amended with 40 mM DIC, a mixture of siderite and magnetite was identified (Figure 4.3C), whereas siderite was the

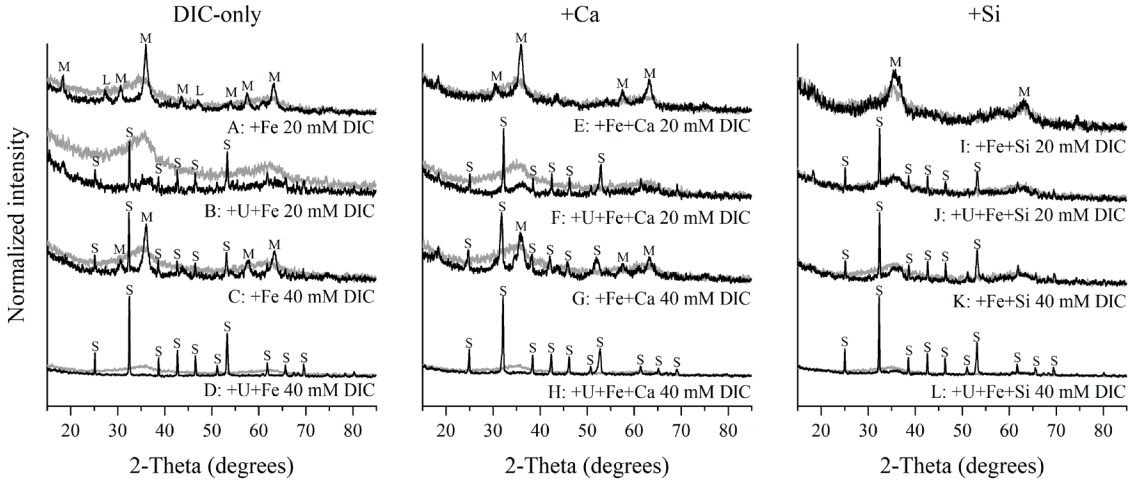

Figure 4.3 Powder X-ray diffraction (XRD) patterns of solid phase products in incubations amended with 5 mM ferrihydrite (+Fe) or both 180 µM U(VI) and 5 mM ferrihydrite (+U+Fe) as terminal electron acceptors, and either 20 or 40 mM (A-D) DIC-only, (E-H) DIC and 800 µM calcium (+Ca), and (I-L) DIC and 300 µM silica (+Si). Black lines represent biotic incubations and grey lines represent abiotic controls. Signals are normalized to the maximum intensity in each condition and smoothed using a 10-point moving average. Peaks are indexed with M for magnetite, L for lepidocrocite, and S for siderite.

only phase identified in otherwise identical incubations amended with uranium (Figure 4.3D). In the ferrihydrite-only incubations with 20 mM DIC and calcium, magnetite was the sole crystalline iron phase identified with no evidence of lepidocrocite (Figure 4.3E). In the remaining incubations amended with calcium, secondary mineralization products of ferrihydrite were identical to those identified in DIC-only incubations under the same conditions (Figure 4.3F-H). Diffraction patterns of biotic incubations amended with silica showed a strong resemblance to the unaltered 2-line ferrihydrite identified in control incubations (Figure 4.3I-L), indicating that ferrihydrite was not entirely consumed by microbial respiration or secondary mineralization. Weak, broad peaks attributed to magnetite were identified in the ferrihydrite-only incubations amended with 20 mM DIC and silica (Figure 4.3I), whereas siderite was the sole phase identified in the other silica-amended incubations (Figure 4.3J-L). The average U:Fe molar ratios of the final solid phase products in incubations amended with *S. putrefaciens* ranged from 0.0049 to 0.0083 (Table C.5). U:Fe molar ratios were an order of magnitude larger than abiotic control incubations under the same conditions, indicating that uranium strongly associated with the iron solid phase over the course of incubations with *S. putrefaciens*. U:Fe molar ratios were inversely related to DIC concentrations, and this effect was most pronounced in the DIC-only and silica-amended incubations.

4.4.4 Biogeochemical kinetic model

The kinetic model successfully reproduced the initial removal of uranium across all uranium-only incubations using the proposed speciation-dependent rate law which accounted for the aqueous speciation of U(VI), variable reduction kinetics of non-carbonate and carbonate uranyl species, and the effect of uranyl toxicity on *S. putrefaciens*

(Figure C.6, Table 4.3). These optimized parameters for U(VI) bioreduction were applied to the modeling of incubations containing both U(VI) and ferrihydrite, and rate constants of ferrihydrite respiration, ferrihydrite conversion to magnetite, siderite precipitation, U(VI) reduction by Fe(II), U(IV) oxidation by ferrihydrite, and uranium incorporation into secondary mineralization products were optimized to best fit the model output to the measured data (Table 4.3). The model reproduced the simultaneous decrease of dissolved uranium and production of total Fe(II), the production and consumption of dissolved Fe(II), the decrease in amorphous solid phase iron (i.e. ferrihydrite and magnetite), the final solid phase iron speciation (Figure 4.4, Figure C.7, and Figure C.8), and the final concentration of solid-associated uranium (Table C.5) for all incubation conditions extremely well. Uranium incorporation into the crystal lattice of secondary minerals had to be included in the model to reproduce the faster rates of uranium removal in the presence of ferrihydrite. In addition, when standard state redox potentials (E_h^0) of U(VI)/UO_2 were used to calculate the ΔG_r of U(IV) oxidation by ferrihydrite at each time step, U(IV) oxidation was always predicted to be unfavorable (not shown), and the model was therefore unable to reproduce the rebound in dissolved uranium that was observed midway through the incubations (Figure 4.1A-C). Only after the U(VI)/UO_2 E_h^0 was decreased by 84 mV could the model reproduce time series of total dissolved uranium over the entire incubation period (Figure 4.4, Figure C.7, and Figure C.8). Finally, the model could not sustain sufficient U(IV) oxidation to reproduce the rebound in dissolved uranium in the 20 mM DIC incubations amended with calcium and silica as ferrihydrite was predicted to be consumed by the time the reaction became thermodynamically favorable (Figure C.7 and Figure C.8). In turn, the model overestimated the rebound in dissolved uranium in the 40 mM DIC incubations

Table 4.3 Optimized parameters for the PHREEQC kinetic model

	DIC-only		+Ca		+Si	
Parameter	20 mM DIC	40 mM DIC	20 mM DIC	40 mM DIC	20 mM DIC	40 mM DIC
U(VI) respiration						
k_{U1} (non-carbonate) (L/cell/s)	2.1×10^{-10}		2.1×10^{-10}		2.1×10^{-10}	
k_{U2} (carbonate) (L/cell/s)	4.9×10^{-18}		4.9×10^{-18}		4.9×10^{-18}	
IC_{50} (mol/L)	1.3×10^{-15}		1.3×10^{-15}		1.3×10^{-15}	
p	2		2		2	
Ferrihydrite respiration						
k_{Fe} (L/cell/s)	5.2×10^{-18}		5.2×10^{-18}		3.5×10^{-18}	
Siderite precipitation						
k_{Sid1} (mol/L/s)	0	0	0	0	1.5×10^{-10}	1.5×10^{-10}
k_{Sid2} (mol/L/s)	3.0×10^{-10}	1.0×10^{-9}	5.5×10^{-10}	1.0×10^{-9}	3.0×10^{-10}	1.0×10^{-9}
Magnetite formation						
k_{Mag} (mol/L/s)	6×10^{-10}	2.5×10^{-10}	3.5×10^{-10}	2.0×10^{-10}	5.0×10^{-10}	2.0×10^{-10}
Uranium incorporation						
k_{incorp} (1/s)	0.1	0.4	0	0	0.1	0.45
U(IV) oxidation by ferrihydrite						
k_{Uox} (L/mol/s)	3.0×10^{-3}		3.0×10^{-3}		3.0×10^{-3}	
U(VI) reduction by Fe(II)						
k_{Ured} (L/mol/s)	6.65		6.65		6.65	

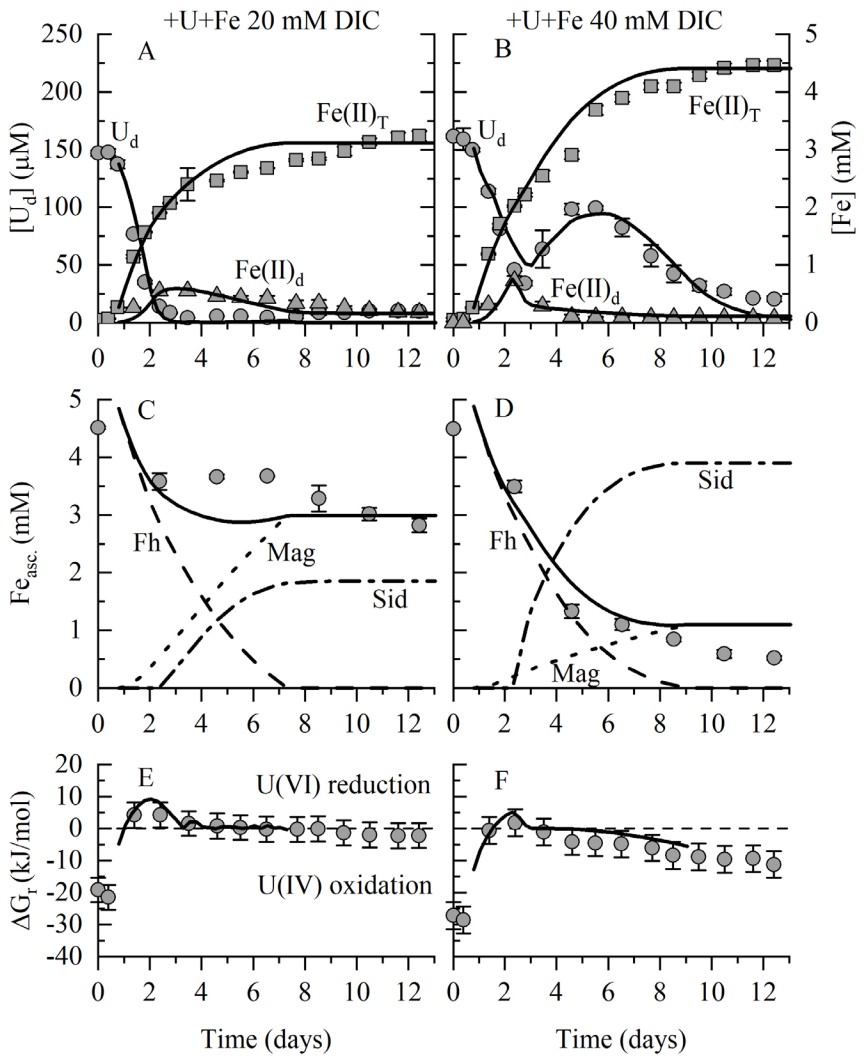

Figure 4.4 Measured and modeled time series of DIC-only incubations conducted with *S. putrefaciens* in the presence of 5 mM ferrihydrite and 180 µM U(VI) as terminal electron acceptors and (A, C, and E) 20 mM or (B, D, and F) 40 mM DIC. The same experimental data are presented in Figure 4.1. Symbols represent measured concentrations of dissolved uranium (U_d) (circles), dissolved Fe(II) ($Fe(II)_d$) (triangles), and total Fe(II) ($Fe(II)_T$) (squares). Lines represent output of the kinetic model using the optimized rate parameters from Table 4.3. (C and D) Dashed lines representing solid phase iron species are indexed with Fh for ferrihydrite, Mag for magnetite, and Sid for siderite. The solid line represents the sum of the amorphous iron species (i.e., ferrihydrite and magnetite). (E and F) The solid line represents the Gibbs free energy of reaction (ΔG_r) for the oxidation of monomeric U(IV) by ferrihydrite calculated by the model at each time step. The dashed line represents the threshold ΔG_r, above which adsorbed U(VI) is reduced by adsorbed Fe(II) and below which monomeric U(IV) is oxidized by ferrihydrite.

amended with calcium (Figure C.7B) and the removal of uranium in the later part of the 40 mM DIC incubations amended with silica (Figure C.8B).

4.5 Discussion

4.5.1 Effect of solution composition on uranium removal in the absence of ferrihydrite

The oxidation state of uranium plays a large role in controlling its mobility in subsurface environments, and efforts to decrease dissolved uranium concentrations by sequestering uranium as reduced U(IV) solids have shown promise (Bargar et al., 2013; Long et al., 2015; Williams et al., 2011). Although iron-bearing minerals are ubiquitous in both natural and contaminated environments and may act as both reductants and oxidants of uranium, the geochemical conditions which control the role of iron in uranium redox cycling remain poorly defined. In the absence of iron, aqueous uranyl speciation is the primary control of U(VI) bioreduction kinetics (Belli et al., 2015; Brooks et al., 2003; Sheng and Fein, 2014; Ulrich et al., 2011), and the various concentrations of DIC, calcium, and silica used in the present study were expected to alter aqueous uranyl speciation and, thus, the rate of uranium removal from solution. The rate constant for uranyl non-carbonate species optimized in the PHREEQC kinetic model was eight orders of magnitude larger than the rate constant for uranyl carbonate species (Table 4.3), consistent with past studies that identified uranyl non-carbonate species as the most bioavailable and readily reducible fraction of U(VI) (Belli et al., 2015; Stewart et al., 2011; Ulrich et al., 2011). Overall, the experimentally-derived pseudo-first order rate constants of uranium removal (k_{obs}) increased proportionally to the initial concentration of uranyl non-carbonate species up to a concentration of 22 pM, above which the rate constants decreased (Figure 4.5). These

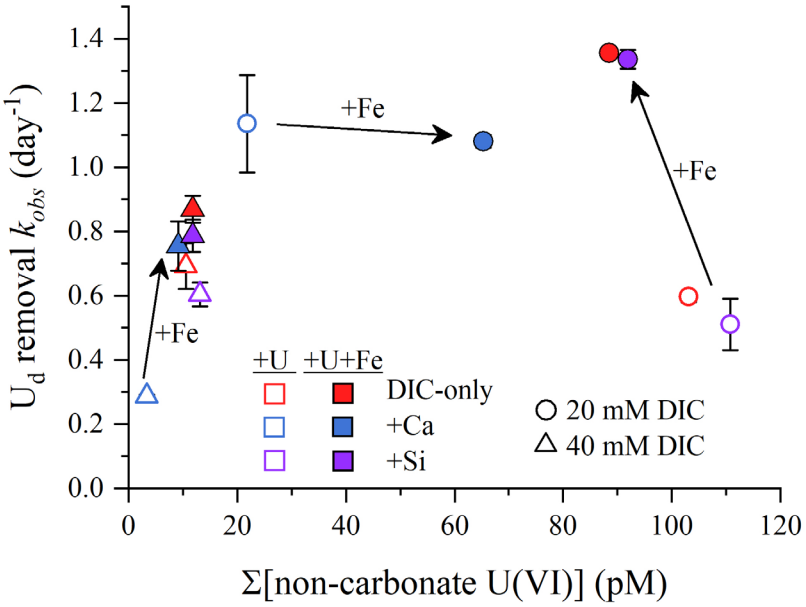

Figure 4.5 Pseudo-first order rate constants (k_{obs}) of uranium removal versus the initial concentration of uranyl non-carbonate species in incubations of *S. putrefaciens* amended with either 180 µM U(VI) (+U, open symbols) or both 180 µM U(VI) and 5 mM ferrihydrite (+U+Fe, closed symbols) as terminal electron acceptors and either 20 mM (circles) or 40 mM (triangles) DIC only (red), DIC and 800 µM calcium (blue), or DIC and 300 µM silica (purple). Arrows indicate the effect of ferrihydrite on k_{obs} and aqueous uranyl speciation. Values of k_{obs} were calculated for individual incubations and presented as the average and standard deviation for each condition (n=3).

results are in line with the effect of uranium toxicity to *S. putrefaciens* evidenced at elevated concentrations of bioavailable uranyl species (Belli et al., 2015). The abrupt decrease in the rate of uranium removal midway through the incubation period in 20 mM DIC-only and silica-amended incubations (Figure 4.1A and Figure 4.1C), conditions with the highest concentrations of bioavailable U(VI) and in which uranium toxicity to *S. putrefaciens* is evident (Figure 4.5), suggests that the change in the rate of uranium removal is also associated with uranium toxicity to cells. Precipitation of U(IV) solids on the cell surface can lead to encrustation and a loss in cell viability (Shao et al., 2014), which may account for the decrease in uranium removal rate following an initial period of more rapid U(VI) bioreduction.

4.5.2 Effect of ferrihydrite on uranium removal

4.5.2.1 Enhanced uranium removal in the presence of ferrihydrite

The increase in the pseudo-first order rate constant (k_{obs}) of uranium removal in the presence of ferrihydrite compared to otherwise identical uranium-only incubations (Figure 4.2A) suggests that in addition to U(VI) bioreduction, iron plays a role in enhancing uranium removal during the first 3-4 days of incubation. An increase in biomass in the presence of additional TEA would lead to enhanced rates of U(VI) bioreduction, however, biomass growth was not detected under the experimental conditions of the present study (data not shown). Alternatively, ferrihydrite may indirectly enhance uranium removal by altering aqueous uranyl speciation and increasing the fraction of bioavailable uranyl non-carbonate species (Belli et al., 2015; Sheng et al., 2011; Ulrich et al., 2011). In the DIC-only and silica-amended incubations, however, the presence of ferrihydrite did not alter

aqueous uranyl speciation significantly (<20%) compared to otherwise identical uranium-only incubations (Table C.4), yet the pseudo-first order rate constants of uranium removal increased by >100% in the 20 mM DIC incubations and ~30% in the 40 mM DIC incubations (arrows in Figure 4.5). Thus, in addition to U(VI) bioreduction, iron played a direct role in enhancing uranium removal during the initial 3-4 days of the incubation. The U:Fe molar ratios of the final solids indicate that 23-38 μM uranium was strongly associated with the solid phase, likely via incorporation into or occlusion by secondary mineralization products of ferrihydrite (Boland et al., 2014a; Massey et al., 2014a; Nico et al., 2009; Roberts et al., 2017; Stewart et al., 2009) or possibly adsorption onto high surface area particles formed during transformation of ferrihydrite (Table C.5). U:Fe molar ratios of the final solids decreased with increasing DIC concentrations and fell on the low end of previously reported values (Massey et al., 2014a; Nico et al., 2009), reflecting the higher concentration of DIC used in the present study and the ability of DIC to limit U(VI) adsorption, a prerequisite for uranium incorporation in the crystal lattice of secondary minerals (Massey et al., 2014a). The final concentration of solid-associated uranium in DIC-only and silica-amended incubations exceeded the initial concentration of adsorbed uranium for each condition (Table C.5), confirming that uranium incorporation/occlusion or enhanced adsorption contributed to the increase in the rate of uranium removal from solution. Enhanced association of uranium with the solid phase, however, cannot account for the >100% increase in the k_{obs} of uranium removal in the presence of 20 mM DIC (Figure 4.2A). These findings indicate that additional processes increased the rate of removal of uranium in the presence of ferrihydrite.

Abiotic reduction of U(VI) by adsorbed or solid phase Fe(II) (Liger et al., 1999; O'Loughlin et al., 2010) may work in consort with enhanced solid-association of uranium to account for increased uranium removal in the presence of ferrihydrite. The initial period of uranium removal coincided with elevated concentrations of dissolved Fe(II), which increase the thermodynamic favorability of U(VI) reduction. Siderite was identified in all incubations containing uranium (Figure 4.3B, D, F, H, J, and L), however, the capacity of siderite to reduce U(VI) is limited (Ithurbide et al., 2009, 2010). Although additional iron phases were not identified by XRD in incubations containing uranium, iron mass balance calculations revealed the presence of amorphous Fe(II)-bearing solids (Figure C.5), and the final color of the 20 mM DIC incubations ranged from dark brown to black (Figure C.9), suggesting the presence of magnetite. The lack of reflections in the XRD patterns indicate that the biogenic Fe(II)-bearing solids formed in the presence of uranium were characterized by decreased crystallinity, short-range ordering, and/or small particle size, similar to biogenic magnetite formed in the presence of humic acid and ΣPO_4^{3-} (Amstaetter et al., 2012). In contrast, the 40 mM DIC incubations amended with U(VI) and ferrihydrite appeared brown-grey (Figure C.10) and amorphous Fe(II)-bearing solids were not detected (Figure C.5), reflecting the absence of magnetite. The larger increase in the pseudo-first order rate constants of uranium removal in the 20 mM DIC incubations compared to the 40 mM DIC incubations indicates more efficient abiotic reduction of U(VI) by Fe(II), likely due to the greater concentration of adsorbed U(VI) at lower DIC concentrations (Behrends and Van Cappellen, 2005) and/or the larger concentration of reactive Fe(II) solids (Figure C.5).

Finally, all incubations amended with calcium were initially supersaturated with respect to calcite, aragonite, and dolomite (data not shown), and the removal of dissolved calcium (Figure C.1A), but not magnesium (Figure C.1B), below the input concentration in both abiotic and biotic incubations amended with ferrihydrite suggests that the ferrihydrite surface initiated heterogeneous precipitation of an amorphous calcium carbonate phase (Mejri et al., 2015), which was not identified by XRD (Figure 4.3E-H). The removal of calcium from solution over the course of the uranium-only incubation amended with 40 mM DIC but not the otherwise identical 20 mM DIC incubation and corresponding abiotic controls (Figure C.1) suggests that U(IV) solids may also initiate calcium carbonate precipitation under highly saturated conditions. Although incubations were also supersaturated with respect to magnesite (data not shown), the slow kinetics of low-temperature magnesium carbonate precipitation likely kept magnesium in solution (Figure C.1B) (Power et al., 2017). Regardless of the exact mechanism, the removal of calcium from solution more than tripled the fraction of uranyl non-carbonate species compared to uranium-only incubations amended with calcium (Table C.4). These findings suggest that the increase in the k_{obs} of uranium removal associated with ferrihydrite in the 40 mM DIC calcium-amended incubations (Figure 4.2A) was due, at least in part, to an increase in the fraction of bioavailable U(VI). Abiotic reduction of U(VI) by adsorbed Fe(II) on the calcium carbonate surface (Chakrabrty et al., 2010) or the formation of a more reactive Fe(II) solid in the presence of calcium (e.g., green rust) (Kukkadapu et al., 2005) may also contribute to enhanced uranium removal. The negligible effect of ferrihydrite on the k_{obs} of uranium removal in the 20 mM DIC calcium-amended incubation (Figure 4.2A) might be due to a combination of uranium toxicity to *S. putrefaciens* at the elevated

concentration of uranyl non-carbonate species and enhanced abiotic U(VI) reduction by Fe(II) (Figure 4.5).

4.5.2.2 Abiotic U(IV) oxidation by Fe(III)

Following its initial removal period, a rebound in dissolved uranium was observed in almost all incubations containing ferrihydrite, except for the 20 mM DIC-only incubation (Figure 4.1A-C). In incubations amended with 40 mM DIC, the large rebound in uranium concentration coincided with an increase in total Fe(II), which was not observed in the ferrihydrite-only incubations under the same conditions (Figure 4.1D-F). Taken together, these data suggest that U(IV) solids were oxidized and solubilized by Fe(III).

Although Fe(II) production during the initial days of the calcium-amended incubations was significantly higher in the presence of uranium compared to otherwise identical ferrihydrite incubations (Figure 4.1E), additional evidence of U(IV) oxidation (e.g., decreased rate of uranium removal or rebound in dissolved uranium) is not observed during this period (Figure 4.1B). Low rates of microbial ferrihydrite respiration in the ferrihydrite-only incubations amended with calcium were attributed to precipitation of calcium carbonate on the cell (Zeng and Tice, 2014) or ferrihydrite surface (Mejri et al., 2015), and it was therefore speculated that this mechanism is not operative in the presence of uranium. The kinetic model supports this interpretation as time series of total Fe(II) in the calcium-amended incubations were successfully reproduced using the same rate constants for microbial ferrihydrite respiration as the DIC-only incubations (Figure C.7, Table 4.3), however, direct evidence of these processes was not obtained.

Although dissolved Fe(III) under the form of bacterially-produced soluble organic-Fe(III) complexes (Taillefert et al., 2007) could be responsible for the oxidation of U(IV) (Stewart et al., 2013), the presence of uranium did not systematically affect dissolved Fe(III) concentrations compared to the ferrihydrite-only incubations (Figure C.4), suggesting that ferrihydrite was the primary oxidant of dissolved or nanoparticulate U(IV) (Ginder-Vogel et al., 2010; Wang et al., 2013c). Irrespective of the mechanism, the additional increase in total Fe(II) produced from this reaction is nearly an order of magnitude larger than the corresponding increase in dissolved uranium, indicating that uranium is cycled multiple times between reduction by *S. putrefaciens* and oxidation by Fe(III). Previous studies have demonstrated electron shuttling of uranium between MRB and Fe(III)-bearing clays (Luan et al., 2014; Zhang et al., 2009; Zhang et al., 2011) or ferrihydrite (Nevin and Lovley, 2000), and between sulfate-reducing bacteria and Fe(III) oxides (Sani et al., 2005), although in some cases an increase in dissolved uranium was only observed after complete consumption of the electron donor (Spycher et al., 2011). The results of the present study confirm that uranium is an effective electron shuttle between MRB and Fe(III) oxides and reveal that oxidative dissolution of U(IV) by ferrihydrite can be significant even under iron-reducing conditions and in the presence of excess electron donor.

4.5.3 Geochemical controls of iron as a reductant or oxidant of uranium

The kinetic model was able to reproduce the dominant features of dissolved uranium time series as long as the thermodynamics of abiotic uranium-iron redox cycling was accounted for (Figure 4.4, Figure C.7, and Figure C.8). However, thermodynamic data for amorphous uraninite was not sufficient to predict the oxidation of U(IV) by ferrihydrite.

The potential of the U(VI)/UO_2(am) redox couple was always greater than the $Fe(OH)_3$/Fe(II) redox couple once dissolved Fe(II) was detected in solution (not shown), and consequently, the ΔG_r of the oxidation of uraninite by ferrihydrite was predicted to be thermodynamically unfavorable (i.e., $\Delta G_r > 0$). Decreasing the standard state U(VI)/UO_2(am) redox potential (E_h^0) by 84 mV was necessary to reproduce the incubation data using the kinetic model, suggesting that the non-uraninite U(IV) solid formed in the incubations is a stronger reductant than amorphous uraninite. Indeed, less stable monomeric U(IV) solids ($U(IV)_{mono}$) (Cerrato et al., 2013), rather than uraninite, were presumed to form preferentially in the incubations as a result of the 100 µM phosphate included in the growth medium (Boyanov et al., 2011; Stylo et al., 2013). These results highlight the paucity of thermodynamic data for monomeric U(IV) solids and indicate the stability of monomeric U(IV) solids produced by U(VI) bioreduction in contaminated aquifers (Alessi et al., 2014a; Bargar et al., 2013) cannot be predicted accurately.

The abrupt transition from U(VI) reduction to U(IV) oxidation in the incubations amended with both ferrihydrite and U(VI) implies a sudden shift in potential of either the U(VI)/$U(IV)_{mono}$ or $Fe(OH)_3$/Fe(II) redox couple which altered the role of iron from a reductant to an oxidant of uranium. Amongst the different treatments, DIC concentrations had the largest effect on the rate and extent of U(IV) oxidation (Figure 4.1A-C), as high DIC concentrations enhance the formation of uranyl carbonate species which are more thermodynamically favorable as U(IV) oxidation products (Ginder-Vogel et al., 2006; Ginder-Vogel et al., 2010). The overall E_h of the U(VI)/$U(IV)_{mono}$ redox couple, however, was unaffected by DIC concentrations (Figure 4.6A-C), suggesting that the enhanced U(IV) oxidation at the highest DIC concentration was instead due to a shift in the potential

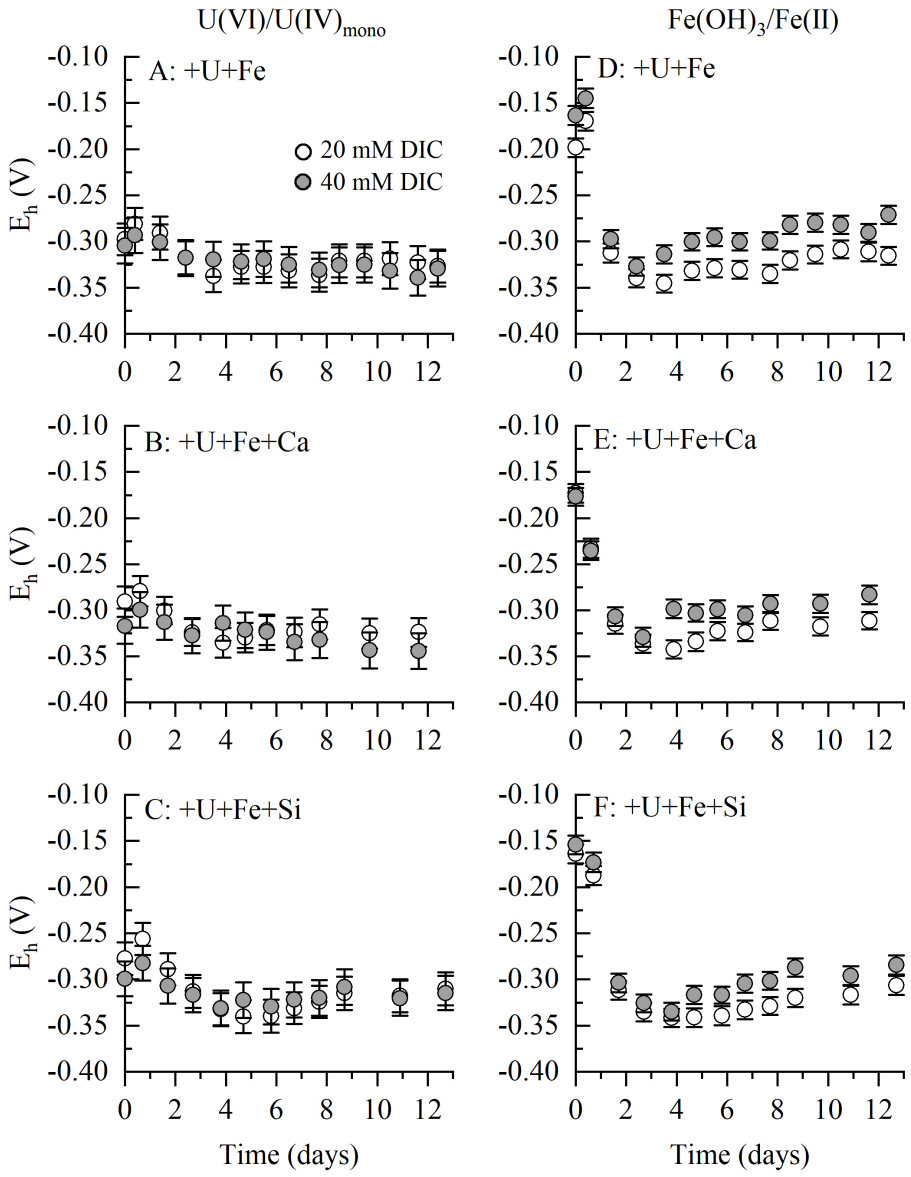

Figure 4.6 Time series of calculated (A-C) U(VI)/U(IV)$_{mono}$ and (D-F) Fe(OH)$_3$/Fe(II) redox potentials (E$_h$) at each sampled time point in incubations of *S. putrefaciens* amended with 5 mM ferrihydrite and 180 µM U(VI), and either 20 mM (open) or 40 mM (closed) (A and D) DIC only, (B and E) DIC and 800 µM calcium, or (C and F) DIC and 300 µM silica. Symbols and error bars represent the average and standard deviation of 10,000 Monte Carlo sampled E$_h$ values of individual aquous U(VI) and Fe(II) complexes.

of the $Fe(OH)_3$/Fe(II) redox couple over the course of the incubations in proportion to the concentration of dissolved Fe(II) (Figure 4.6D-F). In incubations amended with 40 mM DIC, rebounds in dissolved uranium (Figure 4.1A-C) coincided with a sudden decrease in dissolved Fe(II) (Figure 4.1G-I) and a corresponding increase in the potential of the $Fe(OH)_3$/Fe(II) redox couple (Figure 4.6D-F). In incubations amended with 20 mM DIC, the removal of Fe(II) from solution and the increase in the $Fe(OH)_3$/Fe(II) E_h was slower and, as a result, the rebound in dissolved uranium was significantly diminished in magnitude (Figure 4.1A) and shifted later during the incubations (Figure 4.1B-C), consistent with dissolved Fe(II) limiting the oxidation of U(IV) by ferrihydrite (Senko et al., 2005). Thus, under the present experimental conditions, the concentration of dissolved Fe(II) appears to be the primary control of the coupled abiotic redox cycling of uranium and iron, and the effect of DIC concentration on the removal rate of Fe(II) from solution accounts for the observed effect of DIC concentrations on U(IV) oxidation.

The removal of dissolved Fe(II) from solution was responsible for the initiation of U(IV) oxidation by ferrihydrite, and in the 40 mM DIC incubations, the faster rate of dissolved Fe(II) removal was attributed to the more rapid precipitation of siderite (Table 4.3). Once U(IV) oxidation was initiated, sustained oxidation of U(IV) in *S. putrefaciens* batch incubations was limited by the consumption of ferrihydrite via microbial respiration and Fe(II)-induced secondary mineralization. The kinetic model revealed that the depletion of ferrihydrite was responsible for limiting the rebound in dissolved uranium in the 40 mM DIC-only incubations (Figure 4.4), whereas silica decreased the rates of ferrihydrite respiration and secondary mineralization (Table 4.3) (Jones et al., 2009) which preserved ferrihydrite and sustained U(IV) oxidation over a longer period of time (Figure C.8). In the

calcium-amended incubations with 40 mM DIC, however, the model overestimated the duration of U(IV) oxidation (Figure C.7B), perhaps because only a fraction of ferrihydrite was available to react with U(IV) due to surface passivation by calcium carbonate precipitates. Similarly, the model was unable to reproduce the rebound in dissolved uranium in the 20 mM DIC calcium- and silica-amended incubations because ferrihydrite was predicted to be consumed before U(IV) oxidation became thermodynamically favorable (Figure C.7 and Figure C.8). Ferrihydrite consumption in the model may have been overestimated, as surface passivation and aggregation may have decreased the bioavailability of ferrihydrite (Bonneville et al., 2006; Liu et al., 2001). Overall, these results underscore the complexity of the uranium-iron-MRB system and the need to consider the abundance and reactivity of solid Fe(III) when investigating the stability of reduced U(IV) solids.

4.5.4 Implications for uranium bioremediation

Oxidation of U(IV) is a significant concern for remediation strategies which rely upon sequestration of uranium as reduced U(IV) solid phases. Natural amorphous Fe(III) oxides (e.g., ferrihydrite) are more recalcitrant towards transformation into crystalline phases than pure, synthetic ferrihydrite suggests (Stewart et al., 2015; ThomasArrigo et al., 2017), allowing Fe(III) to serve as an oxidant of U(IV) even after years of continuous reducing conditions (Wan et al., 2005; Wan et al., 2008). For example, electron donor injection into the subsurface at the US Department of Energy (DOE) Integrated Field Research Challenge (IFRC) site in Rifle, Colorado leads to the accumulation of DIC and Fe(II) (Williams et al., 2011), products of microbial Fe(III) respiration, which may have contrasting effects on the thermodynamic favorability of U(IV) oxidation by ferrihydrite

(Figure 4.7). An increase in DIC concentration decreases the E_h of the U(VI)/UO_2(am) redox couple as aqueous uranyl speciation shifts from non-carbonate to carbonate and ternary carbonate uranyl species. This effect, however, is limited above 20 mM DIC as the uranyl ion becomes saturated with carbonate ligands (Figure 4.7A). Simultaneously, the E_h of the $Fe(OH)_3$/Fe(II) redox couple is mostly unaffected by DIC concentrations (neglecting the precipitation of Fe(II) carbonate solids). Instead, the concentration of dissolved Fe(II) is the primary determinant of the $Fe(OH)_3$/Fe(II) redox potential across all DIC concentrations (Figure 4.7A). Taken together, both the concentration of DIC and dissolved Fe(II) act in consort to control the Gibbs energy of reaction (ΔG_r) for the oxidation of U(IV) by ferrihydrite at low concentrations of DIC, whereas above a DIC concentration of ~20 mM, the ΔG_r is controlled primarily by the concentration of dissolved Fe(II) (Figure 4.7B). Groundwater DIC concentrations up to ~40 mM have been measured following biostimulation at the IFRC Rifle site due to microbial activity (Williams et al., 2011) or due to a bicarbonate injection prior to biostimulation (Long et al., 2015). Regardless of the source of DIC, the results of the current study indicate that under these field conditions, dissolved Fe(II) concentration primarily controls the stability of U(IV) solid phases towards oxidation by Fe(III) oxides, and maintaining elevated dissolved Fe(II) concentrations may be required to ensure the long-term stability of U(IV) solids.

4.6 Conclusions

The similar potentials of the $Fe(OH)_3$/Fe(II) and U(VI)/U(IV) redox couples allow iron to act as both a reductant and an oxidant of uranium which may potentially enhance or hinder bioremediation efforts to immobilize uranium as reduced U(IV) solid phases. The results of the present study indicate that above a DIC concentration of 20 mM, the

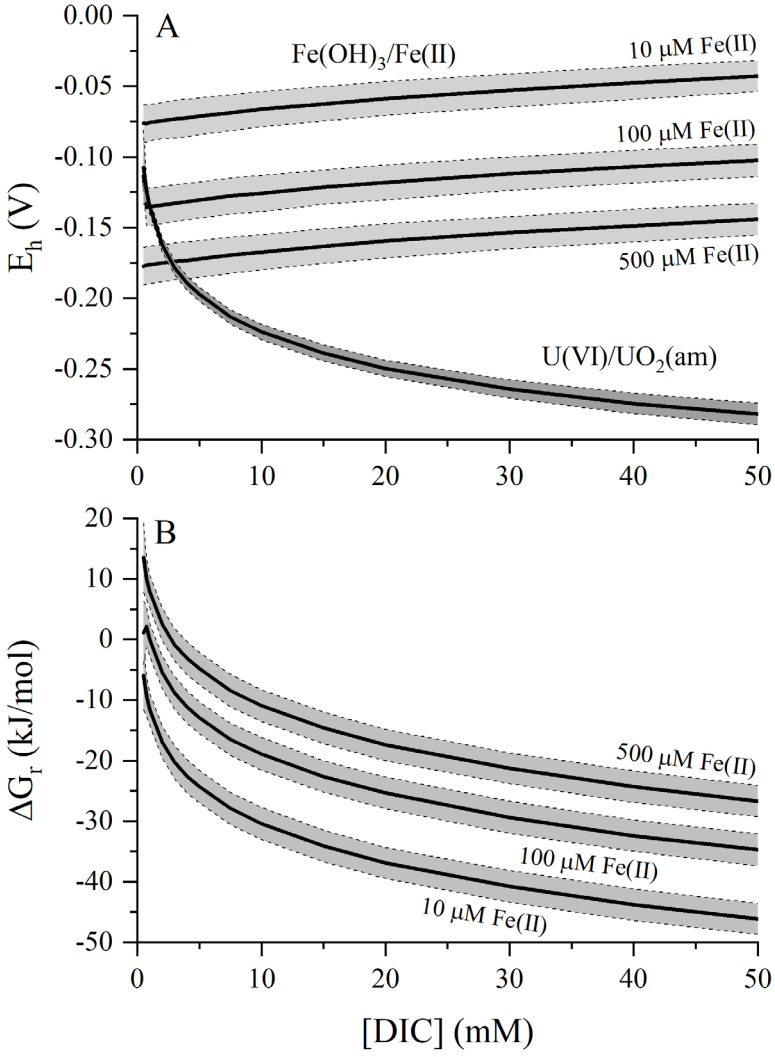

Figure 4.7 Calculated (A) potentials (E_h) of the $Fe(OH)_3$/Fe(II) and U(VI)/UO_2(am) redox couples and (B) the Gibbs energy of reaction (ΔG_r) of the oxidation of amorphous uraninite by ferrihydrite as a function of DIC concentration at the US Department of Energy (DOE) Integraded Field Research Challenge (IFRC) site in Rifle, Colorado. Calculations were conducted at pH 7 using a total U(VI) concentration of 1 µM, total Fe(II) concentrations of 10, 100, and 500 µM, and background Rifle groundwater composition (Zachara et al., 2013). Solid lines and shaded envelopes represent the average and standard deviation of 10,000 Monte Carlo sampled E_h and ΔG_r values.

concentration of dissolved Fe(II) regulates the potential of the $Fe(OH)_3$/Fe(II) redox couple and controls uranium-iron redox cycling. Secondary influences on uranium-iron redox cycling include concentrations of DIC, calcium, and silica, which may promote U(IV) oxidation by Fe(III) via enhanced removal of Fe(II) from solution (e.g., precipitation of siderite) or sustain the oxidation of U(IV) by inhibiting ferrihydrite consumption through microbial reduction and secondary mineralization. The kinetic model developed as part of this study highlights the complexity of the uranium-iron-MRB system and the importance of considering the thermodynamic favorability of abiotic uranium-iron redox reactions in reactive transport models. In addition, thermodynamic data for amorphous uraninite was insufficient to accurately predict the stability of monomeric U(IV) solids in the presence of ferrihydrite, emphasizing the need for constraining the geochemical properties of this phase and recently identified U(IV)-surface complexes (Alessi et al., 2014b; Bone et al., 2017; Wang et al., 2015) in future studies. Given the ubiquity and recalcitrance of amorphous Fe(III) oxides in the environment, understanding the geochemical controls of the coupled biogeochemical cycling of uranium and iron will be necessary to design successful, site-specific remediation strategies and ensure the long-term stability of U(IV) solids.

4.7 Acknowledgements

This research was supported by the US Department of Energy Subsurface Biogeochemical Research (SBR) program (Grant No. DE-SC0005520) and the US Environmental Protection Agency (EPA) Science to Achieve Results (STAR) Graduate Fellowship to KMB (Assistance Agreement No. FP-91767401-0). This publication has not been formally reviewed by the EPA, and the views expressed herein are solely those of the

authors. This work was performed in part at the Georgia Tech Institute for Electronics and Nanotechnology, a member of the National Nanotechnology Coordinated Infrastructure, which is supported by the National Science Foundation (Grant ECCS-1542174).

CHAPTER 5. EFFECTS OF ALUMINUM-SUBSTITUTED FERRIHYRDITE ON THE MICROBIALLY MEDIATED REDOX CYCLING OF URANIUM

5.1 Abstract

Natural iron oxy(hydr)oxides are rarely pure, and impurities in the mineral structure affect the biogeochemical cycling of iron by altering its biological and chemical reactivity. Iron can serve as both a reductant of U(VI) and an oxidant of U(IV) and therefore affects remediation efforts which promote microbial reduction of U(VI) and subsequent precipitation of uranium as insoluble U(IV) solids. In this study, bioreduction incubations with *Shewanella putrefaciens* were conducted with U(VI) and/or (Al-)ferrihydrite to investigate the effects of aluminum substitution on the removal of uranium from solution. By preserving ferrihydrite against consumption via microbial reduction and secondary mineralization, aluminum substitution enhanced the abiotic oxidation of U(IV) by ferrihydrite and decreased the pseudo-first order rate constant of uranium reduction. Abiotic incubations demonstrated that U(IV) oxidation rate was independent of the Al content of ferrihydrite, indicating that the primary effect of Al substitution on uranium-iron redox cycling was altering the $Fe(OH)_3$/Fe(II) redox potential and increasing the thermodynamic favorability of the oxidation of U(IV) solids by ferrihydrite. These results indicate that naturally occurring ferrihydrite may be a more effective and longer-lived oxidant of U(IV) than previously thought.

5.2 Introduction

Iron oxy(hydr)oxides (iron oxides hereafter) are ubiquitous in soils and sediments (Cornell and Schwertman, 2003; Jambor and Dutrizac, 1998) and play a critical role in the redox cycling and transport of subsurface contaminants such as uranium, a widespread contaminant at former US Department of Energy mining and processing sites (Riley et al., 1992; Zachara et al., 2013). Iron oxides limit the mobility of uranium via adsorption of uranyl species (U(VI)) (Fox et al., 2012; Stewart et al., 2010; Waite et al., 1994), enhancing reduction of soluble U(VI) by Fe(II) to insoluble U(IV) solids (Latta et al., 2012b; Liger et al., 1999; O'Loughlin et al., 2010), and incorporation of U(VI)/U(V) into the crystal lattice of secondary mineralization products (Boland et al., 2014a; Massey et al., 2014a; Roberts et al., 2017; Stewart et al., 2009). Stimulation of native, subsurface metal-reducing bacteria (MRB) via electron donor injection has shown promise as a remediation strategy (Long et al., 2015; Williams et al., 2011) with the goal of immobilizing uranium as sparingly soluble U(IV) solid phases formed via a combination of microbial U(VI) reduction and abiotic U(VI) reduction by reduced respiration products, such as Fe(II) and ΣH_2S (Bargar et al., 2013; Shiel et al., 2016). Reoxidation and dissolution of U(IV) solids, however, poses a challenge to this approach, and Fe(III) oxides have been implicated as oxidants of U(IV) (Ginder-Vogel et al., 2006; Ginder-Vogel et al., 2010), even under sustained reducing conditions (Wan et al., 2005; Wan et al., 2008). Thus, understanding the biogeochemical role of iron in uranium redox cycling is essential to assess the feasibility of U(VI) bioreduction at contaminated sites and predict the fate of uranium following biostimulation of the subsurface.

Ferrihydrite, a highly reactive, poorly crystalline iron oxide, is generally thought to be short lived in subsurface environments as pure, synthesized ferrihydrite is rapidly respired by iron-reducing bacteria (Bonneville et al., 2009; Roden and Zachara, 1996) and converted to more crystalline phases via Fe(II)-induced secondary mineralization (Boland et al., 2014b; Hansel et al., 2005; Hansel et al., 2003; Zachara et al., 2002). Natural ferrihydrite, however, is highly impure as organic and inorganic solutes from the surrounding environment co-precipitate with and/or substitute for Fe^{3+} in the crystal lattice during formation (Cismasu et al., 2011; Cornell and Schwertman, 2003; Stewart et al., 2015). As a result, natural ferrihydrite is more recalcitrant toward microbial reduction (Ekstrom et al., 2010) and secondary mineralization (Hansel et al., 2011; Shimizu et al., 2013; ThomasArrigo et al., 2017), which extends its residence time in the environment and influences its role in the cycling of contaminants, including uranium. For instance, Al- and Si-substituted ferrihydrite favor adsorption of U(VI) as the dominant uranium removal mechanism during Fe(II)-induced secondary mineralization (Boland et al., 2011; Massey et al., 2014b), whereas pure ferrihydrite favors reduction and incorporation of U(V) into secondary mineralization products (Boland et al., 2014a), which is more stable against fluctuating geochemical conditions (Stewart et al., 2009). Despite the importance of MRB on the redox cycling of uranium and iron, the effects of ferrihydrite impurities on the microbially mediated redox cycling of uranium remains unexplored. As structural impurities preserve ferrihydrite against consumption by biogeochemical processes (Ekstrom et al., 2010; Hansel et al., 2011; Jones et al., 2009; Masue-Slowey et al., 2011; Vempati and Loeppert, 1989) and have been demonstrated to enhance the oxidative reactivity of ferrihydrite (Jentzsch and Penn, 2006), natural ferrihydrite may serve as a

longer-lived and more effective oxidant of U(IV) than suggested by studies using pure ferrihydrite. In this study, the effects of ferrihydrite Al impurities, the most common iron oxide impurity (Cornell and Schwertman, 2003), on the redox cycling of uranium and iron were investigated in bioreduction incubations with *Shewanella putrefaciens*, a model MRB. It was hypothesized that Al substitution decreases net uranium removal from solution via microbial U(VI) reduction by enhancing the rate of abiotic oxidative dissolution of U(IV) solids by ferrihydrite and sustaining U(IV) oxidation by preserving ferrihydrite against consumption via microbial reduction and secondary mineralization.

5.3 Materials and Methods

5.3.1 Synthesis of 2-line (Al-)ferrihydrite

Pure and Al-substituted 2-line ferrihydrite (called ferrihydrite hereafter) was synthesized with 0, 5, and 10 mol% Al (mol% = [Al]/([Al]+[Fe])×100) by rapidly titrating (4 mL/min) a sterile solution of $AlCl_3 \cdot 6H_2O$ and $FeCl_3 \cdot 6H_2O$ of the desired molar ratio to pH 7.5 with 1 N NaOH (Cismasu et al., 2012). All chemicals used in this study were of high purity. The resulting suspension was washed three times with sterile Milli-Q water and stored at room temperature for no more than 5 days prior to inoculation. The Al content of the stock suspensions was confirmed to be within 10% of the desired amount by dissolving the solid in 1 N HNO_3 and measuring total Al and Fe as described below. X-ray diffraction (described below) confirmed the purity of the stock suspensions (Figure D.1).

5.3.2 Bioreduction incubations

Batch incubations were conducted with *Shewanella putrefaciens* strain 200, a model MRB capable of utilizing U(VI) (Wade and DiChristina, 2000) and solid Fe(III) oxides (DiChristina and Delong, 1994) as terminal electron acceptors (TEAs). Prior to all bioreduction incubations, *S. putrefaciens* was grown anaerobically on a defined salt medium (modified M1 medium, Table S1) (Myers and Nealson, 1988) amended with lactate (15 mM) and fumarate (60 mM) as the electron donor and acceptor, respectively. Cells were harvested during late-log phase and washed once with growth medium prior to inoculation. Triplicate bioreduction incubations were conducted in 160 mL serum bottles containing 120 mL total volume of the modified M1 medium (Table D.1) amended with either 20 or 40 mM $NaHCO_3$. Dissolved U(VI) (180 μM uranyl acetate, Spectrum) and/or (Al-)ferrihydrite (5 mM) were supplied as TEAs and lactate (15 mM) served as the electron donor. The solution pH was buffered with 15 mM PIPES, and minor pH adjustments throughout the incubation with small amounts of 1 M HCl or NaOH ensured an average pH of 8.0±0.1. Incubations were inoculated at t=0 with an initial cell concentration of approximately 2×10^7 cell/mL. Serum bottles were individually wrapped in aluminum foil to prevent photochemical reactions, continually mixed with magnetic stir bars (290 rpm), and kept inside an anaerobic chamber (26°C; 5% H_2, 95% N_2 atmosphere) where all sampling and oxygen-sensitive analyses took place. Unfiltered subsamples were used to measure pH, total Fe(II), and ascorbate-extractable solid-phase iron. The remaining subsamples were filtered (0.22 μm PES membrane, Tisch Scientific) to measure dissolved Fe(II) and total dissolved uranium, iron, and aluminum.

5.3.3 Abiotic U(IV) oxidation incubations

Uranium-only incubations containing 40 mM DIC and otherwise identical to those described above were inoculated with *S. putrefaciens*, incubated for 18 days to reduce U(VI), then autoclaved to inactivate live cells, and allowed to cool to room temperature. Duplicate, sterilized incubations containing biogenic U(IV) solids were then amended with 1 mM (Al-)ferrihydrite from degassed stock suspensions to initiate abiotic U(IV) oxidation by Fe(III). Identical incubations amended with the same volume of anoxic Milli-Q water served as iron-free controls, and incubations containing autoclaved, fumarate-grown cells (approximately 2×10^7 cell/mL) amended with 1 mM (Al-)ferrihydrite served as uranium-free controls. Total dissolved uranium and ferrozine-extractable Fe(II) were measured over time. Ferrozine-extractable Fe(II), which includes dissolved and adsorbed Fe(II), was chosen to determine the kinetics of abiotic U(IV) oxidation by (Al-)ferrihydrite over HCl-extractable Fe(II), total dissolved uranium, or dissolved Fe(II) due to analytical artifacts associated with HCl-extractable Fe(II) in the presence of U(IV) (described below) and the adsorption of U(VI) and Fe(II) onto ferrihydrite (Ginder-Vogel et al., 2006; Ginder-Vogel et al., 2010).

5.3.4 Analytical techniques

Total dissolved uranium (U_d) and aluminum (Al_d) were measured by ICP-MS (Agilent 7500a series) in filtered subsamples diluted in 2% trace metal grade HNO_3 (Fisher Scientific, Inc.). Total Fe(II) ($Fe(II)_T$) was quantified by dissolving an unfiltered subsample in 1 M HCl for 24 hours in the dark in the anaerobic chamber and measuring Fe(II) by the ferrozine assay (Stookey, 1970). $Fe(II)_T$ measurements were corrected for reduction of Fe(III) by U(IV) during the acidification step as previously described (Belli and Taillefert, In review). Dissolved Fe(II) ($Fe(II)_d$) was measured in filtered subsamples by the ferrozine

assay, whereas total initial iron ($Fe_{T,0}$) and total dissolved iron (Fe_{Td}) were measured in unfiltered and filtered subsamples by the ferrozine assay following reduction with hydroxylamine (0.2 M hydroxylamine, 0.1 M HCl). Dissolved Fe(III) ($Fe(III)_d$) was calculated by difference from measurements of Fe_{Td} and $Fe(II)_d$ (Viollier et al., 2000). Ferrozine-extractable Fe(II) ($Fe(II)_{ext}$) was measured in abiotic U(IV) oxidation incubations as described previously (Ginder-Vogel et al., 2010), and the extraction procedure recovered between 87 and 105% of dissolved and adsorbed Fe(II) regardless of the ferrihydrite Al content (Figure D.2). Solution pH was measured using a double-junction pH electrode (Orion). Amorphous solid-phase iron was selectively extracted from pelleted solids of unfiltered aliquots by a citrate-ascorbate solution for 24 hours in the dark and quantified by detection of Fe(II) in the supernatant using the ferrozine assay (Kostka and Luther, 1994).

At the end of the incubations, the final solid phase products were collected via filtration (0.22 μm PES membrane, Millipore), rinsed with anoxic Milli-Q water, dried under the anaerobic chamber atmosphere, finely ground using a mortar and pestle, and identified by powder X-ray diffraction (XRD). Diffraction data of samples mounted on a zero background holder were collected on a PANalytical Empyrean diffractometer (Cu Kα radiation). Phase identification was performed with HighScore Plus using reference diffraction patterns from the PDF-4+ database (ICDD, 2015). Finally, to determine U:Fe molar ratios of the final solid phase, 10 mg of the powdered solid was extracted with an oxygenated solution of 1 M $NaHCO_3$ (pH 8.7) on a rotary wheel for 48 hours and washed twice with aerated 0.1 M $NaHCO_3$ to remove solid and adsorbed uranium (Alessi et al.,

2012). The washed pellet was digested in 4 M HNO_3 and analyzed for total Fe and U as described above.

5.3.5 Kinetic calculations

The initial rates of U_d removal and Fe(III) reduction in bioreduction incubations with *S. putrefaciens* are the summation of a suite of parallel reactions which can be represented by pseudo-first order rate laws (Belli and Taillefert, In review). Pseudo-first order rate constants (k_{obs}) of U_d removal and Fe(III) reduction were determined from the slope of the linearized, integrated first-order rate equation of consumption of U_d and Fe(III) oxides (Equation 5.1, where $[S]_0$ and $[S]_t$ are the concentration of either U_d or total Fe(III) at t=0 and time *t*, respectively) over the time interval following the lag phase that conformed to the pseudo-first order rate law (i.e., the smallest R^2 value of the linear regression of the data represented using Equation 5.1). The average k_{obs} for each condition was calculated from the individual values determined for triplicate incubations.

$$\ln\left(\frac{[S]_t}{[S]_0}\right) = -k_{obs} \cdot t \tag{5.1}$$

Rates of abiotic U(IV) oxidation were calculated in accordance with the stoichiometry of Equation 5.2 from rates of Fe(II) production determined from the slope of the linear regression of $Fe(II)_{ext}$ concentrations represented versus time. The average rate for each ferrihydrite Al content was calculated from the individual rates determined for duplicate incubations.

$$U^{4+}_{mono}(s) + 2Fe(OH)_3(s) + 2H^+ \rightarrow UO_2^{2+} + 2Fe^{2+} + 4H_2O \tag{5.2}$$

5.3.6 Thermodynamic calculations

The Gibbs free energy of reaction (ΔG_r) for the oxidation of U(IV) by Fe(III) was calculated at each time point to assess the thermodynamic favorability of the reaction throughout the incubations. First, reduction potentials (E_h) were calculated for half-reactions of U(VI) reduction to monomeric U(IV) ($U(IV)_{mono}$) and ferrihydrite ($Fe(OH)_3$) reduction to Fe(II) for each aqueous U(VI) and Fe(II) complex. Monomeric U(IV) was assumed to be the dominant U(IV) solid present due to the presence of phosphate in the incubation medium (Stylo et al., 2013), and the redox potential of $U(IV)_{mono}$ was previously determined to be approximately 84 mV lower than published values for amorphous uraninite under the geochemical conditions of this study (Belli and Taillefert, In review). Equilibrium concentrations of the necessary species were calculated in PHREEQC using pH and measured solution composition as inputs. The included PHREEQC database was updated with the most recently published thermodynamic data for aqueous and solid-phase U(VI), U(IV), Fe(III), and Fe(II) compounds (Dong and Brooks, 2006; Guillaumont et al., 2003; Gustafsson, 2012). A Monte Carlo approach was used to calculate ΔG_r to account for the effect of aqueous U(VI) and Fe(II) speciation on the E_h of the U(VI)/$U(IV)_{mono}$ and $Fe(OH)_3$/Fe(II) redox couples (Belli and Taillefert, In review). 10,000 Monte Carlo sampled pairs of E_h values for individual aqueous U(VI) and Fe(II) complexes were used to calculate the average and standard deviation of the ΔG_r at each time point. Discrete sampling probabilities were prescribed to the E_h of each aqueous U(VI) and Fe(II) complex at each time point based on the normalized equilibrium concentration of the complex to the total dissolved concentration of U(VI) and Fe(II). The ΔG_r of $U(IV)_{mono}$ oxidation by ferrihydrite was calculated according to Equation 5.3,

$$\Delta G_r = -2 \cdot F \cdot \left(E_{h,ox} - E_{h,red}\right) \quad (5.3)$$

where F is Faraday's constant and $E_{h,ox}$ and $E_{h,red}$ are the potentials of the $Fe(OH)_3$/Fe(II) and $U(VI)/U(IV)_{mono}$ half-reactions, respectively.

5.4 Results

5.4.1 Bioreduction incubations amended with U(VI) and ferrihydrite as sole TEAs

When U(VI) was provided as the sole TEA in bioreduction incubations with *S. putrefaciens*, the decrease in total dissolved uranium (U_d) commenced after a brief 1 day lag phase, whereas U_d remained constant at the initial concentration in abiotic controls (Figure 5.1A). Uranyl carbonate species and the ternary $MgUO_2(CO_3)_3^{2-}$ complex dominated aqueous uranyl speciation at both DIC concentrations due to the alkaline pH and the background Mg^{2+} included in the growth medium (Table D.2). Regardless of the DIC concentration, pseudo-first order rate constants (k_{obs}) of uranium removal were similar (Figure 5.2A), and >90% of uranium was removed from solution after nearly 13 days.

Regardless of its Al content, when (Al-)ferrihydrite was provided as the sole TEA to *S. putrefaciens*, total Fe(II) ($Fe(II)_T$) was produced initially at a fast rate, but at a slower rate after 2-4 days and for the duration of the incubations (Figure 5.1D-F). The final extent of $Fe(II)_T$ production was inversely proportional to the ferrihydrite Al content (-4.4±0.5% per mol% Al), yet was unaffected by DIC concentration. Across all incubation conditions, the majority of Fe(II) was associated with the solid phase (Figure D.3). In incubations with 0 and 10 mol% Al-ferrihydrite, the concentration of dissolved Fe(II) ($Fe(II)_d$) reached a maximum in the first 4 days then decreased to a steady state

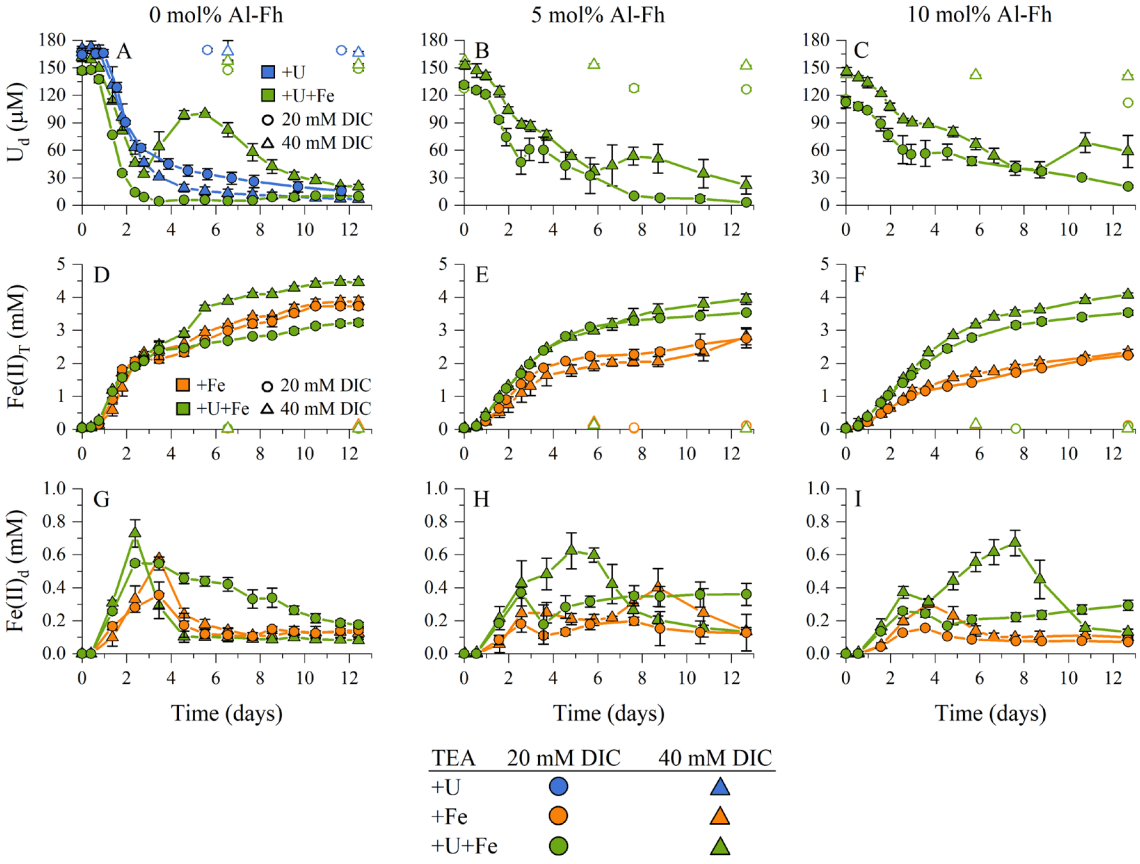

Figure 5.1 Time series of (A-C) total dissolved uranium (U_d), (D-F) total Fe(II) ($Fe(II)_T$), and (G-I) dissolved Fe(II) ($Fe(II)_d$) in incubations amended with either 20 mM (circles) or 40 mM (triangles) DIC and either 180 μM U(VI) (blue), 5 mM of 0 (left), 5 (center), or 10 (right) mol% Al-ferrihydrite (orange), or both (green) as terminal electron acceptors. Filled symbols and lines represent biotic incubations with *S. putrefaciens* whereas open symbols represent abiotic controls. Symbols and error bars represent the average and standard deviation from triplicate incubations.

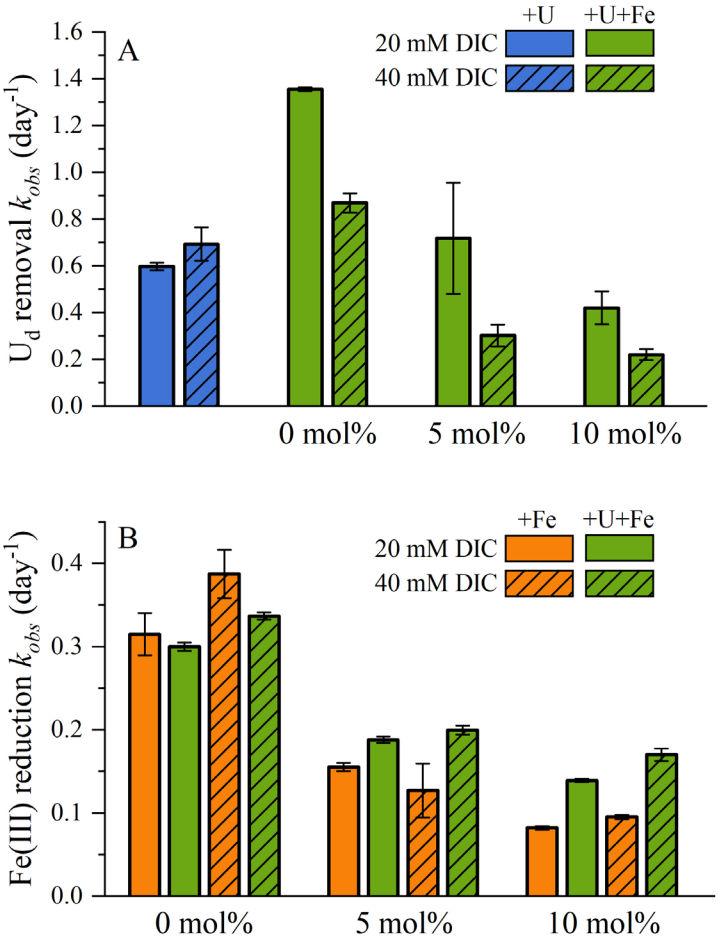

Figure 5.2 Pseudo-first order rate constants (k_{obs}) of the initial (A) removal of total dissolved uranium (U_d) and (B) production of total Fe(II) ($Fe(II)_T$) in incubations of *S. putrefaciens* amended with either 180 µM U(VI) (blue), 5 mM 0, 5, or 10 mol% Al-ferrihydrite (orange), or both (green) as terminal electron acceptors, and either 20 mM (solid bars) or 40 mM (hashed bars) DIC. Values of k_{obs} were calculated for individual incubations and presented as the average and standard deviation for each condition (n=3).

concentration (Figure 5.1G, I), whereas $Fe(II)_d$ concentrations in incubations with 5 mol% Al-ferrihydrite fluctuated and reached maximum concentrations later in the incubations (Figure 5.1H). Maximum $Fe(II)_d$ concentrations were higher in the 40 mM DIC incubations and decreased with increasing Al content, although the steady state $Fe(II)_d$ values were similar. Across all incubations, $Fe(III)_d$ was produced to a maximum concentration <50 μM then consumed over the course of the incubation (Figure D.4). In incubations amended with Al-ferrihydrite, dissolved Al (Al_d) never exceeded 5 μM and remained relatively constant throughout the incubation (Figure D.5). Pseudo-first order rate constants (k_{obs}) of Fe(III) reduction were inversely proportional to the Al content of ferrihydrite (-7.5±1.4% per mol% Al) and largely unaffected by DIC concentration, although rate constants were slightly higher in the 40 mM DIC incubations amended with 0 and 10 mol% Al-ferrihydrite (Figure 5.2B).

5.4.2 Bioreduction incubations amended with both U(VI) and ferrihydrite

When ferrihydrite was included with U(VI) in bioreduction incubations, adsorption of U(VI) accounted for the removal of 5-32% of U_d prior to inoculation (Figure 5.1A-C). Adsorbed uranium (U_{ads}) increased with increasing ferrihydrite Al content and decreased at the higher DIC concentration (Table 5.1). Following inoculation (t=0) and a brief 1 day lag phase, the decrease in U_d varied according to the ferrihydrite Al content and the DIC concentration. In the incubation amended with pure ferrihydrite and 20 mM DIC, U_d decreased rapidly to a minimum by day 4 then gradually increased to 7±1% of the initial concentration by the end of the incubation (Figure 5.1A). In contrast, when the pure ferrihydrite incubation was amended with 40 mM DIC, an initial period of uranium removal was followed by a large rebound in U_d concentration (up to 62±1% of initial U_d)

Table 5.1 Measured concentration of initial adsorbed U(VI) (U_{ads}), measured final U:Fe molar ratio, and calculated final concentration of solid-associated uranium (U_{SA}) in incubations with *S. putrefaciens* containing both U(VI) and ferrihydrite as TEAs

Incubation	U_{ads} (μM)[a]	U:Fe ratio	U_{SA} (μM)[b]
+U+0Al-Fh 20DIC	17±8	$8.08\pm0.02\times10^{-3}$	40±1
+U+0Al-Fh 20DIC Abiotic	17	7.22×10^{-4}	4
+U+0Al-Fh 40DIC	9±4	$4.94\pm0.08\times10^{-3}$	25±1
+U+0Al-Fh 40DIC Abiotic	13	3.99×10^{-4}	2
+U+5Al-Fh 20DIC	38±3	$7.12\pm0.35\times10^{-3}$	37±1
+U+5Al-Fh 20DIC Abiotic	41	1.72×10^{-3}	10
+U+5Al-Fh 40DIC	14±4	$1.02\pm0.21\times10^{-2}$	51±11
+U+5Al-Fh 40DIC Abiotic	9	6.02×10^{-4}	3
+U+10Al-Fh 20DIC	57±6	$7.31\pm0.27\times10^{-3}$	38±2
+U+10Al-Fh 20DIC Abiotic	54	2.18×10^{-3}	12
+U+10Al-Fh 40DIC	21±5	$9.76\pm1.03\times10^{-3}$	51±5
+U+10Al-Fh 40DIC Abiotic	24	7.52×10^{-4}	4

Reported values represent the average and standard deviation of triplicate biotic incubations and single abiotic controls.

[a]Adsorbed uranium was calculated as the difference between the initial concentration of dissolved uranium measured in incubations with and without ferrihydrite.

[b]Solid-associated uranium was calculated from the measured U:Fe molar ratio in the final solid and the final concentration of solid phase iron ($Fe_{solid,final} = Fe_{T,0} - Fe(II)_{d,final} - Fe(III)_{d,final}$).

which began around day 3 (Figure 5.1A). After the rebound in U_d, uranium was removed from solution to 13% of the initial concentration by the end of the incubation. When Al-ferrihydrite was included in incubations with U(VI), minimum U_d concentrations were not achieved until at least day 8 in the 20 mM DIC incubations, and much smaller rebounds in U_d were observed in the incubations amended with 40 mM DIC (Figure 5.1B-C). Whereas similar final extents of uranium removal were achieved in incubations amended with 0 and 5 mol% Al-ferrihydrite (Figure 5.1A-B), 18±1% (20 mM DIC) and 40±12% (40 mM DIC) of initial U_d remained in solution by the end of 10 mol% Al-ferrihydrite incubation (Figure 5.1C).

The presence of pure ferrihydrite increased the pseudo-first order constant (k_{obs}) of uranium removal at both DIC concentrations compared to uranium-only incubations, albeit to a more significant extent at the lower DIC concentration (Figure 5.2A). Aluminum substitution decreased the k_{obs} of uranium removal at both DIC concentrations compared to incubations with pure ferrihydrite. In fact, the k_{obs} of uranium removal in the 5 mol% Al-ferrihydrite incubation amended with 40 mM DIC and in both 10 mol% Al-ferrihydrite incubations were lower than the k_{obs} values measured in otherwise identical uranium-only incubations.

In turn, the presence of uranium affected the extent of $Fe(II)_T$ production and the speciation of Fe(II). In incubations with pure ferrihydrite, uranium decreased the final extent of $Fe(II)_T$ production in the 20 mM DIC incubation and increased the final extent of $Fe(II)_T$ production in the 40 mM DIC incubation (Figure 5.1D). In contrast, the final extent of $Fe(II)_T$ production in incubations amended with Al-ferrihydrite increased significantly in the presence of uranium regardless of DIC concentration (Figure 5.1E-F). Across all

incubations, uranium enhanced the initial net rate of production and the maximum concentration of dissolved Fe(II) ($Fe(II)_d$) compared to ferrihydrite-only incubations (Figure 5.1G-I). In 20 mM DIC incubations, the maximum $Fe(II)_d$ concentration decreased with increasing ferrihydrite Al content, and after reaching a maximum, $Fe(II)_d$ concentrations either decreased slowly (0 mol% Al, Fig. 1G) or remained constant (5 and 10 mol% Al, Figure 5.1H-I). In contrast, the initial net production rate of $Fe(II)_d$ in 40 mM DIC incubations was inversely proportional to the ferrihydrite Al content, and $Fe(II)_d$ decreased rapidly upon reaching the maximum concentration, which was similar regardless of ferrihydrite Al content (Figure 5.1G-I). Unlike $Fe(II)_d$, concentrations of $Fe(III)_d$ (Figure D.4) and Al_d (Figure D.5) were not affected by uranium. Finally, the pseudo-first order rate constant (k_{obs}) of Fe(III) reduction in the presence of uranium varied by <15% in incubations with pure ferrihydrite compared to otherwise identical ferrihydrite-only incubations (Figure 5.2B). However, uranium significantly increased the k_{obs} of Fe(III) reduction in all incubations amended with Al-ferrihydrite, and the enhancement of the rate constant compared to otherwise identical ferrihydrite-only incubations was proportional to both the DIC concentration and the ferrihydrite Al content.

5.4.3 Characterization of the solid phase produced in the bioreduction incubations

Magnetite and, to a lesser extent, lepidocrocite were identified as the final iron mineralization products in the 20 mM DIC incubation amended with pure ferrihydrite (Figure 5.3A), whereas siderite was the sole iron phase identified under otherwise identical conditions in the presence of uranium (Figure 5.3B). Similarly, both magnetite and siderite were identified in the final solid phase of the pure ferrihydrite-only incubation amended with 40 mM DIC (Figure 5.3C), but only siderite was identified in the presence of uranium

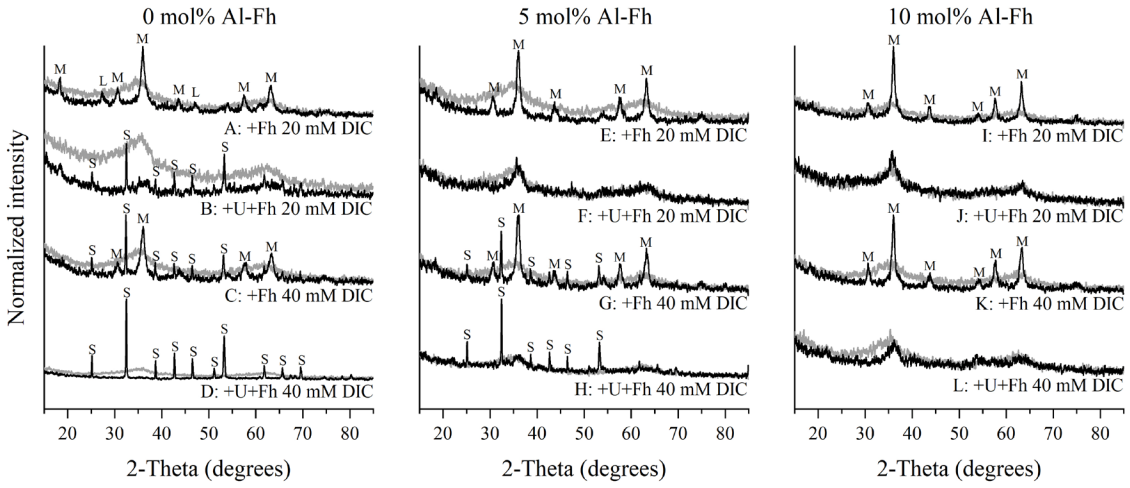

Figure 5.3 Powder X-ray diffraction (XRD) patterns of final solid phase products in incubations amended with 5 mM of (A-D) 0, (E-H) 5, or (I-L) 10 mol% Al-ferrihydrite (+Fh) or both 180 µM U(VI) and 5 mM (Al-)ferrihydrite (+U+Fh) as terminal electron acceptors, and either 20 or 40 mM DIC. Black lines represent biotic incubations and grey lines represent abiotic controls. Signals are normalized to the maximum intensity in each condition and smoothed using a 10-point moving average. Peaks are indexed with M for magnetite, L for lepidocrocite, and S for siderite.

(Figure 5.3D). In incubations amended with Al-ferrihydrite, magnetite (and sometimes siderite in 40 mM DIC incubations) was always identified in ferrihydrite-only incubations, but never in the presence of uranium (Figure 5.3E-L). Mass balance between the measured concentration of ascorbate-extractable solid phase iron (Fe_{asc}) and the calculated concentration of solid Fe(III) ($Fe(III)_{solid} = Fe_{T,0} - Fe(II)_T - Fe(III)_d$) at each time point revealed the formation of ascorbate-extractable (i.e., amorphous) Fe(II)-bearing solids in all 20 mM DIC incubations amended with uranium (Figure D.7). The final color of these incubations was black (0 mol% Al) or black/green (5 and 10 mol% Al) (Figure D.6), suggesting the formation of magnetite and/or green rust which evaded detection by XRD in the presence of uranium due to either poor crystallinity, short range ordering, and/or

small particle size. Although amorphous Fe(II)-bearing solids were also detected in the 40 mM DIC Al-ferrihydrite incubations containing uranium (Figure D.7B-C), the light color of the incubations suggests that magnetite formation was less significant under these conditions (Figure D.8).

The primary effect of Al substitution on the final solid phase iron speciation was the inhibition of siderite formation. Despite the formation of siderite in the pure ferrihydrite incubation amended with uranium and 20 mM DIC (Figure 5.3B), siderite was not identified when incubations were amended with Al-ferrihydrite under otherwise identical conditions (Figure 5.3F, J). Likewise, siderite formation was inhibited in 10 mol% Al-ferrihydrite incubations amended with 40 mM DIC, regardless of the presence of uranium (Figure 5.3K, L). The green color of the Al-ferrihydrite incubations amended with uranium (Figure D.6 and Figure D.8), together with the ascorbate-extractable Fe(II)-bearing solids identified by mass balance calculations (Figure D.7), suggest the formation of an amorphous green rust phase in place of siderite, particularly at the higher DIC concentration. The speculative amorphous green rust phase was not detectable by XRD and only present in incubations containing both Al-ferrihydrite and uranium.

Measured U:Fe molar ratios of the final solids in incubations with *S. putrefaciens* were 1 to 2 orders of magnitude larger than abiotic controls, indicating that secondary mineralization of ferrihydrite strongly increased the association of uranium with the solid phase (Table 5.1). Calculated concentrations of solid-associated uranium (U_{SA}) ranged from 25±1 to 51±11 μM, and except for the 20 mM DIC incubations amended with 5 and 10 mol% Al-ferrihydrite, U_{SA} exceeded initial U_{ads}, indicating that association of uranium

with the solid phase enhanced the rate of uranium removal from solution under these conditions.

5.4.4 Kinetics of abiotic U(IV) oxidation by (Al-)ferrihydrite

In sterilized incubations containing both biogenic U(IV) solids and (Al-)ferrihydrite, around 3.5 μM Fe(II) was produced after 30 min of reaction (Figure D.9A). Fe(II) was not produced in uranium-free controls with autoclaved fumarate-grown cells (Figure D.9A), indicating that Fe(II) production was the result of ferrihydrite reduction by U(IV) rather than reduced metabolites in cellular debris. Correspondingly, the oxidation of U(IV) by (Al-)ferrihydrite resulted in greater uranium dissolution than the iron-free control (Figure D.9B), albeit to a lower extent than expected (1.8 μM) based on the production of Fe(II) (3.7 μM) and assuming stoichiometric oxidation of U(IV) by Fe(III) (Equation 5.2). Concentrations of U_d produced from U(IV) oxidation were inversely proportional to ferrihydrite Al content (Figure D.9B) despite similar extents of Fe(II) production (Figure D.9A), presumably due to the enhanced adsorption of U(VI) onto Al-ferrihydrite, as observed in the bioreduction incubations (Figure 5.1A-C). The rate of U(IV) oxidation ranged from 85±6 to 102±4 μM/day, and a correlation between the rate of U(IV) oxidation and ferrihydrite Al content was not observed ($R^2 = 0.05$, Figure D.10).

5.5 Discussion

5.5.1 Effect of Al-substitution on microbial reduction of ferrihydrite

Aluminum substitution does not systematically alter mineralogical properties which have previously been linked to rates of microbial iron oxide reduction, such as

surface area, particle size, acid dissolution kinetics, or degree of crystallinity (Cismasu et al., 2012; Ekstrom et al., 2010), and Al toxicity is unable to account for the effects of Al substitution on reduction of different iron oxides by *S. putrefaciens* (Ekstrom et al., 2010). In the present study, incongruent dissolution of Al-ferrihydrite significantly limited the accumulation of Al_d (Figure D.5), and although adsorption or surface precipitation of Al may further decrease the accessibility of Fe(III) to MRB, this effect is unable to account for differences in the initial rates of Fe(III) reduction. Iron oxide solubility has also been linked to rates of microbial Fe(III) reduction (Bonneville et al., 2009), and the solubility of Al-ferrihydrite is assumed to be lower than pure ferrihydrite given that Al substitution decreases the transformation of ferrihydrite to goethite which proceeds via a dissolution/precipitation mechanism (Hansel et al., 2011; Schwertmann et al., 2000). In the current study, a strong correlation (R^2 = 0.75) was observed between the net rate of dissolved Fe(III) ($Fe(III)_d$) production and the pseudo-first order rate constant of Fe(III) reduction in the 40 mM DIC iron-only incubations (Figure D.11). This correlation suggests that $Fe(III)_d$ is an intermediate in dissimilatory iron reduction, in line with the production of endogenous organic ligands by *S. putrefaciens* as a strategy to non-reductively solubilize solid Fe(III) TEAs (Jones et al., 2010; Taillefert et al., 2007). Although the correlation between $Fe(III)_d$ and $Fe(II)_T$ production decreased when both 20 and 40 mM DIC incubations were considered (R^2 = 0.57, Figure D.11), these results suggest that decreased rates of ligand-promoted dissolution of Al-ferrihydrite may explain, in part, lower rates of Al-ferrihydrite reduction by *S. putrefaciens*.

5.5.2 Effect of Al-substitution on uranium and iron redox cycling

Prior to inoculation of *S. putrefaciens*, Al substitution enhanced the adsorption of uranium onto (Al-)ferrihydrite. As the concentration of Fe was 5 mM in all incubations, the mass of (Al-)ferrihydrite solids amended to incubations increased with increasing Al content, however, this was not sufficient to account for enhanced uranyl adsorption (data not shown). Al substitution raises the point of zero charge (pH_{pzc}) of ferrihydrite (Anderson and Benjamin, 1990; Cismasu et al., 2013; Masue et al., 2007), which results in a more positive surface charge at a given pH, and at pH 8, aqueous uranyl speciation is dominated by negatively charged uranyl carbonate species (Table D.2). Enhanced attraction between the positively charged Al-ferrihydrite surface and uranyl carbonate anions likely contributes to increased uranyl adsorption, and changes in the mechanism of uranyl adsorption onto Al-ferrihydrite (Johnston and Chrysochoou, 2016) (e.g., inner- versus outer-sphere, monodentate versus bidentate) may also enhance this effect.

Pure ferrihydrite increased the pseudo-first order rate constant of U_d removal compared to uranium-only incubations regardless of the DIC concentration (Figure 5.2A), consistent with a combination of abiotic U(VI) reduction by solid-associated Fe(II) and increased solid-association of uranium (e.g., incorporation, occlusion, enhanced adsorption) during secondary mineralization of ferrihydrite (Table D.3) acting in consort with microbial uranium reduction (Belli and Taillefert, In review). The diminished enhancement of k_{obs} in the 40 mM DIC incubation was presumably due to complexation by carbonate and decreased adsorption of U(VI) which is a prerequisite for abiotic U(VI) reduction/incorporation (Latta et al., 2012b; Liger et al., 1999; Massey et al., 2014a; Singer et al., 2012a). Following an initial period of enhanced uranium removal, the rebound in U_d observed in the 40 mM DIC incubation (Figure 5.1A) coincides with an increase in $Fe(II)_T$

(Figure 5.1D), indicative of oxidative dissolution of U(IV) solids by Fe(III) (Belli and Taillefert, In review; Luan et al., 2014). These features were not evident in the otherwise identical 20 mM DIC incubation (Figure 5.1A, D) despite similar production $Fe(III)_d$ (Figure D.4), suggesting that ferrihydrite was the dominant oxidant of U(IV) and DIC concentration played a role in controlling U(IV) oxidation. After the rebound in U_d, the second period of uranium removal in the 40 mM DIC incubation (Figure 5.1A) indicates that the net rate of uranium removal, a combination of U(VI) bioreduction, abiotic U(VI) reduction, and solid-phase uranium association, exceeded the rate of U(IV) oxidation as a result of the complete consumption of ferrihydrite by microbial reduction and secondary mineralization (Belli and Taillefert, In review).

In contrast to pure ferrihydrite, Al-ferrihydrite never enhanced the pseudo-first order rate constant of U_d removal compared to uranium-only incubations (Figure 5.2A). The decrease in the pseudo-first order rate constant of U_d removal compared to incubations with pure ferrihydrite (Figure 5.2A), together with the increase in the pseudo-first order rate constant of Al-ferrihydrite reduction in the presence of uranium (Figure 5.2B), indicate that U(IV) oxidation by Al-ferrihydrite occurred immediately following the lag phase in microbial respiration. This behavior is similar to simultaneous microbial reduction of Fe(III)-bearing clay and U(VI) by *S. putrefaciens* (Luan et al., 2014). Uranium(IV) oxidation by Al-ferrihydrite decreased net U_d removal (Figure 5.1B, C) and simultaneously increased the production of $Fe(II)_T$ throughout the incubation (Figure 5.1E, F). These results, together with the small rebounds in U_d observed late in the Al-ferrihydrite incubations, demonstrate that Al substitution sustained U(IV) oxidation throughout the entire duration of the incubations. Furthermore, abiotic U(IV) oxidation occurred

regardless of DIC concentration in incubations with Al-ferrihydrite (Figure 5.1B, C), indicating that DIC concentration was not an absolute control of U(IV) oxidation.

5.5.3 Mechanism of enhanced U(IV) oxidation by Al-ferrihydrite

The ΔG_r of U(IV) oxidation by ferrihydrite is able to predict the redox behavior of uranium and iron in incubations with pure ferrihydrite (Belli and Taillefert, In review) (Figure 5.4). Unlike the 20 mM DIC incubations in which $Fe(II)_d$ remains in solution

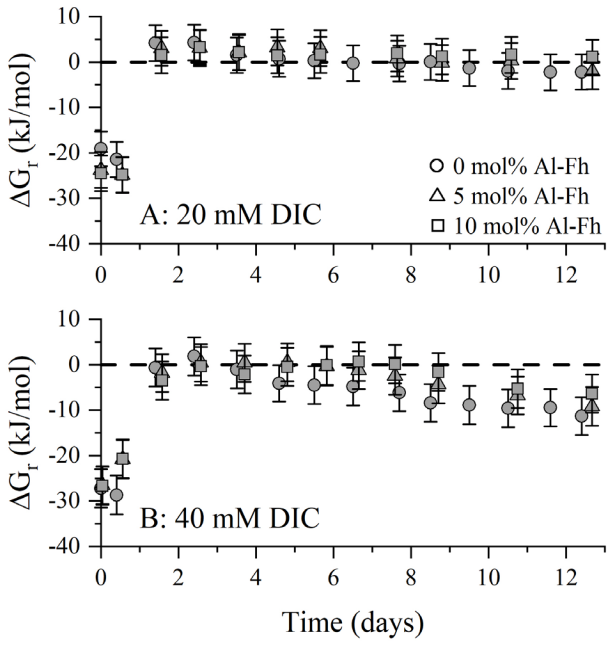

Figure 5.4 Time series of calculated Gibbs energies of reaction (ΔG_r) of $U(IV)_{mono}$ oxidation by pure ferrihydrite at each sampled time point in incubations with *S. putrefaciens* amended with either (A) 20 mM or (B) 40 mM DIC and both 180 µM U(VI) and 5 mM of 0 (circles), 5 (triangles), or 10 (squares) mol% Al-ferrihydrite as terminal electron acceptors. Symbols and error bars represent the average and standard deviation of the ΔG_r calculated from 10,000 Monte Carlo sampled pairs of E_h values for the $U(VI)/U(IV)_{mono}$ and $Fe(OH)_3/Fe(II)$ redox couples.

(Figure 5.1G) and decreases the thermodynamic favorability of U(IV) oxidation (Figure 5.4A), precipitation of siderite and the associated decrease in $Fe(II)_d$ in the 40 mM DIC incubations (Figure 5.1G) makes the oxidation of U(IV) thermodynamically favorable (Figure 5.4B). These results are in line with the concentration of $Fe(II)_d$, via changes in the $Fe(OH)_3$/Fe(II) E_h, controlling the role of iron in uranium redox cycling. Although DIC concentration alters the U(VI)/U(IV) E_h by promoting the formation of uranyl carbonate species (Ginder-Vogel et al., 2006), the saturation of U(VI) by carbonate ligands was found to limit the influence of this effect above a DIC concentration of 20 mM (Belli and Taillefert, In review).

When the ΔG_r^0 of U(IV) oxidation by pure ferrihydrite is used with measured solution composition to calculate the ΔG_r of U(IV) oxidation by Al-ferrihydrite, ΔG_r values are essentially identical to those of pure ferrihydrite for each DIC concentration (Figure 5.4) despite the significant differences identified between uranium redox cycling with pure and Al-substituted ferrihydrite (Figure 5.1 and Figure 5.2). These results indicate that thermodynamic data for pure ferrihydrite are not sufficient to predict the redox behavior of Al-ferrihydrite. Moreover, these results imply that Al substitution increases the E_h of the $Fe(OH)_3$/Fe(II) redox couple which makes the oxidation of U(IV) by Al-ferrihydrite thermodynamically favorable under conditions which are otherwise unfavorable for U(IV) oxidation by pure ferrihydrite (e.g., during the initial days of the incubation period). Thermodynamic data for pure ferrihydrite was sufficient to predict uranium-iron redox cycling in bioreduction incubations amended with silica (Belli and Taillefert, In review), which, like Al substitution, limits microbial Fe(III) reduction (Belli and Taillefert, In review) and secondary mineralization of ferrihydrite (Jones et al., 2009), providing further

evidence that the effect of Al substitution on the redox properties of ferrihydrite is distinct from its effects on the kinetics of microbial reduction and secondary mineralization. Finally, results from abiotic U(IV) oxidation incubations conducted in the present study (Figure D.9) are consistent with dissolution of U(IV) solids as the rate limiting step in U(IV) oxidation by ferrihydrite (Ginder-Vogel et al., 2010) and further support the conclusion that Al substitution alters the redox properties of ferrihydrite, rather than the rate of U(IV) oxidation.

Conventional thermodynamic principles can explain the effect of Al substitution on the E_h of the $Fe(OH)_3$/Fe(II) redox couple. The half-reaction of ferrihydrite reduction (Equation 5.4) can be used to calculate the E_h of the $Fe(OH)_3$/Fe(II) redox couple using Equation 5.5, where E_h^0 is the standard state E_h of the $Fe(OH)_3$/Fe(II) redox couple, R is the ideal gas constant, T is temperature, n is the number of electrons (1), F is Faraday's constant, and brackets denote the activities of the reactants and products in Equation 5.4.

$$Fe(OH)_3(s) + e^- + 3H^+ \rightarrow Fe^{2+} + 3H_2O \tag{5.4}$$

$$E_h = E_h^0 - \frac{RT}{nF} \ln\left(\frac{\{Fe^{2+}\}\{H_2O\}^3}{\{Fe(OH)_3\}\{H^+\}^3}\right) \tag{5.5}$$

Whereas the activity of water is approximated as 1 in dilute aqueous solutions, and the activities of solid phases are approximated as 1 for pure solids, the activities of impure solids (e.g., Al-substituted ferrihydrite) cannot be approximated as 1 and must be considered when calculating E_h. By decreasing the activity of pure ferrihydrite, Al substitution increases the E_h of the Al-$Fe(OH)_3$/Fe(II) redox couple and enhances the thermodynamic favorability of U(IV) oxidation by Al-ferrihydrite (Equation 5.3).

5.5.4 Role of secondary mineralization in uranium removal

In incubations containing pure ferrihydrite, the final concentration of solid-associated uranium (U_{SA}) was proportional to the initial concentration of U_{ads} across both DIC concentrations, consistent with adsorption as a prerequisite for incorporation of uranium into secondary mineralization products (Massey et al., 2014a) (Table 5.1). The inverse relationship between U_{ads} and U_{SA} across both DIC concentrations for each Al-ferrihydrite (Table 5.1) suggests that uranium incorporation proceed via another pathway. Whereas Al substitution limited removal of uranium from solution in the 20 mM DIC incubations (i.e., $U_{SA} \leq U_{ads}$), the high concentration of U_{SA} measured in the 40 mM DIC incubations with Al-ferrihydrite suggests that uranium was entrained during the precipitation of green rust (Roberts et al., 2017), which was speculated to form under these conditions (Figure D.9 and Figure D.10). Although Al substitution increases the concentration of U_{SA} in 40 mM DIC incubations, the rapid oxidation of green rust even under anoxic conditions (Hansen and Koch, 1998; Legrand et al., 2004) suggests that green rust is a less stable host mineral for uranium compared to other crystalline Fe phases (Stewart et al., 2009).

Although U(IV) oxidation by ferrihydrite is thermodynamically favorable after day 3 in 40 mM DIC incubations with pure ferrihydrite (Figure 5.4B), uranium removal commences again around day 6 (Figure 5.1A) as reactive ferrihydrite is consumed by microbial reduction and secondary mineralization (Belli and Taillefert, In review). In contrast, Al substitution preserved ferrihydrite and thereby extended the duration of U(IV) oxidation, which decreased the final extent of uranium removal in incubations with Al-ferrihydrite (Figure 5.1B,C) and increased the final extent of Al-ferrihydrite reduction

(Figure 5.1E,F), both more significantly in the presence of high DIC concentrations. Although Al-ferrihydrite Fe(III) was less accessible for microbial reduction (Ekstrom et al., 2010), it remained chemically reactive as an oxidant of U(IV) throughout the incubation period, supporting the original hypothesis that Al substitution sustains the oxidation of U(IV) by ferrihydrite.

5.5.5 Environmental implications

Accurately predicting the stability of biogenic U(IV) solids in diverse geochemical conditions is crucial to assess the feasibility and long term success of U(VI) bioreduction at contaminated sites. The results of the present study indicate that substitution of Fe^{3+} by Al^{3+}, a common ferrihydrite impurity, enhances the ability of ferrihydrite to mobilize uranium via oxidative dissolution of U(IV) solids. Furthermore, by decreasing the kinetics of ferrihydrite consumption via microbial reduction and secondary mineralization, Al substitution preserves ferrihydrite and sustains the oxidation of U(IV) solids even under iron-reducing conditions. These results indicate that naturally occurring ferrihydrite may be a more effective and longer-lived oxidant of U(IV) than previously thought. Understanding how the redox properties of natural iron oxides differ from their synthetic counterparts will be necessary to predict the fate of uranium and other redox active contaminants in the subsurface accurately.

5.5.6 Acknowledgements

This research was supported by the US Department of Energy Subsurface Biogeochemical Research (SBR) program (Grant No. DE-SC0005520) and the US Environmental Protection Agency (EPA) Science to Achieve Results (STAR) Graduate

Fellowship to KMB (Assistance Agreement No. FP-91767401-0). This publication has not been formally reviewed by the EPA, and the views expressed herein are solely those of the authors. This work was performed in part at the Georgia Tech Institute for Electronics and Nanotechnology, a member of the National Nanotechnology Coordinated Infrastructure, which is supported by the National Science Foundation (Grant ECCS-1542174).

CHAPTER 6. CONCLUSIONS

Uranium bioreduction represents a promising alternative to traditional remediation strategies which are prohibitively expensive on the scale needed to address wide-spread uranium contamination across the United States. The ability to predict the fate of uranium following biostimulation of the subsurface microbial community remains limited, however, due to knowledge gaps in the biogeochemical cycling of uranium and its coupling with the biogeochemical transformation of iron, a ubiquitous component of subsurface environments. This dissertation explored how geochemical conditions, such as pH, solution composition (i.e. carbonates, calcium, magnesium, silica), iron and uranium speciation, and iron oxide mineralogy, including the presence of impurities, affect the kinetics of uranium removal from solution in the presence of metal-reducing bacteria. Kinetic rate laws were proposed to account for experimental results, and a biogeochemical kinetic model was developed to predict the rate of uranium removal across a wide range of geochemical conditions in the presence and absence of iron oxides. During this work, the following hypotheses were tested:

1) The rate of U(VI) bioreduction is controlled by the concentration of non-carbonate uranyl species, which are bioavailable to metal-reducing bacteria yet toxic at high concentrations.
2) Aqueous uranyl speciation alters the U(VI)/U(IV) redox potential and controls whether iron acts either as a reductant or an oxidant of uranium .
3) Aluminum substitution of ferrihydrite decreases uranium removal via U(VI) bioreduction by: enhancing the abiotic oxidative dissolution of U(IV) solids by

ferrihydrite; and sustaining U(IV) oxidation by preserving ferrihydrite against consumption via microbial reduction and secondary mineralization.

To test the first hypothesis, bioreduction incubations with *Shewanella putrefaciens* strain 200 were conducted with U(VI) as the sole terminal electron acceptor (TEA) across a range of pH and concentrations of dissolved inorganic carbon (DIC), calcium, and magnesium to determine the effects of aqueous uranyl speciation on U(VI) bioreduction kinetics. Across all conditions tested, the concentration of non-carbonate uranyl species was found to account for the observed rates of U(VI) bioreduction. Pseudo-first order rate constants of U(VI) bioreduction were proportional to the concentration of uranyl non-carbonate species up to a threshold concentration above which rate constants decreased due to uranyl toxicity to *S. putrefaciens*. Viability assays across a range of aqueous uranyl speciation confirmed that uranyl toxicity to *S. putrefaciens* was associated with the concentration of the 'free' uranyl ion, in line with the free ion activity model of metal toxicity. A speciation-dependent kinetic rate law that accounted for uranyl toxicity was able to reproduce time series of uranium removal across all experimental conditions using a rate constant for uranyl non-carbonate species that was 6 orders of magnitude larger than for uranyl carbonate and ternary uranyl carbonate species, indicating that uranyl non-carbonate species represent the most bioavailable and readily reducible fraction of U(VI) despite being the least abundant in solution. These results demonstrate that in the absence of competing TEAs, uranium bioreduction kinetics can be predicted over a wide range of geochemical conditions based on the bioavailability and toxicity imparted on U(VI) by solution composition. The concentration of uranyl non-carbonate species is therefore expected to be a determining factor controlling uranium bioreduction at contaminated sites.

In addition to U(VI) bioreduction, abiotic redox cycling of uranium also contributes to the net rate of uranium removal from solution. To test the second hypothesis and identify the geochemical conditions that control the oxidative or reductive behavior of iron on uranium, bioreduction incubations with *S. putrefaciens* were conducted with either U(VI), ferrihydrite, or both as TEAs simultaneously under otherwise identical geochemical conditions. Initial concentrations of DIC, calcium, and silica were varied to assess the roles of aqueous uranyl speciation and secondary mineralization pathways of ferrihydrite on uranium redox cycling. The presence of ferrihydrite increased the pseudo-first order rate constants of uranium removal in nearly all conditions compared to uranium-only controls due to a combination of abiotic U(VI) reduction by Fe(II) and incorporation of uranium into the secondary mineralization products of ferrihydrite. Following an initial period of uranium removal, U(IV) was oxidized by ferrihydrite which led to a rebound in dissolved uranium. The U(VI)/U(IV) redox potential was found to be relatively constant over the course of the incubations despite the effects of DIC and calcium on aqueous uranyl speciation. In contrast, changes in the Fe(III)/Fe(II) redox potential controlled by dissolved Fe(II) concentrations corresponded with the rebound in dissolved uranium and the abrupt change in iron acting as a reductant of U(VI) to an oxidant of U(IV). A biogeochemical kinetic model developed to diagnose these complex processes could reproduce incubation time series of uranium and iron speciation provided the thermodynamic favorability of abiotic uranium-iron redox cycling was accounted for. The modeling exercise revealed that silica sustained U(IV) oxidation by preserving ferrihydrite against consumption via microbial reduction and secondary mineralization. The model also revealed that non-uraninite U(IV) solids formed in the incubations have a redox potential approximately 84

mV lower than that of amorphous uraninite, highlighting the need for a thermodynamic characterization of non-uraninite U(IV) solids. This study identified dissolved Fe(II) concentration, rather than aqueous uranyl speciation, as the primary geochemical control of the role of iron in uranium redox cycling at moderate to high DIC concentrations. These results emphasize the importance of considering dissolved Fe(II) concentration when designing site-specific, in situ bioremediation strategies.

In contrast to pure, synthesized ferrihydrite often used in geochemical studies to study the effect of iron on uranium biogeochemical cycling, natural ferrihydrite minerals include impurities which alter their biological and chemical reactivity. To test the third hypothesis and characterize the effect of ferrihydrite impurities on the coupled biogeochemical cycling of uranium and iron, U(VI) bioreduction incubations with *S. putrefaciens* were conducted at two initial DIC concentrations with pure and Al-substituted ferrihydrite, the most common impurity in iron oxide minerals. In contrast to pure ferrihydrite which increased the pseudo-first order rate constant of uranium reduction, Al substitution enhanced abiotic U(IV) oxidation by ferrihydrite and decreased the rate constant of uranium removal across all conditions. Aluminum substitution preserved ferrihydrite from consumption via microbial reduction and secondary mineralization and sustained ferrihydrite-driven abiotic oxidation of U(IV) throughout the entire incubation period. Abiotic incubations also demonstrated that Al substitution did not affect the kinetics of U(IV) oxidation by ferrihydrite, suggesting that Al impurities altered the redox properties of ferrihydrite. Time series of the Gibbs energy of reaction (ΔG_r) of U(IV) oxidation by ferrihydrite were identical at each DIC concentration investigated regardless of the Al content of ferrihydrite, indicating that thermodynamic data for pure ferrihydrite was insufficient to describe the

redox behavior of Al-substituted ferrihydrite. Moreover, these results suggest that Al substitution raised the standard state potential of the $Fe(OH)_3$/Fe(II) redox couple. This study indicates that naturally occurring ferrihydrite may be a more effective and longer-lived oxidant of U(IV) than previously thought, and further characterization of the redox properties of natural iron oxides will be needed to predict the long-term stability of U(IV) solids in the subsurface.

Overall, the results of this dissertation clarify the multitude of ways in which pH, solution composition, and iron oxide mineralogy influence the removal of uranium from solution following biostimulation of the subsurface. Although the rate of U(VI) bioreduction may be optimized by achieving a balance between the bioavailability and toxicity of U(VI), the rate of uranium removal from solution and the long-term success of this strategy will rely on maintaining geochemical conditions that stabilize U(IV) solids in the presence of reactive Fe(III) phases. The rate laws and modeling framework proposed in this dissertation also provide a unique opportunity to incorporate speciation-dependent U(VI) bioreduction kinetics and the thermodynamics of uranium-iron redox cycling into new age reactive transport models able to more accurately predict the fate of uranium at contaminated sites. These models will enhance the ability to identify sites which are strong candidates for U(VI) bioreduction based on the geochemistry and mineralogy of the contaminated aquifer. Finally, this work prompts new questions regarding the redox reactivity of naturally impure iron oxides which will have broad geochemical consequences in the cycling of other redox-active contaminants and nutrients.

6.1 Recommendations for future work

Pure culture batch incubations are a useful tool to investigate the biogeochemical mechanisms controlling subsurface uranium mobility as they allow for the isolation and manipulation of relevant variables, such as pH, solution composition, and solid-phase mineralogy. Batch incubations simplify the kinetic rate expressions needed to describe the biogeochemical reactions being studied, thus, relatively simple kinetic models can be used to probe complex reaction pathways. However, batch incubation studies are limited in their application to natural subsurface environments which are characterized by heterogeneous mineral assemblages, diffusion, advection, and diverse microbial communities. In order to advance the knowledge gained from batch incubation experiments and apply it to field conditions, follow up studies that employ flow through reactors with natural inoculum and representative soils/sediments will be necessary to investigate these processes under more relevant environmental conditions.

The results presented in Chapter 3 suggest that carbonates produced during the biostimulation of uranium-contaminated aquifers and divalent cations naturally present in groundwater (e.g., Ca^{2+} and Mg^{2+}) may decrease rates of U(VI) bioreduction via the formation of aqueous carbonate and ternary carbonate uranyl complexes which suppress the concentration of more bioavailable non-carbonate uranyl species. A recent field study at the US DOE IFRC Rifle site found that injection of bicarbonate into the subsurface along with an organic carbon source led to *faster* overall rates of uranium removal compared to an organic carbon injection alone, despite the dominance of aqueous U(VI) by carbonate complexes (Long et al., 2015). One possible explanation is that injection of bicarbonate into the aquifer decreased the toxicity of U(VI) to the native microbial community and

enhanced the rate of U(VI) bioreduction, similar to the results presented in Chapter 3. Regardless, questions remain about whether the speciation-dependent U(VI) reduction kinetics of *S. putrefaciens* can be broadly applied to native metal-reducing microbial communities and how advection might mitigate the effects of aqueous uranyl speciation on the kinetics of U(VI) bioreduction. Future studies utilizing flow through reactors and soils from the Rifle site could clarify these questions.

In Chapter 4, the concentration of Fe(II) was revealed to be the primary factor controlling whether iron acts as either a reductant of U(VI) or an oxidant of U(IV), especially under moderate-to-high DIC concentrations. Although secondary mineralization and Fe(II)-carbonate precipitation were the dominant mechanisms of Fe(II) removal from solution in the bioreduction incubations, advection and diffusion will also contribute to the removal of Fe(II) produced locally and therefore influence the thermodynamic stability of U(IV) solids against oxidation by Fe(III) oxides. Additionally, given that Al-substituted ferrihydrite dissolved incongruently with respect to aluminum (Chapter 5), advection/diffusion of iron from the local environment is expected to increase the Al content of ferrihydrite and exacerbate the effects of Al substitution. Future flow through reactor studies may help identify the effect of transport on the stability of U(IV) against oxidation by pure and Al-substituted iron oxides.

The results of Chapter 5 revealed that Al substitution alters the redox properties of ferrihydrite. These results raise additional questions about the effects of other impurities (e.g., silica, dissolved organic matter) on the redox properties of ferrihydrite and the effects of impurities on the redox properties of more crystalline iron oxides (e.g., goethite, lepidocrocite, magnetite, hematite). Experimental confirmation of the effects of structural

impurities on either the standard state redox potential (E_h^0) or solubility of iron oxides will be useful to identify the mechanism by which impurities alter the redox properties of iron oxides and to predict the behavior of naturally impure iron oxides on the redox cycling of redox active contaminants and nutrients. Relatively straightforward pH titrations with simultaneous redox potential measurements may be performed to experimentally determine the redox potential of nano-particulate iron oxides (Bonneville et al., 2004). If larger particle sizes prohibit E_h measurements, solubilities of Al-substituted iron oxides may be determined using dialysis bags to separate solid and dissolved Fe(III) (Bonneville et al., 2009). Comparisons of results between synthetic and natural iron oxides could be useful to identify the relevance of laboratory studies with synthetic minerals.

APPENDIX A. SUPPLEMENTARY DATA FOR CHAPTER 2

Table A.1 Ferrihydrite surface complexation constants added to the PHREEQC database[a]

Sorbate	Complex[b]	Denticity	log K	Reference
H^+	Hfo_sOH_2^+	mono	7.29	Dzombak and Morel, 1990
H^+	Hfo_sO^-	mono	-8.93	Dzombak and Morel, 1990
H^+	Hfo_wOH_2^+	mono	7.29	Dzombak and Morel, 1990
H^+	Hfo_wO^-	mono	-8.93	Dzombak and Morel, 1990
UO_2^{2+}	(Hfo_s)$_2UO_2$	bi	-2.78	Waite et al., 1994[c]
UO_2^{2+}	(Hfo_w)$_2UO_2$	bi	-6.49	Waite et al., 1994[c]
UO_2^{2+}	(Hfo_s)$_2UO_2CO_3^{2-}$	bi	3.03	Waite et al., 1994[c]
UO_2^{2+}	(Hfo_w)$_2UO_2CO_3^{2-}$	bi	-1.06	Waite et al., 1994[c]
Fe^{2+}	Hfo_wOFe^+	mono	-2.98	Appelo et al., 2002
Fe^{2+}	Hfo_wOFeOH	mono	-11.55	Appelo et al., 2002
Fe^{2+}	Hfo_sOFe^+	mono	-0.95	Appelo et al., 2002
CO_3^{2-}	Hfo_wOCO_2^-	mono	12.78	Appelo et al., 2002
CO_3^{2-}	Hfo_wOCO_2H	mono	20.37	Appelo et al., 2002
H_4SiO_4	Hfo_wH_3SiO_4	mono	4.28	Swedlund and Webster, 1999
H_4SiO_4	Hfo_w$H_2SiO_4^-$	mono	-3.22	Swedlund and Webster, 1999
H_4SiO_4	Hfo_w$HSiO_4^{2-}$	mono	-11.69	Swedlund and Webster, 1999
Mg^{2+}	Hfo_wOMg^+	mono	-4.60	PHREEQC Database[d]
SO_4^{2-}	Hfo_wSO_4^-	mono	7.78	PHREEQC Database[d]
SO_4^{2-}	Hfo_w$OHSO_4^{2-}$	mono	0.79	PHREEQC Database[d]

[a]PHREEQC internally corrects complexation constants for ionic strength and uses an exponent of 1 for unoccupied surface species (e.g. Hfo_sOH) in mass action equations of bidentate surface complexes. All surface complexation constants were taken from experimental studies that included a diffuse double layer (DDL) adsorption model.

[b] Hfo_s and Hfo_w represent strong and weak ferrihydrite surface sites, respectively.

[c] Values have been corrected to I=0. [d] (USGS, 2012)

Table A.2 Magnetite surface complexation constants added to the PHREEQC database[a]

Sorbate	Complex[b]	Denticity	log K	Reference
H^+	$MagOH_2^+$	mono	5.10	Missana et al., 2003
H^+	$MagO^-$	mono	-9.10	Missana et al., 2003
UO_2^{2+}	$MagOUO_2^+$	mono	-0.10	Missana et al., 2003
UO_2^{2+}	$MagOUO_2OH$	mono	-5.40	Missana et al., 2003
Fe^{2+}	MagOFeOH	mono	-10.30	Klausen et al., 1995[c]

[a]PHREEQC internally corrects complexation constants for ionic strength and uses an exponent of 1 for unoccupied surface species (e.g. Hfo_sOH) in mass action equations of bidentate surface complexes. All surface complexation constants were taken from experimental studies that included a diffuse double layer (DDL) adsorption model.
[b]Mag represents magnetite surface sites.
[c] Data from Klausen et al. (1995) Figure 5 were fitted with a DDL, single site adsorption model to obtain the surface complexation constant for the MagOFeOH surface complex. The adsorption model was implemented in PHREEQC and optimized in PEST. Two variables were optimized: the logK of MagOFe_diOH (-10.30) and the number of surface sites (0.11 mol sites/mol Fe_3O_4).

Table A.3 Mineral surface properties of iron oxides included in the PHREEQC surface complexation model

Mineral	Site Density	Surface Area	Reference
Ferrihydrite	0.873 mol weak sites/mol $Fe(OH)_3$ 0.0018 mol strong sites/mol $Fe(OH)_3$	600 m^2/g	Waite et al., 1994; Dzombak and Morel, 1990
Magnetite	0.11 mol sites/mol	56 m^2/g	Klausen et al., 1995

Table A.4 Solubility products (K_{sp}) of solid phases added to the PHREEQC database

Reaction	$LogK_{sp}$	Reference
$Fe(OH)_3(s) + 3H^+ \leftrightarrow Fe^{3+} + 3H_2O$	4.891	PHREEQC Database
$Fe_3O_4(s) + 8H^+ \leftrightarrow 2Fe^{3+} + Fe^{2+} + 4H_2O$	3.737	PHREEQC Database
$FeCO_3(s) \leftrightarrow Fe^{2+} + CO_3^{2-}$	-8.1	Calculated from data
$UO_2(am) + 2H_2O \leftrightarrow U^{4+} + 4OH^-$	-54.4	(Guillaumont et al., 2003)

Table A.5 Formation constants of aqueous complexes added to the PHREEQC database

Reaction	LogK	Reference
Organic acid complexes		
$Ace^- + H^+ \leftrightarrow HAce$	4.757	Visual MINTEQ Database
$Ace^- + Na^+ \leftrightarrow NaAce$	-0.12	Visual MINTEQ Database
$Ace^- + Ca^{2+} \leftrightarrow CaAce^+$	1.18	Visual MINTEQ Database
$Lac^- + H^+ \leftrightarrow HLac$	3.86	Visual MINTEQ Database
$Lac^- + Ca^{2+} \leftrightarrow CaLac^+$	1.48	Visual MINTEQ Database
$2Lac^- + Ca^{2+} \leftrightarrow CaLac_2$	2.48	Visual MINTEQ Database
$Lac^- + Mg^{2+} \leftrightarrow MgLac^+$	1.37	Visual MINTEQ Database
$2Lac^- + Mg^{2+} \leftrightarrow MgLac_2$	2.01	Visual MINTEQ Database
Ammonium complexes		
$NH_4^+ + SO_4^{2-} \leftrightarrow NH_4SO_4^-$	1.03	Visual MINTEQ Database
$Ca^{2+} + NH_4^+ - H^+ \leftrightarrow CaNH_3^{2+}$	-9.04	Visual MINTEQ Database
$Ca^{2+} + 2NH_4^+ - 2H^+ \leftrightarrow Ca(NH_3)_2^{2+}$	-18.59	Visual MINTEQ Database
$Mg^{2+} + 2NH_4^+ - 2H^+ \leftrightarrow Mg(NH_3)_2^{2+}$	-19.29	Visual MINTEQ Database
Fe^{2+} complexes		
$Fe^{2+} + H_2O \leftrightarrow FeOH^+ + H^+$	-9.5	MINTEQ Database
$Fe^{2+} + 2H_2O \leftrightarrow Fe(OH)_2 + 2H^+$	-20.57	MINTEQ Database
$Fe^{2+} + 3H_2O \leftrightarrow Fe(OH)_3^- + 3H^+$	-31	MINTEQ Database
$Fe^{2+} + Cl^- \leftrightarrow FeCl^+$	0.14	
$Fe^{2+} + CO_3^{2-} \leftrightarrow FeCO_3$	4.38	
$Fe^{2+} + HCO_3^- \leftrightarrow FeHCO_3^+$	2.0	
$Fe^{2+} + SO_4^{2-} \leftrightarrow FeSO_4$	2.25	MINTEQ Database
$Fe^{2+} + HSO_4^- \leftrightarrow FeHSO_4^+$	1.08	

$Fe^{2+} + HPO_4^{2-} \leftrightarrow FeHPO_4$	3.6	
$Fe^{2+} + H_2PO_4^{-} \leftrightarrow FeH_2PO_4^{+}$	2.7	
$Fe^{2+} + Ace^{-} \leftrightarrow FeAce^{+}$	1.4	
$Fe^{2+} + Lac^{-} \leftrightarrow FeLac^{+}$	-1.82	Liu et al., 2001
Fe^{3+} complexes		
$Fe^{3+} + H_2O \leftrightarrow FeOH^{2+} + H^{+}$	-2.19	MINTEQ Database
$Fe^{3+} + 2H_2O \leftrightarrow Fe(OH)_2^{+} + 2H^{+}$	-5.67	MINTEQ Database
$Fe^{3+} + 3H_2O \leftrightarrow Fe(OH)_3 + 3H^{+}$	-12.56	
$Fe^{3+} + 4H_2O \leftrightarrow Fe(OH)_4^{-} + 4H^{+}$	-21.6	MINTEQ Database
$2Fe^{3+} + 2H_2O \leftrightarrow Fe_2(OH)_2^{4+} + 2H^{+}$	-2.95	MINTEQ Database
$3Fe^{3+} + 4H_2O \leftrightarrow Fe_3(OH)_4^{5+} + 4H^{+}$	-6.3	MINTEQ Database
$Fe^{3+} + Cl^{-} \leftrightarrow FeCl^{2+}$	1.48	MINTEQ Database
$Fe^{3+} + 2Cl^{-} \leftrightarrow FeCl_2^{+}$	2.13	MINTEQ Database
$Fe^{3+} + 3Cl^{-} \leftrightarrow FeCl_3$	1.13	MINTEQ Database
$Fe^{3+} + SO_4^{2-} \leftrightarrow FeSO_4^{+}$	4.04	
$Fe^{3+} + HSO_4^{-} \leftrightarrow FeHSO_4^{2+}$	2.48	
$Fe^{3+} + 2SO_4^{2-} \leftrightarrow Fe(SO_4)_2^{-}$	5.38	
$Fe^{3+} + HPO_4^{2-} \leftrightarrow FeHPO_4^{+}$	5.43	
$Fe^{3+} + H_2PO_4^{-} \leftrightarrow FeH_2PO_4^{2+}$	5.43	
UO_2^{2+} complexes		
$UO_2^{2+} + H_2O - H^{+} \leftrightarrow UO_2OH^{+}$	-5.25	(Guillaumont et al., 2003)
$UO_2^{2+} + 2H_2O - 2H^{+} \leftrightarrow UO_2(OH)_2$	-12.15	(Guillaumont et al., 2003)
$UO_2^{2+} + 3H_2O - 3H^{+} \leftrightarrow UO_2(OH)_3^{-}$	-20.25	(Guillaumont et al., 2003)
$UO_2^{2+} + 4H_2O - 4H^{+} \leftrightarrow UO_2(OH)_4^{2-}$	-32.4	(Guillaumont et al., 2003)
$2UO_2^{2+} + H_2O - H^{+} \leftrightarrow (UO_2)_2OH^{3+}$	-2.7	(Guillaumont et al., 2003)
$2UO_2^{2+} + 2H_2O - 2H^{+} \leftrightarrow (UO_2)_2(OH)_2^{2+}$	-5.62	(Guillaumont et al., 2003)
$3UO_2^{2+} + 4H_2O - 4H^{+} \leftrightarrow (UO_2)_3(OH)_4^{2+}$	-11.9	(Guillaumont et al., 2003)
$3UO_2^{2+} + 5H_2O - 5H^{+} \leftrightarrow (UO_2)_3(OH)_5^{+}$	-15.55	(Guillaumont et al., 2003)
$3UO_2^{2+} + 7H_2O - 7H^{+} \leftrightarrow (UO_2)_3(OH)_7^{-}$	-32.20	(Guillaumont et al., 2003)
$4UO_2^{2+} + 7H_2O - 7H^{+} \leftrightarrow (UO_2)_4(OH)_7^{+}$	-21.90	(Guillaumont et al., 2003)
$UO_2^{2+} + CO_3^{2-} \leftrightarrow UO_2CO_3$	9.94	(Guillaumont et al., 2003)
$UO_2^{2+} + 2\ CO_3^{2-} \leftrightarrow UO_2(CO_3)_2^{2-}$	16.61	(Guillaumont et al., 2003)
$UO_2^{2+} + 3\ CO_3^{2-} \leftrightarrow UO_2(CO_3)_3^{4-}$	21.84	(Guillaumont et al., 2003)
$3UO_2^{2+} + 6\ CO_3^{2-} \leftrightarrow (UO_2)_3(CO_3)_6^{6-}$	54	(Guillaumont et al., 2003)
$2UO_2^{2+} + CO_3^{2-} + 3H_2O - 3H^{+} \leftrightarrow (UO_2)_2CO_3(OH)_3^{-}$	-0.855	(Guillaumont et al., 2003)
$3UO_2^{2+} + CO_3^{2-} + 3H_2O - 3H^{+} \leftrightarrow (UO_2)_3O(OH)_2(HCO_3)^{+}$	0.655	(Guillaumont et al., 2003)

$11UO_2^{2+} + 6\ CO_3^{2-} + 12H_2O - 12H^+ \leftrightarrow (UO_2)_{11}(CO_3)_6(OH)_{12}^{2-}$	-54.35	(Guillaumont et al., 2003)
$UO_2^{2+} + Ca+2 + 3CO_3^{2-} \leftrightarrow CaUO_2(CO_3)_3^{2-}$	27.18	(Dong and Brooks, 2006)
$UO_2^{2+} + 2Ca^{2+} + 3CO_3^{2-} \leftrightarrow Ca_2UO_2(CO_3)_3$	30.7	(Dong and Brooks, 2006)
$UO_2^{2+} + Mg^{2+} + 3CO_3^{2-} \leftrightarrow MgUO_2(CO_3)_3^{2-}$	26.11	(Dong and Brooks, 2006)
$UO_2^{2+} + Ace^- \leftrightarrow UO_2Ace^+$	3.11	Visual MINTEQ Database
$UO_2^{2+} + 2Ace^- \leftrightarrow UO_2(Ace)_2$	5.04	Visual MINTEQ Database
$UO_2^{2+} + 3Ace^- \leftrightarrow UO_2(Ace)_3^-$	7.06	Visual MINTEQ Database
$UO_2^{2+} + Lac^- \leftrightarrow UO_2Lac^+$	3.13	Visual MINTEQ Database
$UO_2^{2+} + 2Lac^- \leftrightarrow UO_2(Lac)_2$	5.16	Visual MINTEQ Database
$UO_2^{2+} + 3Lac^- \leftrightarrow UO_2(Lac)_3^-$	6.31	Visual MINTEQ Database
$UO_2^{2+} + Cl^- \leftrightarrow UO_2Cl^+$	0.17	(Guillaumont et al., 2003)
$UO_2^{2+} + 2Cl^- \leftrightarrow UO_2Cl_2$	-1.1	(Guillaumont et al., 2003)
$UO_2^{2+} + SO_4^{2-} \leftrightarrow UO_2SO_4$	3.15	(Guillaumont et al., 2003)
$UO_2^{2+} + 2SO_4^{2-} \leftrightarrow UO_2(SO_4)_2^{2-}$	4.14	(Guillaumont et al., 2003)
$UO_2^{2+} + 3SO_4^{2-} \leftrightarrow UO_2(SO_4)_3^{4-}$	3.02	(Guillaumont et al., 2003)
$UO_2^{2+} + NO_3^- \leftrightarrow UO_2NO_3^+$	0.3	(Guillaumont et al., 2003)
$UO_2^{2+} + PO_4^{3-} \leftrightarrow UO_2PO_4^-$	13.23	(Guillaumont et al., 2003)
$UO_2^{2+} + PO_4^{3-} + H^+ \leftrightarrow UO_2HPO_4$	19.59	
$UO_2^{2+} + PO_4^{3-} + 2H^+ \leftrightarrow UO_2H_2PO_4^+$	20.682	(Guillaumont et al., 2003)
$UO_2^{2+} + PO_4^{3-} + 3H^+ \leftrightarrow UO_2H_3PO_4^{2+}$	22.462	(Guillaumont et al., 2003)
$UO_2^{2+} + 2PO_4^{3-} + 4H^+ \leftrightarrow UO_2(H_2PO_4)_2$	44.044	(Guillaumont et al., 2003)
$UO_2^{2+} + 2PO_4^{3-} + 5H^+ \leftrightarrow UO2(H_2PO_4)(H_3PO_4)^+$	45.054	(Guillaumont et al., 2003)
$UO_2^{2+} + H_4SiO_4 \leftrightarrow UO_2H_3SiO_4^+ + H^+$	-1.91	Visual MINTEQ Database
U^{4+} complexes		
$U^{4+} + H_2O - H^+ \leftrightarrow UOH^{3+}$	-0.54	(Guillaumont et al., 2003)
$U^{4+} + 4H_2O - 4H^+ \leftrightarrow U(OH)_4$	-10	(Guillaumont et al., 2003)
$U^{4+} + 4CO_3^{2-} \leftrightarrow U(CO_3)_4^{4-}$	35.12	(Guillaumont et al., 2003)
$U^{4+} + 5CO_3^{2-} \leftrightarrow U(CO_3)_5^{6-}$	34.00	(Guillaumont et al., 2003)
$U^{4+} + Cl^- \leftrightarrow UCl^{3+}$	1.72	(Guillaumont et al., 2003)
$U^{4+} + SO_4^{2-} \leftrightarrow USO_4^{2+}$	6.58	(Guillaumont et al., 2003)
$U^{4+} + 2SO_4^{2-} \leftrightarrow U(SO_4)_2$	10.51	(Guillaumont et al., 2003)
$U^{4+} + NO_3^- \leftrightarrow UNO_3^{3+}$	1.47	(Guillaumont et al., 2003)
$U^{4+} + 2NO_3^- \leftrightarrow U(NO_3)_2^{2+}$	2.3	(Guillaumont et al., 2003)

APPENDIX B. SUPPLEMENTARY DATA FOR CHAPTER 3

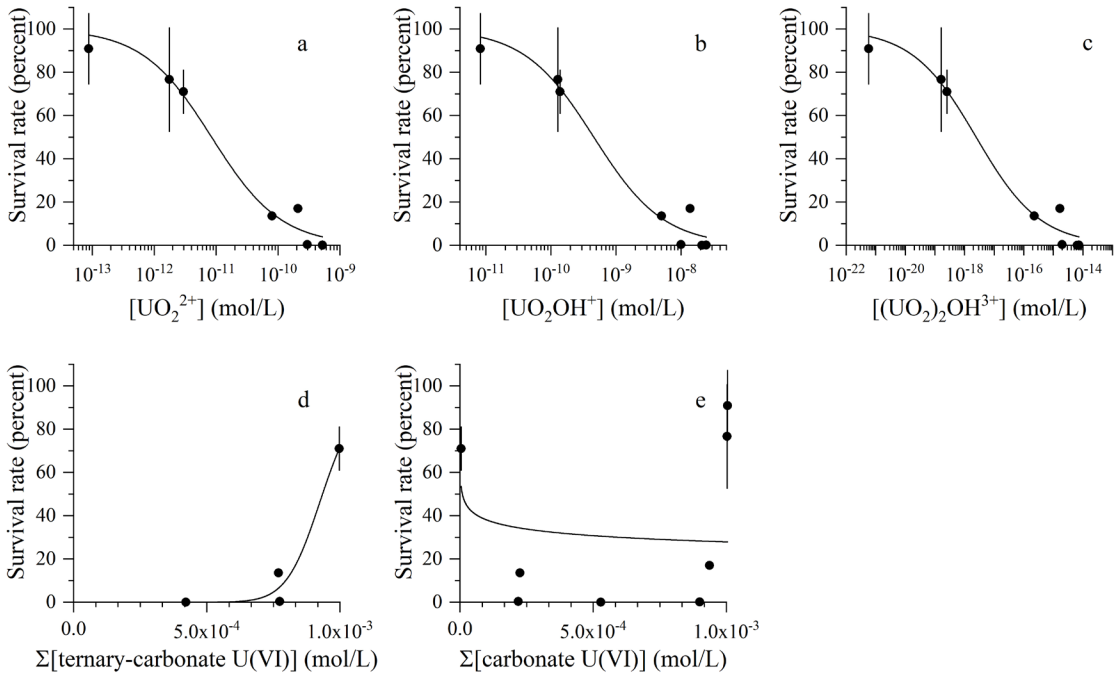

Figure B.1. Correlation between survival rate of *S. putrefaciens* strain 200 and the concentration of a) UO_2^{2+} (R^2 = 0.98), b) UO_2OH^+ (R^2 = 0.98), c) $(UO_2)_2OH^{3+}$ (R^2 = 0.98), d) the sum of all the ternary uranyl carbonate species (R^2 = 0.97), and e) the sum of all the uranyl carbonate species (R^2 = 0.04) in viability assays of cells exposed to 1 mM U(VI) at pH 7.2±0.2 in the presence of various concentrations of DIC, Ca^{2+}, and Mg^{2+} (Table 3.2). A two-parameter logistic function (Equation 3.9) was fitted to the data. Standard deviations represent propagated error from fitting the exponential region of growth curves to obtain survival rates.

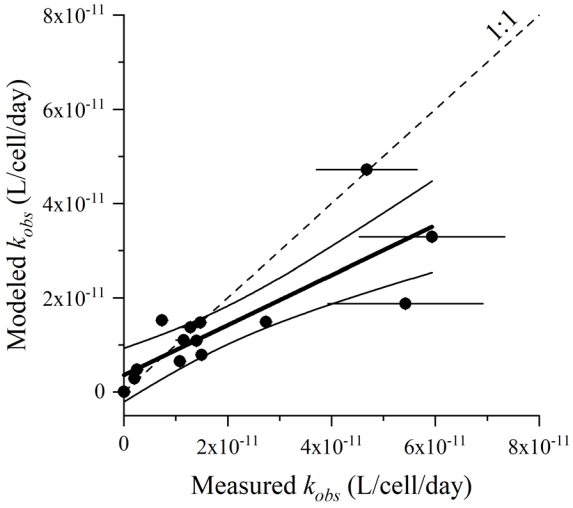

Figure B.2. Correlation between measured and modeled overall pseudo-first order rate constants k_{obs} for all bioreduction incubation conditions. A linear regression (bold solid line) was fitted to the data ($R^2 = 0.69$). The slope of the linear regression (0.53±0.10) is less than 1.0 and the y-intercept ($3.6\pm2.6\times10^{-12}$ L/cell/day) is near the origin, indicating that the model generally underpredicts k_{obs} for incubations with the largest measured values. Neglecting the three incubations with the largest measured k_{obs} values improves the correlation between modeled and measured k_{obs} ($R^2 = 0.80$) and the slope of the linear regression (0.83±0.13), reflecting the difficulty in modeling rates accurately when uranium bioreduction kinetics transitions from being controlled by bioavailability to being controlled by toxicity. Error bars represent the standard deviation of the slope of the linear regression used to obtain k_{obs} from averaged duplicate incubations or model output. Solid lines represent the 95% confidence band for the linear regression.

Table B.1. Groundwater composition at DOE IFRC sites used in aqueous uranyl speciation calculations for Figure 3.5.

	IFRC Site		
Cations (mM)	Hanford[a]	Rifle[a]	Oak Ridge[b]
Na^+	0.979	6.773	32.9
K^+			2.4
Ca^{2+}	1.195	4.786	25.1
Mg^{2+}	0.461	4.629	6.8
NH_4^+		0.044	
UO_2^{2+}	0.172	0.442	0.212
Anions (mM)			
Cl^-	0.604	2.835	7.3
NO_3^-	0.395	0.060	133
SO_4^{2-}	0.542	8.386	9.9
CO_3^{2-}	1.629	3.325	5.07[c]
pH	7.07-8.70	6.62-7.42	3.5-6.64[c]

[a] (Zachara et al., 2013)
[b] (Wu et al., 2006a)
[c] (Watson et al., 2013)

PEST Template file (caseV.tpl)

```
ptf @  # @ symbol defines model variables within PHREEQC code
Title Speciation dependent U reduction with U(IV) precipitation

Solution_master_species
U       UO2+2   0.0 238.0289    238.0289
U(+6)    UO2+2   0.0 238.0289
U_four  U_four+4     0.0 238.0289    238.0289
U_four(+4)  U_four+4   0.0 238.0289
Lac     Lac-    0.0 89.07  89.07
Lac(-1) Lac-    0.0 89.07 89.07
Ace     Ace-    0.0  59.044 59.044
Ace(-1) Ace-    0.0 59.044 59.044
Amm     AmmH+   0.0 AmmH 17.0  # represents NH4+
Bio     Bio     0.0 1 1  # represents biomass


Solution_species

UO2+2 = UO2+2
      log_k   0.0

Lac- = Lac-
      log_k   0.0

Ace- = Ace-
      log_k   0.0

U_four+4 = U_four+4
      log_k   0.0

AmmH+ = AmmH+
      log_k 0.0

Bio = Bio
      log_k   0.0

# Acids

Ace- + H+ = HAce
      log_k   4.757  #Visual Minteq

Ace- + Na+ = NaAce
      log_k   -0.12  #Visual Minteq

Ace- + Ca+2 = CaAce+
      log_k   1.18  #Visual Minteq

Lac- + H+ = HLac
      log_k   3.86  #Visual Minteq
```

```
Lac- + Ca+2 = CaLac+
      log_k   1.48  #Visual Minteq

2Lac- + Ca+2 = CaLac2
      log_k   2.48  #Visual Minteq

Lac- + Mg+2 = MgLac+
      log_k   1.37  #Visual Minteq

2Lac- + Mg+2 = MgLac2
      log_k   2.01  #Visual Minteq

Lac- + Sr+2 = SrLac+
      log_k   0.97  #Visual Minteq

2Lac- + Sr+2 = SrLac2
      log_k   1.4  #Visual Minteq

# Ammonium Species

AmmH+ = Amm + H+
      log_k -9.244

AmmH+ + SO4-2 = AmmHSO4-
      log_k 1.03  #Visual Minteq

Ca+2 + AmmH+ - H+ = CaAmm+2
      log_k -9.04  #Visual Minteq

Ca+2 + 2AmmH+ - 2H+ = Ca(Amm)2+2
      log_k -18.59  #Visual Minteq

Ba+2 + AmmH+ - H+ = BaAmm+2
      log_k -9.34  #Visual Minteq

Mg+2 + 2AmmH+ - 2H+ = Mg(Amm)2+2
      log_k -19.29  #Visual Minteq

Sr+2 + AmmH+ - H+ = SrAmm+2
      log_k -9.24  #Visual Minteq

# Uranyl Hydroxide Species

UO2+2 + H2O - H+ = UO2OH+
      log_k   -5.25  #NEA Vol 5

UO2+2 + 2H2O - 2H+ = UO2(OH)2
      log_k   -12.15  #NEA Vol 5

UO2+2 + 3H2O - 3H+ = UO2(OH)3-
      log_k   -20.25  #NEA Vol 5
```

```
UO2+2 + 4H2O - 4H+ = UO2(OH)4-2
      log_k   -32.4  #NEA Vol 5

2UO2+2 + H2O - H+ = (UO2)2OH+3
      log_k   -2.7  #NEA Vol 5

2UO2+2 + 2H2O - 2H+ = (UO2)2(OH)2+2
      log_k   -5.62  #NEA Vol 5

3UO2+2 + 4H2O - 4H+ = (UO2)3(OH)4+2
      log_k   -11.9  #NEA Vol 5

3UO2+2 + 5H2O - 5H+ = (UO2)3(OH)5+
      log_k   -15.55  #NEA Vol 5

3UO2+2 + 7H2O - 7H+ = (UO2)3(OH)7-
      log_k   -32.20  #NEA Vol 5

4UO2+2 + 7H2O - 7H+ = (UO2)4(OH)7+
      log_k   -21.90  #NEA Vol 5

# Uranyl Carbonate Species

UO2+2 + CO3-2 = UO2CO3
      log_k   9.94  #NEA Vol 5

UO2+2 + 2CO3-2 = UO2(CO3)2-2
      log_k   16.61  #NEA Vol 5

UO2+2 + 3CO3-2 = UO2(CO3)3-4
      log_k   21.84  #NEA Vol 5

3UO2+2 + 6CO3-2 = (UO2)3(CO3)6-6
      log_k   54  #NEA Vol 5

2UO2+2 + CO3-2 + 3H2O - 3H+ = (UO2)2CO3(OH)3-
      log_k   -0.855  #NEA Vol 5

3UO2+2 + CO3-2 + 3H2O - 3H+ = (UO2)3O(OH)2(HCO3)+
      log_k   0.655  #NEA Vol 5

11UO2+2 + 6CO3-2 + 12H2O - 12H+ = (UO2)11(CO3)6(OH)12-2
      log_k   -54.35  #NEA Vol 5

# Ternary Uranyl Carbonate Species

UO2+2 + Ca+2 + 3CO3-2 = CaUO2(CO3)3-2
      log_k   27.18  #Dong and Brooks, 2006

UO2+2 + 2Ca+2 + 3CO3-2 = Ca2UO2(CO3)3
      log_k   30.7  #Dong and Brooks, 2006
```

```
UO2+2 + Mg+2 + 3CO3-2 = MgUO2(CO3)3-2
      log_k   26.11  #Dong and Brooks, 2006

UO2+2 + Sr+2 + 3CO3-2 = SrUO2(CO3)3-2
      log_k   26.86  #Dong and Brooks, 2006

UO2+2 + Ba+2 + 3CO3-2 = BaUO2(CO3)3-2
      log_k   26.68  #Dong and Brooks, 2006

UO2+2 + 2Ba+2 + 3CO3-2 = Ba2UO2(CO3)3
      log_k   29.75  #Dong and Brooks, 2006

# Uranyl Acetate Species

UO2+2 + Ace- = UO2Ace+
      log_k   3.11  #Visual Minteq

UO2+2 + 2Ace- = UO2(Ace)2
      log_k   5.04  #Visual Minteq

UO2+2 + 3Ace- = UO2(Ace)3-
      log_k   7.06  #Visual Minteq

# Uranyl Lactate Species

UO2+2 + Lac- = UO2Lac+
      log_k   3.13  #Visual Minteq

UO2+2 + 2Lac- = UO2(Lac)2
      log_k   5.16  #Visual Minteq

UO2+2 + 3Lac- = UO2(Lac)3-
      log_k   6.31  #Visual Minteq

# Uranyl Chloride Species

UO2+2 + Cl- = UO2Cl+
      log_k   0.17  #NEA Vol 5

UO2+2 + 2Cl- = UO2Cl2
      log_k   -1.1  #NEA Vol 5

# Uranyl Sulfate Species

UO2+2 + SO4-2 = UO2SO4
      log_k   3.15  #NEA Vol 5

UO2+2 + 2SO4-2 = UO2(SO4)2-2
      log_k   4.14  #NEA Vol 5

UO2+2 + 3SO4-2 = UO2(SO4)3-4
```

```
      log_k   3.02  #NEA Vol 5

# Uranyl Nitrate Species

UO2+2 + NO3- = UO2NO3+
      log_k   0.3  #NEA Vol 5

# Uranyl Phosphate Species

UO2+2 + PO4-3 = UO2PO4-
      log_k   13.23  #NEA Vol 5

UO2+2 + PO4-3 + H+ = UO2HPO4
      log_k   19.59  #NEA Vol 5

UO2+2 + PO4-3 + 2H+ = UO2H2PO4+
      log_k   20.682  #NEA Vol 5

UO2+2 + PO4-3 + 3H+ = UO2H3PO4+2
      log_k   22.462  #NEA Vol 5

UO2+2 + 2PO4-3 + 4H+ = UO2(H2PO4)2
      log_k   44.044  #NEA Vol 5

UO2+2 + 2PO4-3 + 5H+ = UO2(H2PO4)(H3PO4)+
      log_k   45.054  #NEA Vol 5

# U(IV) species

U_four+4 + H2O - H+ = U_fourOH+3
      log_k   -0.54  #NEA Vol 5

U_four+4 + 4H2O - 4H+ = U_four(OH)4
      log_k   -10  #NEA Vol 5

U_four+4 + 4CO3-2 = U_four(CO3)4-4
      log_k   35.12  #NEA Vol 5

U_four+4 + 5CO3-2 = U_four(CO3)5-6
      log_k   34.00  #NEA Vol 5

U_four+4 + Cl- = U_fourCl+3
      log_k   1.72  #NEA Vol 5

U_four+4 + SO4-2 = U_fourSO4+2
      log_k   6.58  #NEA Vol 5

U_four+4 + 2SO4-2 = U_four(SO4)2
      log_k   10.51  #NEA Vol 5

U_four+4 + NO3- = U_fourNO3+3
      log_k   1.47  #NEA Vol 5
```

```
U_four+4 + 2NO3- = U_four(NO3)2+2
      log_k   2.3  #NEA Vol 5


PHASES
Gummite
      UO3 = UO2+2 + H2O - 2H+
      log_k 7.6718  #Visual Minteq

Schoepite
      UO3(H2O)2 = UO2+2 + 3H2O - 2H+
      log_k 5.39  #Visual Minteq

UO2(OH)2
      UO2(OH)2 = UO2+2 + 2H2O - 2H+
      log_k 5.6116  #Visual Minteq

UO3
      UO3 = UO2+2 + H2O - 2H+
      log_k 7.7  #Visual Minteq

Rutherfordine
      UO2CO3 = UO2+2 + CO3-2
      log_k -14.76  #NEA Vol 5

UO2(NO3)2
      UO2(NO3)2 = UO2+2 + 2NO3-
      log_k 12.1476  #Visual Minteq

UO2(NO3)2(H2O)2
      UO2(NO3)2(H2O)2 = UO2+2 + 2NO3- + 2H2O
      log_k 4.851  #Visual Minteq

UO2(NO3)2(H2O)3
      UO2(NO3)2(H2O)3 = UO2+2 + 2NO3- + 3H2O
      log_k 3.39  #Visual Minteq

UO2(NO3)2(H2O)6
      UO2(NO3)2(H2O)6 = UO2+2 + 2NO3- + 6H2O
      log_k 2.0464  #Visual Minteq

(UO2)3(PO4)2
      (UO2)3(PO4)2 = 3UO2+2 + 2PO4-3
      log_k -49.4  #Visual Minteq

Autunite
      Ca(UO2)2(PO4)2 = Ca+2 + 2UO2+2 + 2PO4-3
      log_k -43.927  #Visual Minteq

H-Autunite
      (UO2)2(HPO4)2 = 2UO2+2 + 2H+ + 2PO4-3
```

```
      log_k -47.931  #Visual Minteq

K-Autunite
      (UO2)2(KPO4)2 = 2UO2+2 + 2K+ + 2PO4-3
      log_k -48.244  #Visual Minteq

Na-Autunite
      (UO2)2(NaPO4)2 = 2UO2+2 + 2Na+ + 2PO4-3
      log_k -47.409  #Visual Minteq

Sr-Autunite
      (UO2)2Sr(PO4)2 = 2UO2+2 + Sr+2 + 2PO4-3
      log_k -44.457  #Visual Minteq

Saleeite
      (UO2)2Mg(PO4)2 = 2UO2+2 + Mg+2 + 2PO4-3
      log_k -43.646  #Visual Minteq

Uranocircite
      (UO2)2Ba(PO4)2 = 2UO2+2 + Ba+2 + 2PO4-3
      log_k -44.631  #Visual Minteq

UO2HPO4
      UO2HPO4 = UO2+2 + H+ + PO4-3
      log_k -24.225  #Visual Minteq

UO2HPO4(H2O)4
      UO2HPO4(H2O)4 = UO2+2 + H+ + PO4-3 + 4H2O
      log_k -24.202  #Visual Minteq

Uramphite
      (UO2)2(AmmH)2(PO4)2 = 2UO2+2 + 2AmmH+ + 2PO4-3
      log_k -51.749  #Visual Minteq

(UO2)3(PO4)2(H2O)4
      (UO2)3(PO4)2(H2O)4 = 3UO2+2 + 2PO4-3 + 4H2O
      log_k -49.364  #NEA Vol 5

UO2HPO4(H2O)4
      UO2HPO4(H2O)4 = UO2+2 + H+ + PO4-3 + 4H2O
      log_k -24.202

UO2SO4(H2O)2.5
      UO2SO4(H2O)2.5 = UO2+2 + SO4-2 + 2.5H2O
      log_k -1.589  #NEA Vol 5

UO2SO4(H2O)3
      UO2SO4(H2O)3 = UO2+2 + SO4-2 + 3H2O
      log_k -0.754  #NEA Vol 5

UO2SO4(H2O)3.5
      UO2SO4(H2O)3.5 = UO2+2 + SO4-2 + 3.5H2O
```

```
      log_k -1.585  #NEA Vol 5

Uraninite
      U_fourO2 = U_four+4 + 4OH- - 2H2O
      log_k -60.669   #Visual Minteq

Bio-Uraninite
      U_fourO2 = U_four+4 + 4OH- - 2H2O
      log_k -54.4  #NEA Vol 5

Ningyoite
      CaU_four(PO4)2(H2O)2 = U_four+4 + Ca+2 + 2PO4-3 + 2H2O
      log_k -53.906  #Visual Minteq

U(HPO4)2(H2O)4
      U_four(HPO4)2(H2O)4 = U_four+4 + 2H+ + 2PO4-3 + 4H2O
      log_k -55.194    #NEA Vol 5

U(OH)2SO4
      U_four(OH)2SO4 = U_four+4 + 2OH- + SO4-2
      log_k -31.17  #NEA Vol 5

fix_pH
      H+ = H+
      log_k 0


EQUILIBRIUM_PHASES 1
Bio-Uraninite   0.0 0.0
fix_pH     -6.49 HCl

EQUILIBRIUM_PHASES 2
Bio-Uraninite   0.0 0.0
fix_pH     -6.58 HCl

EQUILIBRIUM_PHASES 3
Bio-Uraninite   0.0 0.0
fix_pH     -7.19 NaOH

EQUILIBRIUM_PHASES 4
Bio-Uraninite   0.0 0.0
fix_pH     -7.61 NaOH

EQUILIBRIUM_PHASES 5
Bio-Uraninite   0.0 0.0
fix_pH     -7.60 NaOH

EQUILIBRIUM_PHASES 6
Bio-Uraninite   0.0 0.0
fix_pH     -8.16 NaOH

EQUILIBRIUM_PHASES 7
```

```
Bio-Uraninite    0.0 0.0
fix_pH     -8.07 NaOH

EQUILIBRIUM_PHASES 8
Bio-Uraninite    0.0 0.0
fix_pH     -8.09 NaOH

EQUILIBRIUM_PHASES 9
Bio-Uraninite    0.0 0.0
fix_pH     -8.29 NaOH

EQUILIBRIUM_PHASES 10
Bio-Uraninite    0.0 0.0
fix_pH     -8.17 NaOH

EQUILIBRIUM_PHASES 11
Bio-Uraninite    0.0 0.0
fix_pH     -8.17 NaOH

EQUILIBRIUM_PHASES 12
Bio-Uraninite    0.0 0.0
fix_pH     -8.14 NaOH

EQUILIBRIUM_PHASES 13
Bio-Uraninite    0.0 0.0
fix_pH     -8.04 NaOH

EQUILIBRIUM_PHASES 14
Bio-Uraninite    0.0 0.0
fix_pH     -7.93 NaOH

EQUILIBRIUM_PHASES 15
Bio-Uraninite    0.0 0.0
fix_pH     -7.87 NaOH


RATES  # defines rate law
U
-start
10    Unon  =  mol("UO2+2")  +  mol("UO2OH+")  +  mol("UO2(OH)2")  +
mol("UO2(OH)3-")   +   mol("UO2(OH)4-2")   +   mol("(UO2)2OH+3")   +
mol("(UO2)2(OH)2+2") + mol("(UO2)3(OH)4+2") + mol("(UO2)3(OH)5+")
+  mol("(UO2)3(OH)7-")  +  mol("(UO2)4(OH)7+")  +  mol("UO2Ace+")  +
mol("UO2(Ace)2")    +    mol("UO2(Ace)3-")    +    mol("UO2Lac+")    +
mol("UO2(Lac)2")    +    mol("UO2(Lac)3-")    +    mol("UO2Cl+")    +
mol("UO2Cl2")    +    mol("UO2SO4")    +    mol("UO2(SO4)2-2")    +
mol("UO2(SO4)3-4")    +    mol("UO2NO3+")    +    mol("UO2PO4-")    +
mol("UO2HPO4")    +    mol("UO2H2PO4+")    +    mol("UO2H3PO4+2")    +
mol("UO2(H2PO4)2") + mol("UO2(H2PO4)")
20   Ucarb = mol("UO2CO3") + mol("UO2(CO3)2-2") + mol("UO2(CO3)3-
4")    +    mol("(UO2)3(CO3)6-6")    +      mol("(UO2)2CO3(OH)3-")    +
mol("(UO2)3O(OH)2(HCO3)+") + mol("(UO2)11(CO3)6(OH)12-2")
```

```
30     Utern   =   mol("CaUO2(CO3)3-2")   +   mol("Ca2UO2(CO3)3")   +
mol("MgUO2(CO3)3-2") + mol("SrUO2(CO3)3-2") + mol("BaUO2(CO3)3-2")
+ mol("Ba2UO2(CO3)3")
40   knon  =   @knon     @     #L/cell/s, uranyl non-carbonate  rate
constant
50  kcarb =  @kcarb  @   #L/cell/s, uranyl carbonate rate constant
60  ktern =   @ktern  @   #L/cell/s, ternary uranyl carbonate rate
constant
80  X = mol("Bio")  #OD600
100  uranyl = mol("UO2+2")  #mol/L
110 IC = @IC      @    # IC50 for toxicity function
120 p = @p       @     # parameter for toxicity function
140 tox = 1/(1+(uranyl / IC)^p)  #percent
150  rate = tox * X * 2E9 * 1E3 * (knon * Unon + kcarb * Ucarb +
ktern * Utern)  #mol/L/s
160  moles = rate * TIME
200 SAVE moles
-end

# Unit conversions for rate law
# 2E9 cell/mL/(1 OD600)
# 1E3 mL/L
# converts X (OD600) to cell/L


KINETICS 1  # defines reaction stoichiometry associated with rate
law

U
        -Formula  U+6 -2.0   U_four 2.0   Lac -1.0   Ace 1.0   C+4
1.0
        -steps 0 21600 21600 21600 21600 21600 21600 21600 21600
21600 21600 21600 21600 21600 21600 21600 21600 21600 21600 21600
21600 21600 21600 21600 21600 21600 21600 21600 21600 21600 21600
21600 21600 21600 21600 21600 21600 21600 21600 21600 21600 21600
21600 21600 21600 21600 21600 21600 21600 21600 21600 21600 21600
21600 21600 21600 21600 21600 21600 21600 21600 21600 21600 21600
21600 21600 21600 21600 21600 21600 21600 21600 21600 21600 21600
     -step_divide 1e-4
END


INCREMENTAL_REACTIONS true


SELECTED_OUTPUT
        -file caseV.prn #name of output file
        -reset false
```

```
USER_PUNCH  #defines content of output file
-headings  time(day)  Ud(umol/L)  pH  uranyl(mol/L)  Unon(mol/L)
Ucarb(mol/L) Utern(mol/L) CaUcarb(mol/L) MgUcarb(mol/L) UOH(mol/L)
10 PUNCH TOTAL_TIME/60/60/24
20 PUNCH (TOT("U")+TOT("U_four"))*1000*1000
40 pH = -LA("H+")
50 PUNCH pH
60 uranyl = mol("UO2+2")
70 PUNCH uranyl
80  Unon  =  mol("UO2+2")  +  mol("UO2OH+")  +  mol("UO2(OH)2")  +
mol("UO2(OH)3-")  +  mol("UO2(OH)4-2")  +  mol("(UO2)2OH+3")  +
mol("(UO2)2(OH)2+2") + mol("(UO2)3(OH)4+2") + mol("(UO2)3(OH)5+")
+ mol("(UO2)3(OH)7-") + mol("(UO2)4(OH)7+") + mol("UO2Ace+") +
mol("UO2(Ace)2")  +  mol("UO2(Ace)3-")  +  mol("UO2Lac+")  +
mol("UO2(Lac)2")  +  mol("UO2(Lac)3-")  +  mol("UO2Cl+")  +
mol("UO2Cl2")  +  mol("UO2SO4")  +  mol("UO2(SO4)2-2")  +
mol("UO2(SO4)3-4")  +  mol("UO2NO3+")  +  mol("UO2PO4-")  +
mol("UO2HPO4")  +  mol("UO2H2PO4+")  +  mol("UO2H3PO4+2")  +
mol("UO2(H2PO4)2") + mol("UO2(H2PO4)")
90 PUNCH Unon
100 Ucarb = mol("UO2CO3") + mol("UO2(CO3)2-2") + mol("UO2(CO3)3-
4")  +  mol("(UO2)3(CO3)6-6")  +  mol("(UO2)2CO3(OH)3-")  +
mol("(UO2)3O(OH)2(HCO3)+") + mol("(UO2)11(CO3)6(OH)12-2")
110 PUNCH Ucarb
120  Utern  =  mol("CaUO2(CO3)3-2")  +  mol("Ca2UO2(CO3)3")  +
mol("MgUO2(CO3)3-2") + mol("SrUO2(CO3)3-2") + mol("BaUO2(CO3)3-2")
+ mol("Ba2UO2(CO3)3")
130 PUNCH Utern
140 CaUcarb = mol("CaUO2(CO3)3-2") + mol("Ca2UO2(CO3)3")
150 PUNCH CaUcarb
160 MgUcarb = mol("MgUO2(CO3)3-2")
170 PUNCH MgUcarb
180  UOH  =  mol("UO2+2")  +  mol("UO2OH+")  +  mol("UO2(OH)2")  +
mol("UO2(OH)3-")  +  mol("UO2(OH)4-2")  +  mol("(UO2)2OH+3")  +
mol("(UO2)2(OH)2+2") + mol("(UO2)3(OH)4+2") + mol("(UO2)3(OH)5+")
+ mol("(UO2)3(OH)7-") + mol("(UO2)4(OH)7+")
270 PUNCH UOH
-end


SOLUTION 1 pH 6.5, 30 mM DIC
units mol/L
water 0.1 # L
pH       6.49
C(+4)    0.0229
Na       0.04461  #1x C, 1x Lac, 0.00001 NaCl
U(+6)    0.000735
Lac      0.015
Ace      0.0016 #2x U(VI)
Ca       0
S     0.00015 #0.5x Amm, 1x Mg
Cl    0.00001 # 0.00001 NaCl, 2x Ca,
```

```
Mg     0.0001
Amm      0.0001
P      0.0001
K      0.0001
Bio    0.021

USE KINETICS 1
USE EQUILIBRIUM_PHASES 1
END

SOLUTION 2 pH 6.5, 45 mM DIC
units mol/L
water 0.1 # L
pH       6.58
C(+4)    0.0361
Na       0.05871  #1x C, 1x Lac, 0.00001 NaCl
U(+6)    0.000742
Lac      0.015
Ace      0.0016 #2x U(VI)
Ca       0
S      0.00015 #0.5x Amm, 1x Mg
Cl     0.00001 # 0.01 NaCl, 2x Ca,
Mg     0.0001
Amm      0.0001
P      0.0001
K      0.0001
Bio    0.015

USE KINETICS 1
USE EQUILIBRIUM_PHASES 2
END

SOLUTION 3 pH 7.5, 15 mM DIC
units mol/L
water 0.1 # L
pH       7.24
C(+4)    0.0129
Na       0.03001  #1x C, 1x Lac, 0.00001 NaCl
U(+6)    0.000391
Lac      0.015
Ace      0.0016 #2x U(VI)
Ca       0
S      0.00015 #0.5x Amm, 1x Mg
Cl     0.00001 # 0.01 NaCl, 2x Ca,
Mg     0.0001
Amm      0.0001
P      0.0001
K      0.0001
Bio    0.022

USE KINETICS 1
USE EQUILIBRIUM_PHASES 3
```

```
END

SOLUTION 4 pH 7.5, 30 mM DIC
units mol/L
water 0.1 # L
pH       7.61
C(+4)    0.0219
Na       0.04461  #1x C, 1x Lac, 0.00001 NaCl
U(+6)    0.000587
Lac      0.015
Ace      0.0016 #2x U(VI)
Ca       0
S      0.00015 #0.5x Amm, 1x Mg
Cl     0.00001 # 0.01 NaCl, 2x Ca,
Mg     0.0001
Amm      0.0001
P      0.0001
K      0.0001
Bio    0.021

USE KINETICS 1
USE EQUILIBRIUM_PHASES 4
END

SOLUTION 5 pH 7, 45 mM DIC
units mol/L
water 0.1 # L
pH       7.60
C(+4)    0.0346
Na       0.05871  #1x C, 1x Lac, 0.00001 NaCl
U(+6)    0.000550
Lac      0.015
Ace      0.0016 #2x U(VI)
Ca       0
S      0.00015 #0.5x Amm, 1x Mg
Cl     0.00001 # 0.01 NaCl, 2x Ca,
Mg     0.0001
Amm      0.0001
P      0.0001
K      0.0001
Bio    0.021

USE KINETICS 1
USE EQUILIBRIUM_PHASES 5
END

SOLUTION 6 pH 8.1, 15 mM DIC
units mol/L
water 0.1 # L
pH       8.16
C(+4)    0.0103
Na       0.03001  #1x C, 1x Lac, 0.00001 NaCl
```

```
U(+6)     0.000556
Lac       0.015
Ace       0.0016 #2x U(VI)
Ca        0
S      0.00015 #0.5x Amm, 1x Mg
Cl     0.00001 # 0.01 NaCl, 2x Ca,
Mg     0.0001
Amm       0.0001
P      0.0001
K      0.0001
Bio    0.022

USE KINETICS 1
USE EQUILIBRIUM_PHASES 6
END

SOLUTION 7 pH 8.1, 30 mM DIC
units mol/L
water 0.1 # L
pH        8.07
C(+4)     0.0231
Na        0.04461  #1x C, 1x Lac, 0.00001 NaCl
U(+6)     0.000601
Lac       0.015
Ace       0.0016 #2x U(VI)
Ca        0
S      0.00015 #0.5x Amm, 1x Mg
Cl     0.00001 # 0.01 NaCl, 2x Ca,
Mg     0.0001
Amm       0.0001
P      0.0001
K      0.0001
Bio    0.021

USE KINETICS 1
USE EQUILIBRIUM_PHASES 7
END

SOLUTION 8 pH 8.1, 45 mM DIC
units mol/L
water 0.1 # L
pH        8.10
C(+4)     0.0387
Na        0.05871  #1x C, 1x Lac, 0.00001 NaCl
U(+6)     0.000527
Lac       0.015
Ace       0.0016 #2x U(VI)
Ca        0
S      0.00015 #0.5x Amm, 1x Mg
Cl     0.00001 # 0.01 NaCl, 2x Ca,
Mg     0.0001
Amm       0.0001
```

```
P      0.0001
K      0.0001
Bio    0.021

USE KINETICS 1
USE EQUILIBRIUM_PHASES 8
END

SOLUTION 9 pH 8.1, 25 mM DIC, 0.0 mM Ca
units mol/L
water 0.1 # L
pH       8.29
C(+4)    0.0185
Na       0.04001  #1x C, 1x Lac, 0.00001 NaCl
U(+6)    0.000523
Lac      0.015
Ace      0.0016 #2x U(VI)
Ca       0
S      0.00005 #0.5x Amm, 1x Mg
Cl     0.00001 # 0.01 NaCl, 2x Ca,
Mg     0.0
Amm      0.0001
P      0.0001
K      0.0001
Bio    0.027

USE KINETICS 1
USE EQUILIBRIUM_PHASES 9
END

SOLUTION 10      pH 8.1, 25 mM DIC, 0.5 mM Ca
units mol/L
water 0.1 # L
pH       8.20
C(+4)    0.0174
Na       0.04001  #1x C, 1x Lac, 0.00001 NaCl
U(+6)    0.000506
Lac      0.015
Ace      0.0016 #2x U(VI)
Ca       0.0005
S      0.00005 #0.5x Amm, 1x Mg
Cl     0.00101 # 0.00001 NaCl, 2x Ca,
Mg     0.0
Amm      0.0001
P      0.0001
K      0.0001
Bio    0.027

USE KINETICS 1
USE EQUILIBRIUM_PHASES 10
END
```

```
SOLUTION 11      pH 8.1, 25 mM DIC, 1 mM Ca
units mol/L
water 0.1 # L
pH       8.14
C(+4)    0.0173
Na       0.04001  #1x C, 1x Lac, 0.00001 NaCl
U(+6)    0.000729
Lac      0.015
Ace      0.0016 #2x U(VI)
Ca       0.001
S      0.00005 #0.5x Amm, 1x Mg
Cl     0.00201 # 0.01 NaCl, 2x Ca,
Mg     0.0
Amm      0.0001
P      0.0001
K      0.0001
Bio    0.027

USE KINETICS 1
USE EQUILIBRIUM_PHASES 11
END

SOLUTION 12      pH 8.1, 25 mM DIC, 5 mM Ca
units mol/L
water 0.1 # L
pH       8.15
C(+4)    0.0172
Na       0.04001  #1x C, 1x Lac, 0.00001 NaCl
U(+6)    0.000726
Lac      0.015
Ace      0.0016 #2x U(VI)
Ca       0.0049
S      0.00005 #0.5x Amm, 1x Mg
Cl     0.00981 # 0.01 NaCl, 2x Ca,
Mg     0.0
Amm      0.0001
P      0.0001
K      0.0001
Bio    0.026

USE KINETICS 1
USE EQUILIBRIUM_PHASES 12
END

SOLUTION 13      pH 8.1, 20 mM DIC, 0 mM Mg
units mol/L
water 0.1 # L
pH       8.04
C(+4)    0.0188
Na       0.03491  #1x C, 1x Lac, 0.00001 NaCl
U(+6)    0.000563
Lac      0.015
```

```
Ace       0.0016 #2x U(VI)
Ca        0.0
S      0.00015 #0.5x Amm, 1x Mg
Cl     0.00001 # 0.01 NaCl, 2x Ca,
Mg     0.0001
Amm       0.0001
P      0.0001
K      0.0001
Bio    0.022

USE KINETICS 1
USE EQUILIBRIUM_PHASES 13
END

SOLUTION 14      pH 8.1, 20 mM DIC, 1 mM Mg
units mol/L
water 0.1 # L
pH        7.91
C(+4)     0.0182
Na        0.03491  #1x C, 1x Lac, 0.00001 NaCl
U(+6)     0.000464
Lac       0.015
Ace       0.0016 #2x U(VI)
Ca        0.0
S      0.00115 #0.5x Amm, 1x Mg
Cl     0.00001 # 0.01 NaCl, 2x Ca,
Mg     0.0011
Amm       0.0001
P      0.0001
K      0.0001
Bio    0.022

USE KINETICS 1
USE EQUILIBRIUM_PHASES 14
END

SOLUTION 15      pH 8.1, 20 mM DIC, 5 mM Mg
units mol/L
water 0.1 # L
pH        7.86
C(+4)     0.0184
Na        0.03471  #1x C, 1x Lac, 0.00001 NaCl
U(+6)     0.000495
Lac       0.015
Ace       0.0016 #2x U(VI)
Ca        0.0
S      0.00515 #0.5x Amm, 1x Mg
Cl     0.00001 # 0.01 NaCl, 2x Ca,
Mg     0.0051
Amm       0.0001
P      0.0001
K      0.0001
```

```
Bio    0.021

USE KINETICS 1
USE EQUILIBRIUM_PHASES 15
END
```

PEST Instruction file (caseV.ins)

```
pif @
@time@
l2 w w !U100!
l2 w w !U101!
l6 w w !U102!
l4 w w !U103!
l3 w w !U104!
l4 w w !U105!
l4 w w !U106!
l4 w w !U107!
l4 w w !U108!
l8 w w !U109!
l4 w w !U110!
l3 w w !U111!
l9 w w !U112!
l21 w w !U200!
l2 w w !U201!
l6 w w !U202!
l4 w w !U203!
l3 w w !U204!
l4 w w !U205!
l4 w w !U206!
l4 w w !U207!
l4 w w !U208!
l8 w w !U209!
l4 w w !U210!
l3 w w !U211!
l9 w w !U212!
l21 w w !U300!
l4 w w !U301!
l4 w w !U302!
l4 w w !U303!
l8 w w !U304!
l56 w w !U400!
l4 w w !U401!
l4 w w !U402!
l8 w w !U403!
l4 w w !U404!
l20 w w !U405!
```

```
l12 w w !U406!
l24 w w !U500!
l4 w w !U501!
l4 w w !U502!
l8 w w !U503!
l4 w w !U504!
l16 w w !U505!
l13 w w !U506!
l27 w w !U600!
l4 w w !U601!
l4 w w !U602!
l4 w w !U603!
l12 w w !U604!
l8 w w !U605!
l44 w w !U700!
l4 w w !U701!
l4 w w !U702!
l4 w w !U703!
l4 w w !U704!
l16 w w !U705!
l16 w w !U706!
l28 w w !U800!
l4 w w !U801!
l4 w w !U802!
l4 w w !U803!
l4 w w !U804!
l4 w w !U805!
l4 w w !U806!
l4 w w !U807!
l12 w w !U808!
l36 w w !U900!
l4 w w !U901!
l4 w w !U902!
l7 w w !U903!
l9 w w !U904!
l7 w w !U905!
l45 w w !U1000!
l8 w w !U1001!
l8 w w !U1002!
l7 w w !U1003!
l53 w w !U1100!
l4 w w !U1101!
l4 w w !U1102!
l4 w w !U1103!
l4 w w !U1104!
l8 w w !U1105!
l4 w w !U1106!
l4 w w !U1107!
l8 w w !U1108!
l8 w w !U1109!
l7 w w !U1110!
l21 w w !U1200!
```

```
l4 w w !U1201!
l4 w w !U1202!
l4 w w !U1203!
l4 w w !U1204!
l8 w w !U1205!
l4 w w !U1206!
l4 w w !U1207!
l8 w w !U1208!
l8 w w !U1209!
l7 w w !U1210!
l21 w w !U1300!
l2 w w !U1301!
l2 w w !U1302!
l7 w w !U1303!
l65 w w !U1400!
l2 w w !U1401!
l2 w w !U1402!
l2 w w !U1403!
l2 w w !U1404!
l4 w w !U1405!
l64 w w !U1500!
l2 w w !U1501!
l2 w w !U1502!
l2 w w !U1503!
l2 w w !U1504!
l4 w w !U1505!
```

PEST control file (caseV.pst)

```
pcf
* control data
restart estimation
5 115 1 0 1
1 1 single point 1 0 0
10.0 2.0 0.3 0.03 10 999
3.0 3.0 0.001
0.1
30 0.001 3 3 0.01 3
1 1 1
* parameter groups
k relative 1e-2 0.0 switch 2 parabolic
* parameter data
knon  log factor 3.96e-12 1e-30 1 k 1.0 0.0 1
kcarb log factor 6.25e-18 1e-30 1 k 1.0 0.0 1
ktern log factor 1.58e-18 1e-30 1 k 1.0 0.0 1
IC    log factor 1.02e-12 1e-30 1 k 1.0 0.0 1
p     log factor 1.68 0.1 5 k 1.0 0.0 1
```

```
* observation groups
group_1
* observation data
U100  607.1 1     group_1
U101  746.6 1     group_1
U102  785.2 1     group_1
U103  663.4 1     group_1
U104  772.0 1     group_1
U105  736.8 1     group_1
U106  738.3 1     group_1
U107  703.7 1     group_1
U108  746.5 1     group_1
U109  750.2 1     group_1
U110  725.2 1     group_1
U111  744.3 1     group_1
U112  731.6 1     group_1
U200  747.1 1     group_1
U201  749.2 1     group_1
U202  741.0 1     group_1
U203  755.9 1     group_1
U204  769.1 1     group_1
U205  727.1 1     group_1
U206  713.8 1     group_1
U207  757.7 1     group_1
U208  753.2 1     group_1
U209  754.5 1     group_1
U210  732.7 1     group_1
U211  736.1 1     group_1
U212  739.9 1     group_1
U300  391.3 1     group_1
U301  197.0 1     group_1
U302  127.3 1     group_1
U303  57.1  1     group_1
U304  9.2   1     group_1
U400  587.1 1     group_1
U401  249.3 1     group_1
U402  1.8   1     group_1
U403  0.0   1     group_1
U404  0.0   1     group_1
U405  0.0   1     group_1
U406  10.1  1     group_1
U500  550.2 1     group_1
U501  437.9 1     group_1
U502  287.7 1     group_1
U503  25.1  1     group_1
U504  0.3   1     group_1
U505  7.3   1     group_1
U506  0.8   1     group_1
U600  556.3 1     group_1
U601  246.9 1     group_1
U602  6.3   1     group_1
U603  4.6   1     group_1
```

U604	0.4	1	group_1
U605	2.7	1	group_1
U700	605.6	1	group_1
U701	472.3	1	group_1
U702	178.1	1	group_1
U703	4.5	1	group_1
U704	0.6	1	group_1
U705	0.1	1	group_1
U706	7.5	1	group_1
U800	527.0	1	group_1
U801	300.5	1	group_1
U802	284.8	1	group_1
U803	107.4	1	group_1
U804	13.0	1	group_1
U805	2.4	1	group_1
U806	2.8	1	group_1
U807	8.6	1	group_1
U808	0.0	1	group_1
U900	522.9	1	group_1
U901	282.7	1	group_1
U902	100.0	1	group_1
U903	6.6	1	group_1
U904	6.4	1	group_1
U905	10.2	1	group_1
U1000	505.8	1	group_1
U1001	296.2	1	group_1
U1002	63.7	1	group_1
U1003	12.8	1	group_1
U1100	728.9	1	group_1
U1101	744.1	1	group_1
U1102	583.0	1	group_1
U1103	556.5	1	group_1
U1104	495.9	1	group_1
U1105	316.6	1	group_1
U1106	238.6	1	group_1
U1107	87.0	1	group_1
U1108	8.8	1	group_1
U1109	7.3	1	group_1
U1110	4.8	1	group_1
U1200	725.8	1	group_1
U1201	669.6	1	group_1
U1202	576.5	1	group_1
U1203	542.8	1	group_1
U1204	460.4	1	group_1
U1205	265.1	1	group_1
U1206	230.9	1	group_1
U1207	108.0	1	group_1
U1208	53.9	1	group_1
U1209	7.5	1	group_1
U1210	6.0	1	group_1
U1300	562.6	1	group_1
U1301	371.5	1	group_1

```
U1302 30.7  1     group_1
U1303 0.0   1     group_1
U1400 463.6 1     group_1
U1401 251.0 1     group_1
U1402 154.9 1     group_1
U1403 72.5  1     group_1
U1404 7.2   1     group_1
U1405 0.4   1     group_1
U1500 494.7 1     group_1
U1501 371.0 1     group_1
U1502 273.7 1     group_1
U1503 174.9 1     group_1
U1504 82.7  1     group_1
U1505 0.5   1     group_1
* model command line
Phreeqc                     caseV.phrq                     caseV.out
C:\Users\kbelli3\Desktop\USGS\phreeqc-3.4.0-12927-
x64\database\phreeqc.dat scr.out
* model input/output
caseV.tpl caseV.phrq
caseV.ins caseV.prn
* prior information
```

Windows Batch File (caseV.bat)

```
@echo on
pest caseV
pause
```

APPENDIX C. SUPPLEMENTARY DATA FOR CHAPTER 4

Details of redox potential (E_h) calculations at each sampled time point in batch incubations with S. putrefaciens

Redox potentials (E_h) of the U(VI)/U(IV)$_{mono}$ and $Fe(OH)_3$/Fe(II) redox couples were calculated at each sampled time point as shown in Figure 4.6 of the manuscript. These calculations require values for concentrations of individual aqueous U(VI) and Fe(II) species along with concentrations of HCO_3^-, Ca^{2+}, Mg^{2+}, and H^+. Equilibrium calculations were performed with PHREEQC to obtain concentrations of the necessary species at each time point.

PHREEQC requires the solution composition of the system as input. In addition to the background medium, measured concentrations of dissolved Fe(II) and total dissolved uranium (assumed to be U(VI)), calcium, magnesium, silica, and pH were known at each time point. Initial concentrations of lactate, acetate, and DIC at the time of inoculation were either known (lactate and acetate) or measured (DIC). 15 mM lactate was supplied in all incubations. The initial concentration of acetate for incubations containing U(VI) was 360 μM, as 180 μM $UO_2(acetate)_2$ was the source of U(VI) in these incubations. For ferrihydrite-only incubations, the initial concentration of acetate was set to 1×10^{-6} M. Over the course of the incubation, lactate was consumed and acetate and DIC were produced by respiration of U(VI) and Fe(III). Thus, total concentrations of lactate, acetate, and DIC at each time point were calculated from their initial values assuming they were consumed (lactate) or produced (acetate and DIC) proportionally to the removal of uranium and/or production of Fe(II) in accordance with reaction stoichiometry of U(VI) and ferrihydrite

respiration. Due to abiotic U(IV) oxidation by ferrihydrite, the production of Fe(II) in incubations containing both U(VI) and ferrihydrite cannot be assumed to be due entirely to respiration. Thus, for incubations containing both U(VI) and ferrihydrite, concentrations of lactate, acetate, and DIC were calculated using Fe(II) production from the ferrihydrite-only incubation of the same condition. This assumption did not have a significant impact on the final values of E_h.

Growth medium composition along with the calculated concentrations of total lactate, acetate, DIC and measured concentrations of dissolved Fe(II), and total dissolved uranium, calcium, magnesium, silica, and pH at each time point were entered as input variables in PHREEQC. Redox equilibrium between components was not considered in the PHREEQC calculations. The non-redox equilibrium concentrations of the required aqueous species (PHREEQC output) were then used to calculate the E_h of the U(VI)/$U(IV)_{mono}$ and Fe(III)/Fe(II) redox couples for the most abundant aqueous U(VI) and Fe(II) complexes as reactants of U(VI) reduction and products of ferrihydrite reduction, respectively, using the E_h^0 values listed in Table C.1 as described in Chapter 4 section 4.3.6.

Table C.1. Standard state redox potentials (E_h^0) for half-reactions of U(VI)/UO_2(am), $Fe(OH)_3$/Fe(II), and U(VI)/$U(IV)_{mono}$ redox couples used to calculate the overall E_h at each sampled time point

Half-reaction	E_h^0 (V)[a]	U(VI)/$U(IV)_{mono}$ E_h^0 (V)[b]
$UO_2(OH)_2 + 2H^+ + 2e^- \rightarrow UO_2(am) + 2H_2O$	0.581	0.497
$UO_2(OH)_3^- + 3H^+ + 2e^- \rightarrow UO_2(am) + 3H_2O$	0.821	0.737
$UO_2PO_4^- + H^+ + 2e^- \rightarrow UO_2(am) + HPO_4^{2-}$	0.196	0.112
$UO_2CO_3 + H^+ + 2e^- \rightarrow UO_2(am) + HCO_3^-$	0.233	0.149
$UO_2(CO_3)_2^{2-} + 2H^+ + 2e^- \rightarrow UO_2(am) + 2HCO_3^-$	0.341	0.257
$UO_2(CO_3)_3^{4-} + 3H^+ + 2e^- \rightarrow UO_2(am) + 3HCO_3^-$	0.492	0.408
$MgUO_2(CO_3)_3^{2-} + 3H^+ + 2e^- \rightarrow UO_2(am) + 3HCO_3^- + Mg^{2+}$	0.366	0.282
$CaUO_2(CO_3)_3^{2-} + 3H^+ + 2e^- \rightarrow UO_2(am) + 3HCO_3^- + Ca^{2+}$	0.340	0.256
$Ca_2UO_2(CO_3)_3 + 3H^+ + 2e^- \rightarrow UO_2(am) + 3HCO_3^- + 2Ca^{2+}$	0.241	0.157
$Fe(OH)_3(s) + 3H^+ + e^- \rightarrow Fe^{2+} + 3H_2O$	0.848	
$Fe(OH)_3(s) + 2H^+ + e^- \rightarrow FeOH^+ + 2H_2O$	0.286	
$Fe(OH)_3(s) + 3H^+ + Cl^- + e^- \rightarrow FeCl^+ + 3H_2O$	0.856	
$Fe(OH)_3(s) + 3H^+ + SO_4^{2-} + e^- \rightarrow FeSO4 + 3H_2O$	0.981	
$Fe(OH)_3(s) + 4H^+ + SO_4^{2-} + e^- \rightarrow FeHSO_4 + 3H_2O$	1.029	
$Fe(OH)_3(s) + 3H^+ + HPO_4^{2-} + e^- \rightarrow FeHPO_4 + 3H_2O$	1.061	
$Fe(OH)_3(s) + 4H^+ + HPO_4^{2-} + e^- \rightarrow FeH_2PO_4^+ + 3H_2O$	1.434	
$Fe(OH)_3(s) + 2H^+ + HCO_3^- + e^- \rightarrow FeCO_3 + 3H_2O$	0.496	
$Fe(OH)_3(s) + 3H^+ + HCO_3^- + e^- \rightarrow FeHCO_3^+ + 3H_2O$	0.966	

[a]U(VI)/UO_2(am) E_h^0 values were calculated using published thermodynamic data for aqueous U(VI) complexes and amorphous uraninite (Guillaumont et al., 2003)
[b]U(VI)/$U(IV)_{mono}$ E_h^0 values were calculated by decreasing the U(VI)/UO_2(am) E_h^0 values by 84 mV to reflect the lower redox potential of the monomeric U(IV) solid phase formed in the incubations. U(VI)/$U(IV)_{mono}$ E_h^0 values were used for all thermodynamic calculations included in the kinetic model and the ΔG_r and E_h values presented in Figure 4.4 and Figure 4.6 of Chapter 4.

Table C.2. Surface complexation constants included in PHREEQC[a]

Sorbent	Sorbate	Complex[b]	log K	Source
Ferrihydrite	H^+	Hfo_sOH_2^+	7.29	Dzombak and Morel, 1990
Ferrihydrite	H^+	Hfo_sO^-	-8.93	Dzombak and Morel, 1990
Ferrihydrite	H^+	Hfo_wOH_2^+	7.29	Dzombak and Morel, 1990
Ferrihydrite	H^+	Hfo_wO^-	-8.93	Dzombak and Morel, 1990
Ferrihydrite	UO_2^{2+}	$(Hfo\_sO)_2UO_2$	-2.78	Waite et al., 1994[c]
Ferrihydrite	UO_2^{2+}	$(Hfo\_wO)_2UO_2$	-6.49	Waite et al., 1994[c]
Ferrihydrite	UO_2^{2+}	$(Hfo\_sO)_2UO_2CO_3^{2-}$	3.03	Waite et al., 1994[c]
Ferrihydrite	UO_2^{2+}	$(Hfo\_wO)_2UO_2CO_3^{2-}$	-1.06	Waite et al., 1994[c]
Ferrihydrite	Fe^{2+}	Hfo_wOFe^+	-2.98	Appelo et al., 2002
Ferrihydrite	Fe^{2+}	Hfo_wOFeOH	-11.55	Appelo et al., 2002
Ferrihydrite	Fe^{2+}	Hfo_sOFe^+	-0.95	Appelo et al., 2002
Ferrihydrite	CO_3^{2-}	Hfo_wOCO_2^-	12.78	Appelo et al., 2002
Ferrihydrite	CO_3^{2-}	Hfo_wOCO_2H	20.37	Appelo et al., 2002
Ferrihydrite	H_4SiO_4	Hfo_wH_3SiO_4	4.28	Swedlund and Webster, 1999
Ferrihydrite	H_4SiO_4	Hfo_w$H_2SiO_4^-$	-3.22	Swedlund and Webster, 1999
Ferrihydrite	H_4SiO_4	Hfo_w$HSiO_4^{2-}$	-11.69	Swedlund and Webster, 1999
Ferrihydrite	Mg^{2+}	Hfo_wOMg^+	-4.60	PHREEQC Database[d]
Ferrihydrite	SO_4^{2-}	Hfo_wSO_4^-	7.78	PHREEQC Database[d]
Ferrihydrite	SO_4^{2-}	Hfo_w$OHSO_4^{2-}$	0.79	PHREEQC Database[d]
Magnetite	H^+	MagOH_2^+	5.10	Missana et al., 2003
Magnetite	H^+	MagO^-	-9.10	Missana et al., 2003
Magnetite	UO_2^{2+}	MagOUO_2^+	-0.10	Missana et al., 2003
Magnetite	UO_2^{2+}	MagOUO_2OH	-5.40	Missana et al., 2003
Magnetite	Fe^{2+}	MagOFeOH	-10.30	Klausen et al., 1995[e]

[a] PHREEQC internally corrects complexation constants for ionic strength and uses an exponent of 1 for unoccupied surface species (e.g. Hfo_sOH) in mass action equations of bidentate surface complexes. All surface complexation constants were taken from experimental studies that included a diffuse double layer adsorption model.

[b] Hfo_s and Hfo_w represent strong and weak ferrihydrite surface sites, respectively. Mag represents magnetite surface sites.

[c] Values have been corrected to I=0.

[d] (USGS, 2012)

[e] Data from Klausen et al. (1995) Figure 5 were digitized and fitted with a diffuse double layer, single site adsorption model to obtain the surface complexation constant for the MagOFeOH surface complex. The adsorption model was implemented in PHREEQC and optimized in PEST. Two variables were optimized: the logK of MagOFe_diOH (-10.30) and the number of surface sites (0.11 mol sites/mol Fe_3O_4).

Table C.3. Mineral surface properties of iron oxides included in the PHREEQC surface complexation model

Mineral	Site Density	Surface Area	Reference
Ferrihydrite	0.873 mol weak sites/mol $Fe(OH)_3$ 0.0018 mol strong sites/mol $Fe(OH)_3$	600 m^2/g	Waite et al., 1994; Dzombak and Morel, 1990
Magnetite	0.11 mol sites/mol	56 m^2/g	Klausen et al., 1995

Table C.4. Measured initial solution composition and calculated aqueous uranyl speciation assuming thermodynamic equilibrium in batch incubations with *S. putrefaciens*

Incubation	[DIC] (mM)	[Ca_d] (μM)	[Si_d] (μM)	[U_d] (μM)	[$U(VI)_{non\text{-}carb}$] (%)	[$U(VI)_{carb}$] (%)	[$U(VI)_{tern}$] (%)
+U20	19.6±0.3			164±7	6.3×10^{-5}	58	42
+U+Fe20	19.8±0.5			147±2	6.0×10^{-5}	58	42
+U40	39.1±0.6			171±3	6.1×10^{-6}	69	31
+U+Fe40	37.2±0.3			162±2	7.3×10^{-6}	68	32
+U+Ca20	18.9±0.8	814±51		171±9	1.3×10^{-5}	11	89
+U+Fe+Ca20	19.5±0.6	87±18		135±1	4.8×10^{-5}	44	56
+U+Ca40	36.8±0.4	778±10		176±9	1.9×10^{-6}	18	82
+U+Fe+Ca40	37.9±0.7	38±8		147±3	6.2×10^{-6}	62	38
+U+Si20	19.4±0.8		301±3	169±1	6.5×10^{-5}	58	42
+U+Fe+Si20	19.4±0.7		109±1	143±2	6.4×10^{-5}	57	43
+U+Si40	37.0±0.4		300±3	175±2	7.5×10^{-6}	68	32
+U+Fe+Si40	37.0±0.6		120±2	158±2	7.4×10^{-6}	68	32

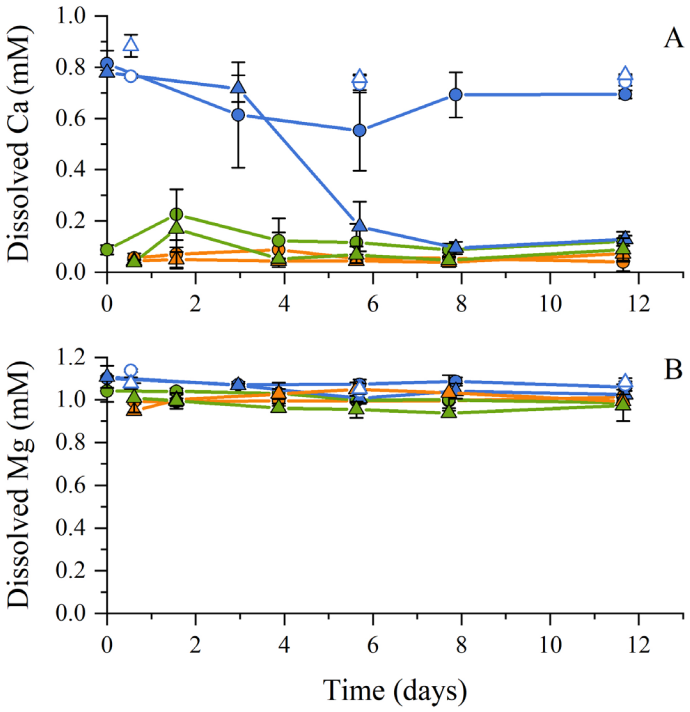

Figure C.1. Time series of (A) dissolved calcium and (B) dissolved magnesium in incubations with *S. putrefaciens* amended with 800 µM calcium, 20 mM (circles) or 40 mM DIC (triangles), and either 180 µM U(VI) (blue), 5 mM ferrihydrite (orange), or both (green) as terminal electron acceptors. Filled symbols and lines represent biotic incubations and open symbols represent abiotic controls. Symbols and error bars represent the average and standard deviation of measurements from triplicate incubations.

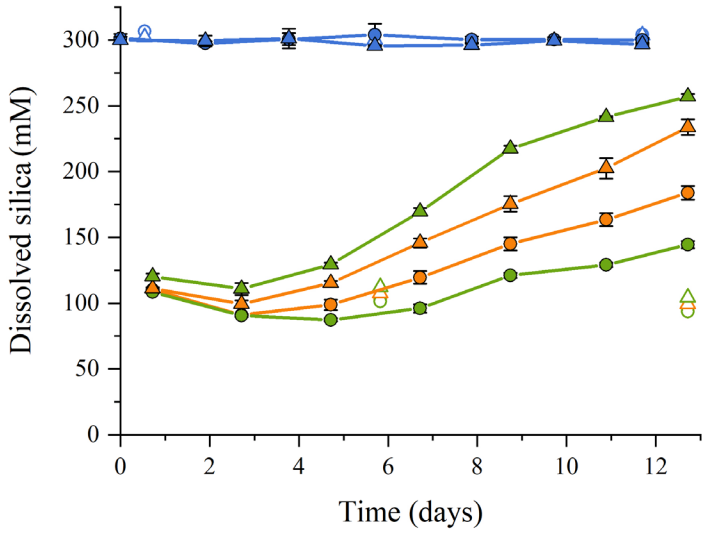

Figure C.2. Time series of dissolved silica in incubations with *S. putrefaciens* amended with 300 µM silica, 20 mM (circles) or 40 mM DIC (triangles), and either 180 µM U(VI) (blue), 5 mM ferrihydrite (orange), or both (green) as terminal electron acceptors. Filled symbols and lines represent biotic incubations and open symbols represent abiotic controls. Symbols and error bars represent the average and standard deviation of measurements from triplicate incubations.

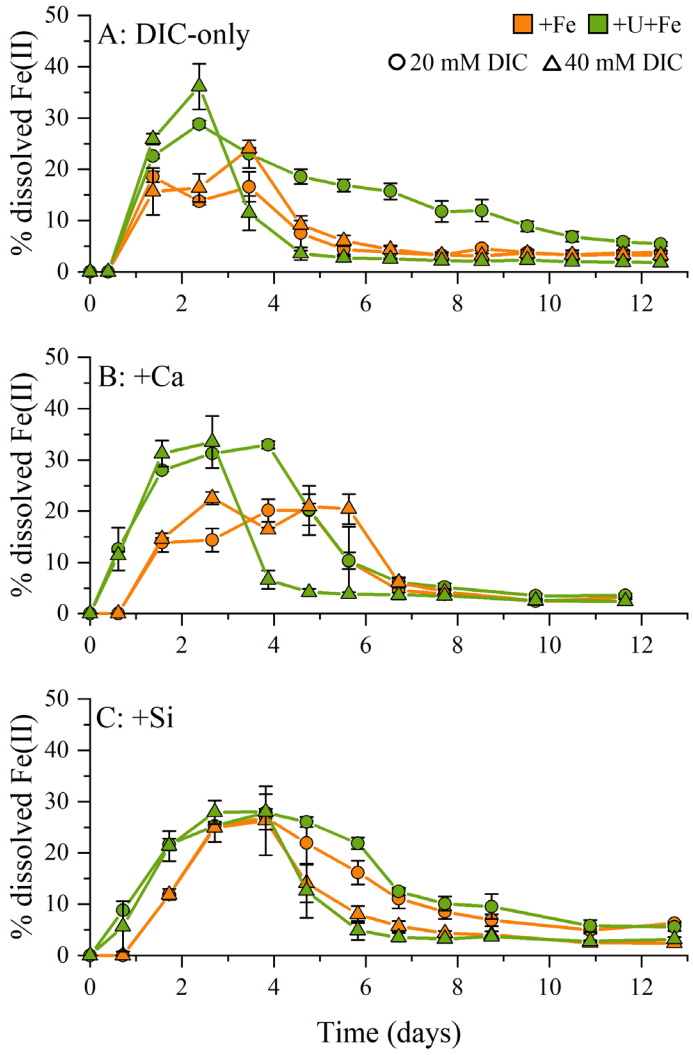

Figure C.3. Time series of percent dissolved Fe(II) in incubations with *S. putrefaciens* amended with 20 mM (circles) or 40 mM (triangles) (A) DIC-only, (B) DIC and 800 µM calcium, and (C) DIC and 300 µM silica, and either 5 mM ferrihydrite (orange) or both 180 µM U(VI) and 5 mM ferrihydrite (green) as terminal electron acceptors. Symbols and error bars represent the average and standard deviation of measurements from triplicate incubations.

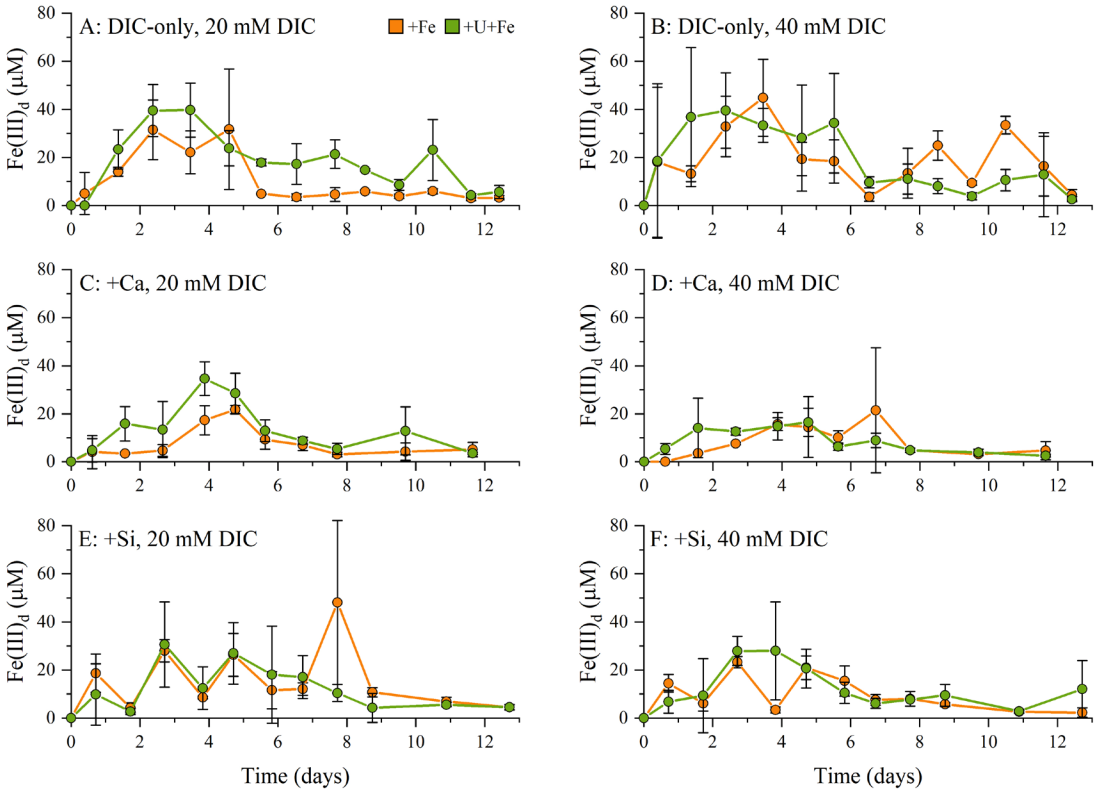

Figure C.4. Time series of dissolved Fe(III) ($Fe(III)_d$) in incubations with *S. putrefaciens* amended with 20 mM (right) or 40 mM (left) (A-B) DIC-only, (C-D) DIC and 800 µM calcium, or (E-F) DIC and 300 µM silica, and either 5 mM ferrihydrite (orange) or both 180 µM U(VI) and 5 mM ferrihydrite (green) as terminal electron acceptors. Symbols and error bars represent the average and standard deviation of triplicate incubations.

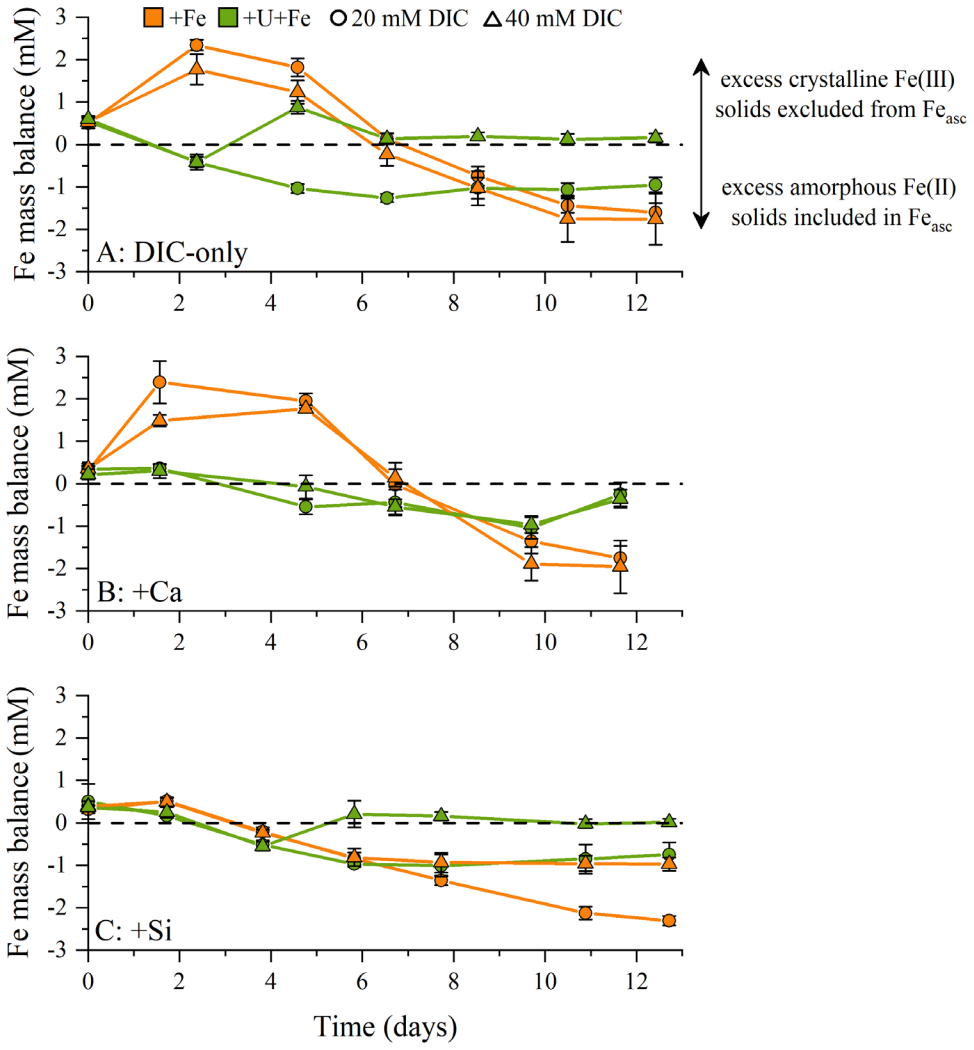

Figure C.5. Time series of iron mass balance ([Fe(III)$_{solid}$] - [Fe$_{asc}$]) in incubations with *S. putrefaciens* amended with 20 mM (circles) or 40 mM (triangles) (A) DIC-only, (B) DIC and 800 µM calcium, and (C) DIC and 300 µM silica, and either 5 mM ferrihydrite (orange) or both 180 µM U(VI) and 5 mM ferrihydrite (green) as terminal electron acceptors. Symbols and error bars represent the average and standard deviation of measurements from triplicate incubations. The concentration of Fe(III)$_{solid}$ was calculated from measured concentrations of total iron, total Fe(II), and dissolved Fe(III) ([Fe(III)$_{solid}$] = [Fe$_{T,0}$] - [Fe(II)$_T$] – [Fe(III)$_d$]). Positive values indicate an excess of crystalline Fe(III)-bearing solids which were excluded from Fe$_{asc}$, whereas negative values indicate an excess of Fe(II)-bearing solids which were included in Fe$_{asc}$.

Table C.5. Measured concentration of initial adsorbed U(VI), measured final U:Fe molar ratio, calculated final concentration of solid-associated uranium, and modeled final concentration of solid-associated uranium in *S. putrefaciens* incubations containing both U(VI) and ferrihydrite as TEAs

Incubation	U_{ads} (μM)[a]	U:Fe ratio	$U_{solid\text{-}associated}$ (μM)[b]	Modeled $U_{solid\text{-}associated}$ (μM)[c]
+U+Fe20	17±8	$8.08\pm0.02\times10^{-3}$	40±1	39
+U+Fe20 Abiotic	17	7.22×10^{-4}	4	
+U+Fe40	9±4	$4.94\pm0.08\times10^{-3}$	25±1	27
+U+Fe40 Abiotic	13	3.99×10^{-4}	2	
+U+Fe+Ca20	37±9	$6.57\pm0.48\times10^{-3}$	33±3	37
+U+Fe+Ca20 Abiotic	35	6.07×10^{-4}	3	
+U+Fe+Ca40	30±10	$5.96\pm0.11\times10^{-3}$	29±1	30
+U+Fe+Ca40 Abiotic	27	2.01×10^{-4}	1	
+U+Fe+Si20	26±2	$8.34\pm1.04\times10^{-3}$	42±5	42
+U+Fe+Si20 Abiotic	22	9.39×10^{-4}	5	
+U+Fe+Si40	16±3	$5.69\pm0.31\times10^{-3}$	29±2	28
+U+Fe+Si40 Abiotic	13	3.73×10^{-4}	2	

[a] Adsorbed uranium was calculated as the difference between the initial concentration of dissolved uranium measured in incubations with and without ferrihydrite. Reported values represent the average and standard deviation of triplicate biotic incubations and single abiotic controls.

[b] Solid-associated uranium was calculated from the measured U:Fe molar ratio in the final solid and the final concentration of solid phase iron ($Fe_{solid,final} = Fe_{T,0} - Fe(II)_{d,final} - Fe(III)_{d,final}$). Values represent the average and standard deviation of triplicate biotic incubations and single abiotic controls.

[c] Final concentration of solid-associated uranium as predicted by the kinetic model from the incorporation of uranium into the secondary mineralization products of ferrihydrite (R4 in Table 4.2) after 13 days of simulation. The concentrations include the final modeled concentration of uranium removed from solution via incorporation into magnetite and the measured concentration of initially adsorbed uranium, which are both assumed to be incorporated into the crystal lattice during secondary mineralization of ferrihydrite.

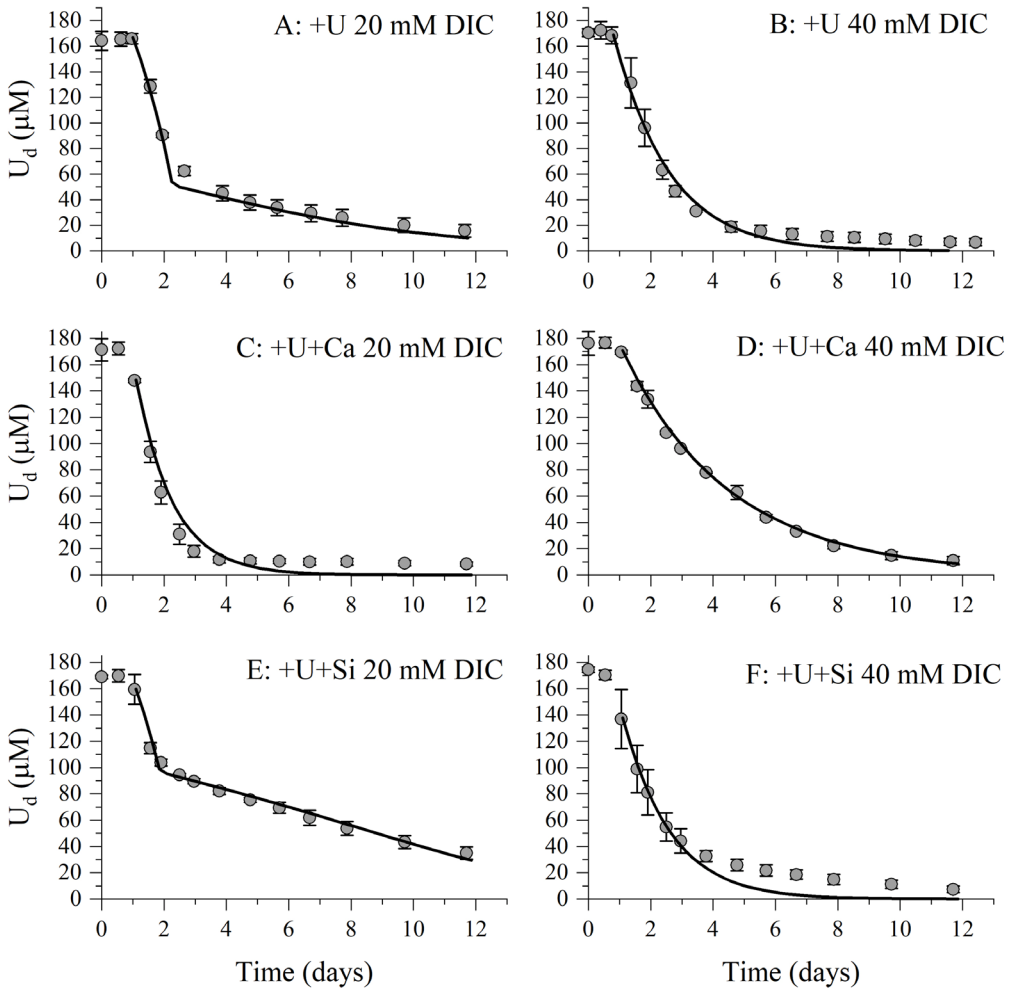

Figure C.6. Time series to total dissolved uranium (U_d) in incubations with *S. putrefaciens* amended with 180 µM U(VI) as the sole TEA and either 20 mM (left) or 40 mM (right) (A-B) DIC-only, (C-D) DIC and 800 µM calcium, and (E-F) DIC and 300 µM silica. Symbols and error bars represent the average and standard deviation of measurements from triplicate incubations. The solid black line represents the output from the kinetic model using the optimized parameters listed in Table 4.3. In order to reproduce the abrupt decrease in uranium removal rate observed halfway through the (A) DIC-only and (E) silica-amended 20 mM DIC incubations, rate constants of U(VI) bioreduction were decreased to 5 percent of the optimized values after 2 days of simulation.

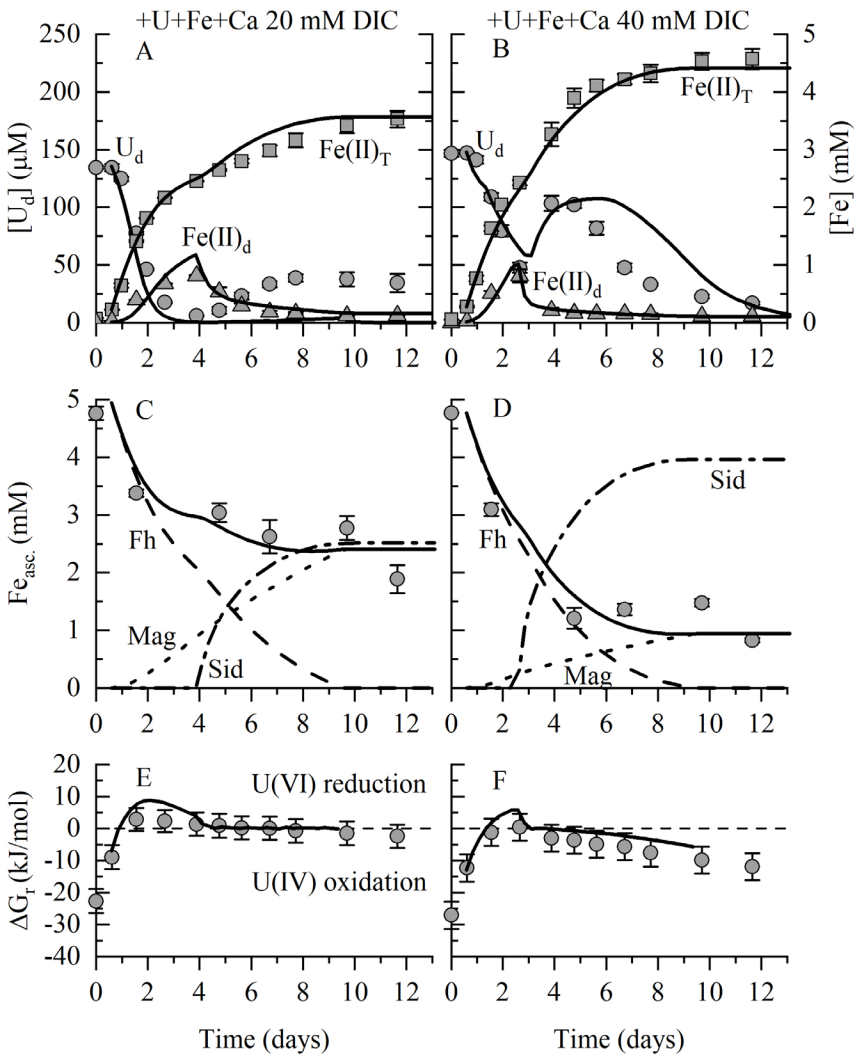

Figure C.7. Measured and modeled time series of calcium-amended incubations with *S. putrefaciens* conducted in the presence of 5 mM ferrihydrite and 180 µM U(VI) as terminal electron acceptors and (A, C, and E) 20 mM or (B, D, and F) 40 mM DIC. The same experimental data are presented in Figure 4.1. Symbols represent measured concentrations of dissolved uranium (U_d) (circles), dissolved Fe(II) ($Fe(II)_d$) (triangles), and total Fe(II) ($Fe(II)_T$) (squares). Lines represent output of the kinetic model using the optimized rate parameters from Table 4.3. (C and D) Lines representing solid phase iron species are indexed with Fh for ferrihydrite, Mag for magnetite, and Sid for siderite. The solid black line represents the sum of the amorphous iron species (i.e., ferrihydrite and magnetite). (E and F) The solid black line represents the Gibbs energy of reaction (ΔG_r) for the oxidation of monomeric U(IV) by ferrihydrite calculated by the model at each time step. The dashed black line represents the threshold ΔG_r, above which adsorbed U(VI) is reduced by adsorbed Fe(II) and below which U(IV) is oxidized by ferrihydrite.

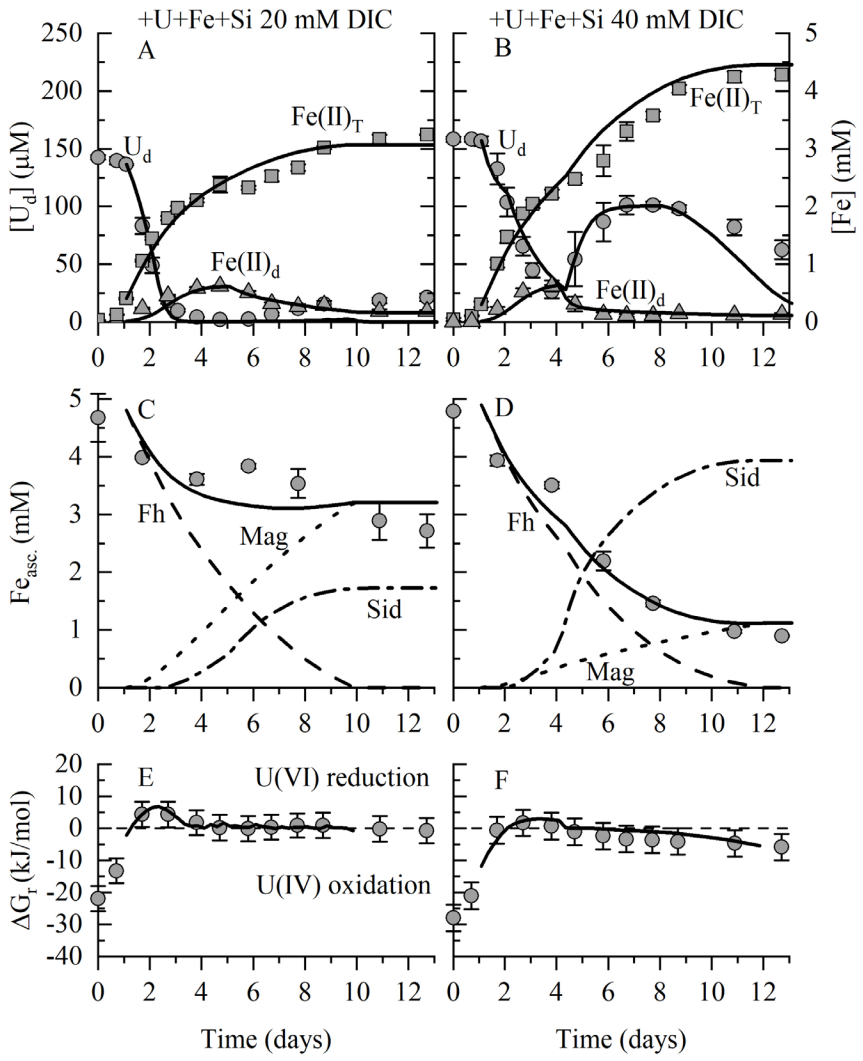

Figure C.8. Measured and modeled time series of silica-amended incubations with *S. putrefaciens* conducted in the presence of 5 mM ferrihydrite and 180 μM U(VI) as terminal electron acceptors and (A, C, and E) 20 mM or (B, D, and F) 40 mM DIC. The same experimental data are presented in Figure 4.1. Symbols represent measured concentrations of dissolved uranium (U_d) (circles), dissolved Fe(II) ($Fe(II)_d$) (triangles), and total Fe(II) ($Fe(II)_T$) (squares). Lines represent output of the kinetic model using the optimized rate parameters from Table 4.3. (C and D) Lines representing solid phase iron species are indexed with Fh for ferrihydrite, Mag for magnetite, and Sid for siderite. The solid black line represents the sum of the amorphous iron species (i.e., ferrihydrite and magnetite). (E and F) The solid black line represents the Gibbs energy of reaction (ΔG_r) for the oxidation of monomeric U(IV) by ferrihydrite calculated by the model at each time step. The dashed black line represents the threshold ΔG_r, above which adsorbed U(VI) is reduced by adsorbed Fe(II) and below which U(IV) is oxidized by ferrihydrite.

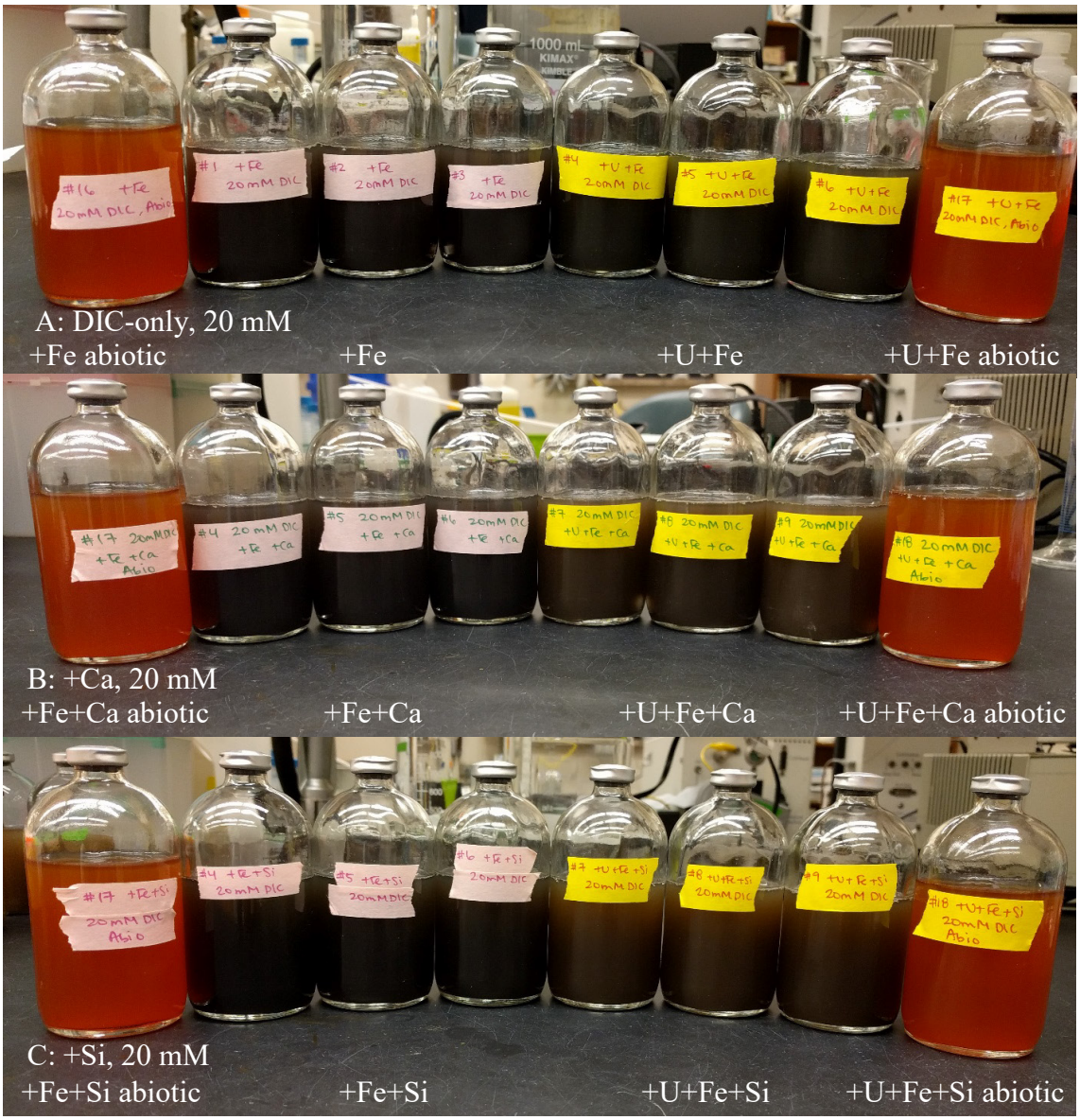

Figure C.9. Images of incubations amended with 20 mM (A) DIC-only, (B) DIC and 800 µM calcium, and (C) DIC and 300 µM silica after 12 days of reaction.

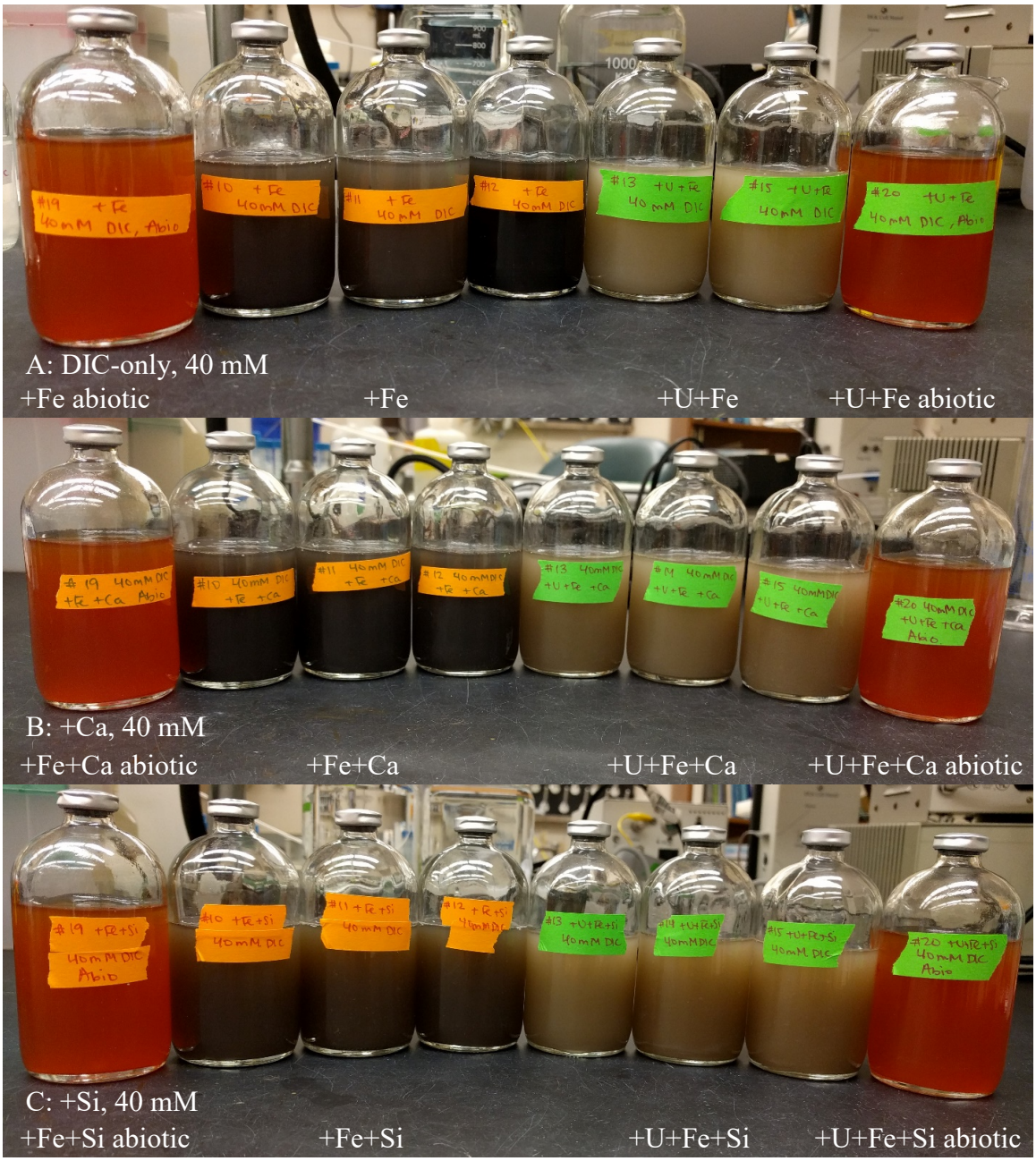

Figure C.10. Images of incubations amended with 40 mM (A) DIC-only, (B) DIC and 800 µM calcium, and (C) DIC and 300 µM silica after 12 days of reaction.

PHREEQC input file for 20 and 40 mM DIC-only incubations amended with U(VI) and ferrihydrite

```
Solution_master_species
U           UO2+2       0.0 238.03 238.03
U(+6)       UO2+2       0.0 238.03
U_four      U_four+4    0.0 238.03 238.03
U_four(+4)  U_four+4    0.0 238.03 # for biouraninite
U_iv        U_iv+4      0.0 238.03 238.03 # for Uincorp (uraninite)
Lac         Lac-        0.0 89.07 89.07
Lac(-1)     Lac-        0.0 89.07 89.07
Ace         Ace-        0.0 59.044 59.044
Ace(-1)     Ace-        0.0 59.044 59.044
Amm         AmmH+       0.0 AmmH 17.0
Bio          Bio        0.0 0.10 0.10
Fe_di       Fe_di+2     0.0 55.847 55.847
Fe_tri      Fe_tri+3    0.0 55.847 55.847
Feiii       Feiii+3     0.0 55.847 55.847     # For goethite
Feii        Feii+2      0.0 55.847 55.847     # For siderite
Fe_two      Fe_two+2    0.0 55.847 55.847     # For magnetite
Fe_three    Fe_three+3  0.0 55.847 55.847     # For magnetite


Solution_species
H2O = OH- + H+
      log_k   -14
      delta_h 13.362 kcal
      -gamma 3.5  0.0

UO2+2 = UO2+2
      log_k   0.0

Lac- = Lac-
      log_k   0.0

Ace- = Ace-
      log_k   0.0

U_four+4 = U_four+4
      log_k   0.0

U_iv+4 = U_iv+4
      log_k 0.0

AmmH+ = AmmH+
      log_k 0.0

Bio = Bio
      log_k   0.0
```

```
Fe_di+2 = Fe_di+2
      log_k 0.0

Fe_tri+3 = Fe_tri+3
      log_k 0.0

Feiii+3 = Feiii+3
      log_k 0.0

Feii+2 = Feii+2
      log_k 0.0

Fe_two+2 = Fe_two+2
      log_k 0.0

Fe_three+3 = Fe_three+3
      log_k 0.0

#   Acids

Ace- + H+ = HAce
      log_k   4.757  #Visual Minteq

Ace- + Na+ = NaAce
      log_k   -0.12  #Visual Minteq

Ace- + Ca+2 = CaAce+
      log_k   1.18  #Visual Minteq

Lac- + H+ = HLac
      log_k   3.86  #Visual Minteq

Lac- + Ca+2 = CaLac+
      log_k   1.48  #Visual Minteq

2Lac- + Ca+2 = CaLac2
      log_k   2.48  #Visual Minteq

Lac- + Mg+2 = MgLac+
      log_k   1.37  #Visual Minteq

2Lac- + Mg+2 = MgLac2
      log_k   2.01  #Visual Minteq

Lac- + Sr+2 = SrLac+
      log_k   0.97  #Visual Minteq

2Lac- + Sr+2 = SrLac2
      log_k   1.4  #Visual Minteq

#     Ammonium Species
```

```
AmmH+ = Amm + H+
      log_k -9.244

AmmH+ + SO4-2 = AmmHSO4-
      log_k 1.03  #Visual Minteq

Ca+2 + AmmH+ - H+ = CaAmm+2
      log_k -9.04  #Visual Minteq

Ca+2 + 2AmmH+ - 2H+ = Ca(Amm)2+2
      log_k -18.59  #Visual Minteq

Mg+2 + 2AmmH+ - 2H+ = Mg(Amm)2+2
      log_k -19.29  #Visual Minteq

#     Fe species

Fe_di+2 = Fe_di+2
             log_k   0.0

Fe_tri+3 = Fe_tri+3
        log_k   0.0

Fe_di+2 + H2O = Fe_diOH+ + H+
        log_k   -9.5
        delta_h 13.20   kcal

Fe_di+2 + 2H2O = Fe_di(OH)2 + 2H+
        log_k   -20.57  #MINTEQ database

Fe_di+2 + 3H2O = Fe_di(OH)3- + 3H+
        log_k   -31 #MINTEQ database

Fe_di+2 + Cl- = Fe_diCl+
        log_k   0.14

Fe_di+2 + CO3-2 = Fe_diCO3
        log_k   4.38

Fe_di+2 + HCO3- = Fe_diHCO3+
        log_k   2.0

Fe_di+2 + SO4-2 = Fe_diSO4
        log_k   2.25
        delta_h 3.230   kcal

Fe_di+2 + HSO4- = Fe_diHSO4+
        log_k   1.08

Fe_di+2 + HPO4-2 = Fe_diHPO4
        log_k   3.6
```

```
Fe_di+2 + H2PO4- = Fe_diH2PO4+
        log_k   2.7

Fe_di+2 + F- = Fe_diF+
        log_k   1.0

Fe_di+2 + Ace- = Fe_diAce+
     log_k 1.4

Fe_di+2 + Lac- = Fe_diLac+
     log_k -1.82 #Liu et al., 2001

Fe_tri+3 + H2O = Fe_triOH+2 + H+
        log_k   -2.19
        delta_h 10.4    kcal

Fe_tri+3 + 2 H2O = Fe_tri(OH)2+ + 2 H+
        log_k   -5.67
        delta_h 17.1    kcal

Fe_tri+3 + 3 H2O = Fe_tri(OH)3 + 3 H+
        log_k   -12.56
        delta_h 24.8    kcal

Fe_tri+3 + 4 H2O = Fe_tri(OH)4- + 4 H+
        log_k   -21.6
        delta_h 31.9    kcal

2Fe_tri+3 + 2 H2O = Fe_tri2(OH)2+4 + 2 H+
        log_k   -2.95
        delta_h 13.5    kcal

3Fe_tri+3 + 4 H2O = Fe_tri3(OH)4+5 + 4 H+
        log_k   -6.3
        delta_h 14.3    kcal

Fe_tri+3 + Cl- = Fe_triCl+2
        log_k   1.48
        delta_h 5.6     kcal

Fe_tri+3 + 2 Cl- = Fe_triCl2+
        log_k   2.13

Fe_tri+3 + 3 Cl- = Fe_triCl3
        log_k   1.13

Fe_tri+3 + SO4-2 = Fe_triSO4+
        log_k   4.04
        delta_h 3.91    kcal

Fe_tri+3 + HSO4- = Fe_triHSO4+2
```

```
        log_k   2.48

Fe_tri+3 + 2 SO4-2 = Fe_tri(SO4)2-
        log_k   5.38
        delta_h 4.60    kcal

Fe_tri+3 + HPO4-2 = Fe_triHPO4+
        log_k   5.43
        delta_h 5.76    kcal

Fe_tri+3 + H2PO4- = Fe_triH2PO4+2
        log_k   5.43

# Silica species

H4SiO4 + SO4-2 = H4SiO4SO4-2
      log_k      -0.54  #Visual Minteq

#   Uranyl Hydroxide Species

UO2+2 + H2O - H+ = UO2OH+
      log_k   -5.25  #NEA Vol 5

UO2+2 + 2H2O - 2H+ = UO2(OH)2
      log_k   -12.15  #NEA Vol 5

UO2+2 + 3H2O - 3H+ = UO2(OH)3-
      log_k   -20.25  #NEA Vol 5

UO2+2 + 4H2O - 4H+ = UO2(OH)4-2
      log_k   -32.4  #NEA Vol 5

2UO2+2 + H2O - H+ = (UO2)2OH+3
      log_k   -2.7  #NEA Vol 5

2UO2+2 + 2H2O - 2H+ = (UO2)2(OH)2+2
      log_k   -5.62  #NEA Vol 5

3UO2+2 + 4H2O - 4H+ = (UO2)3(OH)4+2
      log_k   -11.9  #NEA Vol 5

3UO2+2 + 5H2O - 5H+ = (UO2)3(OH)5+
      log_k   -15.55  #NEA Vol 5

3UO2+2 + 7H2O - 7H+ = (UO2)3(OH)7-
      log_k   -32.20  #NEA Vol 5

4UO2+2 + 7H2O - 7H+ = (UO2)4(OH)7+
      log_k   -21.90  #NEA Vol 5

# Uranyl Carbonate Species
```

```
UO2+2 + CO3-2 = UO2CO3
      log_k   9.94  #NEA Vol 5

UO2+2 + 2CO3-2 = UO2(CO3)2-2
      log_k   16.61  #NEA Vol 5

UO2+2 + 3CO3-2 = UO2(CO3)3-4
      log_k   21.84  #NEA Vol 5

3UO2+2 + 6CO3-2 = (UO2)3(CO3)6-6
      log_k   54  #NEA Vol 5

2UO2+2 + CO3-2 + 3H2O - 3H+ = (UO2)2CO3(OH)3-
      log_k   -0.855  #NEA Vol 5

3UO2+2 + CO3-2 + 3H2O - 3H+ = (UO2)3O(OH)2(HCO3)+
      log_k   0.655  #NEA Vol 5

11UO2+2 + 6CO3-2 + 12H2O - 12H+ = (UO2)11(CO3)6(OH)12-2
      log_k   -54.35  #NEA Vol 5

#   Ca, Mg Uranyl Carbonate Species

UO2+2 + Ca+2 + 3CO3-2 = CaUO2(CO3)3-2
      log_k   27.18  #Dong and Brooks, 2006

UO2+2 + 2Ca+2 + 3CO3-2 = Ca2UO2(CO3)3
      log_k   30.7  #Dong and Brooks, 2006

UO2+2 + Mg+2 + 3CO3-2 = MgUO2(CO3)3-2
      log_k   26.11  #Dong and Brooks, 2006

#   Uranyl Acetate Species

UO2+2 + Ace- = UO2Ace+
      log_k   3.11  #Visual Minteq

UO2+2 + 2Ace- = UO2(Ace)2
      log_k   5.04  #Visual Minteq

UO2+2 + 3Ace- = UO2(Ace)3-
      log_k   7.06  #Visual Minteq

#   Uranyl Lactate Species

UO2+2 + Lac- = UO2Lac+
      log_k   3.13  #Visual Minteq

UO2+2 + 2Lac- = UO2(Lac)2
      log_k   5.16  #Visual Minteq

UO2+2 + 3Lac- = UO2(Lac)3-
```

```
      log_k   6.31  #Visual Minteq

#     Uranyl Chloride Species

UO2+2 + Cl- = UO2Cl+
      log_k   0.17  #NEA Vol 5

UO2+2 + 2Cl- = UO2Cl2
      log_k   -1.1  #NEA Vol 5

#     Uranyl Sulfate Species

UO2+2 + SO4-2 = UO2SO4
      log_k   3.15  #NEA Vol 5

UO2+2 + 2SO4-2 = UO2(SO4)2-2
      log_k   4.14  #NEA Vol 5

UO2+2 + 3SO4-2 = UO2(SO4)3-4
      log_k   3.02  #NEA Vol 5

#     Uranyl Nitrate Species

UO2+2 + NO3- = UO2NO3+
      log_k   0.3  #NEA Vol 5

#     Uranyl Phosphate Species

UO2+2 + PO4-3 = UO2PO4-
      log_k   13.23  #NEA Vol 5

UO2+2 + PO4-3 + H+ = UO2HPO4
      log_k   19.59  #NEA Vol 5

UO2+2 + PO4-3 + 2H+ = UO2H2PO4+
      log_k   20.682  #NEA Vol 5

UO2+2 + PO4-3 + 3H+ = UO2H3PO4+2
      log_k   22.462  #NEA Vol 5

UO2+2 + 2PO4-3 + 4H+ = UO2(H2PO4)2
      log_k   44.044  #NEA Vol 5

UO2+2 + 2PO4-3 + 5H+ = UO2(H2PO4)(H3PO4)+
      log_k   45.054  #NEA Vol 5

#     Uranyl Silicate species

UO2+2 + H4SiO4 = UO2H3SiO4+ + H+
      log_k -1.91      # Visual Minteq

#   U(IV) species
```

```
U_four+4 + H2O - H+ = U_fourOH+3
     log_k   -0.54  #NEA Vol 5

U_four+4 + 4H2O - 4H+ = U_four(OH)4
     log_k   -10  #NEA Vol 5

U_four+4 + 4CO3-2 = U_four(CO3)4-4
     log_k   35.12  #NEA Vol 5

U_four+4 + 5CO3-2 = U_four(CO3)5-6
     log_k   34.00  #NEA Vol 5

U_four+4 + Cl- = U_fourCl+3
     log_k   1.72  #NEA Vol 5

U_four+4 + SO4-2 = U_fourSO4+2
     log_k   6.58  #NEA Vol 5

U_four+4 + 2SO4-2 = U_four(SO4)2
     log_k   10.51  #NEA Vol 5

U_four+4 + NO3- = U_fourNO3+3
     log_k   1.47  #NEA Vol 5

U_four+4 + 2NO3- = U_four(NO3)2+2
     log_k   2.3  #NEA Vol 5



PHASES

Uraninite
     U_ivO2 = U_iv+4 + 4OH- - 2H2O
     log_k -60.669   #Visual Minteq

Bio-Uraninite
     U_fourO2 = U_four+4 + 4OH- - 2H2O
     log_k -54.4  #NEA Vol 5

Ferrihydrite
     Fe_tri(OH)3 + 3 H+ = Fe_tri+3 + 3H2O
     -log_k     4.891 #PHREEQC Database

Magnetite
     Fe_three2Fe_twoO4 + 8H+ = 2Fe_three+3 + Fe_two+2 + 4H2O
     log_k 3.737  #Minteq database

Maghemite
     Feiii2O3 + 6H+ = 2Feiii+3 + 3H2O
     log_k 6.386  # MINTEQ database
```

```
Siderite
      FeiiCO3 = Feii+2 + CO3-2
      -log_k     -10.89 #-8.1     #Calculated from data, -10.89
from PHREEQC Database
      -delta_h  -2.480 kcal
fix_pH
      H+ = H+
      log_k 0


SURFACE_MASTER_SPECIES
      Mag   MagOH


SURFACE_SPECIES

MagOH = MagOH
      -log_k     0

# Ferrihidrite protonation constants

Hfo_sOH + H+ = Hfo_sOH2+
      log_k 7.29  #Dzombak and Morel, 1990

Hfo_sOH = Hfo_sO- + H+
      log_k -8.93  #Dzombak and Morel, 1990

Hfo_wOH + H+ = Hfo_wOH2+
      log_k 7.29  #Dzombak and Morel, 1990

Hfo_wOH = Hfo_wO- + H+
      log_k -8.93  #Dzombak and Morel, 1990


# Uranyl adsorption on Ferrihydrite

2Hfo_sOH + UO2+2 = (Hfo_sO)2UO2 + 2H+
      log_k -2.78  #Waite, 1994 - diffuse double layer

2Hfo_wOH + UO2+2 = (Hfo_wO)2UO2 + 2H+
      log_k -6.49  #Waite, 1994 - diffuse double layer

2Hfo_sOH + UO2+2 + CO3-2 = (Hfo_sO)2UO2CO3-2 + 2H+
      log_k 3.03  #Waite, 1994 - diffuse double layer

2Hfo_wOH + UO2+2 + CO3-2 = (Hfo_wO)2UO2CO3-2 + 2H+
      log_k -1.06  #Waite, 1994 - diffuse double layer

# Fe(II) adsorption to ferrihydrite

Hfo_wOH + Fe_di+2 = Hfo_wOFe_di+ + H+
      log_k -2.98 #Appelo, 2002 - double layer model
```

```
Hfo_wOH + Fe_di+2 + H2O = Hfo_wOFe_diOH + 2H+
      log_k -11.55     #Appelo, 2002- double layer model

Hfo_sOH + Fe_di+2 = Hfo_sOFe_di+ + H+
      log_k -0.95 #Appelo, 2002- double layer model

# Carbonate adsorption on Ferrihydrite

Hfo_wOH + CO3-2 + H+ = Hfo_wOCO2- + H2O
      log_k 12.78  #Appelo, 2002 - double layer model

Hfo_wOH + CO3-2 + 2H+ = Hfo_wOCO2H + H2O
      log_k 20.37  #Appelo, 2002 - double layer model

# Si adsorption on Ferrihydrite

Hfo_wOH + H4SiO4 = Hfo_wH3SiO4 + H2O
      log_k 4.28  #Swedlund, 1999 - double layer model

Hfo_wOH + H4SiO4 = Hfo_wH2SiO4- + H+ + H2O
      log_k -3.22  #Swedlund, 1999 - double layer model

Hfo_wOH + H4SiO4 = Hfo_wHSiO4-2 + 2H+ + H2O
      log_k -11.69  #Swedlund, 1999 - double layer model

# Mg adsorption on ferrihydrite

Hfo_wOH + Mg+2 = Hfo_wOMg+ + H+
      -log_k -4.6  #PHREEQC database

# Sulfate adsorption on Ferrihydrite
Hfo_wOH + SO4-2 + H+ = Hfo_wSO4- + H2O
      -log_k     7.78  #PHREEQC database

Hfo_wOH + SO4-2 = Hfo_wOHSO4-2
      -log_k     0.79  #PHREEQC database

# Magnetite protonation constants

MagOH + H+ = MagOH2+
      log_k 5.1  # Missana, 2003 - diffuse double layer

MagOH = MagO- + H+
      log_k -9.1  # Missana, 2003 - diffuse double layer

# U(VI) adsorption on Magnetite

MagOH + UO2+2 = MagOUO2+ + H+
      log_k -0.10 # Missana, 2003 - diffuse double layer

MagOH + UO2+2 + H2O = MagOUO2OH + 2H+
```

```
      log_k -5.40 # Missana, 2003 - diffuse double layer

# Fe(II) adsorption on Magnetite

MagOH + Fe_di+2 + H2O = MagOFe_diOH + 2H+
      log_k -10.3   # optimized from Klausen, 1995 Fig 5. - DDL


EQUILIBRIUM_PHASES 2  #pH 8, +U+Fe
Bio-Uraninite    0.0 0.0
Ferrihydrite     0.0 0.0005814
Magnetite        0.0 0.0
Siderite         0.0 0.0
Uraninite        0.0 0.0
fix_pH           -8.0  NaOH

EQUILIBRIUM_PHASES 5  #pH 8, +U+Fe
Bio-Uraninite    0.0 0.0
Ferrihydrite     0.0 0.0005855
Magnetite        0.0 0.0
Siderite         0.0 0.0
Uraninite        0.0 0.0
fix_pH           -8.0  NaOH


SURFACE 2  #pH 8, +U+Fe
      Hfo_s Ferrihydrite equilibrium 0.0018  63600  #0.005
      Hfo_w Ferrihydrite equilibrium 0.873 63600 #0.2
      Mag   Magnetite equilibrium  0.11 12699

SURFACE 5  #pH 8, +U+Fe
      Hfo_s Ferrihydrite equilibrium 0.0018  63600 #0.005
      Hfo_w Ferrihydrite equilibrium 0.873 63600 #0.2
      Mag   Magnetite equilibrium  0.11 12699

#Ferrihydrite:  106g/mol (from molecular formula)
#surface area: 600 m^2/g = 63600 m2/mol
#site density: 0.2 mol weak sites and 0.005 mol strong sites per
mol Fe, total: 0.875 mol/mol Fe, strong: 0.0018 mol/mole Fe
(Waite, 1994)

#Magnetite, 231.54 g/mol (from molecular formula)
#surface area: 56 m^2/g = 12699 m2/mol
#site density: 5.13 sites/nm^2 (optimized from Klausen, 1995) =
0.11 mol sites/mol Fe


RATES
Ubio
-start
10  uranyl = mol("UO2+2")  #mol/L
```

```
20  Unon = mol("UO2+2") + mol("UO2OH+") + mol("UO2(OH)2") +
mol("UO2(OH)3-") + mol("UO2(OH)4-2") + mol("(UO2)2OH+3") +
mol("(UO2)2(OH)2+2") + mol("(UO2)3(OH)4+2") + mol("(UO2)3(OH)5+")
+ mol("(UO2)3(OH)7-") + mol("(UO2)4(OH)7+") + mol("UO2Ace+") +
mol("UO2(Ace)2") + mol("UO2(Ace)3-") + mol("UO2Lac+") +
mol("UO2(Lac)2") + mol("UO2(Lac)3-") + mol("UO2Cl+") +
mol("UO2Cl2") + mol("UO2SO4") + mol("UO2(SO4)2-2") +
mol("UO2(SO4)3-4") + mol("UO2NO3+") + mol("UO2PO4-") +
mol("UO2HPO4") + mol("UO2H2PO4+") + mol("UO2H3PO4+2") +
mol("UO2(H2PO4)2") + mol("UO2(H2PO4)") + mol("UO2H3SiO4+")
30  Ucarb = mol("UO2CO3") + mol("UO2(CO3)2-2") + mol("UO2(CO3)3-
4") + mol("(UO2)3(CO3)6-6") +  mol("(UO2)2CO3(OH)3-") +
mol("(UO2)3O(OH)2(HCO3)+") + mol("(UO2)11(CO3)6(OH)12-2") +
mol("CaUO2(CO3)3-2") + mol("Ca2UO2(CO3)3") + mol("MgUO2(CO3)3-2")
+ mol("SrUO2(CO3)3-2") + mol("BaUO2(CO3)3-2") +
mol("Ba2UO2(CO3)3")
60  knon =  2.05e-10 #L/cell/s,
70  kcarb =  4.9e-18 #L/cell/s,
90  X = mol("Bio")  # mol cell/L
140 QU = MOL("Ace-") * MOL("HCO3-") * MOL("H+")^5 /
MOL("UO2+2")^2 / MOL("Lac-")  # 2UO22+ + Lac- + 2H2O = 2UO2(am) +
Ace- + HCO3- + 5H+
150 LnQU = LOG(QU)
160 DeltaGrxnU = -52.96 + 0.008314 * 299 * LnQU
200 GC = -67.5  # kJ/mol - energy conserved from ATP
210 FT = 1 - exp((DeltaGrxnU - GC) / (4*0.008314*299))
220 IF FT<0 THEN FT=0
300 p = 2
310 IC50 = 1.3e-15
320 Ftox = 1/(1 + (uranyl/IC50)^p)
540 rate = X * 6.022e23 * (knon * Unon + kcarb * Ucarb) * FT *
Ftox  #mol/L/s, mult. by 6.022e23 to turn mol cell/L into cell/L
600 moles = rate * TIME
610 SAVE moles
-end

Ferribio_20
-start
10 X = mol("Bio")  #OD600
70 kFe = 5.2e-18 # L/cell/s
220 QFh = MOL("Ace-") * MOL("HCO3-") * MOL("Fe_di+2")^4 /
MOL("H+")^7 / MOL("Lac-")
230 LnQFh = LOG(QFh)  # 4Fe(OH)3 + Lac- + 7H+ --> 4Fe+2 + Ace- +
HCO3- + 10H2O
240 DeltaGrxnFh = -294.645 + 0.008314 * 299 * LnQFh
300 GC = -67.5  # kJ/mol - energy conserved from ATP
320 FT = 1 - exp((DeltaGrxnFh - GC) / (4*0.008314*299))
330 IF FT<0 THEN FT=0
360 rate = X * 6.022e23 * kFe * (EQUI("Ferrihydrite")/0.12) * FT
500 moles = rate * TIME
600 SAVE moles
-end
```

```
Ferribio_40
-start
10 X = mol("Bio")  #OD600
70 kFe = 5.2e-18 # L/cell/s
220 QFh = MOL("Ace-") * MOL("Fe_diHCO3+")^4 / MOL("H+")^7 /
MOL("HCO3-")^3 / MOL("Lac-")
230 LnQFh = LOG(QFh)  # 4Fe(OH)3 + Lac- + 3HCO3- + 7H+ -->
4FeHCO3+ + Ace- + 10H2O
240 DeltaGrxnFh = -340.3 + 0.008314 * 299 * LnQFh
300 GC = -67.5  # kJ/mol - energy conserved from ATP
320 FT = 1 - exp((DeltaGrxnFh - GC) / (4*0.008314*299))
330 IF FT<0 THEN FT=0
360 rate = X * 6.022e23 * kFe * (EQUI("Ferrihydrite")/0.12) * FT
500 moles = rate * TIME
600 SAVE moles
-end

Siderite_20
-start
10 k = 0 # mol/L/s
20 IF TOTAL_TIME>138240 THEN k=3e-10
30 Ksp = 10^-8.1
100 rate = k * (MOL("Fe_di+2") * MOL("CO3-2") / Ksp - 1)
110 IF rate<0 THEN rate=0
200 moles = rate * TIME
300 SAVE moles
-end

Siderite_40
-start
10 k = 0 # mol/L/s
20 IF TOTAL_TIME>140832 THEN k=1e-9
30 Ksp = 10^-8.1
100 rate = k * (MOL("Fe_di+2") * MOL("CO3-2") / Ksp - 1)
110 IF rate<0 THEN rate=0
200 moles = rate * TIME
300 SAVE moles
-end

Ferritomag_20
-start
10 kFerritomag = 6e-10 # mol/L/s
30 FeIIads = mol("Hfo_wOFe_di+") + mol("Hfo_wOFe_diOH") +
mol("Hfo_sOFe_di+")
40 rate = kFerritomag * FeIIads / (EQUI("Ferrihydrite")/0.12)
170 moles = rate * TIME
200 SAVE moles
-end

Ferritomag_40
-start
```

```
10 kFerritomag = 2.5e-10 # mol/L/s
30 FeIIads = mol("Hfo_wOFe_di+") + mol("Hfo_wOFe_diOH") +
mol("Hfo_sOFe_di+")
40 rate = kFerritomag * FeIIads / (EQUI("Ferrihydrite")/0.12)
170 moles = rate * TIME
200 SAVE moles
-end

Uoxabio_20  #Abiotic U(IV) oxidation by ferrihydrite
-start
10 kUox = 3.0e-3  # L/mol/s
20 PUT(kUOx, 2)
30 EhUO2CO33knot = 0.492-0.084 #adjusted to reflect lower Eh of
mononuclear U(IV) solids
40 PUT(EhUO2CO33knot, 3)
50 QUO2CO33 = MOL("UO2(CO3)3-4") * MOL("H+")^3 / MOL("HCO3-")^3 #
UO2(CO3)3-4 + 3H+ + 2e- == UO2(am) + 3HCO3-
60 LnQUO2CO33 = LOG(QUO2CO33)
70 EhUO2CO33 = EhUO2CO33knot + 0.008314 * 299 / 2 / 96.484 *
LnQUO2CO33  # Eh = E0 + (RT/nF) * Ln(Ox/Red)
80 QFe2 = MOL("Fe_di+2") / MOL("H+")^3 # Fe(OH)3(s) + e- + 3H+ =
Fe2+ + 3H2O
90 LnQFe2 = LOG(QFe2)
100 EhFe2 = 0.848 - 0.008314 * 299 / 96.484 * LnQFe2 # Eh = E0 -
(RT/nF) * LnQ
110 rate = kUox * (EQUI("Ferrihydrite")/0.12) * (EQUI("Bio-
Uraninite")/0.12)
120 IF (EQUI("Ferrihydrite")/0.12)>0.00063 THEN rate = kUox *
0.00063 * (EQUI("Bio-Uraninite")/0.12)
130 IF EhUO2CO33>=EhFe2 THEN rate=0
200  moles = rate * TIME
300 SAVE moles
-end

Uoxabio_40  #Abiotic U(IV) oxidation by ferrihydrite
-start
10 kUox = GET(2) # L/mol/s
30 EhUO2CO33knot = GET(3)
40 QUO2CO33 = MOL("UO2(CO3)3-4") * MOL("H+")^3 / MOL("HCO3-")^3 #
UO2(CO3)3-4 + 3H+ + 2e- == UO2(am) + 3HCO3-
50 LnQUO2CO33 = LOG(QUO2CO33)
60 EhUO2CO33 = EhUO2CO33knot + 0.008314 * 299 / 2 / 96.484 *
LnQUO2CO33  # Eh = E0 + (RT/nF) * Ln(Ox/Red)
70 QFeHCO3 = MOL("Fe_diHCO3+") / MOL("H+")^3 / MOL("HCO3-") #
Fe(OH)3(s) + e- + HCO3- + 3H+ = FeHCO3+ + 3H2O
80 LnQFeHCO3 = LOG(QFeHCO3)
90 EhFeHCO3 = 0.966 - 0.008314 * 299 / 96.484 * LnQFeHCO3  # Eh =
E0 - (RT/nF) * LnQ
100 rate = kUox * (EQUI("Ferrihydrite")/0.12) * (EQUI("Bio-
Uraninite")/0.12)
110 IF (EQUI("Ferrihydrite")/0.12)>0.00063 THEN rate = kUox *
0.00063 * (EQUI("Bio-Uraninite")/0.12)
```

```
120 IF EhUO2CO33>=EhFeHCO3 THEN rate=0
200  moles = rate * TIME
300 SAVE moles
-end

UredabioFerri_20  #Abiotic U(VI) reduction by adsorbed Fe(II) on
ferrihydrite
-start
10 kUred = 399 / 60 # L/mol/s = (399 1/M/min) / (60 s/min), from
Liger, 1999
20 Uads = mol("(Hfo_sO)2UO2") + mol("(Hfo_wO)2UO2") +
mol("(Hfo_sO)2UO2CO3-2") + mol("(Hfo_wO)2UO2CO3-2")
30 EhUO2CO33knot = GET(3)
50 QUO2CO33 = MOL("UO2(CO3)3-4") * MOL("H+")^3 / MOL("HCO3-")^3 #
UO2(CO3)3-4 + 3H+ + 2e- == UO2(am) + 3HCO3-
60 LnQUO2CO33 = LOG(QUO2CO33)
70 EhUO2CO33 = EhUO2CO33knot + 0.008314 * 299 / 2 / 96.484 *
LnQUO2CO33  # Eh = E0 + (RT/nF) * Ln(Ox/Red)
80 QFe2 = MOL("Fe_di+2") / MOL("H+")^3 # Fe(OH)3(s) + e- + 3H+ =
Fe2+ + 3H2O
90 LnQFe2 = LOG(QFe2)
100 EhFe2 = 0.848 - 0.008314 * 299 / 96.484 * LnQFe2 # Eh = E0 -
(RT/nF) * LnQ
110 rate = kUred * mol("Hfo_wOFe_diOH") * Uads
120 IF EhUO2CO33<=EhFe2 THEN rate=0
170 moles = rate * TIME
200 SAVE moles
-end

UredabioFerri_40  #Abiotic U(VI) reduction by adsorbed Fe(II) on
ferrihydrite
-start
10 kUred = 399 / 60 # L/mol/s = (399 1/M/min) / (60 s/min), from
Liger, 1999
20 Uads = mol("(Hfo_sO)2UO2") + mol("(Hfo_wO)2UO2") +
mol("(Hfo_sO)2UO2CO3-2") + mol("(Hfo_wO)2UO2CO3-2")
30 EhUO2CO33knot = GET(3)
40 QUO2CO33 = MOL("UO2(CO3)3-4") * MOL("H+")^3 / MOL("HCO3-")^3 #
UO2(CO3)3-4 + 3H+ + 2e- == UO2(am) + 3HCO3-
50 LnQUO2CO33 = LOG(QUO2CO33)
60 EhUO2CO33 = EhUO2CO33knot + 0.008314 * 299 / 2 / 96.484 *
LnQUO2CO33  # Eh = E0 + (RT/nF) * Ln(Ox/Red)
70 QFeHCO3 = MOL("Fe_diHCO3+") / MOL("H+")^3 / MOL("HCO3-") #
Fe(OH)3(s) + e- + HCO3- + 3H+ = FeHCO3+ + 3H2O
80 LnQFeHCO3 = LOG(QFeHCO3)
90 EhFeHCO3 = 0.966 - 0.008314 * 299 / 96.484 * LnQFeHCO3  # Eh =
E0 - (RT/nF) * LnQ
100 rate = kUred * mol("Hfo_wOFe_diOH") * Uads
110 IF EhUO2CO33<=EhFeHCO3 THEN rate=0
170 moles = rate * TIME
200 SAVE moles
-end
```

```
UredabioMag_20  #Abiotic U(VI) reduction by adsorbed U(VI) on
magnetite
-start
10 kUred = 399 / 60 # L/mol/s = (399 1/M/min) / (60 s/min), from
Liger, 1999
20 Uads = MOL("MagOUO2+") + MOL("MagOUO2OH")
30 EhUO2CO33knot = GET(3)
50 QUO2CO33 = MOL("UO2(CO3)3-4") * MOL("H+")^3 / MOL("HCO3-")^3 #
UO2(CO3)3-4 + 3H+ + 2e- == UO2(am) + 3HCO3-
60 LnQUO2CO33 = LOG(QUO2CO33)
70 EhUO2CO33 = EhUO2CO33knot + 0.008314 * 299 / 2 / 96.484 *
LnQUO2CO33  # Eh = E0 + (RT/nF) * Ln(Ox/Red)
80 QFe2 = MOL("Fe_di+2") / MOL("H+")^3 # Fe(OH)3(s) + e- + 3H+ =
Fe2+ + 3H2O
90 LnQFe2 = LOG(QFe2)
100 EhFe2 = 0.848 - 0.008314 * 299 / 96.484 * LnQFe2 # Eh = E0 -
(RT/nF) * LnQ170 moles = rate * TIME
110 rate = kUred * MOL("MagOFe_diOH") * Uads
120 IF EhUO2CO33<=EhFe2 THEN rate=0
200 SAVE moles
-end

UredabioMag_40  #Abiotic U(VI) reduction by adsorbed U(VI) on
magnetite
-start
10 kUred = 399 / 60 # L/mol/s = (399 1/M/min) / (60 s/min), from
Liger, 1999
20 Uads = MOL("MagOUO2+") + MOL("MagOUO2OH")
30 EhUO2CO33knot = GET(3)
40 QUO2CO33 = MOL("UO2(CO3)3-4") * MOL("H+")^3 / MOL("HCO3-")^3 #
UO2(CO3)3-4 + 3H+ + 2e- == UO2(am) + 3HCO3-
50 LnQUO2CO33 = LOG(QUO2CO33)
60 EhUO2CO33 = EhUO2CO33knot + 0.008314 * 299 / 2 / 96.484 *
LnQUO2CO33  # Eh = E0 + (RT/nF) * Ln(Ox/Red)
70 QFeHCO3 = MOL("Fe_diHCO3+") / MOL("H+")^3 / MOL("HCO3-") #
Fe(OH)3(s) + e- + HCO3- + 3H+ = FeHCO3+ + 3H2O
80 LnQFeHCO3 = LOG(QFeHCO3)
90 EhFeHCO3 = 0.966 - 0.008314 * 299 / 96.484 * LnQFeHCO3  # Eh =
E0 - (RT/nF) * LnQ
100 rate = kUred * MOL("MagOFe_diOH") * Uads
110 IF EhUO2CO33<=EhFeHCO3 THEN rate=0
120 moles = rate * TIME
200 SAVE moles
-end

Uincorp_20
-start
10 kUincorp = 0.1 # mol/L/s
30 FeIIads = mol("Hfo_wOFe_di+") + mol("Hfo_wOFe_diOH") +
mol("Hfo_sOFe_di+")
```

```
40 Uads = mol("(Hfo_sO)2UO2") + mol("(Hfo_wO)2UO2") +
mol("(Hfo_sO)2UO2CO3-2") + mol("(Hfo_wO)2UO2CO3-2")
50 rate = kUincorp * Uads * FeIIads / (EQUI("Ferrihydrite")/0.12)
170 moles = rate * TIME
200 SAVE moles
-end

Uincorp_40
-start
10 kUincorp = 0.4  # mol/L/s
30 FeIIads = mol("Hfo_wOFe_di+") + mol("Hfo_wOFe_diOH") +
mol("Hfo_sOFe_di+")
40 Uads = mol("(Hfo_sO)2UO2") + mol("(Hfo_wO)2UO2") +
mol("(Hfo_sO)2UO2CO3-2") + mol("(Hfo_wO)2UO2CO3-2")
50 rate = kUincorp * Uads * FeIIads / (EQUI("Ferrihydrite")/0.12)
170 moles = rate * TIME
200 SAVE moles
-end

#2E9 cell/mL/(1 OD600)
#1E3 mL/L
#converts X (OD600) to cell/L


INCREMENTAL_REACTIONS true


KNOBS
-step_size 10


KINETICS 2
Ubio
      -Formula U+6 -2.0 Bio-Uraninite 2.0 Lac -1.0 Ace 1.0 C+4
1.0
Ferribio_20
       -Formula Ferrihydrite -4.0 Fe_di 4.0 Lac -1.0 Ace 1.0 C+4
1.0
Siderite_20
      -Formula Fe_di -1.0 C -1.0 Siderite 1.0
Ferritomag_20
      -Formula Ferrihydrite -2.0 Fe_di -1.0 Magnetite 1.0
Uoxabio_20
      -Formula Bio-Uraninite -1.0 U+6 1.0 Ferrihydrite -2.0 Fe_di
2.0
UredabioFerri_20
      -Formula U+6 -1.0 Bio-Uraninite 1.0 Fe_di -2.0 Ferrihydrite
2.0
UredabioMag_20
      -Formula U+6 -1.0 Bio-Uraninite 1.0 Magnetite -3.0
Maghemite 4.0 Fe_di 1.0 #UO2+2 + 3Fe3O4 = UO2(am) + 4Fe2O3 + Fe+2
Uincorp_20
```

```
      -Formula U+6 -1.0 Uraninite 1.0
       -steps 0 21600 21600 21600 21600 21600 21600 21600 21600
21600 21600 21600 21600 21600 21600 21600 21600 21600 21600 21600
21600 21600 21600 21600 21600 21600 21600 21600 21600 21600 21600
21600 21600 21600 21600 21600 21600 21600 21600 21600 21600 21600
21600 21600 21600 21600 21600 21600 21600 21600 21600 21600 21600
      -step_divide 1e-4

KINETICS 5
Ubio
      -Formula U+6 -2.0 Bio-Uraninite 2.0 Lac -1.0 Ace 1.0 C+4
1.0
Ferribio_40
       -Formula Ferrihydrite -4.0 Fe_di 4.0 Lac -1.0 Ace 1.0 C+4
1.0
Siderite_40
      -Formula Fe_di -1.0 C -1.0 Siderite 1.0
Ferritomag_40
      -Formula Ferrihydrite -2.0 Fe_di -1.0 Magnetite 1.0
Uoxabio_40
      -Formula Bio-Uraninite -1.0 U+6 1.0 Ferrihydrite -2.0 Fe_di
2.0
UredabioFerri_40
      -Formula U+6 -1.0 Bio-Uraninite 1.0 Fe_di -2.0 Ferrihydrite
2.0
UredabioMag_40
      -Formula U+6 -1.0 Bio-Uraninite 1.0 Magnetite -3.0
Maghemite 4.0 Fe_di 1.0 #UO2+2 + 3Fe3O4 = UO2(am) + 4Fe2O3 + Fe+2
Uincorp_40
      -Formula U+6 -1.0 Uraninite 1.0
       -steps 0 21600 21600 21600 21600 21600 21600 21600 21600
21600 21600 21600 21600 21600 21600 21600 21600 21600 21600 21600
21600 21600 21600 21600 21600 21600 21600 21600 21600 21600 21600
21600 21600 21600 21600 21600 21600 21600 21600 21600 21600 21600
21600 21600 21600 21600 21600 21600 21600 21600 21600 21600 21600
      -step_divide 1e-4


SELECTED_OUTPUT
      -file ufeopt-output.txt
      -selected_out true
      -solution true
      -distance false
      -pe false
      -simulation false
      -pH true
      -totals Hfo_s Hfo_w Mag
      -molalities
      (Hfo_sO)2UO2 (Hfo_wO)2UO2 (Hfo_sO)2UO2CO3-2
(Hfo_wO)2UO2CO3-2
      Hfo_wOFe_di+ Hfo_wOFe_diOH Hfo_sOFe_di+
      Hfo_wOCO2- Hfo_wOCO2H
```

```
      MagOUO2+ MagOUO2OH
      MagOFe_di+ MagOFe_diOH


USER_PUNCH
-headings _time_ Usoln_M Uads_M Uincorp_M uranyl_M Unon-carb_M
Ucarb_M Utern_M DeltaGrxnU_kJ/mol Ferri_M Mag_M Maghe_M Sid_M
Amorph_M Fe(II)T_M Fe(II)soln_M Fe(II)ads_M  Febalance_M %Fesoln
%Feads %FeMag %FeSid %FeMaghe %FeFerri FeIIDeltaG_M
DeltaGrxnFe_kJ/mol DeltaGrxnGoeth_kJ/mol DeltaGrxnMag_kJ/mol
DeltaGdiff_kJ/mol EhUO2(OH)2_kJ/mol EhUO2(OH)3_kJ/mol
EhUO2PO4_kJ/mol EhUO2CO3_kJ/mol EhUO2(CO3)2_kJ/mol
EhUO2(CO3)3_kJ/mol EhMgUO2(CO3)3_kJ/mol EhFe_kJ/mol EhFeOH_kJ/mol
EhFeCl_kJ/mol EhFeSO4_kJ/mol EhFeHSO4_kJ/mol EhFeHPO4_kJ/mol
EhFeH2PO4_kJ/mol EhFeCO3_kJ/mol EhFeHCO3_kJ/mol FTU FTFerri
FTGoeth FTMag DeltaGUox20_kJ/mol DeltaGUox40_kJ/mol
10 PUNCH TOTAL_TIME/3600/24
# U speciation
20 Usoln = (TOT("U") + TOT("U_four"))
30 PUNCH Usoln

40 Uads = (mol("(Hfo_sO)2UO2") + mol("(Hfo_wO)2UO2") +
mol("(Hfo_sO)2UO2CO3-2") + mol("(Hfo_wO)2UO2CO3-2") +
mol("MagOUO2+") + mol("MagOUO2OH") + mol("GoeOUO2+") +
mol("GoeOUO2OH"))
50 PUNCH Uads

60 PUNCH EQUI("Uraninite")/0.12

70 uranyl = mol("UO2+2")
80 PUNCH uranyl

90 Unon = mol("UO2+2") + mol("UO2OH+") + mol("UO2(OH)2") +
mol("UO2(OH)3-") + mol("UO2(OH)4-2") + mol("(UO2)2OH+3") +
mol("(UO2)2(OH)2+2") + mol("(UO2)3(OH)4+2") + mol("(UO2)3(OH)5+")
+ mol("(UO2)3(OH)7-") + mol("(UO2)4(OH)7+") + mol("UO2Ace+") +
mol("UO2(Ace)2") + mol("UO2(Ace)3-") + mol("UO2Lac+") +
mol("UO2(Lac)2") + mol("UO2(Lac)3-") + mol("UO2Cl+") +
mol("UO2Cl2") + mol("UO2SO4") + mol("UO2(SO4)2-2") +
mol("UO2(SO4)3-4") + mol("UO2NO3+") + mol("UO2PO4-") +
mol("UO2HPO4") + mol("UO2H2PO4+") + mol("UO2H3PO4+2") +
mol("UO2(H2PO4)2") + mol("UO2(H2PO4)")
100 PUNCH Unon

110 Ucarb = mol("UO2CO3") + mol("UO2(CO3)2-2") + mol("UO2(CO3)3-
4") + mol("(UO2)3(CO3)6-6") +  mol("(UO2)2CO3(OH)3-") +
mol("(UO2)3O(OH)2(HCO3)+") + mol("(UO2)11(CO3)6(OH)12-2")
120 PUNCH Ucarb

130 Utern = mol("CaUO2(CO3)3-2") + mol("Ca2UO2(CO3)3") +
mol("MgUO2(CO3)3-2") + mol("SrUO2(CO3)3-2") + mol("BaUO2(CO3)3-
2") + mol("Ba2UO2(CO3)3")
```

```
140 PUNCH Utern

#U(VI) respiration DeltaG
150 QU = MOL("Ace-") * MOL("HCO3-") * MOL("H+")^5 /
MOL("UO2+2")^2 / MOL("Lac-")  # 2UO22+ + Lac- + 2H2O = 2UO2(am) +
Ace- + HCO3- + 5H+
160 LnQU = LOG(QU)
170 DeltaGrxnU = -52.96 + 0.008314 * 299 * LnQU
180 IF TOT("U")=0 THEN DeltaGrxnU = 0
190 PUNCH DeltaGrxnU

#Iron speciation
200 Ferri = EQUI("Ferrihydrite")/0.12
210 PUNCH Ferri

220 Mag = EQUI("Magnetite")/0.12*3  # 1 mol Mag = 3 mol Fe
230 PUNCH Mag

240 Maghe = EQUI("Maghemite")/0.12*2 # 1 mol Maghe = 2 mol Fe
250 PUNCH Maghe

260 Sid = EQUI("Siderite")/0.12
270 PUNCH Sid

280 PUNCH (Ferri + Mag)  # amorphous Fe oxides

290 FeIIT = (TOT("Fe_di") + mol("Hfo_wOFe_di+") +
mol("Hfo_wOFe_diOH") + mol("Hfo_sOFe_di+") +
EQUI("Magnetite")/0.12 + EQUI("Siderite")/0.12 +
mol("MagOFe_di+") + mol("MagOFe_diOH") + mol("GoeOFe_di+") +
mol("GoeOFe_diOH"))
300 PUNCH FeIIT

310 FeIIsoln = TOT("Fe_di")
320 PUNCH FeIIsoln

330 FeIIads = (mol("Hfo_wOFe_di+") + mol("Hfo_wOFe_diOH") +
mol("Hfo_sOFe_di+") + mol("MagOFe_diOH") + mol("GoeOFe_di+") +
mol("GoeOFe_diOH"))
340 PUNCH FeIIads

350 Febalance = (EQUI("Ferrihydrite")/0.12 + TOT("Fe_di") +
EQUI("Magnetite")/0.12*3 + EQUI("Siderite")/0.12 +
EQUI("Maghemite")/0.12*2) + FeIIads
360 PUNCH Febalance
370 PUNCH FeIIsoln / Febalance * 100
380 PUNCH FeIIads / Febalance * 100
390 PUNCH Mag / Febalance * 100
400 PUNCH Sid / Febalance * 100
410 PUNCH Maghe  / Febalance * 100
420 PUNCH Ferri / Febalance * 100
```

```
#Iron Respiration DeltaG values
430 FeII = MOL("Fe_di+2")
450 PUNCH FeII

460 QFerri = MOL("Ace-") * MOL("HCO3-") * FeII^4 / MOL("H+")^7 /
MOL("Lac-")
470 LnQFerri = LOG(QFerri)  # 4Fe(OH)3 (ferrihydrite) + Lac- +
7H+ --> 4Fe(II) + Ace- + HCO3- + 10H2O
480 DeltaGrxnFerri = -294.645 + 0.008314 * 299 * LnQFerri
490 PUNCH DeltaGrxnFerri

500 QGoeth = FeII^4 * MOL("Ace-") * MOL("HCO3-") / MOL("Lac-") /
MOL("H+")^7
510 LnQGoeth = LOG(QGoeth)  # 4FeOOH (goethite) + Lac- + 7H+ -->
4Fe(II) Ace- + HCO3- + 6H2O
520 DeltaGrxnGoeth = -248.485 + 0.008314 * 299 * LnQGoeth
530 PUNCH DeltaGrxnGoeth

600 QMag = FeII^6 * MOL("Ace-") * MOL("HCO3-") / MOL("Lac-") /
MOL("H+")^11
610 LnQMag = LOG(QMag)
620 DeltaGrxnMag = -307.085 + 0.008314 * 299 * LnQMag # 2Fe3O4(s)
+ Lac- + 11H+ --> 6Fe+2 + Ace- + HCO3- + 6H2O
630 PUNCH DeltaGrxnMag

700 DeltaGdiff = DeltaGrxnFerri - DeltaGrxnU
710 PUNCH DeltaGdiff

# UO2(am)/U(VI) species half-reaction DeltaGr (kJ/mol)
1000 QUO2OH2 = MOL("UO2(OH)2") * MOL("H+")^2
1010 LnQUO2OH2 = LOG(QUO2OH2)
1020 EhUO2OH2 = 0.581-0.084  + 0.008314 * 299 / 2 / 96.484 *
LnQUO2OH2  # Eh = E0 + (RT/nF) * Ln(Ox/Red)
1030 PUNCH EhUO2OH2 # UO2(OH)2 + 2H+ + 2e- == UO2(am) + 2H2O

1100 QUO2OH3 = MOL("UO2(OH)3-") * MOL("H+")^3
1110 LnQUO2OH3 = LOG(QUO2OH3)
1120 EhUO2OH3 = 0.821-0.084  + 0.008314 * 299 / 2 / 96.484 *
LnQUO2OH3 # Eh = E0 + (RT/nF) * Ln(Ox/Red)
1130 PUNCH EhUO2OH3  # UO2(OH)3- + 3H+ + 2e- == UO2(am) + 3H2O

1200 QUO2PO4 = MOL("UO2PO4-") * MOL("H+") / MOL("HPO4-2")
1210 LnQUO2PO4 = LOG(QUO2PO4)
1220 EhUO2PO4 = 0.196-0.084  + 0.008314 * 299 / 2 / 96.484 *
LnQUO2PO4  # Eh = E0 + (RT/nF) * Ln(Ox/Red)
1230 PUNCH EhUO2PO4  # UO2PO4- + H+ + 2e- == UO2(am) + HPO4-2

1300 QUO2CO3 = MOL("UO2CO3") * MOL("H+") / MOL("HCO3-")
1310 LnQUO2CO3 = LOG(QUO2CO3)
1320 EhUO2CO3 = 0.233-0.084  + 0.008314 * 299 / 2 / 96.484 *
LnQUO2CO3  # Eh = E0 + (RT/nF) * Ln(Ox/Red)
1330 PUNCH EhUO2CO3  # UO2CO3 + H+ + 2e- == UO2(am) + HCO3-
```

```
1400 QUO2CO32 = MOL("UO2(CO3)2-2") * MOL("H+")^2 / MOL("HCO3-")^2
1410 LnQUO2CO32 = LOG(QUO2CO32)
1420 EhUO2CO32 = 0.341-0.084  + 0.008314 * 299 / 2 / 96.484 *
LnQUO2CO32  # Eh = E0 + (RT/nF) * Ln(Ox/Red)
1430 PUNCH EhUO2CO32 # UO2(CO3)2-2 + 2H+ + 2e- == UO2(am)  +
2HCO3-

1500 QUO2CO33 = MOL("UO2(CO3)3-4") * MOL("H+")^3 / MOL("HCO3-")^3
1510 LnQUO2CO33 = LOG(QUO2CO33)
1520 EhUO2CO33 = 0.492-0.084  + 0.008314 * 299 / 2 / 96.484 *
LnQUO2CO33  # Eh = E0 + (RT/nF) * Ln(Ox/Red)
1530 PUNCH EhUO2CO33  # UO2(CO3)3-4 + 3H+ + 2e- == UO2(am) +
3HCO3-

1540 QMgUO2CO33 = MOL("MgUO2(CO3)3-2") * MOL("H+")^3 /
(MOL("HCO3-")^3) / MOL("Mg+2")
1550 LnQMgUO2CO33 = LOG(QMgUO2CO33)
1560 EhMgUO2CO33 = 0.366-0.084  + 0.008314 * 299 / 2 / 96.484 *
LnQMgUO2CO33 # Eh = E0 + (RT/nF) * Ln(Ox/Red)
1570 PUNCH EhMgUO2CO33  # MgUO2(CO3)3-2 + 3H+ + 2e- == UO2(am) +
3HCO3- + Mg2+

# Fe(OH)3/Fe(II) Eh (V)

1600 QFe2 = MOL("Fe_di+2") / MOL("H+")^3
1610 LnQFe2 = LOG(QFe2)
1620 EhFe2 = 0.848 - 0.008314 * 299 / 96.484 * LnQFe2 # Eh = E0 -
(RT/nF) * LnQ
1630 PUNCH EhFe2  # Fe(OH)3(s) + e- + 3H+ = Fe2+ + 3H2O

1700 QFeOH = MOL("Fe_diOH+") / MOL("H+")^2
1710 LnQFeOH = LOG(QFeOH)
1720 EhFeOH = 0.286 - 0.008314 * 299 / 96.484 * LnQFeOH  # Eh =
E0 - (RT/nF) * LnQ
1730 PUNCH EhFeOH  # Fe(OH)3(s) + e- 2H+ = FeOH+ + 2H2O

1800 QFeCl = MOL("Fe_diCl+") / MOL("H+")^3 / MOL("Cl-")
1810 LnQFeCl = LOG(QFeCl)
1820 EhFeCl = 0.856 - 0.008314 * 299 / 96.484 * LnQFeCl  # Eh =
E0 - (RT/nF) * LnQ
1830 PUNCH EhFeCl  # Fe(OH)3(s) + e- + Cl- + 3H+ = FeCl+ + 3H2O

1900 QFeSO4 = MOL("Fe_diSO4") / MOL("H+")^3 / MOL("SO4-2")
1910 LnQFeSO4 = LOG(QFeSO4)
1920 EhFeSO4 = 0.981 - 0.008314 * 299 / 96.484 * LnQFeSO4  # Eh =
E0 - (RT/nF) * LnQ
1930 PUNCH EhFeSO4  # Fe(OH)3(s) + e- + SO4-2 + 3H+ = FeSO4 +
3H2O

2000 QFeHSO4 = MOL("Fe_diHSO4+") / MOL("H+")^4 / MOL("SO4-2")
2010 LnQFeHSO4 = LOG(QFeHSO4)
```

```
2020 EhFeHSO4 = 1.029 - 0.008314 * 299 / 96.484 * LnQFeHSO4  # Eh
= E0 - (RT/nF) * LnQ
2030 PUNCH EhFeHSO4  # Fe(OH)3(s) + e- + SO4-2 + 4H+ = FeHSO4 +
3H2O

2100 QFeHPO4 = MOL("Fe_diHPO4") / MOL("H+")^3 / MOL("HPO4-2")
2110 LnQFeHPO4 = LOG(QFeHPO4)
2120 EhFeHPO4 = 1.061 - 0.008314 * 299 / 96.484 * LnQFeHPO4  # Eh
= E0 - (RT/nF) * LnQ
2130 PUNCH EhFeHPO4  # Fe(OH)3(s) + e- + HPO4-2 + 3H+ = FeHPO4 +
3H2O

2200 QFeH2PO4 = MOL("Fe_diH2PO4+") / MOL("H+")^4 / MOL("HPO4-2")
2210 LnQFeH2PO4 = LOG(QFeH2PO4)
2220 EhFeH2PO4 = 1.434 - 0.008314 * 299 / 96.484 * LnQFeH2PO4  #
Eh = E0 - (RT/nF) * LnQ
2230 PUNCH EhFeH2PO4  # Fe(OH)3(s) + e- + HPO4-2 + 4H+ = FeH2PO4+
+ 3H2O

2300 QFeCO3 = MOL("Fe_diCO3") / MOL("H+")^2 / MOL("HCO3-")
2310 LnQFeCO3 = LOG(QFeCO3)
2320 EhFeCO3 = 0.496 - 0.008314 * 299 / 96.484 * LnQFeCO3  # Eh =
E0 - (RT/nF) * LnQ
2330 PUNCH EhFeCO3  # Fe(OH)3(s) + e- + HCO3- + 2H+  = FeCO3 +
3H2O

2400 QFeHCO3 = MOL("Fe_diHCO3+") / MOL("H+")^3 / MOL("HCO3-")
2410 LnQFeHCO3 = LOG(QFeHCO3)
2420 EhFeHCO3 = 0.966 - 0.008314 * 299 / 96.484 * LnQFeHCO3  # Eh
= E0 - (RT/nF) * LnQ
2430 PUNCH EhFeHCO3  # Fe(OH)3(s) + e- + HCO3- + 3H+ = FeHCO3+ +
3H2O

# Thermodynamic Driving Force FT values
2500 FTU = 1 - EXP((DeltaGrxnU + 67.5)/(4*0.008314*299))
2510 IF FTU<=0 THEN FTU = 0
2520 PUNCH FTU

2630 FTFe = 1 - EXP((DeltaGrxnFerri + 67.5)/(4*0.008314*299))
2640 IF FTFe<=0 THEN FTFe = 0
2650 PUNCH FTFe

2760 FTGoeth = 1 - EXP((DeltaGrxnGoeth + 67.5)/(4*0.008314*299))
2770 IF FTGoeth<=0 THEN FTGoeth = 0
2780 PUNCH FTGoeth

2800 FTMag = 1 - EXP((DeltaGrxnMag + 67.5)/(4*0.008314*299))
2810 IF FTMag<=0 THEN FTMag = 0
2820 PUNCH FTMag

# DeltaGr UO2 oxidation by Fh to UTC and Fe+2 (20DIC)
3230 DeltaGUox20 = -2 * 96.484 * (EhFe2 - EhUO2CO33)
```

```
3240 PUNCH DeltaGUox20

# DeltaGr UO2 oxidation by Fh to UTC and FeHCO3+ (40DIC)
3320 DeltaGUox40 = -2 * 96.484 * (EhFeHCO3 - EhUO2CO33)
3330 PUNCH DeltaGUox40


SOLUTION 2  # pH 8, 20 mM DIC, +Fe
units mol/L
water 0.12 # L
temp 26 #C
pH       8.0
C(+4)    0.01960
Na       0.03461  #1x C, 1x Lac, 0.00001 NaCl
Lac      0.015
Ace      360e-6
Ca       0.0
S        0.00105 #0.5x Amm, 1x Mg
Cl       0.00001 # 0.00001 NaCl, 2x Ca,
Mg       0.001
Amm      0.0001
P        0.0001
K        0.0001
Bio      3.32e-14
Fe_di    265e-6
U        137e-6

USE KINETICS 2
USE EQUILIBRIUM_PHASES 2
USE SURFACE 2
END

SOLUTION 5  # pH 8, 40 mM DIC +Fe
units mol/L
water 0.12 # L
temp 26 #C
pH       8.0
C(+4)    0.0373
Na       0.05231  #1x C, 1x Lac, 0.00001 NaCl
Lac      0.015
Ace      360e-6
Ca       0.0
S        0.00105 #0.5x Amm, 1x Mg
Cl       0.00001 # 0.00001 NaCl, 2x Ca,
Mg       0.001
Amm      0.0001
P        0.0001
K        0.0001
Bio      3.32e-14
Fe_di    261e-6
U        150e-6
```

```
USE KINETICS 5
USE EQUILIBRIUM_PHASES 5
USE SURFACE 5
END
```

APPENDIX D. SUPPLEMENTARY DATA FOR CHAPTER 5

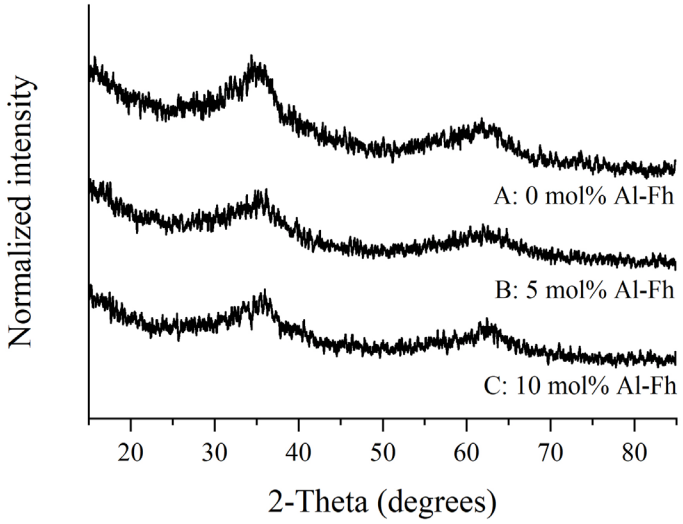

Figure D.1. Powder X-ray diffraction (XRD) patterns of the synthesized (A) 0, (B) 5, and (C) 10 mol% Al-ferrihydrite stock suspensions used in this study. Only two broad peaks attributed to 2-line ferrihydrite were identified, demonstrating the absence of secondary Al phases formed during synthesis. Signals are normalized to the maximum intensity of each pattern and smoothed using a 10-point moving average.

Table D.1. Composition of modified M1 medium[a]

Component	Concentration
$CoCl_2$	5 µM
$NiCl_2$	5 µM
NaCl	10 µM
H_3BO_4	56.6 µM
$ZnSO_4$	1.04 µM
Na_2MoO_4	3.87 µM
$MnSO_4 \cdot H_2O$	1.26 µM
$CuSO_4$	200 nM
$MgSO_4$	1 mM
$FeSO_4$[b]	5.4 µM
$CaCl_2$[b]	485.2 µM
Na_2EDTA[b]	67.2 µM
L-serine	381 µM
L-arginine	115 µM
L-glutamine	137 µM
$(NH_4)_2SO_4$	50 µM
Na_2SeO_4	1.5 µM
$FeCl_3$[b]	100 µM
KH_2PO_4	100 µM

[a]Adapted from Myers and Nealson(1988)
[b]Omitted from incubations amended with U(VI) and/or ferrihydrite as terminal electron acceptors

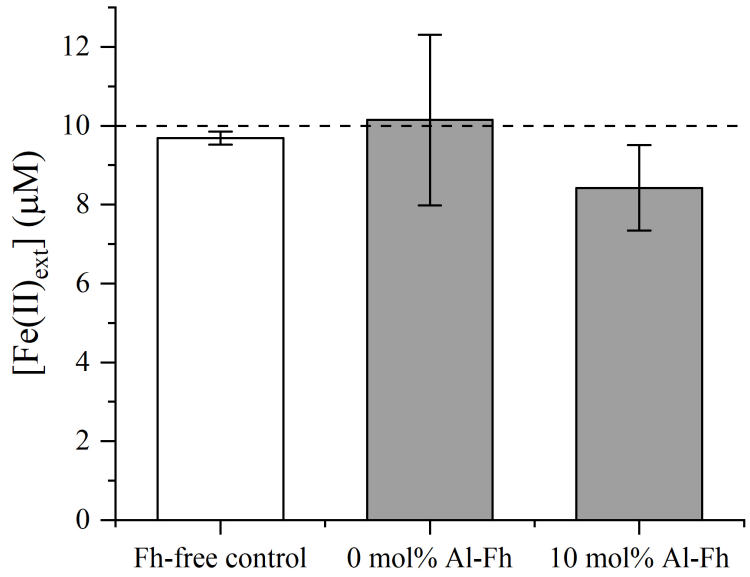

Figure D.2. Determination of ferrozine extraction efficiency for measuring dissolved and adsorbed Fe(II) in the presence of (Al-)ferrihydrite. 10 μM Fe(II) ($Fe(NH_4)_2(SO_4)2{\cdot}6H_2O$ in 0.1 M HCl) was amended to uranium-free incubations containing modified M1 medium, 15 mM PIPES (pH 8), 40 mM DIC, and autoclaved, fumarate-grown cells of *S. putrefaciens* (approximately 2×10^7 cell/mL) with (solid bar) or without (open bar) 1 mM (Al-)ferrihydrite. After 30 minutes of equilibration, ferrozine-extractable Fe(II) ($Fe(II)_{ext}$) was measured in unfiltered aliquots as described previously (Ginder-Vogel et al., 2010). The dashed line represents the input concentration of Fe(II). Error bars represent triplicate measurements of each incubation. 97±2% of added Fe(II) was recovered in the ferrihydrite-free control, demonstrating that Fe(II) was not oxidized during the equilibration period. The ferrozine extraction recovered between 87±11% and 105±22% of dissolved and adsorbed Fe(II) in incubations amended with (Al-)ferrihydrite, validating the extraction procedure.

Table D.2. Measured initial solution composition and calculated aqueous uranyl speciation assuming thermodynamic equilibrium in batch incubations with *S. putrefaciens*

Incubation	$[U_d]$ (μM)	$[UO_2^{2+}]$ (M)	$[U(VI)_{non\text{-}carb}]$ (pM)	$[U(VI)_{carb}]$ (μM)	$[U(VI)_{tern}]$ (μM)
+U, 20 mM DIC	164±7	4.18×10^{-15}	103	95	69
+U, 40 mM DIC	171±3	4.98×10^{-16}	11	118	54
+U+0Al-Fh, 20 mM DIC	147±2	3.59×10^{-15}	88	85	62
+U+0Al-Fh, 40 mM DIC	162±2	5.51×10^{-16}	12	110	53
+U+5Al-Fh, 20 mM DIC	131±3	3.07×10^{-15}	76	76	56
+U+5Al-Fh, 40 mM DIC	153±4	4.13×10^{-16}	9	106	48
+U+10Al-Fh, 20 mM DIC	112±6	2.60×10^{-15}	64	65	48
+U+10Al-Fh, 40 mM DIC	146±5	3.93×10^{-16}	8	101	46

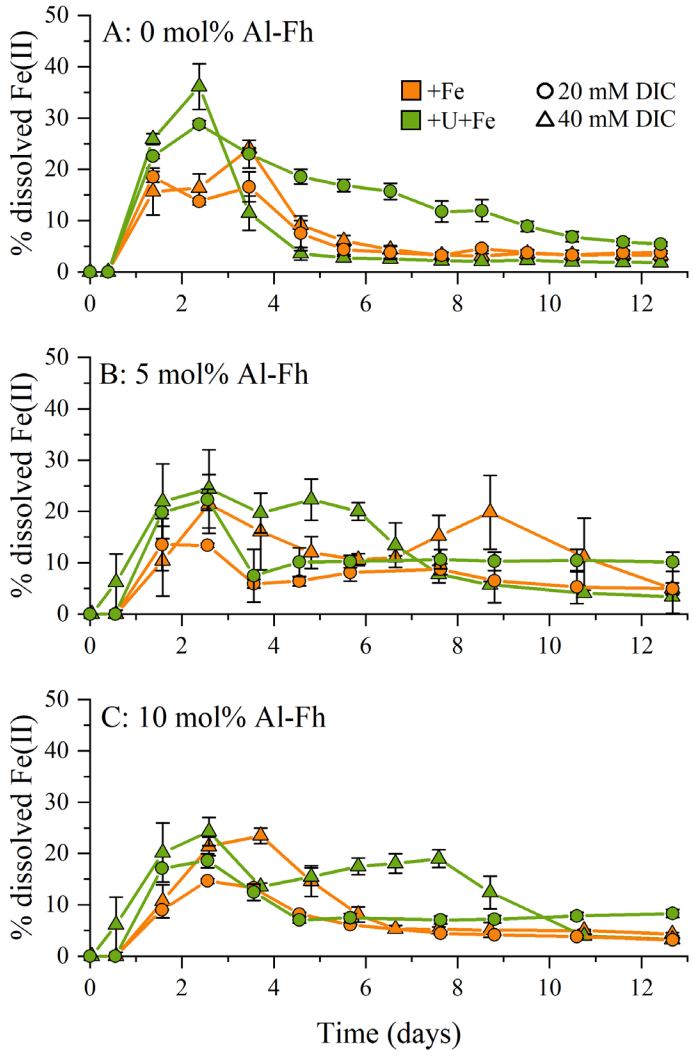

Figure D.3. Time series of percent dissolved Fe(II) normalized to total Fe(II) in incubations with *S. putrefaciens* amended with either 5 mM of: (A) 0, (B) 5, or (C) 10 mol% Al-ferrihydrite (orange) or both 180 µM U(VI) and 5 mM (Al-)ferrihydrite (green) as terminal electron acceptors, and either 20 mM (circles) or 40 mM (triangles). Symbols and error bars represent the average and standard deviation of measurements from triplicate incubations.

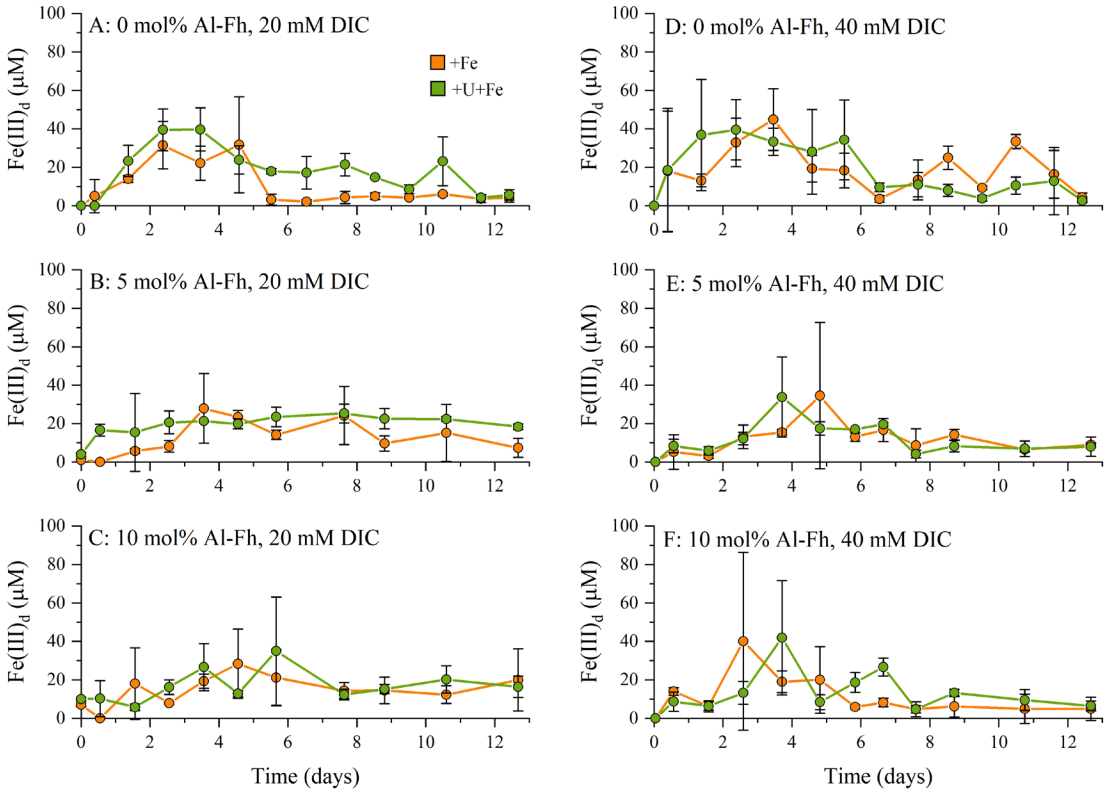

Figure D.4. Time series of dissolved Fe(III) ($Fe(III)_d$) in incubations with *S. putrefaciens* amended with either 5 mM of: (A and D) 0, (B and E) 5, or (C and F) 10 mol% Al-ferrihydrite (orange) or both 180 µM U(VI) and 5 mM (Al-)ferrihydrite (green) as terminal electron acceptors and either 20 mM (right) or 40 mM (left) DIC. Symbols and error bars represent the average and standard deviation of triplicate incubations.

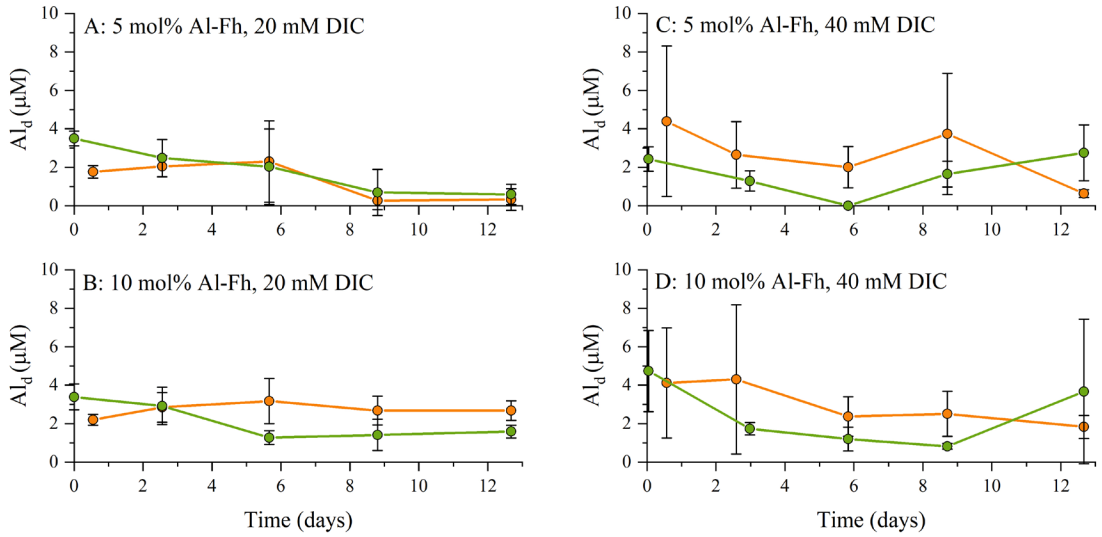

Figure D.5. Time series of total dissolved aluminum (Al_d) in incubations with *S. putrefaciens* amended with either 5 mM of: (A and C) 5 or (B and D) 10 mol% Al-ferrihydrite (orange) or both 180 µM U(VI) and 5 mM (Al-)ferrihydrite (green) as terminal electron acceptors and either 20 mM (right) or 40 mM (left) DIC. Symbols and error bars represent the average and standard deviation of measurements from triplicate incubations.

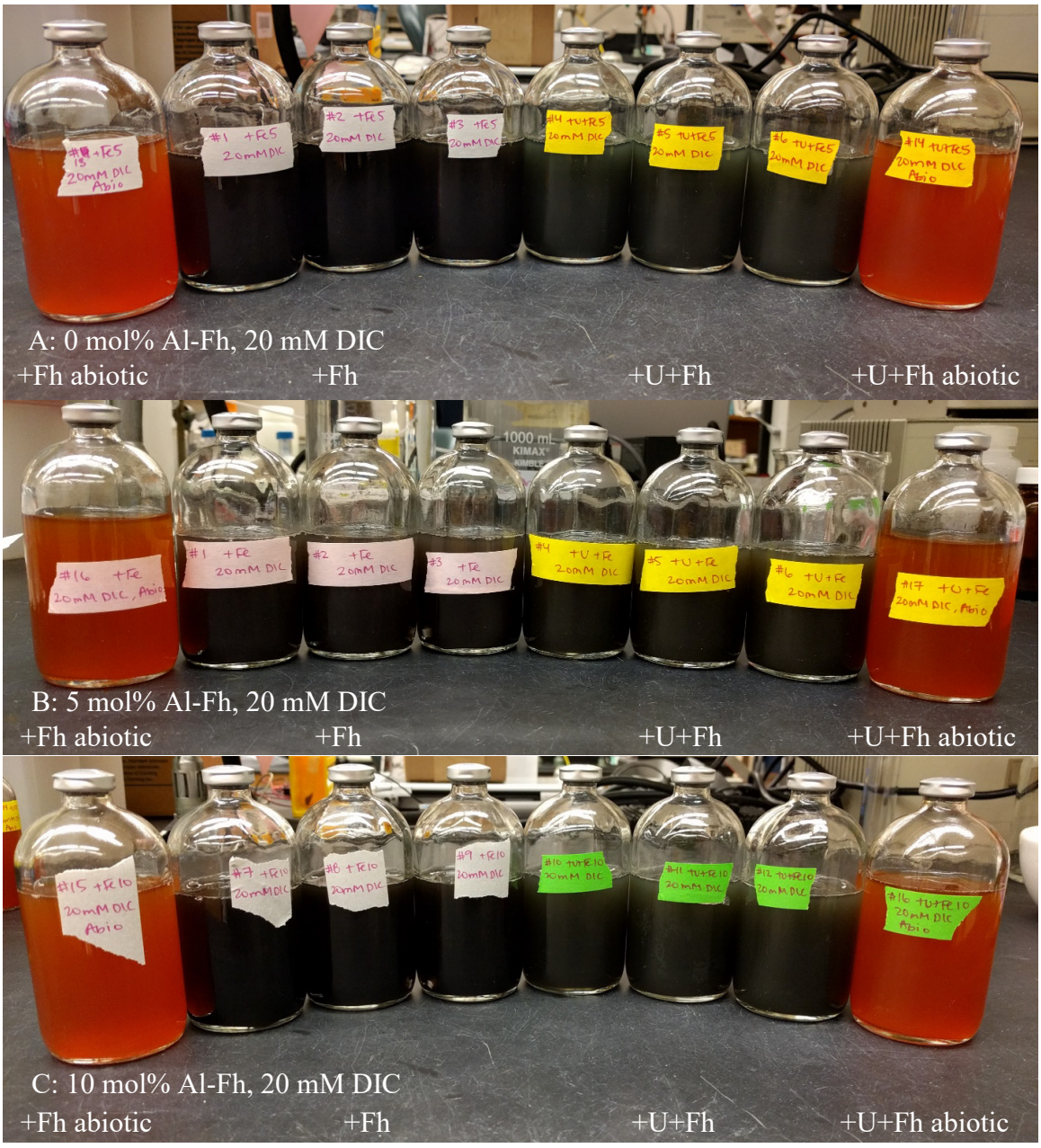

Figure D.6. Images of incubations amended with 20 mM DIC and (A) 0, (B) 5, and (C) 10 mol% Al-ferrihydrite after 12 days of reaction.

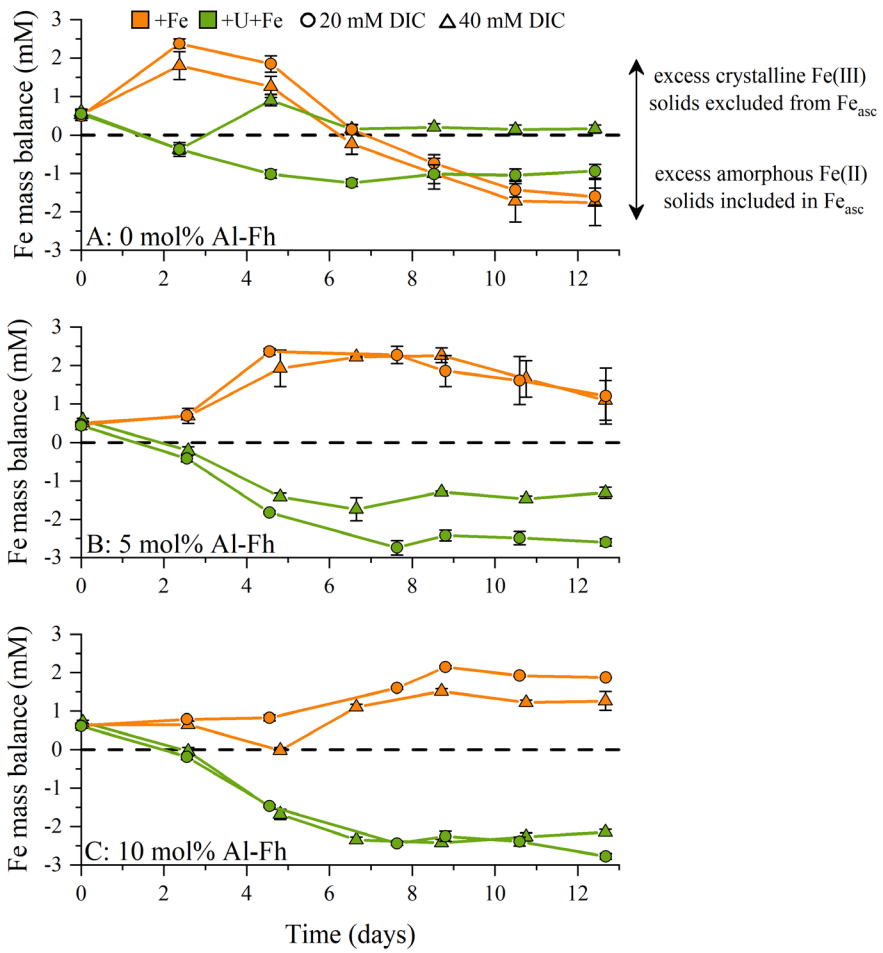

Figure D.7. Time series of iron mass balance ([Fe(III)$_{solid}$] - [Fe$_{asc}$]) in incubations with *S. putrefaciens* amended with either 5 mM of: (A) 0, (B) 5, or (C) 10 mol% Al-ferrihydrite (orange) or both 180 µM U(VI) and 5 mM (Al-)ferrihydrite (green) as terminal electron acceptors, and either 20 mM (circles) or 40 mM (triangles) DIC. Symbols and error bars represent the average and standard deviation of measurements from triplicate incubations. The concentration of solid Fe(III) (Fe(III)$_{solid}$) was calculated from measured concentrations of initial total iron (Fe$_{T,0}$), total Fe(II) (Fe(II)$_T$), and dissolved Fe(III) (Fe(III)$_d$) (i.e., [Fe(III)$_{solid}$] = [Fe$_{T,0}$] - [Fe(II)$_T$] - [Fe(III)$_d$]). The difference between the calculated concentration of Fe(III)$_{solid}$ and the measured concentration of ascorbate-extractable solid phase iron (Fe$_{asc}$) indicates the redox state and crystallinity of the total solid phase at each time point. Positive values ([Fe(III)$_{solid}$] > [Fe$_{asc}$]) indicate an excess of crystalline Fe(III)-bearing solids which were excluded from the ascorbate-extractable fraction of solid phase iron, whereas negative values ([Fe(III)$_{solid}$] < [Fe$_{asc}$]) indicate an excess of Fe(II)-bearing solids which were included in the ascorbate-extractable fraction of solid phase iron.

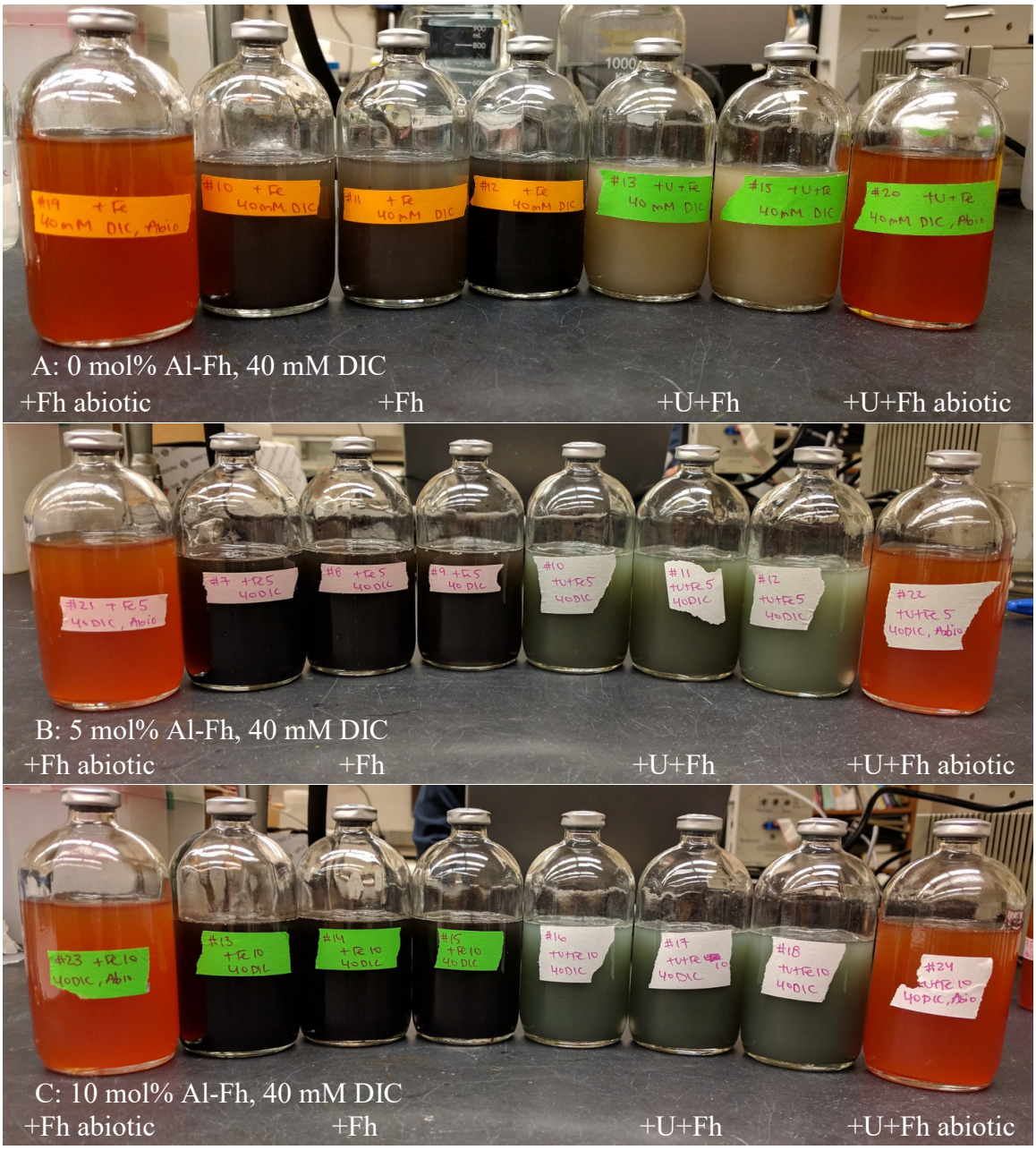

Figure D.8. Images of incubations amended with 40 mM DIC and (A) 0, (B) 5, and (C) 10 mol% Al-ferrihydrite after 12 days of reaction.

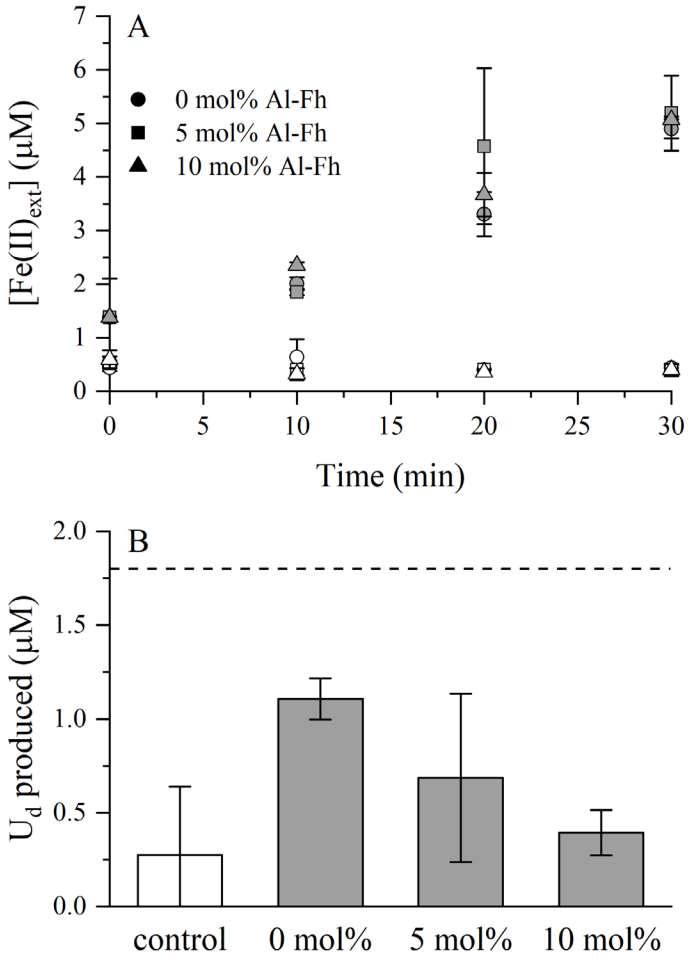

Figure D.9. Time series of (A) ferrozine-extractable Fe(II) ($Fe(II)_{ext}$) and (B) total dissolved uranium (U_d) produced in abiotic U(IV) oxidation incubations with 0, 5, or 10 mol% Al-ferrihydrite. Filled symbols represent incubations containing both U(IV) solids and (Al-)ferrihydrite, whereas open symbols represent control incubations without either (A) uranium or (B) iron. (B) The dashed line represents the expected concentration of U_d based on the production of Fe(II) assuming stoichiometric oxidation of U(IV) by Fe(III). Symbols and error bars represent the average and standard deviation of duplicate incubations.

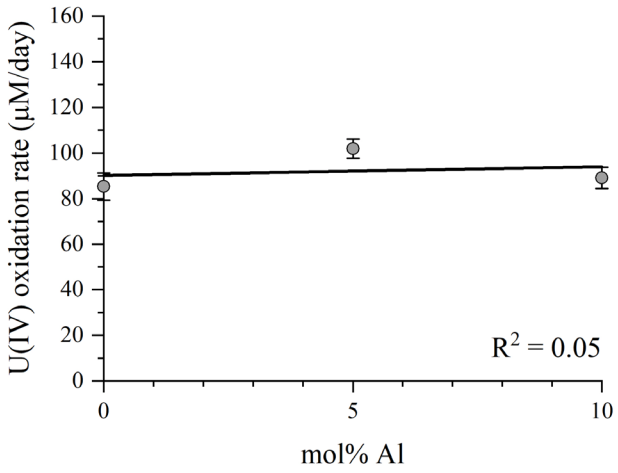

Figure D.10. U(IV) oxidation rate versus the Al content of ferrihydrite in abiotic U(IV) oxidation incubations. A linear regression (black line) was fitted to the data (R^2 = 0.05). U(IV) oxidation rates were calculated for individual incubations and presented as the average and standard deviation for each condition (n=2).

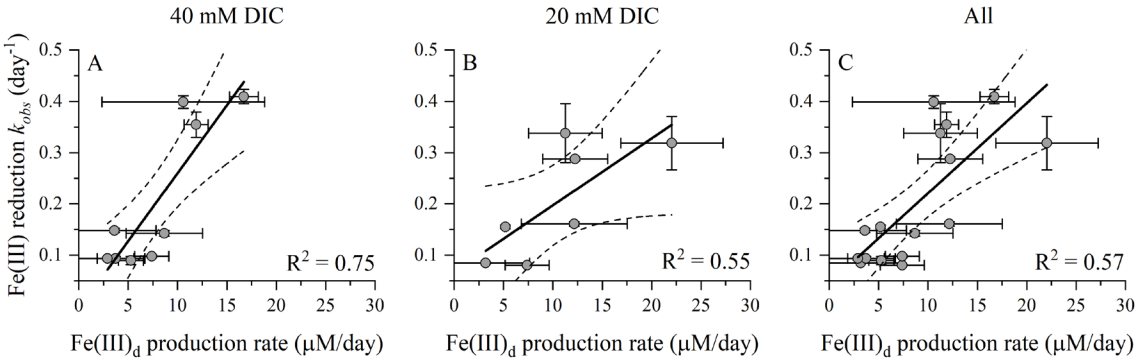

Figure D.11. Pseudo-first order rate constants (k_{obs}) of Fe(III) reduction versus dissolved Fe(III) ($Fe(III)_d$) net production rates for incubations with *S. putrefaciens* amended with 5 mM (Al-)ferrihydrite as the sole terminal electron acceptor. Linear regressions (black lines) were fitted to data from incubations amended with (A) 40 mM DIC, (B) 20 mM DIC, or (C) all (Al-)ferrihydrite-only incubations. Symbols represent data for individual incubations, and error bars represent the standard error of the slope of the linear regression used to calculate the k_{obs} or rate for each incubation. Dashed lines represent the 95% confidence band for the linear regression.

REFERENCES

Alessi, D.S., Lezama-Pacheco, J.S., Janot, N., Suvorova, E.I., Cerrato, J.M., Giammar, D.E., Davis, J.A., Fox, P.M., Williams, K.H., Long, P.E., Handley, K.M., Bernier-Latmani, R. and Bargar, J.R. (2014a) Speciation and Reactivity of Uranium Products Formed during in Situ Bioremediation in a Shallow Alluvial Aquifer. Environ. Sci. Technol. 48, 12842-12850.

Alessi, D.S., Lezama-Pacheco, J.S., Stubbs, J.E., Janousch, M., Bargar, J.R., Persson, P. and Bernier-Latmani, R. (2014b) The product of microbial uranium reduction includes multiple species with U(IV)-phosphate coordination. Geochim. Cosmochim. Acta 131, 115-127.

Alessi, D.S., Uster, B., Veeramani, H., Suvorova, E.I., Lezama-Pacheco, J.S., Stubbs, J.E., Bargar, J.R. and Bernier-Latmani, R. (2012) Quantitative Separation of Monomeric U(IV) from UO2 in Products of U(VI) Reduction. Environ. Sci. Technol. 46, 6150-6157.

Amstaetter, K., Borch, T. and Kappler, A. (2012) Influence of humic acid imposed changes of ferrihydrite aggregation on microbial Fe(III) reduction. Geochim. Cosmochim. Acta 85, 326-341.

Anderson, P.R. and Benjamin, M.M. (1990) Surface and bulk characteristics of binary oxide suspensions. Environ. Sci. Technol. 24, 692-698.

Anderson, R.T., Vrionis, H.A., Ortiz-Bernad, I., Resch, C.T., Long, P.E., Dayvault, R., Karp, K., Marutzky, S., Metzler, D.R., Peacock, A., White, D.C., Lowe, M. and Lovley, D.R. (2003) Stimulating the in situ activity of Geobacter species to remove uranium from the groundwater of a uranium-contaminated aquifer. Applied and Environmental Microbiology 69, 5884-5891.

Appelo, C.A.J., Van der Weiden, M.J.J., Tournassat, C. and Charlet, L. (2002) Surface complexation of ferrous iron and carbonate on ferrihydrite and the mobilization of arsenic. Environ. Sci. Technol. 36, 3096-3103.

Arey, J.S., Seaman, J.C. and Bertsch, P.M. (1999) Immobilization of uranium in contaminated sediments by hydroxyapatite addition. Environmental Science and Technology 33, 337-342.

Arnold, R.G., Olson, T.M. and Hoffmann, M.R. (1986) KINETICS AND MECHANISM OF DISSIMILATIVE FE(III) REDUCTION BY PSEUDOMONAS-SP-200. Biotechnology and bioengineering 28, 1657-1671.

Bachmaf, S. and Broder, J.M. (2011) Estimating water chemistry parameters from experimental data using PEST with PHREEQC. Freiberg Online Geology 28.

Bargar, J.R., Reitmeyer, R., Lenhart, J.J. and Davis, J.A. (2000) Characterization of U(VI)-carbonato ternary complexes on hematite: EXAFS and electrophoretic mobility measurements. Geochim. Cosmochim. Acta 64, 2737-2749.

Bargar, J.R., Williams, K.H., Campbell, K.M., Long, P.E., Stubbs, J.E., Suvorova, E.I., Lezama-Pacheco, J.S., Alessi, D.S., Stylo, M., Webb, S.M., Davis, J.A., Giammar, D.E., Blue, L.Y. and Bernier-Latmani, R. (2013) Uranium redox transition pathways in acetate-amended sediments. Proceedings of the National Academy of Sciences of the United States of America 110, 4506-4511.

Behrends, T. and Van Cappellen, P. (2005) Competition between enzymatic and abiotic reduction of uranium(VI) under iron reducing conditions. Chemical Geology 220, 315-327.

Beller, H.R. (2005) Anaerobic, nitrate-dependent oxidation of U(IV) oxide minerals by the chemolithoautotrophic bacterium Thiobacillus denitrificans. Applied and Environmental Microbiology 71, 2170-2174.

Beller, H.R., Legler, T.C., Bourguet, F., Letain, T.E., Kane, S.R. and Coleman, M.A. (2009) Identification of c-type cytochromes involved in anaerobic, bacterial U(IV) oxidation. Biodegradation 20, 45-53.

Belli, K. and Taillefert, M. (In review) Geochemical controls of the microbially-mediated redox cycling of uranium and iron. Geochim. Cosmochim. Acta.

Belli, K.M., DiChristina, T.J., Van Cappellen, P. and Taillefert, M. (2014) Speciation of uranium controls its kinetics of reduction by metal-reducing bacteria. Submitted.

Belli, K.M., DiChristina, T.J., Van Cappellen, P. and Taillefert, M. (2015) Effects of aqueous uranyl speciation on the kinetics of microbial uranium reduction. Geochim. Cosmochim. Acta 157, 109-124.

Belli, K.M. and Taillefert, M. (2016) Biogeochemical Processes Regulating the Mobility of Uranium in Sediments, in: Rinklebe, J., Knox, A.S., Paller, M. (Eds.), Trace Elements in Waterlogged Soils and Sediments. CRC Press, pp. 185-223.

Bencheikh-Latmani, R. and Leckie, J.O. (2003) Association of uranyl with the cell wall of Pseudomonas fluorescens inhibits metabolism. Geochim. Cosmochim. Acta 67, 4057-4066.

Bernhard, G., Geipel, G., Reich, T., Brendler, V., Amayri, S. and Nitsche, H. (2001) Uranyl(VI) carbonate complex formation: Validation of the Ca2UO2(CO3)(3)(aq.) species. Radiochimica Acta 89, 511-518.

Bernier-Latmani, R., Veeramani, H., Vecchia, E.D., Junier, P., Lezama-Pacheco, J.S., Suvorova, E.I., Sharp, J.O., Wigginton, N.S. and Bargar, J.R. (2010) Non-uraninite Products of Microbial U(VI) Reduction. Environ. Sci. Technol. 44, 9456-9462.

Bhattacharyya, A., Campbell, K.M., Kelly, S.D., Roebbert, Y., Weyer, S., Bernier-Latmani, R. and Borch, T. (2017) Biogenic non-crystalline U-(IV) revealed as major component in uranium ore deposits. Nat. Commun. 8, 8.

Bi, Y.Q. and Hayes, K.F. (2014) Nano-FeS Inhibits UO2 Reoxidation under Varied Oxic Conditions. Environ. Sci. Technol. 48, 632-640.

Bi, Y.Q., Hyun, S.P., Kukkadapu, R.K. and Hayes, K.F. (2013) Oxidative dissolution of UO2 in a simulated groundwater containing synthetic nanocrystalline mackinawite. Geochim. Cosmochim. Acta 102, 175-190.

Biermann, V., Simon, F.G., Csovari, M., Csicsak, J., Folding, G. and Simoncsics, G. (2006) Long-term performance of reactive materials in PRBs for uranium remediation. Springer-Verlag Berlin, Berlin.

Blanchard, R.L., Eadie, G.G., Hans, J.M. and Kaufmann, R.F. (1983) Potential Health and Environmental Hazards of Uranium Mine Wastes, in: Environmental Protection Agency, U.S. (Ed.), Washington, D.C.

Boland, D.D., Collins, R.N., Glover, C.J., Payne, T.E. and Waite, T.D. (2014a) Reduction of U(VI) by Fe(II) during the Fe(II)-Accelerated Transformation of Ferrihydrite. Environ. Sci. Technol. 48, 9086-9093.

Boland, D.D., Collins, R.N., Miller, C.J., Glover, C.J. and Waite, T.D. (2014b) Effect of Solution and Solid-Phase Conditions on the Fe(II)-Accelerated Transformation of Ferrihydrite to Lepidocrocite and Goethite. Environ. Sci. Technol. 48, 5477-5485.

Boland, D.D., Collins, R.N., Payne, T.E. and Waite, T.D. (2011) Effect of Amorphous Fe(III) Oxide Transformation on the Fe(II)-Mediated Reduction of U(VI). Environ. Sci. Technol. 45, 1327-1333.

Bone, S.E., Dynes, J.J., Cliff, J. and Bargar, J.R. (2017) Uranium(IV) adsorption by natural organic matter in anoxic sediments. Proceedings of the National Academy of Sciences of the United States of America 114, 711-716.

Bonneville, S., Behrends, T. and Van Cappellen, P. (2009) Solubility and dissimilatory reduction kinetics of iron(III) oxyhydroxides: A linear free energy relationship. Geochim. Cosmochim. Acta 73, 5273-5282.

Bonneville, S., Behrends, T., Van Cappellen, P., Hyacinthe, C. and Roling, W.F.M. (2006) Reduction of Fe(III) colloids by Shewanella putrefaciens: A kinetic model. Geochim. Cosmochim. Acta 70, 5842-5854.

Bonneville, S., Vancappellen, P. and Behrends, T. (2004) Microbial reduction of iron(III) oxyhydroxides: effects of mineral solubility and availability. Chemical Geology 212, 255-268.

Boyanov, M.I., Fletcher, K.E., Kwon, M.J., Rui, X., O'Loughlin, E.J., Loffler, F.E. and Kemner, K.M. (2011) Solution and Microbial Controls on the Formation of Reduced U(IV) Species. Environ. Sci. Technol. 45, 8336-8344.

Brendel, P.J. and Luther, G.W. (1995) Development of a gold amalgam voltammetric microelectrode for the determination of dissolved Fe, Mn, O2, and S(-II) in porewaters of marine and fresh-water sediments Environ. Sci. Technol. 29, 751-761.

Brennecka, G.A., Wasylenki, L.E., Bargar, J.R., Weyer, S. and Anbar, A.D. (2011) Uranium Isotope Fractionation during Adsorption to Mn-Oxyhydroxides. Environ. Sci. Technol. 45, 1370-1375.

Bristow, G. and Taillefert, M. (2008) VOLTINT: A Matlabg (R)-based program for semi-automated processing of geochemical data acquired by voltammetry. Comput. Geosci. 34, 153-162.

Brooks, S.C., Fredrickson, J.K., Carroll, S.L., Kennedy, D.W., Zachara, J.M., Plymale, A.E., Kelly, S.D., Kemner, K.M. and Fendorf, S. (2003) Inhihition of bacterial U(VI) reduction by calcium. Environ. Sci. Technol. 37, 1850-1858.

Bruno, J., De Pablo, J., Duro, L. and Figuerola, E. (1995) Experimental study and modeling of U(VI)-Fe(OH)3 surface precipitation/coprecipitation equilibria. Geochim. Cosmochim. Acta 59, 4113-4123.

Burgos, W.D., McDonough, J.T., Senko, J.M., Zhang, G.X., Dohnalkova, A.C., Kelly, S.D., Gorby, Y. and Kemner, K.M. (2008) Characterization of uraninite nanoparticles produced by Shewanella oneidensis MR-1. Geochim. Cosmochim. Acta 72, 4901-4915.

Burgos, W.D., Senko, J.M., Dempsey, B.A., Roden, E.E., Stone, J.J., Kemner, K.M. and Kelly, S.D. (2007) Soil Humic Acid Decreases Biological Uranium(VI) Reduction by Shewanella putrefaciens CN32. Environmental Engineering Science 24, 755-761.

Burns, P.C. and Finch, R.J. (1999) Wyartite: Crystallographic evidence for the first pentavalent-uranium mineral. American Mineralogist 84, 1456-1460.

Butterfield, C.N., Soldatova, A.V., Lee, S.W., Spiro, T.G. and Tebo, B.M. (2013) Mn(II, III) oxidation and MnO2 mineralization by an expressed bacterial multicopper oxidase. Proceedings of the National Academy of Sciences of the United States of America 110, 11731-11735.

Campbell, K.M., Kukkadapu, R.K., Qafoku, N.P., Peacock, A.D., Lesher, E., Williams, K.H., Bargar, J.R., Wilkins, M.J., Figueroa, L., Ranville, J., Davis, J.A. and Long, P.E. (2012) Geochemical, mineralogical and microbiological characteristics of sediment from a naturally reduced zone in a uranium-contaminated aquifer. Appl. Geochem. 27, 1499-1511.

Campbell, K.M., Veeramani, H., Urich, K.U., Blue, L.Y., Giammar, D.E., Bernier-Latmani, R., Stubbs, J.E., Suvorova, E., Yabusaki, S., Lezama-Pacheco, J.S., Mehta, A.,

Long, P.E. and Bargar, J.R. (2011) Oxidative Dissolution of Biogenic Uraninite in Groundwater at Old Rifle, CO. Environ. Sci. Technol. 45, 8748-8754.

Campbell, P.G.C. (1995) In Metal Speciation and Bioavailability in Aquatic Systems, First ed. John Wiley, New York.

Cantrell, K.J., Kaplan, D.I. and Wiestma, T.W. (1995) Zero-valent iron for the in situ remediation of selected metals in groundwater. J. Hazard. Mater. 42, 201-212.

Carvajal, D.A., Katsenovich, Y.P. and Lagos, L.E. (2012) The effects of aqueous bicarbonate and calcium ions on uranium biosorption by Arthrobacter G975 strain. Chemical Geology 330, 51-59.

Catalano, J.G. and Brown Jr., G.E. (2005) Uranyl adsorption onto montmorillonite: Evaluation of binding sites and carbonate complexation. Geochim. Cosmochim. Acta 69, 2995-3005.

Cerrato, J.M., Ashner, M.N., Alessi, D.S., Lezama-Pacheco, J.S., Bernier-Latmani, R., Bargar, J.R. and Giammar, D.E. (2013) Relative Reactivity of Biogenic and Chemogenic Uraninite and Biogenic Noncrystalline U(IV). Environ. Sci. Technol. 47, 9756-9763.

Chakraborty, S., Favre, F., Banerjee, D., Scheinost, A.C., Mullet, M., Ehrhardt, J.J., Brendle, J., Vidal, L. and Charlet, L. (2010) U(VI) Sorption and Reduction by Fe(II) Sorbed on Montmorillonite. Environ. Sci. Technol. 44, 3779-3785.

Chakrabrty, S., Bardelli, F. and Charlet, L. (2010) Reactivities of Fe(II) on Calcite: Selenium Reduction. Environ. Sci. Technol. 44, 1288-1294.

Charles, A.L., Markich, S.J., Stauber, J.L. and De Filippis, L.F. (2002) The effect of water hardness on the toxicity of uranium to a tropical freshwater alga (Chlorella sp.). Aquatic Toxicology 60, 61-73.

Chen, C.M., Kukkadapu, R. and Sparks, D.L. (2015) Influence of Coprecipitated Organic Matter on Fe-(aq)(2+)-Catalyzed Transformation of Ferrihydrite: Implications for Carbon Dynamics. Environ. Sci. Technol. 49, 10927-10936.

Cheng, T., Barnett, M.O., Roden, E.E. and Zhuang, J.L. (2004) Effects of phosphate on uranium(VI) adsorption to goethite-coated sand. Environ. Sci. Technol. 38, 6059-6065.

Chinni, S., Anderson, C.R., Ulrich, K.U., Giammar, D.E. and Tebo, B.M. (2008) Indirect UO(2) Oxidation by Mn(II)-oxidizing Spores of Bacillus sp Strain SG-1 and the Effect of U and Mn Concentrations. Environ. Sci. Technol. 42, 8709-8714.

Chisholm-Brause, C.J., Berg, J.M., Matzner, R.A. and Morris, D.E. (2001) Uranium(VI) sorption complexes on montmorillonite as a function of solution chemistry. Journal of Colloid and Interface Science 233, 38-49.

Christen, P., Vega, A., Casalot, L., Simon, G. and Auria, R. (2012) Kinetics of aerobic phenol biodegradation by the acidophilic and hyperthermophilic archaeon Sulfolobus solfataricus 98/2. Biochemical Engineering Journal 62, 56-61.

Ciavatta, L., Ferri, D., Grenthe, I., Salvatore, F. and Spahiu, K. (1983) Studies on metal carbonate equilibria. 4. Reduction of the tris(carbonato)dioxouranate(VI) ion, UO2(CO3)34-, in hydrogen carbonate solutions Inorganic Chemistry 22, 2088-2092.

Cismasu, A.C., Levard, C., Michel, F.M. and Brown, G.E. (2013) Properties of impurity-bearing ferrihydrite II: Insights into the surface structure and composition of pure, Al- and Si-bearing ferrihydrite from Zn(II) sorption experiments and Zn K-edge X-ray absorption spectroscopy. Geochim. Cosmochim. Acta 119, 46-60.

Cismasu, A.C., Michel, F.M., Stebbins, J.F., Levard, C. and Brown, G.E. (2012) Properties of impurity-bearing ferrihydrite I. Effects of Al content and precipitation rate on the structure of 2-line ferrihydrite. Geochim. Cosmochim. Acta 92, 275-291.

Cismasu, A.C., Michel, F.M., Tcaciuc, A.P., Tyliszczak, T. and Brown, G.E. (2011) Composition and structural aspects of naturally occurring ferrihydrite. C. R. Geosci. 343, 210-218.

Clark, D.L., Conradson, S.D., Donohoe, R.J., Keogh, D.W., Morris, D.E., Palmer, P.D., Rogers, R.D. and Tait, C.D. (1999) Chemical speciation of the uranyl ion under highly alkaline conditions. Synthesis, structures, and oxo ligand exchange dynamics. Inorganic Chemistry 38, 1456-1466.

Clark, D.L., Hobart, D.E. and Neu, M.P. (1995) Actinide carbonate complexes and their importance in actinide environmental chemistry Chem. Rev. 95, 25-48.

Cologgi, D.L., Lampa-Pastirk, S., Speers, A.M., Kelly, S.D. and Reguera, G. (2011) Extracellular reduction of uranium via Geobacter conductive pili as a protective cellular mechanism. Proceedings of the National Academy of Sciences of the United States of America 108, 15248-15252.

Conca, J.L. and Wright, J. (2006) An apatite II permeable reactive barrier to remediate groundwater containing Zn, Pb and Cd (vol 21, pg 1288, 2006). Appl. Geochem. 21, 2187-2200.

Condomines, M., Gauthier, P.J. and Sigmarsson, G. (2003) Timescales of magma chamber processes and dating of young volcanic rocks. Uranium-Series Geochemistry 52, 125-174.

Cornell, R.M. and Schwertman, U. (2003) The Iron Oxides: Structure, Properties, Reactions, Occurences and Uses, 2nd ed. Wiley-VCH Verlag GmbH & Co., KGaA, Weinheim.

Cotton, F.A., Wilkinson, G., Murillo, C.A. and Bochmann, M. (1999) Advanced Inorganic Chemistry. John Wiley & Sons, Inc., New York.

Crane, R.A., Dickinson, M., Popescu, I.C. and Scott, T.B. (2011) Magnetite and zero-valent iron nanoparticles for the remediation of uranium contaminated environmental water. Water Research 45, 2931-2942.

Dawson, G.W. and Gilman, J. (2001) Land reclamation technology - expanding the geotechnical engineering envelope. Proc. Inst. Civil Eng.-Geotech. Eng. 149, 49-61.

Department of Energy, U.S. (1997) Linking Legacies Report. U.S. Department of Energy, Washington, D.C.

Di Toro, D.M., Allen, H.E., Bergman, H.L., Meyer, J.S., Paquin, P.R. and Santore, R.C. (2001) Biotic ligand model of the acute toxicity of metals. 1. Technical basis. Environmental Toxicology and Chemistry 20, 2383-2396.

DiChristina, T.J. and Delong, E.F. (1994) Isolation of anaerobic respiratory mutants of Shewanella putrefaciens and genetic analysis of mutants deficient in anaerobic growth on Fe3+. Journal of Bacteriology 176, 1468-1474.

Djogic, R. and Branica, M. (1995a) Direct determination of dissolved uranyl(VI) in sea-water by cathodic stripping voltammetry. The Analyst 120, 1989.

Djogic, R. and Branica, M. (1995b) Square-wave cathodic stripping voltammetry of hydrolyzed uranyl species. Analytica Chimica Acta 305, 159-164.

Djogic, R., Pizeta, I. and Branica, M. (2001) Electrochemical determination of dissolved uranium in Krka river estuary. Water Research 35, 1915-1920.

Djogic, R., Sipos, L. and Branica, M. (1986) Characterization of uranium(VI) in seawater. Limnology and Oceanography 31, 1122-1131.

Dong, W. and Brooks, S.C. (2006) Determination of the formation constants of ternary complexes of uranyl and carbonate with alkaline earth metals (Mg2+, Ca2+, Sr2+, and Ba2+) using anion exchange method. Environ. Sci. Technol. 40, 4689-4695.

Dong, W.M. and Brooks, S.C. (2008) Formation of aqueous MgUO2(CO3)(3)(2-) complex and uranium anion exchange mechanism onto an exchange resin. Environ. Sci. Technol. 42, 1979-1983.

Drot, R. and Simoni, E. (1999) Uranium(VI) and Europium(III) speciation at the phosphate compounds - solution interface. Langmuir 15, 4820-4827.

Du, X., Boonchayaanant, B., Wu, W.M., Fendorf, S., Bargar, J. and Criddle, C.S. (2011) Reduction of Uranium(VI) by Soluble Iron(II) Conforms with Thermodynamic Predictions. Environ. Sci. Technol. 45, 4718-4725.

Duff, M.C., Coughlin, J.U. and Hunter, D.B. (2002) Uranium co-precipitation with iron oxide minerals. Geochim. Cosmochim. Acta 66, 3533-3547.

Dunham-Cheatham, S., Rui, X., Bunker, B., Menguy, N., Hellmann, R. and Fein, J. (2011) The effects of non-metabolizing bacterial cells on the precipitation of U, Pb and Ca phosphates. Geochim. Cosmochim. Acta 75, 2828-2847.

Duro, L., El Aamrani, S., Rovira, M., de Pablo, J. and Bruno, J. (2008) Study of the interaction between U(VI) and the anoxic corrosion products of carbon steel. Appl. Geochem. 23, 1094-1100.

Dzombak, D.A. and Morel, F.M.M. (1990) Surface Complexation Modeling - Hydrous Ferric Oxide. Wiley, New York.

Edwards, L., Kusel, K., Drake, H. and Kostka, J.E. (2007) Electron flow in acidic subsurface sediments co-contaminated with nitrate and uranium. Geochim. Cosmochim. Acta 71, 643-654.

Edwards, R.L., Gallup, C.D. and Cheng, H. (2003) Uranium-series dating of marine and lacustrine carbonates. Uranium-Series Geochemistry 52, 363-405.

Ekstrom, A. (1974) Kinetics and mechanism of disproportionation of uranium(V). Inorganic Chemistry 13, 2237-2241.

Ekstrom, E.B., Learman, D.R., Madden, A.S. and Hansel, C.M. (2010) Contrasting effects of Al substitution on microbial reduction of Fe(III) (hydr)oxides. Geochim. Cosmochim. Acta 74, 7086-7099.

Finch, R. and Murakami, T. (1999) Systematics and Paragenesis of Uranium Minerals. Rev. Miner. 38, 91-179.

Finneran, K.T., Housewright, M.E. and Lovley, D.R. (2002) Multiple influences of nitrate on uranium solubility during bioremediation of uranium-contaminated subsurface sediments. Environ. Microbiol. 4, 510-516.

Foerstendorf, H., Heim, K. and Rossberg, A. (2012) The complexation of uranium(VI) and atmospherically derived CO2 at the ferrihydrite-water interface probed by time-resolved vibrational spectroscopy. Journal of Colloid and Interface Science 377, 299-306.

Fortin, C., Denison, F.H. and Garnier-Laplace, J. (2007) Metal-phytoplankton interactions: Modeling the effect of competing ions (H+, Ca2+, and Mg2+) on uranium uptake. Environmental Toxicology and Chemistry 26, 242-248.

Fortin, C., Dutel, L. and Garnier-Laplace, J. (2004) Uranium complexation and uptake by a green alga in relation to chemical speciation: The importance of the free uranyl ion. Environmental Toxicology and Chemistry 23, 974-981.

Fowle, D.A., Fein, J.B. and Martin, A.M. (2000) Experimental study of uranyl adsorption onto Bacillus subtilis. Environmental Science and Technology 34, 3737-3741.

Fox, P.M., Davis, J.A., Hay, M.B., Conrad, M.E., Campbell, K.M., Williams, K.H. and Long, P.E. (2012) Rate-limited U(VI) desorption during a small-scale tracer test in a heterogeneous uranium-contaminated aquifer. Water Resources Research 48, W05512.

Fox, P.M., Davis, J.A., Kukkadapu, R., Singer, D.M., Bargar, J. and Williams, K.H. (2013) Abiotic U(VI) reduction by sorbed Fe(II) on natural sediments. Geochim. Cosmochim. Acta 117, 266-282.

Fox, P.M., Davis, J.A. and Zachara, J.M. (2006) The effect of calcium on aqueous uranium(VI) speciation and adsorption to ferrihydrite and quartz. Geochim. Cosmochim. Acta 70, 1379-1387.

Francis, A.J. and Dodge, C.J. (2008) Bioreduction of Uranium(VI) Complexed with Citric Acid by Clostridia Affects Its Structure and Solubility. Environ. Sci. Technol. 42, 8277-8282.

Francis, C.W., Timpson, M.E., Lee, S.Y., Elless, M.P. and Wilson, J.H. (1998) The use of carbonate lixiviants to remove uranium from uranium-contaminated soils. Journal of Radioanalytical and Nuclear Chemistry 228, 15-20.

Fredrickson, J.K., Kota, S., Kukkadapu, R.K., Liu, C.X. and Zachara, J.M. (2003) Influence of electron donor/acceptor concentrations on hydrous ferric oxide (HFO) bioreduction. Biodegradation 14, 91-103.

Fredrickson, J.K., Zachara, J.M., Kennedy, D.W., Liu, C.X., Duff, M.C., Hunter, D.B. and Dohnalkova, A. (2002) Influence of Mn oxides on the reduction of uranium(VI) by the metal-reducing bacterium Shewanella putrefaciens. Geochim. Cosmochim. Acta 66, 3247-3262.

Fuller, C.C., Bargar, J.R. and Davis, J.A. (2003) Molecular-scale characterization of uranium sorption by bone apatite materials for a permeable reactive barrier demonstration. Environmental Science and Technology 37, 4642-4649.

Fuller, C.C., Bargar, J.R., Davis, J.A. and Piana, M.J. (2002) Mechanisms of uranium interactions with hydroxyapatite: Implications for groundwater remediation. Environ. Sci. Technol. 36, 158-165.

Gabriel, U., Gaudet, J.P., Spadini, L. and Charlet, L. (1998) Reactive transport of uranyl in a goethite column: an experimental and modelling study. Chemical Geology 151, 107-128.

Ganesh, R., Robinson, K.G., Chu, L.L., Kucsmas, D. and Reed, G.D. (1999) Reductive precipitation of uranium by Desulfovibrio desulfuricans: Evaluation of cocontaminant effects and selective removal. Water Research 33, 3447-3458.

Ganesh, R., Robinson, K.G., Reed, G.D. and Sayler, G.S. (1997) Reduction of hexavalent uranium from organic complexes by sulfate- and iron-reducing bacteria. Applied and Environmental Microbiology 63, 4385-4391.

Geipel, G., Amayri, S. and Bernhard, G. (2008) Mixed complexes of alkaline earth uranyl carbonates: A laser-induced time-resolved fluorescence spectroscopic study. Spectroc. Acta Pt. A-Molec. Biomolec. Spectr. 71, 53-58.

Ghafar, M., Abdul-Hadi, A. and Alhassanieh, O. (2002) Distribution of some elements in a solid-aqueous system: Mineral phosphate in contact with groundwater. Journal of Radioanalytical and Nuclear Chemistry 254, 159-163.

Ginder-Vogel, M., Criddle, C.S. and Fendorf, S. (2006) Thermodynamic constraints on the oxidation of biogenic UO2 by Fe(III) (hydr) oxides. Environ. Sci. Technol. 40, 3544-3550.

Ginder-Vogel, M., Stewart, B. and Fendorf, S. (2010) Kinetic and Mechanistic Constraints on the Oxidation of Biogenic Uraninite by Ferrihydrite. Environ. Sci. Technol. 44, 163-169.

Gonzalez, E., Ballesteros, M.C. and Rueda, E.H. (2002) Reductive dissolution kinetics of Al-substituted goethites. Clays and Clay Minerals 50, 470-477.

Gu, B., Brooks, S.C., Roh, Y. and Jardine, P.M. (2003) Geochemical reactions and dynamics during titration of a contaminated groundwater with high uranium, aluminum, and calcium. Geochim. Cosmochim. Acta 67, 2749-2761.

Gu, B., Liang, L., Dickey, M.J., Yin, X. and Dai, S. (1998) Reductive precipitation of uranium(VI) by zero-valent iron. Environ. Sci. Technol. 32, 3366-3373.

Gu, B.H., Yan, H., Zhou, P., Watson, D.B., Park, M. and Istok, J. (2005) Natural humics impact uranium bioreduction and oxidation. Environ. Sci. Technol. 39, 5268-5275.

Guillaumont, R., Fanghänel, T., Fuger, J., Grenthe, I., Neck, V., Palmer, D. and Rand, M. (2003) Update on the Chemical Thermodynamics of Uranium, Neptunium, Plutonium, Americium, and Technetium. Elsevier, Amsterdam, The Netherlands.

Guo, Z., Yan, C., Xu, J. and Wu, W. (2009) Sorption of U(VI) and phosphate on γ-alumina: Binary and ternary sorption systems. Colloids and Surfaces A: Physicochemical and Engineering Aspects 336, 123-129.

Gustafsson, J.P. (2012) Visual MINTEQ, 3.0 ed, KTH Royal Institute of Technology.

Haas, J.R., Dichristina, T.J. and Wade, R. (2001) Thermodynamics of U(VI) sorption onto Shewanella putrefaciens. Chemical Geology 180, 33-54.

Haas, J.R. and Northup, A. (2004) Effects of aqueous complexation on reductive precipitation of uranium by Shewanella putrefaciens. Geochemical Transactions 5, 41.

Hall, P.O. and Aller, R.C. (1992) Rapid, small-volume, flow-injection analysis for sigma-CO_2 and NH_4^+ in marine and fresh-waters. Limnology and Oceanography 37, 1113-1119.

Hansel, C.M., Benner, S.G. and Fendorf, S. (2005) Competing Fe(II)-induced mineralization pathways of ferrihydrite. Environ. Sci. Technol. 39, 7147-7153.

Hansel, C.M., Benner, S.G., Neiss, J., Dohnalkova, A., Kukkadapu, R.K. and Fendorf, S. (2003) Secondary mineralization pathways induced by dissimilatory iron reduction of ferrihydrite under advective flow. Geochim. Cosmochim. Acta 67, 2977-2992.

Hansel, C.M., Learman, D.R., Lentini, C.J. and Ekstrom, E.B. (2011) Effect of adsorbed and substituted Al on Fe(II)-induced mineralization pathways of ferrihydrite. Geochim. Cosmochim. Acta 75, 4653-4666.

Hansen, H.C.B. and Koch, C.B. (1998) Reduction of nitrate to ammonium by sulphate green rust: activation energy and reaction mechanism. Clay Min. 33, 87-101.

Hirose, A. and Fawell, J.K. (2012) Uranium in Drinking Water, Background document for preparation of WHO Guidelines for drinking-water quality. World Health Organization, Geneva.

Hsi, C.K.D. and Langmuir, D. (1985) Adsorption of uranyl onto ferric oxyhydroxides - application of the surface complexation site-binding model Geochim. Cosmochim. Acta 49, 1931-1941.

Hu, M.Z.C., Norman, J.M., Faison, B.D. and Reeves, M.E. (1996) Biosorption of uranium by Pseudomonas aeruginosa strain CSU: Characterization and comparison studies. Biotechnology and bioengineering 51, 237-247.

Hua, B. and Deng, B. (2008) Reductive Immobilization of Uranium(VI) by Amorphous Iron Sulfide. Environ. Sci. Technol. 42, 8703-8708.

Hua, B., Xu, H., Terry, J. and Deng, B. (2006) Kinetics of uranium(VI) reduction by hydrogen sulfide in anoxic aqueous systems. Environ. Sci. Technol. 40, 4666-4671.

Huber, F., Schild, D., Vitova, T., Rothe, J., Kirsch, R. and Schafer, T. (2012) U(VI) removal kinetics in presence of synthetic magnetite nanoparticles. Geochim. Cosmochim. Acta 96, 154-173.

Hyun, S.P., Davis, J.A., Sun, K. and Hayes, K.F. (2012) Uranium(VI) Reduction by Iron(II) Monosulfide Mackinawite. Environ. Sci. Technol. 46, 3369-3376.

ICDD (2015) PDF-4+ 2015. edited by Dr. Soorya Kabekkodu, International Centre for Diffraction Data, Newtown Square, PA, USA.

Ikeda, A., Hennig, C., Tsushima, S., Takao, K., Ikeda, Y., Scheinost, A.C. and Bernhard, G. (2007) Comparative study of uranyl(VI) and -(V) carbonato complexes in an aqueous solution. Inorganic Chemistry 46, 4212-4219.

Ilton, E.S., Boily, J.F., Buck, E.C., Skomurski, F.N., Rosso, K.M., Cahill, C.L., Bargar, J.R. and Felmy, A.R. (2010) Influence of Dynamical Conditions on the Reduction of U-VI at the Magnetite-Solution Interface. Environ. Sci. Technol. 44, 170-176.

Ilton, E.S., Haiduc, A., Cahill, C.L. and Felmy, A.R. (2005) Mica surfaces stabilize pentavalent uranium. Inorganic Chemistry 44, 2986-2988.

Istok, J.D., Senko, J.M., Krumholz, L.R., Watson, D., Bogle, M.A., Peacock, A., Chang, Y.J. and White, D.C. (2004) In situ bioreduction of technetium and uranium in a nitrate-contaminated aquifer. Environ. Sci. Technol. 38, 468-475.

Ithurbide, A., Peulon, S., Miserque, F., Beaucaire, C. and Chausse, A. (2009) Interaction between uranium(VI) and siderite (FeCO3) surfaces in carbonate solutions. Radiochimica Acta 97, 177-180.

Ithurbide, A., Peulon, S., Miserque, F., Beaucaire, C. and Chausse, A. (2010) Retention and redox behaviour of uranium(VI) by siderite (FeCO3). Radiochimica Acta 98, 563-568.

Jambor, J.L. and Dutrizac, J.E. (1998) Occurrence and constitution of natural and synthetic ferrihydrite, a widespread iron oxyhydroxide. Chem. Rev. 98, 2549-2585.

Jang, J.H., Dempsey, B.A. and Burgos, W.D. (2008) Reduction of U(VI) by Fe(II) in the presence of hydrous ferric oxide and hematite: Effects of solid transformation, surface coverage, and humic acid. Water Research 42, 2269-2277.

Jardine, P.M., Watson, D.B., Blake, D.A., Beard, L.P., Brooks, S.C., Carley, J.M., Criddle, C.S., Doll, W.E., Fields, M.W., Fendorf, S.E., Geesey, G.G., Ginder-Vogel, M., Hubbard, S.S., Istok, J.D., Kelly, S., Kemner, K.M., Peacock, A.D., Spalding, B.P., White, D.C., Wolf, A., Wu, W. and Zhou, J. (2004) Techniques for assessing the performance of in situ bioreduction and immobilization of metals and radionuclides in contaminated subsurface environments, Lawrence Berkeley National Laboratory.

Jensen, D.L., Boddum, J.K., Tjell, J.C. and Christensen, T.H. (2002) The solubility of rhodochrosite (MnCO3) and siderite (FeCO3) in anaerobic aquatic environments. Appl. Geochem. 17, 503-511.

Jentzsch, T.L. and Penn, R.L. (2006) Influence of aluminum doping on ferrihydrite nanoparticle reactivity. J. Phys. Chem. B 110, 11746-11750.

Jerden, J.L. and Sinha, A.K. (2003) Phosphate based immobilization of uranium in an oxidizing bedrock aquifer. Appl. Geochem. 18, 823-843.

Jin, Q.S. (2012) Energy conservation of anaerobic respiration. Am. J. Sci. 312, 573-628.

Jin, Q.S. and Bethke, C.M. (2003) A new rate law describing microbial respiration. Applied and Environmental Microbiology 69, 2340-2348.

Jin, Q.S., Roden, E.E. and Giska, J.R. (2013) Geomicrobial Kinetics: Extrapolating Laboratory Studies to Natural Environments. Geomicrobiol. J. 30, 173-185.

Johnston, C.P. and Chrysochoou, M. (2016) Mechanisms of Chromate, Selenate, and Sulfate Adsorption on Al-Substituted Ferrihydrite: Implications for Ferrihydrite Surface Structure and Reactivity. Environ. Sci. Technol. 50, 3589-3596.

Jones, A.M., Collins, R.N., Rose, J. and Waite, T.D. (2009) The effect of silica and natural organic matter on the Fe(II)-catalysed transformation and reactivity of Fe(III) minerals. Geochim. Cosmochim. Acta 73, 4409-4422.

Jones, M.E., Fennessey, C.M., DiChristina, T.J. and Taillefert, M. (2010) Shewanella oneidensis MR-1 mutants selected for their inability to produce soluble organic-Fe(III) complexes are unable to respire Fe(III) as anaerobic electron acceptor. Environ. Microbiol. 12, 938-950.

Jung, H.B., Boyanov, M.I., Konishi, H., Sun, Y., Mishra, B., Kemner, K.M., Roden, E.E. and Xu, H. (2012) Redox behavior of uranium at the nanoporous aluminum oxide water interface: Implications for uranium remediation. Environmental Science and Technology 46, 7301-7309.

Kanematsu, M., Perdrial, N., Um, W., Chorover, J. and O'Day, P.A. (2014) Influence of Phosphate and Silica on U(VI) Precipitation from Acidic and Neutralized Wastewaters. Environ. Sci. Technol. 48, 6097-6106.

Kantar, C. and Honeyman, B.D. (2006) Citric acid enhanced remediation of soils contaminated with uranium by soil flushing and soil washing. J. Environ. Eng.-ASCE 132, 247-255.

Katsenovich, Y., Carvajal, D., Guduru, R., Lagos, L. and Li, C.Z. (2013) Assessment of the Resistance to Uranium (VI) Exposure by Arthrobacter sp Isolated from Hanford Site Soil. Geomicrobiol. J. 30, 120-130.

Kelly, S.D., Kemner, K.M. and Brooks, S.C. (2007) X-ray absorption spectroscopy identifies calcium-uranyl-carbonate complexes at environmental concentrations. Geochim. Cosmochim. Acta 71, 821-834.

Kelly, S.D., Kemner, K.M., Carley, J., Criddle, C., Jardine, P.M., Marsh, T.L., Phillips, D., Watson, D. and Wu, W.M. (2008) Speciation of uranium in sediments before and after in situ biostimulation. Environ. Sci. Technol. 42, 1558-1564.

Kelly, S.D., Kemner, K.M., Fein, J.B., Fowle, D.A., Boyanov, M.I., Bunker, B.A. and Yee, N. (2002) X-ray absorption fine structure determination of pH-dependent U-bacterial cell wall interactions. Geochim. Cosmochim. Acta 66, 3855-3871.

Kerr, R.S. (1990) Basics of pump-and-tret ground-water remediation technology, in: Agency, U.E.P. (Ed.), Ada, OK.

Khijniak, T.V., Medvedeva-Lyalikova, N.N. and Simonoff, M. (2003) Reduction of pertechnetate by haloalkaliphilic strains of Halomonas. Fems Microbiology Ecology 44, 109-115.

Khijniak, T.V., Slobodkin, A.I., Coker, V., Renshaw, J.C., Livens, F.R., Bonch-Osmolovskaya, E.A., Birkeland, N.K., Medvedeva-Lyalikova, N.N. and Lloyd, J.R. (2005) Reduction of uranium(VI) phosphate during growth of the thermophilic bacterium Thermoterrabacterium ferrireducens. Applied and Environmental Microbiology 71, 6423-6426.

Klausen, J., Trober, S.P., Haderlein, S.B. and Schwarzenbach, R.P. (1995) Reduction of substituted nitrobenzenes by Fe(II) in aqueous mineral suspensions. Environ. Sci. Technol. 29, 2396-2404.

Konopka, A., Plymale, A.E., Carvajal, D.A., Lin, X.J. and McKinley, J.P. (2013) Environmental Controls on the Activity of Aquifer Microbial Communities in the 300 Area of the Hanford Site. Microb. Ecol. 66, 889-896.

Kostka, J.E. and Luther, G.W. (1994) Partitioning and speciation of solid-phase iron in salt-marsh sediments. Geochim. Cosmochim. Acta 58, 1701-1710.

Krestou, A., Xenidis, A. and Panias, D. (2004) Mechanism of aqueous uranium(VI) uptake by hydroxyapatite. Minerals Engineering 17, 373-381.

Kukkadapu, R.K., Zachara, J.M., Fredrickson, J.K., Kennedy, D.W., Dohnalkova, A.C. and McCready, D.E. (2005) Ferrous hydroxy carbonate is a stable transformation product of biogenic magnetite. American Mineralogist 90, 510-515.

Lack, J.G., Chaudhuri, S.K., Kelly, S.D., Kemner, K.M., O'Connor, S.M. and Coates, J.D. (2002) Immobilization of radionuclides and heavy metals through anaerobic bio-oxidation of Fe(II). Applied and Environmental Microbiology 68, 2704-2710.

Langmuir, D. (1978) Uranium solution-mineral equilibria at low-temperatures with applications to sedimentary ore-deposits Geochim. Cosmochim. Acta 42, 547-569.

Langmuir, D. (1997) Aqueous Environmental Geochemistry. Prentice-Hall, Inc., Upper Saddle River, New Jersey

Latta, D.E., Boyanov, M.I., Kemner, K.M., O'Loughlin, E.J. and Scherer, M.M. (2012a) Abiotic reduction of uranium by Fe(II) in soil. Appl. Geochem. 27, 1512-1524.

Latta, D.E., Gorski, C.A., Boyanov, M.I., O'Loughlin, E.J., Kemner, K.M. and Scherer, M.M. (2012b) Influence of Magnetite Stoichiometry on U-VI Reduction. Environ. Sci. Technol. 46, 778-786.

Latta, D.E., Mishra, B., Cook, R.E., Kemner, K.M. and Boyanov, M.I. (2014) Stable U(IV) Complexes Form at High-Affinity Mineral Surface Sites. Environ. Sci. Technol. 48, 1683-1691.

Latta, D.E., Pearce, C.I., Rosso, K.M., Kemner, K.M. and Boyanov, M.I. (2013) Reaction of U-VI with Titanium-Substituted Magnetite: Influence of Ti on U-IV Speciation. Environ. Sci. Technol. 47, 4121-4130.

Legrand, L., Mazerolles, L. and Chausse, A. (2004) The oxidation of carbonate green rust into ferric phases: solid-state reaction or transformation via solution. Geochim. Cosmochim. Acta 68, 3497-3507.

Lenhart, J.J. and Honeyman, B.D. (1999) Uranium(VI) sorption to hematite in the presence of humic acid. Geochim. Cosmochim. Acta 63, 2891-2901.

Liger, E., Charlet, L. and Van Cappellen, P. (1999) Surface catalysis of uranium(VI) reduction by iron(II). Geochim. Cosmochim. Acta 63, 2939-2955.

Lin, H., Szeinbaum, N.H., DiChristina, T.J. and Taillefert, M. (2012) Microbial Mn(IV) reduction requires an initial one-electron reductive solubilization step. Geochim. Cosmochim. Acta 99, 179-192.

Liu, C., Gorby, Y.A., Zachara, J.M., Fredrickson, J.K. and Brown, C.F. (2002a) Reduction kinetics of Fe(III), Co(III), U(VI), Cr(VI), and Tc(VII) in cultures of dissimilatory metal-reducing bacteria. Biotechnology and bioengineering 80, 637-649.

Liu, C.X., Kota, S., Zachara, J.M., Fredrickson, J.K. and Brinkman, C.K. (2001) Kinetic analysis of the bacterial reduction of goethite. Environ. Sci. Technol. 35, 2482-2490.

Liu, C.X., Zachara, J.M., Fredrickson, J.K., Kennedy, D.W. and Dohnalkova, A. (2002b) Modeling the inhibition of the bacterial reduction of U(VI) by beta-MnO2(S)(g). Environ. Sci. Technol. 36, 1452-1459.

Long, P.E., Williams, K.H., Davis, J.A., Fox, P.M., Wilkins, M.J., Yabusaki, S.B., Fang, Y.L., Waichler, S.R., Berman, E.S.F., Gupta, M., Chandler, D.P., Murray, C., Peacock, A.D., Giloteaux, L., Handley, K.M., Lovley, D.R. and Banfield, J.F. (2015) Bicarbonate impact on U(VI) bioreduction in a shallow alluvial aquifer. Geochim. Cosmochim. Acta 150, 106-124.

Lovley, D.R., Phillips, E.J.P., Gorby, Y.A. and Landa, E.R. (1991) Microbial reduction of uranium. Nature 350, 413-416.

Luan, F., Gorski, C.A. and Burgos, W.D. (2014) Thermodynamic Controls on the Microbial Reduction of Iron-Bearing Nontronite and Uranium. Environ. Sci. Technol. 48, 2750-2758.

Luan, F.B. and Burgos, W.D. (2012) Sequential Extraction Method for Determination of Fe(II/III) and U(IV/VI) in Suspensions of Iron-Bearing Phyllosilicates and Uranium. Environ. Sci. Technol. 46, 11995-12002.

Mackay, D.M. and Cherry, J.A. (1989) Groundwater contamination: pump-and-treat remediation. Environ. Sci. Technol. 23, 630-636.

Markich, S.J., Brown, P.L. and Jeffree, R.A. (1996) The use of geochemical speciation modelling to predict the impact of uranium to freshwater biota. Radiochimica Acta 74, 321-326.

Markich, S.J., Brown, P.L., Jeffree, R.A. and Lim, R.P. (2000) Valve movement responses of Velesunio angasi (Bivalvia : Hyriidae) to manganese and uranium: An exception to the free ion activity model. Aquatic Toxicology 51, 155-175.

Marshall, M.J., Beliaev, A.S., Dohnalkova, A.C., Kennedy, D.W., Shi, L., Wang, Z.M., Boyanov, M.I., Lai, B., Kemner, K.M., McLean, J.S., Reed, S.B., Culley, D.E., Bailey, V.L., Simonson, C.J., Saffarini, D.A., Romine, M.F., Zachara, J.M. and Fredrickson, J.K. (2006) c-Type cytochrome-dependent formation of U(IV) nanoparticles by Shewanella oneidensis. PLoS. Biol. 4, 1324-1333.

Marshall, T.A., Morris, K., Law, G.T.W., Mosselmans, J.F.W., Bots, P., Roberts, H. and Shaw, S. (2015) Uranium fate during crystallization of magnetite from ferrihydrite in conditions relevant to the disposal of radioactive waste. Mineral. Mag. 79, 1265-1274.

Massey, M.S., Lezama-Pacheco, J.S., Jones, M.E., Ilton, E.S., Cerrato, J.M., Bargar, J.R. and Fendorf, S. (2014a) Competing retention pathways of uranium upon reaction with Fe(II). Geochim. Cosmochim. Acta 142, 166-185.

Massey, M.S., Lezama-Pacheco, J.S., Michel, F.M. and Fendorf, S. (2014b) Uranium incorporation into aluminum-substituted ferrihydrite during iron(II)-induced transformation. Environ. Sci.-Process Impacts 16, 2137-2144.

Masue-Slowey, Y., Loeppert, R.H. and Fendorf, S. (2011) Alteration of ferrihydrite reductive dissolution and transformation by adsorbed As and structural Al: Implications for As retention. Geochim. Cosmochim. Acta 75, 870-886.

Masue, Y., Loeppert, R.H. and Kramer, T.A. (2007) Arsenate and arsenite adsorption and desorption behavior on coprecipitated aluminum : iron hydroxides. Environ. Sci. Technol. 41, 837-842.

McKinley, J.P., Zachara, J.M., Smith, S.C. and Turnert, G.D. (1995) The influence of uranyl hydrolysis and multiple site-binding reactions on adsorption of U(VI) to montmorillonite. Clays and Clay Minerals 43, 586-598.

Meece, D.E. and Benninger, L.K. (1993) The coprecipitation of Pu and other radionuclides with CaCO3. Geochim. Cosmochim. Acta 57, 1447-1458.

Mejri, W., Ben Salah, I. and Tlili, M.M. (2015) Speciation of Fe(II) and Fe(III) effect on CaCO3 crystallization. Cryst. Res. Technol. 50, 236-243.

Missana, T., Garcia-Gutierrez, M. and Fernndez, V. (2003a) Uranium(VI) sorption on colloidal magnetite under anoxic environment: Experimental study and surface complexation modelling. Geochim. Cosmochim. Acta 67, 2543-2550.

Missana, T., Maffiotte, U. and Garcia-Gutierrez, M. (2003b) Surface reactions kinetics between nanocrystalline magnetite and uranyl. Journal of Colloid and Interface Science 261, 154-160.

Moon, H.S., Komlos, J. and Jaffe, P.R. (2007) Uranium reoxidation in previously bioreduced sediment by dissolved oxygen and nitrate. Environ. Sci. Technol. 41, 4587-4592.

Moon, H.S., Komlos, J. and Jaffe, P.R. (2009) Biogenic U(IV) oxidation by dissolved oxygen and nitrate in sediment after prolonged U(VI)/Fe(III)/SO42- reduction. Journal of contaminant hydrology 105, 18-27.

Moore, W.S. and Shaw, T.J. (2008) Fluxes and behavior of radium isotopes, barium, and uranium in seven Southeastern US rivers and estuaries. Marine Chemistry 108, 236-254.

Morel, F.M.M. (1983) Principles of Aquatic Chemistry, First ed. John Wiley, New York.

Morris, D.E. (2002) Redox energetics and kinetics of uranyl coordination complexes in aqueous solution. Inorganic Chemistry 41, 3542-3547.

Morrison, S.J., Metzler, D.R. and Carpenter, C.E. (2001) Uranium precipitation in a permeable reactive barrier by progressive irreversible dissolution of zerovalent iron. Environ. Sci. Technol. 35, 385-390.

Mougel, V., Biswas, B., Pecaut, J. and Mazzanti, M. (2010) New insights into the acid mediated disproportionation of pentavalent uranyl. Chem. Commun. 46, 8648-8650.

Moyes, L.N., Parkman, R.H., Charnock, D.J., Livens, F.T., Hughes, C.R. and Braithwaite, A. (2000) Uranium uptake from aqueous solution by interaction with goethite, lepidocrocite, muscovite, and mackinawite: An x-ray absorption spectroscopy study. Environmental Science and Technology 34, 1062-1068.

Mukherjee, A., Wheaton, G.H., Blum, P.H. and Kelly, R.M. (2012) Uranium extremophily is an adaptive, rather than intrinsic, feature for extremely thermoacidophilic Metallosphaera species. Proceedings of the National Academy of Sciences of the United States of America 109, 16702-16707.

Myers, C.R. and Nealson, K.H. (1988) Bacterial manganese reduction and growth with manganese oxides as the sole electron-acceptor. Science 240, 1319-1321.

Nair, S. and Merkel, B.J. (2011) Impact of Alkaline Earth Metals on Aqueous Speciation of Uranium(VI) and Sorption on Quartz. Aquatic Geochemistry 17, 209-219.

Nash, K.L., Jensen, M.P. and Schmidt, M.A. (1998) Actinide immobilization in the subsurface environment by in-situ treatment with a hydrolytically unstable organophosphorus complexant: Uranyl uptake by calcium phytate. J. Alloy. Compd. 271-273, 257-261.

Nevin, K.P. and Lovley, D.R. (2000) Potential for nonenzymatic reduction of Fe(III) via electron shuttling in subsurface sediments. Environ. Sci. Technol. 34, 2472-2478.

Nico, P.S., Stewart, B.D. and Fendorf, S. (2009) Incorporation of Oxidized Uranium into Fe (Hydr)oxides during Fe(II) Catalyzed Remineralization. Environ. Sci. Technol. 43, 7391-7396.

Nimmons, M.J. (2007) Evaluation and screening of remedial technologies for uranium at the 300-FF-5 operable unit, Hanford Site, Washington, in: DOE, U. (Ed.), Richland, Washington.

Nyman, J.L., Wu, H.I., Gentile, M.E., Kitanidis, P.K. and Criddle, C.S. (2007) Inhibition of a U(VI)- and sulfate-reducing consortia by U(VI). Environ. Sci. Technol. 41, 6528-6533.

O'Loughlin, E.J., Kelly, S.D., Cook, R.E., Csencsits, R. and Kemner, K.M. (2003) Reduction of Uranium(VI) by mixed iron(II/iron(III) hydroxide (green rust): Formation of UO(2) manoparticies. Environ. Sci. Technol. 37, 721-727.

O'Loughlin, E.J., Kelly, S.D. and Kemner, K.M. (2010) XAFS Investigation of the Interactions of U-VI with Secondary Mineralization Products from the Bioreduction of Fe-III Oxides. Environ. Sci. Technol. 44, 1656-1661.

Obuekwe, C.O., Westlake, D.W.S. and Cook, F.D. (1981) EFFECT OF NITRATE ON REDUCTION OF FERRIC IRON BY A BACTERIUM ISOLATED FROM CRUDE-OIL. Canadian Journal of Microbiology 27, 692-697.

Orellana, R., Leavitt, J.J., Comolli, L.R., Csencsits, R., Janot, N., Flanagan, K.A., Gray, A.S., Leang, C., Izallalen, M., Mester, T. and Lovley, D.R. (2013) U(VI) Reduction by Diverse Outer Surface c-Type Cytochromes of Geobacter sulfurreducens. Applied and Environmental Microbiology 79, 6369-6374.

Parkhurst, D.L. and Appelo, C.A.J. (1999) User's guide to PHREEQC (Version 2) - A computer program for speciation, batch-raction, one-dimential transport, and inverse geochemical calculations U.S.G.S.

Parkhurst, D.L. and Appelo, C.A.J. (2013) Description of input and examples for PHREEQC version 3 - A computer program for speciation, batch-reaction, one-dimentional transport, and inverse geochemical calculations, U.S. Geological Survey Techniques and Methods, p. 497.

Pasilis, S.P. and Pemberton, J.E. (2003) Speciation and coordination chemistry of uranyl(VI)-citrate complexes in aqueous solution. Inorganic Chemistry 42, 6793-6800.

Payne, T.E., Davis, J.A. and Waite, T.D. (1996) Uranium adsorption onto ferrihydrite - effects of phosphate and humic acid. Radiochimica Acta 74, 239-243.

Petrie, L., North, N.N., Dollhopf, S.L., Balkwill, D.L. and Kostka, J.E. (2003) Enumeration and characterization of iron(III)-reducing microbial communities from acidic subsurface

sediments contaminated with uranium (VI). Applied and Environmental Microbiology 69, 7467-7479.

Pible, O., Vidaud, C., Plantevin, S., Pellequer, J.L. and Quemeneur, E. (2010) Predicting the disruption by UO22+ of a protein-ligand interaction. Protein Science 19, 2219-2230.

Plant, J.A., Simpson, P.R., Smith, B. and Windley, B.F. (1999) Uranium Ore Deposits-Products of the Radioactive Earth. Rev. Miner. 38, 255-319.

Power, I.M., Kenward, P.A., Dipple, G.M. and Raudsepp, M. (2017) Room Temperature Magnesite Precipitation. Cryst. Growth Des. 17, 5652-5659.

Prikryl, J.D., Jain, A., Turner, D.R. and Pabalan, R.T. (2001) Uranium(VI) sorption behavior on silicate mineral mixtures. Journal of contaminant hydrology 47, 241-253.

Qafoku, N.P., Kukkadapu, R.K., McKinley, J.P., Arey, B.W., Kelly, S.D., Wang, C.M., Resch, C.T. and Long, P.E. (2009) Uranium in Framboidal Pyrite from a Naturally Bioreduced Alluvial Sediment. Environ. Sci. Technol. 43, 8528-8534.

Rai, D., Felmy, A.R. and Ryan, J.L. (1990) Uranium(IV) hydrolysis constants and solubility product of UO2.xH2O(am). Inorganic Chemistry 29, 260-264.

Rakovan, J., Reeder, R.J., Elzinga, E.J., Cherniak, D.J., Tait, C.D. and Morris, D.E. (2002) Structural characterization of U(VI) in apatite by x-ray absorption spectroscopy. Environmental Science and Technology 36, 3114-3117.

Ray, A.E., Bargar, J.R., Sivaswamy, V., Dohnalkova, A.C., Fujita, Y., Peyton, B.M. and Magnuson, T.S. (2011) Evidence for multiple modes of uranium immobilization by an anaerobic bacterium. Geochim. Cosmochim. Acta 75, 2684-2695.

Reeder, R.J., Nugent, M., Lamble, G.M., Tait, C.D. and Morris, D.E. (2000) Uranyl incorporation in calcite and aragonite: XAFS and luminescence studies. Environmental Science and Technology 34, 638-644.

Reeder, R.J., Nugent, M., Tait, C.D., Morris, D.E., Heald, S.M., Beck, K.M., Hess, W.P. and Lanzirotti, A. (2001) Coprecipitation of uranium(VI) with calcite: XAFS, micro-XAS, and luminescence characterization. Geochim. Cosmochim. Acta 65, 3491-3503.

Renshaw, J.C., Butchins, L.J.C., Livens, F.R., May, I., Charnock, J.M. and Lloyd, J.R. (2005) Bioreduction of uranium: Environmental implications of a pentavalent intermediate. Environ. Sci. Technol. 39, 5657-5660.

Rickard, D. and Luther, G.W. (1997) Kinetics of pyrite formation by the H2S oxidation of iron(II) monosulfide in aqueous solutions between 25 and 125 degrees C: The mechanism. Geochim. Cosmochim. Acta 61, 135-147.

Rihs, S., Gaillard, C., Reich, T. and Kohler, S.J. (2014) Uranyl sorption onto birnessite: A surface complexation modeling and EXAFS study. Chemical Geology 353, 59-70.

Riley, R.G., Zachara, J.M. and Wobber, F.J. (1992) Chemical contaminants on DOE lands and selection of contaminant mixtures for subsurface science research. U.S. Department of Energy.

Roberts, H.E., Morris, K., Law, G.T.W., Mosselmans, J.F.W., Bots, P., Kvashnina, K. and Shaw, S. (2017) Uranium(V) Incorporation Mechanisms and Stability in Fe(II)/Fe(III) (oxyhydr)Oxides. Environ. Sci. Technol. Lett. 4, 421-426.

Robinson, K.G., Ganesh, R. and Reed, G.D. (1998) Impact of organic ligands on uranium removal during anaerobic biological treatment. Water Sci. Technol. 37, 73-80.

Roden, E.E. and Zachara, J.M. (1996) Microbial reduction of crystalline iron(III) oxides: Influence of oxide surface area and potential for cell growth. Environ. Sci. Technol. 30, 1618-1628.

Sanford, R.A., Wu, Q., Sung, Y., Thomas, S.H., Amos, B.K., Prince, E.K. and Loffler, F.E. (2007) Hexavalent uranium supports growth of Anaeromyxobacter dehalogenans and Geobacter spp. with lower than predicted biomass yields. Environ. Microbiol. 9, 2885-2893.

Sani, R.K., Peyton, B.M., Amonette, J.E. and Geesey, G.G. (2004) Reduction of uranium(VI) under sulfate-reducing conditions in the presence of Fe(III)-(hydr)oxides. Geochim. Cosmochim. Acta 68, 2639-2648.

Sani, R.K., Peyton, B.M. and Dohnalkova, A. (2006) Toxic effects of uranium on Desulfovibrio desulfuricans G20. Environmental Toxicology and Chemistry 25, 1231-1238.

Sani, R.K., Peyton, B.M., Dohnalkova, A. and Amonette, J.E. (2005) Reoxidation of reduced uranium with iron(III) (hydr)oxides under sulfate-reducing conditions. Environ. Sci. Technol. 39, 2059-2066.

Santos, I.R., Burnett, W.C., Misra, S., Suryaputra, I., Chanton, J.P., Dittmar, T., Peterson, R.N. and Swarzenski, P.W. (2011) Uranium and barium cycling in a salt wedge subterranean estuary: The influence of tidal pumping. Chemical Geology 287, 114-123.

Sato, T., Murakami, T., Yanase, N., Isobe, H., Payne, T.E. and Airey, P.L. (1997) Iron nodules scavenging uranium from groundwater. Environmental Science and Technology 31, 2854-2858.

Schofield, E.J., Veeramani, H., Sharp, J.O., Suvorova, E., Bernier-Latmani, R., Mehta, A., Stahlman, J., Webb, S.M., Clark, D.L., Conradson, S.D., Ilton, E.S. and Bargar, J.R. (2008) Structure of Biogenic Uraninite Produced by Shewanella oneidensis Strain MR-1. Environ. Sci. Technol. 42, 7898-7904.

Schwertmann, U. and Cornell, R. (2000) Iron Oxides in the Laboratory: Preparation and Characterization Wiley-VCH, Weinheim, Germany.

Schwertmann, U., Friedl, J., Stanjek, H. and Schulze, D.G. (2000) The effect of Al on Fe oxides. XIX. Formation of Al-substituted hematite from ferrihydrite at 25 degrees C and pH 4 to 7. Clays and Clay Minerals 48, 159-172.

Seaman, J.C., Hutchinson, J.M., Jackson, B.P. and Vulava, V.M. (2003) In situ of treatment of metals in contaminated soils with phytate. J. Environ. Qual. 32, 153-161.

Senko, J.M., Istok, J.D., Suflita, J.M. and Krumholz, L.R. (2002) In-situ evidence for uranium immobilization and remobilization. Environ. Sci. Technol. 36, 1491-1496.

Senko, J.M., Kelly, S.D., Dohnalkova, A.C., McDonough, J.T., Kemner, K.M. and Burgos, W.D. (2007) The effect of U(VI) bioreduction kinetics on subsequent reoxidation of biogenic U(IV). Geochim. Cosmochim. Acta 71, 4644-4654.

Senko, J.M., Mohamed, Y., Dewers, T.A. and Krumholz, L.R. (2005) Role for Fe(III) minerals in nitrate-dependent microbial U(IV) oxidation. Environ. Sci. Technol. 39, 2529-2536.

Shao, P.P., Comolli, L.R. and Bernier-Latmani, R. (2014) Membrane Vesicles as a Novel Strategy for Shedding Encrusted Cell Surfaces. Minerals 4, 74-88.

Sheng, L. and Fein, J.B. (2013) Uranium adsorption by Shewanella oneidensis MR-1 as a function of dissolved inorganic carbon concentration. Chemical Geology 358, 15-22.

Sheng, L. and Fein, J.B. (2014) Uranium Reduction by Shewanella oneidensis MR-1 as a Function of NaHCO3 Concentration: Surface Complexation Control of Reduction Kinetics. Environ. Sci. Technol. 48, 3768-3775.

Sheng, L., Szymanowski, J. and Fein, J.B. (2011) The effects of uranium speciation on the rate of U(VI) reduction by Shewanella oneidensis MR-1. Geochim. Cosmochim. Acta 75, 3558-3567.

Shiel, A.E., Johnson, T.M., Lundstrom, C.C., Laubach, P.G., Long, P.E. and Williams, K.H. (2016) Reactive transport of uranium in a groundwater bioreduction study: Insights from high-temporal resolution U-238/U-235 data. Geochim. Cosmochim. Acta 187, 218-236.

Shiel, A.E., Laubach, P.G., Johnson, T.M., Lundstrom, C.C., Long, P.E. and Williams, K.H. (2013) No Measurable Changes in U-238/U-235 due to Desorption-Adsorption of U(VI) from Groundwater at the Rifle, Colorado, Integrated Field Research Challenge Site. Environ. Sci. Technol. 47, 2535-2541.

Shimizu, M., Zhou, J.H., Schroder, C., Obst, M., Kappler, A. and Borch, T. (2013) Dissimilatory Reduction and Transformation of Ferrihydrite-Humic Acid Coprecipitates. Environ. Sci. Technol. 47, 13375-13384.

Simon, F.G., Biermann, V. and Peplinski, B. (2008) Uranium removal from groundwater using hydroxyapatite. Appl. Geochem. 23, 2137-2145.

Simon, F.G., Biermann, V., Segebade, C. and Hedrich, M. (2004) Behaviour of uranium in hydroxyapatite-bearing permeable reactive barriers: investigation using U-237 as a radioindicator. Science of the Total Environment 326, 249-256.

Singer, D.M., Chatman, S.M., Ilton, E.S., Rosso, K.M., Banfield, J.F. and Waychunas, G.A. (2012a) Identification of Simultaneous U(VI) Sorption Complexes and U(IV) Nanoprecipitates on the Magnetite (111) Surface. Environ. Sci. Technol. 46, 3811-3820.

Singer, D.M., Chatman, S.M., Ilton, E.S., Rosso, K.M., Banfield, J.F. and Waychunas, G.A. (2012b) U(VI) Sorption and Reduction Kinetics on the Magnetite (111) Surface. Environ. Sci. Technol. 46, 3821-3830.

Singh, A., Catalano, J.G., Ulrich, K.U. and Giammar, D.E. (2012) Molecular-Scale Structure of Uranium(VI) Immobilized with Goethite and Phosphate. Environ. Sci. Technol. 46, 6594-6603.

Sivaswamy, V., Boyanov, M.I., Peyton, B.M., Viamajala, S., Gerlach, R., Apel, W.A., Sani, R.K., Dohnalkova, A., Kemner, K.M. and Borch, T. (2011) Multiple mechanisms of uranium immobilization by Cellulomonas sp. strain ES6. Biotechnology and bioengineering 108, 264-276.

Smeaton, C.M., Walshe, G.E., Fryer, B.J. and Weisener, C.G. (2012) Reductive Dissolution of Tl(I)-Jarosite by Shewanella putrefaciens: Providing New Insights into Tl Biogeochemistry. Environ. Sci. Technol. 46, 11086-11094.

Soda, S.O., Yamamura, S., Zhou, H., Ike, M. and Fujita, M. (2006) Reduction kinetics of As(V) to As(III) by a dissimilatory arsenate-reducing bacterium, Bacillus sp SF-1. Biotechnology and bioengineering 93, 812-815.

Sorensen, J. and Thorling, L. (1991) Stimulation by lepidocrocite (gamma-FeOOH) of Fe(II)-dependent nitrite reduction. Geochim. Cosmochim. Acta 55, 1289-1294.

Spear, J.R., Figueroa, L.A. and Honeyman, B.D. (1999) Modeling the removal of uranium U(VI) from aqueous solutions in the presence of sulfate reducing bacteria. Environ. Sci. Technol. 33, 2667-2675.

Spycher, N.F., Issarangkun, M., Stewart, B.D., Sengor, S.S., Belding, E., Ginn, T.R., Peyton, B.M. and Sani, R.K. (2011) Biogenic uraninite precipitation and its reoxidation by iron(III) (hydr)oxides: A reaction modeling approach. Geochim. Cosmochim. Acta 75, 4426-4440.

Steele, H. and Taylor, R.J. (2007) A theoretical study of the inner-sphere disproportionation reaction mechanism of the pentavalent actinyl ions. Inorganic Chemistry 46, 6311-6318.

Stewart, B.D., Amos, R.T., Nico, P.S. and Fendorf, S. (2011) Influence of Uranyl Speciation and Iron Oxides on Uranium Biogeochemical Redox Reactions. Geomicrobiol. J. 28, 444-456.

Stewart, B.D., Cismasu, A.C., Williams, K.H., Peyton, B.M. and Nico, P.S. (2015) Reactivity of Uranium and Ferrous Iron with Natural Iron Oxyhydroxides. Environ. Sci. Technol. 49, 10357-10365.

Stewart, B.D., Girardot, C., Spycher, N., Sani, R.K. and Peyton, B.M. (2013) Influence of Chelating Agents on Biogenic Uraninite Reoxidation by Fe(III) (Hydr)oxides. Environ. Sci. Technol. 47, 364-371.

Stewart, B.D., Mayes, M.A. and Fendorf, S. (2010) Impact of Uranyl-Calcium-Carbonato Complexes on Uranium(VI) Adsorption to Synthetic and Natural Sediments. Environ. Sci. Technol. 44, 928-934.

Stewart, B.D., Nico, P.S. and Fendorf, S. (2009) Stability of Uranium Incorporated into Fe (Hydr)oxides under Fluctuating Redox Conditions. Environ. Sci. Technol. 43, 4922-4927.

Stookey, L.L. (1970) Ferrozine - A new spectrophotometric reagent for iron Analytical Chemistry 42, 779.

Strahan, D. (2001) Uranium in glass, glazes and enamels: History, identification and handling. Stud. Conserv. 46, 181-195.

Stylo, M., Alessi, D.S., Shao, P.P., Lezama-Pacheco, J.S., Bargar, J.R. and Bernier-Latmani, R. (2013) Biogeochemical Controls on the Product of Microbial U(VI) Reduction. Environ. Sci. Technol. 47, 12351-12358.

Suzuki, Y., Nankawa, T., Ozaki, T., Ohnuki, T., Francis, A.J., Enokida, Y. and Yamamoto, I. (2007) Electrochemical studies on uranium in the presence of organic acids. J. Nucl. Sci. Technol. 44, 1227-1232.

Suzuki, Y., Nankawa, T., Yoshida, T., Ozaki, T., Ohnuki, T., Francis, A.J., Tsushima, S., Enokida, Y. and Yamamoto, I. (2006) Reduction behavior of uranium in the presence of citric acid. Radiochimica Acta 94, 579-583.

Suzuki, Y., Tanaka, K., Kozai, N. and Ohnuki, T. (2010) Effects of Citrate, NTA, and EDTA on the Reduction of U(VI) by Shewanella putrefaciens. Geomicrobiol. J. 27, 245-250.

Swedlund, P.J. and Webster, J.G. (1999) Adsorption and polymerisation of silicic acid on ferrihydrite, and its effect on arsenic adsorption. Water Research 33, 3413-3422.

Sylvester, E.R., Hudson, E.A. and Allen, P.G. (2000) The structure of uranium(VI) sorption complexes on silica, alumina, and montmorillonite. Geochim. Cosmochim. Acta 64, 2431-2438.

Taillefert, M., Beckler, J.S., Carey, E., Burns, J.L., Fennessey, C.M. and DiChristina, T.J. (2007) Shewanella putrefaciens produces an Fe(III)-solubilizing organic ligand during anaerobic respiration on insoluble Fe(III) oxides. J. Inorg. Biochem. 101, 1760-1767.

Taillefert, M., Luther, G.W. and Nuzzio, D.B. (2000) The application of electrochemical tools for in situ measurements in aquatic systems. Electroanalysis 12, 401-412.

Tao, Z.Y., Chu, T.W., Du, J.Z., Dai, X.X. and Gu, Y.J. (2000) Effect of fulvic acids on sorption of U(VI), Zn, Yb, I, and Se(IV) onto oxides of aluminum, iron, and silicon. Appl. Geochem. 15, 145-151.

Tapia-Rodriguez, A., Luna-Velasco, A., Field, J.A. and Sierra-Alvarez, R. (2012) Toxicity of Uranium to Microbial Communities in Anaerobic Biofilms. Water Air Soil Pollut. 223, 3859-3868.

Taylor, S.D., Marcano, M.C., Rosso, K.M. and Becker, U. (2015) An experimental and ab initio study on the abiotic reduction of uranyl by ferrous iron. Geochim. Cosmochim. Acta 156, 154-172.

Tebo, B.M., Bargar, J.R., Clement, B.G., Dick, G.J., Murray, K.J., Parker, D., Verity, R. and Webb, S.M. (2004) Biogenic manganese oxides: Properties and mechanisms of formation. Annu. Rev. Earth Planet. Sci. 32, 287-328.

Tebo, B.M. and Obraztsova, A.Y. (1998) Sulfate-reducing bacterium grows with Cr(VI), U(VI), Mn(IV), and Fe(III) as electron acceptors. FEMS Microbiol. Lett. 162, 193-198.

ThomasArrigo, L.K., Mikutta, C., Byrne, J., Kappler, A. and Kretzschmar, R. (2017) Iron(II)-Catalyzed Iron Atom Exchange and Mineralogical Changes in Iron-rich Organic Freshwater Flocs: An Iron Isotope Tracer Study. Environ. Sci. Technol. 51, 6897-6907.

Tokunaga, T.K., Wan, J.M., Kim, Y.M., Sutton, S.R., Newville, M., Lanzirotti, A. and Rao, W. (2008) Real-time X-ray absorption spectroscopy of uranium, iron, and manganese in contaminated sediments during bioreduction. Environ. Sci. Technol. 42, 2839-2844.

Tran, D., Massabuau, J.C. and Garnier-Laplace, J. (2004) Effect of carbon dioxide on uranium bioaccumulation in the freshwater clam Corbicula fluminea. Environmental Toxicology and Chemistry 23, 739-747.

Trenfield, M.A., Ng, J.C., Noller, B., Markich, S.J. and van Dam, R.A. (2012) Dissolved organic carbon reduces uranium toxicity to the unicellular eukaryote Euglena gracilis. Ecotoxicology 21, 1013-1023.

Trenfield, M.A., Ng, J.C., Noller, B.N., Markich, S.J. and van Dam, R.A. (2011) Dissolved Organic Carbon Reduces Uranium Bioavailability and Toxicity. 2. Uranium VI Speciation and Toxicity to Three Tropical Freshwater Organisms. Environ. Sci. Technol. 45, 3082-3089.

Tribovillard, N., Algeo, T.J., Lyons, T. and Riboulleau, A. (2006) Trace metals as paleoredox and paleoproductivity proxies: An update. Chemical Geology 232, 12-32.

Tsarev, S., Waite, T.D. and Collins, R.N. (2016) Uranium Reduction by Fe(II) in the Presence of Montmorillonite and Nontronite. Environ. Sci. Technol. 50, 8223-8230.

Ulrich, K.-U., Veeramani, H., Bernier-Latmani, R. and Giammar, D.E. (2011) Speciation-Dependent Kinetics of Uranium(VI) Bioreduction. Geomicrobiol. J. 28, 396-409.

Ulrich, K.U., Ilton, E.S., Veeramani, H., Sharp, J.O., Bernier-Latmani, R., Schofield, E.J., Bargar, J.R. and Giammar, D.E. (2009) Comparative dissolution kinetics of biogenic and chemogenic uraninite under oxidizing conditions in the presence of carbonate. Geochim. Cosmochim. Acta 73, 6065-6083.

Ulrich, K.U., Singh, A., Schofield, E.J., Bargar, J.R., Veeramani, H., Sharp, J.O., Bernier-Latmani, R. and Giammar, D.E. (2008) Dissolution of biogenic and synthetic UO(2) under varied reducing conditions. Environ. Sci. Technol. 42, 5600-5606.

USGS (2012) PHREEQC (Version 2)--A Computer Program for Speciation, Batch-Reaction, One-Dimensional Transport, and Inverse Geochemical Calculations.

Van Cleemput, O. and Baert, L. (1983) Nitrite stability influenced by iron compounds Soil Biol. Biochem. 15, 137-140.

Van Den Berg, C.M.G. and Nimmo, M. (1987) Direct determination of uranium in water by cathodic stripping voltammetry. Analytical Chemistry 59, 924-928.

VanEngelen, M.R., Field, E.K., Gerlach, R., Lee, B.D., Apel, W.A. and Peyton, B.M. (2010a) UO22+ speciation determines uranium toxicity and bioaccumulation in an environmental Pseudomonas sp. isolate. Environmental toxicology and chemistry / SETAC 29, 763-769.

VanEngelen, M.R., Field, E.K., Gerlach, R., Lee, B.D., Apel, W.A. and Peyton, B.M. (2010b) UO22+ speciation determines uranium toxicity and bioaccumulation in an environmental Pseudomonas sp. isolate. Environmental Toxicology and Chemistry 29, 763-769.

VanEngelen, M.R., Szilagyi, R.K., Gerlach, R., Lee, B.D., Apel, W.A. and Peyton, B.M. (2011) Uranium Exerts Acute Toxicity by Binding to Pyrroloquinoline Quinone Cofactor. Environ. Sci. Technol. 45, 937-942.

Veeramani, H., Alessi, D.S., Suvorova, E.I., Lezama-Pacheco, J.S., Stubbs, J.E., Sharp, J.O., Dippon, U., Kappler, A., Bargar, J.R. and Bernier-Latmani, R. (2011) Products of abiotic U(VI) reduction by biogenic magnetite and vivianite. Geochim. Cosmochim. Acta 75, 2512-2528.

Veeramani, H., Scheinost, A.C., Monsegue, N., Qafoku, N.P., Kukkadapu, R., Newville, M., Lanzirotti, A., Pruden, A., Murayama, M. and Hochella, M.F. (2013) Abiotic Reductive Immobilization of U(VI) by Biogenic Mackinawite. Environ. Sci. Technol. 47, 2361-2369.

Vempati, R.K. and Loeppert, R.H. (1989) Influence of structural and adsorbed Si on the transformation of synthetic ferrihydrite. Clays and Clay Minerals 37, 273-279.

Viollier, E., Inglett, P.W., Hunter, K., Roychoudhury, A.N. and Van Cappellen, P. (2000) The ferrozine method revisited: Fe(II)/Fe(III) determination in natural waters. Appl. Geochem. 15, 785-790.

Wade, R. and DiChristina, T.J. (2000) Isolation of U(VI) reduction-deficient mutants of Shewanella putrefaciens. FEMS Microbiol. Lett. 184, 143-148.

Waite, T.D., Davis, J.A., Payne, T.E., Waychunas, G.A. and Xu, N. (1994) Uranium(VI) adsorption to ferrihydrite: Application of a surface complexation model. Geochim. Cosmochim. Acta 58, 5465-5478.

Wan, J.M., Tokunaga, T.K., Brodie, E., Wang, Z.M., Zheng, Z.P., Herman, D., Hazen, T.C., Firestone, M.K. and Sutton, S.R. (2005) Reoxidation of bioreduced uranium under reducing conditions. Environ. Sci. Technol. 39, 6162-6169.

Wan, J.M., Tokunaga, T.K., Kim, Y.M., Brodie, E., Daly, R., Hazen, T.C. and Firestone, M.K. (2008) Effects of Organic Carbon Supply Rates on Uranium Mobility in a Previously Bioreduced Contaminated Sediment. Environ. Sci. Technol. 42, 7573-7579.

Wander, M.C.F., Kerisit, S., Rosso, K.M. and Schoonen, M.A.A. (2006) Kinetics of triscarbonato uranyl reduction by aqueous ferrous iron: A theoretical study. Journal of Physical Chemistry A 110, 9691-9701.

Wang, Y.H., Frutschi, M., Suvorova, E., Phrommavanh, V., Descostes, M., Osman, A.A.A., Geipel, G. and Bernier-Latmani, R. (2013a) Mobile uranium(IV)-bearing colloids in a mining-impacted wetland. Nat. Commun. 4, 2942.

Wang, Z., Lee, S.-W., Catalano, J.G., Lezama-Pacheco, J.S., Bargar, J.R., Tebo, B.M. and Giammar, D.E. (2013b) Adsorption of uranium(VI) to manganese oxides: X-ray absorption spectroscopy and surface complexation modeling. Environmental Science and Technology 47, 850-858.

Wang, Z.M., Lee, S.W., Kapoor, P., Tebo, B.M. and Giammar, D.E. (2013c) Uraninite oxidation and dissolution induced by manganese oxide: A redox reaction between two insoluble minerals. Geochim. Cosmochim. Acta 100, 24-40.

Wang, Z.M., Ulrich, K.U., Pan, C. and Giammar, D.E. (2015) Measurement and Modeling of U(IV) Adsorption to Metal Oxide Minerals. Environ. Sci. Technol. Lett. 2, 227-232.

Wang, Z.M., Xiong, W., Tebo, B.M. and Giammar, D.E. (2014) Oxidative UO2 Dissolution Induced by Soluble Mn(III). Environ. Sci. Technol. 48, 289-298.

Watson, D.B., Wu, W.M., Mehlhorn, T., Tang, G.P., Earles, J., Lowe, K., Gihring, T.M., Zhang, G.X., Phillips, J., Boyanov, M.I., Spalding, B.P., Schadt, C., Kemner, K.M., Criddle, C.S., Jardine, P.M. and Brooks, S.C. (2013) In Situ Bioremediation of Uranium with Emulsified Vegetable Oil as the Electron Donor. Environ. Sci. Technol. 47, 6440-6448.

Webb, S.M., Dick, G.J., Bargar, J.R. and Tebo, B.M. (2005) Evidence for the presence of Mn(III) intermediates in the bacterial oxidation of Mn(II). Proceedings of the National Academy of Sciences of the United States of America 102, 5558-5563.

Webb, S.M., Fuller, C.C., Tebo, B.M. and Bargar, J.R. (2006) Determination of uranyl incorporation into biogenic manganese oxides using X-ray absorption spectroscopy and scattering. Environ. Sci. Technol. 40, 771-777.

Weber, K.A., Thrash, J.C., Van Trump, J.I., Achenbach, L.A. and Coates, J.D. (2011) Environmental and Taxonomic Bacterial Diversity of Anaerobic Uranium(IV) Bio-Oxidation. Applied and Environmental Microbiology 77, 4693-4696.

Wehrli, B., Sulzberger, B. and Stumm, W. (1989) Redox processes catalyzed by hydrous oxide surfaces. Chemical Geology 78, 167-179.

Wellman, D.M., Glovack, J.N., Parker, K. and Richards, E.L. (2008) Sequestration and retention of uranium(VI) in the presence of hydroxylapatite under dynamic geochemical conditions. Environ. Chem. 5, 40-50.

Wellman, D.M., Icenhower, J.P. and Owen, A.T. (2006) Comparative analysis of soluble phosphate amendments for the remediation of heavy metal contaminants: Effect on sediment hydraulic conductivity. Environ. Chem. 3, 219-224.

Wersin, P., Hochella, M.F., Persson, P., Redden, G., Leckie, J.O. and Harris, D.W. (1994) Interaction between aqueous uranium(VI) and sulfide minerals: Spectroscopic evidence for sorption and reduction. Geochim. Cosmochim. Acta 58, 2829-2843.

Wielinga, B., Bostick, B., Hansel, C.M., Rosenzweig, R.F. and Fendorf, S. (2000) Inhibition of bacterially promoted uranium reduction: Ferric (hydr)oxides as competitive electron acceptors. Environ. Sci. Technol. 34, 2190-2195.

Williams, K.H., Long, P.E., Davis, J.A., Wilkins, M.J., N'Guessan, A.L., Steefel, C.I., Yang, L., Newcomer, D., Spane, F.A., Kerkhof, L.J., McGuinness, L., Dayvault, R. and Lovley, D.R. (2011) Acetate Availability and its Influence on Sustainable Bioremediation of Uranium-Contaminated Groundwater. Geomicrobiol. J. 28, 519-539.

Wu, W.M., Carley, J., Fienen, M., Mehlhorn, T., Lowe, K., Nyman, J., Luo, J., Gentile, M.E., Rajan, R., Wagner, D., Hickey, R.F., Gu, B.H., Watson, D., Cirpka, O.A., Kitanidis, P.K., Jardine, P.M. and Criddle, C.S. (2006a) Pilot-scale in situ bioremediation of uranium in a highly contaminated aquifer. 1. Conditioning of a treatment zone. Environ. Sci. Technol. 40, 3978-3985.

Wu, W.M., Carley, J., Gentry, T., Ginder-Vogel, M.A., Fienen, M., Mehlhorn, T., Yan, H., Caroll, S., Pace, M.N., Nyman, J., Luo, J., Gentile, M.E., Fields, M.W., Hickey, R.F., Gu, B.H., Watson, D., Cirpka, O.A., Zhou, J.Z., Fendorf, S., Kitanidis, P.K., Jardine, P.M. and Criddle, C.S. (2006b) Pilot-scale in situ bioremedation of uranium in a highly contaminated aquifer. 2. Reduction of U(VI) and geochemical control of U(VI) bioavailability. Environ. Sci. Technol. 40, 3986-3995.

Wu, W.M., Carley, J., Luo, J., Ginder-Vogel, M.A., Cardenas, E., Leigh, M.B., Hwang, C.C., Kelly, S.D., Ruan, C.M., Wu, L.Y., Van Nostrand, J., Gentry, T., Lowe, K., Mehlhorn, T., Carroll, S., Luo, W.S., Fields, M.W., Gu, B.H., Watson, D., Kemner, K.M., Marsh, T., Tiedje, J., Zhou, J.Z., Fendorf, S., Kitanidis, P.K., Jardine, P.M. and Criddle, C.S. (2007) In situ bioreduction of uranium (VI) to submicromolar levels and reoxidation by dissolved oxygen. Environ. Sci. Technol. 41, 5716-5723.

Yang, L., Steefel, C.I., Marcus, M.A. and Bargar, J.R. (2010) Kinetics of Fe(II)-Catalyzed Transformation of 6-line Ferrihydrite under Anaerobic Flow Conditions. Environ. Sci. Technol. 44, 5469-5475.

Yazzie, M., Gamble, S.L., Civitello, E.R. and Stearns, D.M. (2003) Uranyl acetate causes DNA single strand breaks in vitro in the presence of ascorbate (vitamin C). Chem. Res. Toxicol. 16, 524-530.

Zachara, J.M., Kukkadapu, R.K., Fredrickson, J.K., Gorby, Y.A. and Smith, S.C. (2002) Biomineralization of poorly crystalline Fe(III) oxides by dissimilatory metal reducing bacteria (DMRB). Geomicrobiol. J. 19, 179-207.

Zachara, J.M., Long, P.E., Bargar, J., Davis, J.A., Fox, P., Fredrickson, J.K., Freshley, M.D., Konopka, A.E., Liu, C., McKinley, J.P., Rockhold, M.L., Williams, K.H. and Yabusaki, S.B. (2013) Persistence of uranium groundwater plumes: contrasting mechanisms at two DOE sites in the groundwater-river interaction zone. Journal of contaminant hydrology 147, 45-72.

Zeng, H. and Giammar, D.E. (2011) U(VI) reduction by Fe(II) on hematite nanoparticles. J. Nanopart. Res. 13, 3741-3754.

Zeng, Z. and Tice, M.M. (2014) Promotion and nucleation of carbonate precipitation during microbial iron reduction. Geobiology 12, 362-371.

Zhang, G., Senko, J.M., Kelly, S.D., Tan, H., Kemner, K.M. and Burgos, W.D. (2009) Microbial reduction of iron(III)-rich nontronite and uranium(VI). Geochim. Cosmochim. Acta 73, 3523-3538.

Zhang, G.X., Burgos, W.D., Senko, J.M., Bishop, M.E., Dong, H.L., Boyanov, M.I. and Kemner, K.M. (2011) Microbial reduction of chlorite and uranium followed by air oxidation. Chemical Geology 283, 242-250.

Zhang, M.N., Ginn, B.R., Dichristina, T.J. and Stack, A.G. (2010) Adhesion of Shewanella oneidensis MR-1 to Iron (Oxy)(Hydr)Oxides: Microcolony Formation and Isotherm. Environ. Sci. Technol. 44, 1602-1609.